NORTHWESTERN UNIVERSITY

Materials and Structures for the Electrodes of Solid-State Electrochemical Energy Devices

A DISSERTATION

SUBMITTED TO THE GRADUATE SCHOOL

IN PARTIAL FULFILLMENT OF THE REQUIREMENTS

for the degree

DOCTOR OF PHILOSOPHY

Field of Material Science and Engineering

By

Shobhit A Pandey

EVANSTON, ILLINOIS

December 2021

Abstract

Electrochemical devices play a vital role in the efforts towards a sustainable green future. Solid acid based electrochemical cells, employing super protonic CsH_2PO_4 (CDP) as the electrolyte component, offer unique application advantages due to their operability at intermediate temperatures 250°C. At these temperatures, one can achieve improved reaction kinetics over cooler operating systems and advantages in cost, portability, and system complexity over warmer operating systems. This thesis focuses on both (i) improving the performance and stability of known solid acid fuel cells (SAFC) by applying thin films for cathode fabrication, and (ii) advanced synthesis, characterization, and stability of oxynitrides materials as potential catalysts in CDP based solid acid devices. These oxynitrides are then demonstrated as effective catalysts in proof-of-concept Solid Acid Electrolyzer cells (SAEC). Furthermore, SAECs complement SAFC by producing H_2 from steam splitting at mid temperatures.

First, in an application-focused study, Pt thin films by atomic layer deposition on CDP were applied for Solid Acid Fuel Cell (SAFC) cathodes. Low temperature ALD recipe using ozone at 150°C was optimized to coat Pt films on CDP, resulting in a growth rate of 0.09 ± 0.01 Pt wt%/cycle. Smooth, fully conformal films were obtained after 200 deposition cycles. ALD Pt@CDP based SAFC cathodes show good performance of ~0.5 V for a current density of 200 mA/cm^2. The overpotentials were found to be relatively insensitive to the Pt loading, thereby minimum catalyst utilization. Excellent stability over 100hrs was observed.

Next, several oxynitrides materials, both metallic and semiconducting, were synthesized via ammonolysis and evaluated for their stability with CDP for potential application in Solid acid devices. Out of 9 oxynitride systems pursued, two stable candidates: Tantalum and Molybdenum Oxynitrides, were evaluated in more detail. Controlled ammonolysis was performed to optimize recipes for phase pure products. Introduction of slight humidity during ammonolysis, termed as Wet ammonolysis, was demonstrated as an effective way for tuning the phase of final products. Specifically, wet ammonolysis was shown as a new route to prepare δ-phase molybdenum oxynitride from oxide precursor

Subsequently, a comprehensive chemical and structural characterization study of all 4 phases of molybdenum oxynitrides was conducted. Nominally treated as nitrides in literature, we show that conventional ammonolysis of oxides, in fact, results in hydride incorporated Molybdenum oxynitride phases $Mo_{1-x}(N_{1-y}O_y)H_z$. Combined synchrotron and neutron refinement informed by a gamut of chemical characterization techniques was used to determine the true chemistry, structure and overall chemical tunability of these molybdenum oxynitride phases

Finally, a proof on concept application study of new SAEC devices was performed. Tantalum and Molybdenum oxynitrides from previous studies were demonstrated as promising oxygen evolution and hydrogen catalysts for steam splitting at 250°C. Several phases of these oxynitrides were evaluated. Ta-O-

N based SAEC anodes resulted in phase insensitive yet promising OER performance of upto 2.5 mmol $O_2/cm^2/h$@1.5V, higher than reported Ir-RuO_2 based PEM cells. Similarly, excellent HER performance and stability was observed using Mo-O-N based SAEC cathodes, with all phases giving, upto >10 mmoles of $H_2/hr/cm_2$ @0.75V. In addition, performance was found to be phase-sensitive, with hexagonal phase pushing the HER rate upto 15.8 mmoles of $H_2/hr/cm_{2.}$@0.75V.

Acknowledgements

First and most importantly, I would like to thank my advisor, Professor Sossina Haile, for having me as part of her group. Apart from her continual research guidance throughout my PhD, she was always present to lend her ear as an empathetic listener and supporter throughout my time at Northwestern University. Approaching any research problem as a scientific detective through a hypothesis-driven approach and training your mind to update the understanding of the research problem with new pieces of evidence is a habit she taught me over the years. I would also like to thank my internal committee members Professor Michael Bedzyk and Professor James M Rondinelli, for providing helpful guidance for my research, both as committee advisors and research collaborators. I would also like to thank my external committee member Nathan P Guisinger from Argonne National Laboratory, for being on my committee and providing his guidance. Nathan was also the one who introduced him to the fascinating world of surface science and the advanced tools associated with it through his graduate class, which also offered a wonderful tour to Argonne National Laboratory. Later, he also provided me with valuable teaching experience when I was a teaching assistant for him later, for the same course. Thanks to Professor Scott Barnett, who was also part of my qualifier defense committee and provided valuable insights into my research plan for PhD. Of course, I would like to thank all the professors who taught me various courses during the first two years at Northwestern, which has helped me strengthen my overall material science knowledge and develop my structured problem-solving skills. I would also like to thank Professor Vinayak P Dravid for being an additional mentor and a great collaborator throughout my time here at Northwestern. I will miss the occasional bumping into him in the MSE corridors and leaving much more energetic and motivated each time after our stimulating conversations.

I also owe a deep sense of gratitude to my various senior colleagues who have offered me support. I have been fortunate to work with several of them on collaborative projects throughout my PhD. In this regard, I would like to thank my first research project team on the SAFC project involving Dr. Haemin Paik, Dr Vanessa Owen and Dr Hadi Tavassol. Vanessa helped me fabricate my first solid acid fuel cell as a button cell back in 2016. Special thanks to Dr Haemin Paik, who worked with me and guided me on setting up the SAFC electrochemical testing station. I enjoyed working on several mini projects with her during our overlapping times as graduate students. I fondly owe my several electron microscopy sample making skills to her. I am also very thankful to Dr Chris Kucharczyk for always motivating me with his thoughtful high throughput approach to research ideas. He was the one who introduced me to efficient data analysis using Python and helped me with lab view debugging numerous times. I would also like to thank Dr. Timothy Davenport, Dr. Michael Ignatowich and Anupama Khan for interactive discussions and for helping me lend a hand in research work when needed. Many thanks to Dr. Sheel Sanghvi, who was there as a friend and as a scientific detective helping me brainstorm past several

research questions I had during my PhD. Thanks to Dr. Dae-Kwang Lim, who worked as my cohort in the SAFC project (chapter 2), I learned the nuances of effective SAFC fabrication from him. I remember our learning experience together debugging the SAFC testing station innumerous times. He always inspired me with his kindness and dedication. It would be incomplete without thanking Jill Kathleen Wenderott, who I worked with extensively on the oxynitride projects (chapters 3 and 4) for the last three years of my PhD. More than a mentor and a colleague, she was always there as a friend motivating me to give my best. I will particularly cherish our moments together as HAMsters- a word she coined for our heteroanionic materials group. Additionally, I would like to thank Dr. Ara Jo for our extensive scientific discussions and occasional Korean goodies that she used to surprise us with. Also, thanks to Dr. Abdulmenan Hussein, Dr. Emanuela Mastronardo, Dr. Sihyuk Choi and Dr. Dahee Lee for helpful advice on several research topics and for providing a helping hand when needed.

My time and research at Northwestern wouldn't be the same without my fellow graduate students within the group. I had the opportunity to collaborate with several of them over numerous projects. Specifically, I would like to thank Ellise Goldfine, who constantly collaborated with on the oxynitride project as part of the NSF MRSEC IRG 2 project. Her In-situ XRD experiments were critical in corroborating the oxynitride research discussion presented in chapters 3 and 4. Research would not be as fun without the amazing group of graduate colleagues with whom I shared my upstairs office, our second home. Thanks to Dr. Xin Xu, Dr. Weizi Yuan, Dr. Ruiyun Huang and Dr. Austin Plymill for all the deep scientific conversations followed by sheer joy and laughter in discussing the craziest current affairs. Thanks to my group cohorts Xin Qian, Connor Carr, Dalton Cox, Grace Xiong, Paul Cherry, Patrick Donahue, and Trevor Worthy for providing constructive feedback during my group talks and support throughout. Special thanks to Louis Wang, yet another solid acid team member, for helping me get trained on the TGA instrument. Finally, thanks to my bantering buddies, Isaac Dyer and Dylan Bardgett, I always enjoyed stimulating research discussions and occasional off the chart banters.

The research presented in this work would not have been possible without help from various collaborators beyond the Haile Group. In chronological order, I would like to thank Dr. Calum Chisholm from SAFCell Inc. for being part of the ARPAE project to push research boundaries in the field of SAFC. I have always admired how his positive outlook towards sustainable technologies as a researcher & entrepreneur. Thanks to Jian Liu from Joseph T Hupp's group at Northwestern University for collaborating on ALD processing for the SAFC project. I was grateful to be a part of NSF's fantastic MRSEC IRG 2 project at Materials Science and Engineering department, focused on heteronomy materials. As a part of this multi-PI, multi-institute collaborative research initiate, I collaborated with several researchers across the USA, on the oxynitride project discussed in chapters 3 and 4. On this note, I would like to thank Chi Zhang from Vinayak P Dravid's group at our department for all the supportive TEM work in this work. Her EELS and HRTEM analysis, including SADP studies, provided crucial corroboration in understanding the

chemistry, morphology and structure of oxynitride samples (specifically molybdenum oxynitrides) as part of the MRSEC IRG 2 group. Thanks to Professor Gabriela Gonzalez, from Depaul University for providing her expertise in performing the synchrotron and neutron core refinement analysis as discussed in chapter 4. Also, thanks to her students Daniah Ibrahim and Shriya Sinha, for helping with the co-refinement analysis in various capacities. Special thanks to Rick L Paul and Heather Chen-Mayer from NIST for performing the PGAA measurements on the molybdenum oxynitride samples. Thanks to Sawankumar Patel from Professor Yan-Yan Hu's group at Florida State University for performing NMR studies on oxynitride powders. Thanks to Ioannis Spanopoulos from Mercouri Kanatzidis group for conducting the pycnometry measurements on molybdenum oxynitride powders. I am super thankful to Jiahong Shen, from Professor Chris Wolverton group, who patiently performed several DFT calculations for the oxynitrides study as part of the MRSEC IRG2 effort, a glimpse of which is presented in Appendix. The oxynitride powders synthesized in this work are actively being used for various applications by our collaborators. On this front, I would like to thank Neil M Schweitzer from REACT Northwestern and Sirui Chen from our group for pursuing acetylene hydrogenation and butene isomerization with the synthesized molybdenum oxynitrides. These powders are also being used for HER liquid electrochemistry catalysis, by Matthew Sweers, from Professor Linsey Seitz group. Several facility managers at central research facility labs at Northwestern University have helped me throughout my PhD at Northwestern University. Thanks to Jerrold A Carsello for training me on various XRD instruments at J.B Cohen X-Ray Laboratory. Selim Alayoglu for training me on TPR measurement in REACT. Xinqi Chen for XPS training and help with generic XPS analysis questions. Rebecca Sponenburg from Quantitative Bio-Imaging Center (QBIC) for training me on ICP-OES and ICP-MS techniques, and spending hours figuring out recipes to dissolve powder samples for ICP analysis. Thanks to John Ciraldo, and William Mohr from NU-Fab Clean room for training me on ALD. Thanks to various other staffs from NUANCE EPIC and NUANCE Keck -Biophysics facilities for training me on several critical characterization techniques such as UV-VIS spectrsocopy, Raman Spectroscopy, Secondary ion mass spectroscopy (SIMS), Ellipsometry, Profilometry, Optical and electron microscopes, and AFM.

I would also like to acknowledge my funding sources for various research projects conducted at Northwestern. The work on thin-film based solid acid fuel cells would not have been possible without the financial support from the Advanced Research Projects Agency-Energy (ARPA-E) - Department of Energy (DOE). Similarly, the research project focusing on the preliminary synthesis of various oxynitrides and their stability with CDP was funded by Qatar National Research Fund (QNRF). Finally, I would like to thank NSF for funding the MERSEC IR2 project, without which the extensive collaborative research critical for characterizing oxynitride materials would not have been possible.

I would be remiss if I did not acknowledge my undergraduate research mentors who inspired me to pursue my Ph. D. in the first place. First and most important, many thanks to my mentor and friend,

Professor Anchal Srivastava, from the Department of Physics, Banaras Hindu University, who guided me throughout my undergraduate years to work on numerous 2-D layered nanomaterials-based projects in his Solid State Physic Lab. He taught me the importance of collaborative research to achieve high throughput results and constantly encouraged me to pursue a PhD. I particularly miss strolling down the streets with him to get a cup of tea together while enjoying deep conversations on science and life. I have fond memories of working with several of his, and Professor Preeti Saxena's graduate students from the Department of Zoology, Banaras Hindu University. On this note, thanks to Dr. Siju Abrahim, Dr. Narsingh Nirala, Dr. Sima Umrao and Dr. Himanshu Mishra for providing hands-on experience for materials synthesis, characterization and device fabrication for interdisciplinary applications ranging from Biosensing to Photo-thermal Cancer therapy. I would also like to thank all my professors from Metallurgical Department, Indian Institute of Technology, for teaching me fundamental metallurgical and materials science courses, building the theoretical foundation for my Ph.D. Special thanks to Professor Bratindranath Mukherjee for providing hands-on experience in his lab, and being there as a friend sharing his graduate days memories, motivating me always to be a good person and researcher at the same time. Thanks to Professor Rampada Manna, Professor G.V.S Sastri, Professor N.K Mukhopadhyay and their graduate students, specifically Dr. Deepa Verma for guiding on my B.Tech project on studying mechanical properties of processed interstitial free steel, and introducing me to various analytical and structural materials characterization tools. Thanks to several other undergraduate research cohorts from IIT-BHU who worked with me on various research projects in different capacities. My motivation to join industrial research after my PhD stems its roots from the two summer internships at GE Joh. F. Welch technology global research center, and BHEL R&D center. Special thanks to Prashant Patil and Dr. Anand K from GE who guided me on techno-economic modelling project on GE gasifier plant project.

Finally, I would like to thank my friends and family who have been my emotional pillars showing immeasurable love and support throughout my academic journey. Thanks to my parents, Arvind and Ksahama Pandey, who always believed in me and taught me to become the human I am today. Thanks to my grandparents Moolchandra and Kamala Pandey, whose constant blessings help me tackle all the difficulties life throws at me. Thanks to my loving little brother Satvik Pandey, who I grew up wondering about the world, and who is always there for me. Thanks to my lovable 3 aunts who always supported me in PhD throughout. Special thanks to my loving girlfriend Gomti Bansal for being my lifeline and constant support throughout my Ph.D. Even when times are tough, she makes every day better, and I look forward to several such memories ahead. Thanks to my brother like friends Rohit Agrawal and Tushar Chaudhary for providing much needed banters during stress full times. Our historic escapades make for bonds impossible to break, but our most extraordinary adventures still lie before us. Thanks to all my undergraduate and school friends at different junctures of my life, who supported, motivated and appreciated my academic progression in life in various capacities. Special thanks to my school friends

Pranav Popat and Arun Gandhi, with whom I share several of my childhood memories, and for always being there to discuss and enjoy life at lengths. Finally, thanks to all my well-wishers, who always believed in me.

List of Abbreviations

AFC	Alkali Fuel Cell
ALD	Atomic Layer Deposition
BET	Brunauer–Emmett–Teller
CA	Chronoamperometry
CDP	Cesium Dihydrogen Phosphate, CsH_2PO_4
CVD	Chemical Vapor Deposition
DR UV-VIS	Diffuse Reflectance Ultra-Violet Visible Spectroscopy
DFT	Density Functional Theory
EDS, EDX	Energy Dispersive X-ray Spectroscopy
EIS	Electrochemical Impedance Spectroscopy
EELS	Electron Energy Loss Spectroscopy
EXAFS	Extended X-ray Absorption Fine Structure
GDL	Gas Diffusion Layer
HER	Hydrogen Evolution Reaction
HOR	Hydrogen Oxidation Reaction
MCFC	Molten Carbonate Fuel Cell
MPL	Microporous Layer
MOCVD	Metal-organic Chemical Vapor Deposition
NPD	Neutron Powder Diffraction
ND	Neutron Diffraction
NMR	Nuclear Magnetic Resonance Spectroscopy
PGAA	Prompt Gamma Activation Analysis
ICP-OES	Inductively Coupled Plasma - Optical Emission Spectrometry
OCV	Open-circuit Voltage
ORR	Oxygen Reduction Reaction

OER	Oxygen Evolution Reaction
PAFC	Phosphoric Acid Fuel Cell
PEMFC	Polymer Electrolyte Membrane or Proton Exchange Membrane Fuel Cell
SAEC	Solid Acid Electrolyzer Cells
SAFC	Solid Acid Fuel Cell
SAPEC	Solid Acid Photo Electrolyzer Cell
SEM	Scanning Electron Microscopy
SOEC	Solid Oxide Electrolyzer Cell
SOFC	Solid Oxide Fuel Cell
TEM	Transmission Electron Microscopy
TGA	Thermogravimetric Analysis
TPD	Temperature Programmed Desorption
TPR	Temperature Programmed Reduction
UHP	Ultra-high Purity
XAS	X-Ray Absorption Spectroscopy
XANES	X-ray absorption near edge structure
XPS	X-ray Photoelectron Spectroscopy
XRD	X-ray Diffraction
In-situ XRD	In-situ X-Ray Diffraction Studies

Dedication

To my mother, Kshama Pandey

for her blessings and building me up to the human I am

To my father and idol, Arvind Pandey

who inspired and supported me to make something of myself

To my beloved little brother, Satvik Pandey

who I wish the most successful and happy life ahead

To my friends and family,

who were always there for me every step of the way

Table of Contents

List of Figures

List of Tables

Chapter 1 Introduction/ Overview

Increasing energy demand globally, leading to the inevitable global energy crisis, along with the rise in toxic gas emissions, has put immense efforts in the past decades to speed up renewable energy research.[1-3] Fossil fuels still remain as the primary fuel energy source for the world (coal, oil and natural gas), however with the world slowly realizing the carbon footprint consequences and the fact that many of these non-renewable fossil fuels are depleting fast, several efforts are being in the areas of Solar, Hydrothermal and other renewable resources.[1] However, the intermittent nature of energy production by renewable sources such as wind, solar, hydro, or geothermal calls for effective energy storage strategies.[4-6] Additionally, along with the development of efficient carbon-neutral, carbon-free, and in some cases carbon-negative too.[7] Efforts are also being taken to recapture and re-use carbon dioxide combustion products by developing carbon capture technologies.[8-10] Alternate energy-based economies, where in alternate fuels other than fossil fuels would be used, are an important step towards sustainable development.[11]

Within this sustainable energy umbrella, a concept called the “hydrogen economy” based on a H_2 energy system (originally put forward in the 1970s) is largely pursued, in which hydrogen is the major energy vector, given its low carbon footprint and high energy density (310 kWh/m3).[12, 13] Such an economy relies on developing efficient technologies for hydrogen production using renewable routes, and its subsequent storage, transportation, and usage as fuel. Since the last several decades, hydrogen technologies have been through cycles of excessive expectations followed by disillusion. However, more recently, with improvements in their cost and performance, hydrogen-based technologies not only provide deep decarbonization potential, but also is becoming more and more economically viable.[14]

Within the hydrogen economy, electrochemical devices, specifically solid state electrochemical devices, are increasingly being sought for various energy conversion and storage applications, owing to their high efficiencies, compact structures, and promise of carbon-free closed-loop energy cycles.[15-17] Among these, solid acid electrochemical cells are recently being sought after. Several applications have previously been studied by our lab (Haile Group), using the featured CDP electrolyte. For example, CDP

based Solid Acid Fuel cells (SAFC) that produce clean electricity from hydrogen have been demonstrated as a new emerging class of Fuel cells in the recent past.[16, 18-22] These (CDP) based Solid acid electrochemical devices, including the SAFCs, have a distinct advantage over traditional electrochemical systems in that they can operate at intermediate temperatures near 250 °C. By operating at mid temperatures, these CDP based devices enjoy improved kinetics over cooler operating systems while lowering noble metal catalyst demand or completely getting rid of it, thereby providing a cost-effective solution too. Additionally, an solid state design lowers the cost of auxiliary systems necessary to deal with corrosive liquids.[23] At the same time these systems do not suffer from thermal cycling issues, nor do they require expensive thermally resistant auxiliary systems, as in the case of high temperature Solid oxide fuel cells (>600^{o}C).[24, 25] Therefore CDP based solid acid electrochemical devices bring the best of low temperature and high temperature world for electrocatalytic energy conversion applications. Another CDP based device Solid Acid Hydrogen Pump, which produces hydrogen via efficient ammonia decomposition, has also been recently realized.

The key featured solid acid electrolyte in this work in Cesium dihydrogen phosphate (CDP). In general, solid acids have the generic chemical form of $MHXO_4$, MH_2XO_4 or $M_3H(XO_4)_2$, where M can be an alkali metal or an ammonium ion and X = P, A, S, Se.[26] These represent a class of compounds with unique properties that are intermediate to those of a normal salt and those of a normal acid. In these structures oxyanions $XO_4^{2-/3-}$ are linked by hydrogen bonds and charge balanced by large cations M^+. Near room temperatures, most solid acids with super protonic phase transitions have monoclinic symmetry and the structural protons lead to protonic conductivity of the order of Log(σ) ~ -6 to –9 in most solid acids (due to local defects in the structure and subsequent protonic hopping). However, upon raising temperature, these solid acids undergo structural polymorphic order -disorder super protonic phase transition into higher symmetry structure which is accommodated by oxygen becoming disordered, leading to high ionic conductivity (10^{-2} $\Omega^{-1}cm^{-1}$).[20, 27, 28] With ionic conductivity, approaching that of state of the art of solid electrolytes, Cesium dihydrogen phosphate CsH_2PO_4 (CDP) is one of the most promising super protonic solid acids, showing transition (ordered monoclinic to disordered cubic) at 230° C upto 260°C, where the upper limit is dictated by the dehydration of the solid acid, which can be suppressed by

increasing the water partial pressure in the application as an operating condition in all of the solid acid electrochemical devices studied in this work.

This thesis focusses on advancing the CDP based Solid Acid Electrochemical devices research by both, (i) improving the performance and stability of known solid acid fuel cells (SAFC), and (ii) exploring oxynitrides as potential catalysts for applications in previously known and/or newly proposed CDP based Solid Acid Electrochemical device. Specifically, oxynitride catalysts were demonstrated as effective hydrogen evolution and oxygen evolution catalysts in a proof of concept study of Solid Acid Electrolyzer Cells (SAEC). SAEC complement SAFCs, by producing fuel (H_2) from steam splitting at mid temperatures. Therefore, all three critical areas of applied materials research, that is synthesis, characterization and application were pursued in this work in an attempt to advance CDP based Solid acid electrochemical devise research.

Chapter 2, is an application focused study, where the advantages of using thin films cathodes in Solid Acid Fuel Cells was pursued. Pt thin films by atomic layer deposition on CDP were applied for Solid Acid Fuel Cell (SAFC) cathodes. Particularly challenging was optimizing the Pt recipe, on thermally fragile CDP electrolyte powders, which degrade beyond 150^{o}C with proper operating humidity level as discussed above. Low temperature ALD recipe using Pt metal organic precursor and ozone at 150^{o}C was optimized to coat Pt films on CDP resulting in a growth rate of 0.09 ± 0.01 Pt wt%/cycle. Smooth, fully conformal films were obtained after 200 deposition cycles, and morphology studies were conducted. These were then used to make ALD Pt@CDP based SAFC cathodes, which were tested for Fuel Cell performance. Pt ALD based SAFCs showed good performance ~0.5 V for a current density of 200 mA/cm$_2$, where the effect of Pt loading and crystallite size was studied. Studies over a period of 100hrs were conducted to test the resilience of these SAFC cells. The Pt films coated by ALD showed several advantages over in-housed coated MOCVD films, and a comparative study highlighting the advantages and disadvantages of Pt ALD is also included. Finally, the chapter ends with future outlooks of using ALD for next generation SAFC cathode fabrication.

Chapter 3, shifts focus on synthesis of oxynitride materials, in order to screen them as potential non-noble catalysts for applications in CDP based solid acid electrochemical devices. For CDP based applications, it is critical for these oxynitrides to show good stability by itself and with CDP under the operating conditions of solid acid-based devices. For this stability tests were carried out to screen the as synthesized oxynitride samples, which have been categorized into metallic and semiconducting oxynitrides. Two highlight stable systems, one form each, Tantalum Oxynitrides (semiconducting and known photo-active catalyst), and Molybdenum Oxynitrides (known metallic electrocatalyst, although referred as nitrides in literature) were evaluated in more detail. Controlled ammonolysis was performed to optimize recipes for phase pure products in these oxynitride systems. Specifically, introduction of humidity during ammonolysis (called as “Wet ammonolysis”) was demonstrated as an effective way for tuning the phase of final oxynitride products. For example, some pH_2O in NH3 stream while performing the ammonolysis of Ta2O5 @850oC, was realized as a reproducible way to suppress the competing complete nitride phase. Preliminary studies showing the dependence on pH_2O for choosing between the two competing oxynitride phases (β and γ – TaON) is also discussed. Finally, the pH_2O was optimized to get phase pure β-TaON which is later used for applications. For the Molybdenum Oxynitride system, ammonolysis of carious molybdenum oxide precursor under numerous dry and wet ammonolysis conditions was evaluated. Optimized recipes, were realized for phase pure synthesis of products that can be nominally matched to the 4 molybdenum nitride phases mentioned in literature (later in Chapter 4, these are all determined as Molybdenum Oxynitride hydride). For the most studied cubic y-phase system, dry ammonolysis of MoO3 at high temperatures (700-800^{o}C), is often the most common method of synthesis producing high surface area cubic y-phase powders. However, there are several hypothesis in literature of how this reaction proceeds. In this work, through collaborative studies with , the reaction pathways of this ammonolysis process was probed using both ex-situ and collaborative in-situ XRD studies. Finally, wet ammonolysis was demonstrated as a new route to prepare δ-phase molybdenum oxynitride starting from an oxide precursor. δ-phase in literature is synthesized using non-oxide based Mo precursor nitridation reactions, and is reported as a stoichiometric nitride δ-MoN.[29] Via wet ammonolysis, and oxynitride matching to the structure of δ-phase can be synthesized. The chapter ends with a brief

summary of various collaborative application studies that are being pursued to apply the synthesized Tantalum and molybdenum oxynitride samples.

Chapter 4, is characterization focused, where in literature gaps in understanding the synthesis and true chemistry and structure of molybdenum nitride synthesized via ammonolysis of oxide precursors. For example, in the case of Cubic γ-phase, in a handful of studies, it has been recognized that, despite displaying a readily recognized diffraction pattern, the product of this reaction can, in fact, retain a substantial oxygen content such that the material may be more appropriately considered a molybdenum oxynitride.[28-31] Although deviations from the 2:1 stoichiometric ratio are rather widely recognized,[22] the extent to which the true stoichiometry (reported as Mo_2N, rock salt anion deficient structure) can be tuned is not well-established. Therefore to address this, this chapter shows a comprehensive chemical, crystallographic, electronic, and morphological study of both Cubic and Hexagonal molybdenum nitride phase synthesized in Chapter 3, via ammonolysis of precursor oxides either under dry (Cubic samples) or humidified NH_3 gas. A gamut of chemical characterization techniques including PGAA, combustion analysis, TGA, EELS, XPS were performed to compare the cubic samples synthesized at two different ammonolysis temperatures (700^{o}C and800^{o}C), and also the hexagonal phase. These ammonolysis derived products were conclusively determined as being hydrogen incorporated Molybdenum Oxynitrides with generic formula $MoN_xO_yH_z$. Using these compositions to inform models, the structure of each phase is determined by Rietveld refinement using combined synchrotron X-ray diffraction (XRD) and neutron diffraction (ND) data. The study reveals that these are actually anion rick structures, with the presence of Mo vacancies, and in some cases anion vacancies too. We also comment on the shortcoming of using X-ray and electron based techniques (used in most molybdenum nitride research) in not being able to correctly characterize the structure of these materials to date. Overall, for the first time, the crystal structure of Molybdenum oxynitrides have , mapping the overall cation and anion distribution in these phases, and untapped tunability potential that these oxynitrides have to offer. The clarification provided here of the true composition and crystal chemical features of the product of these heavily studied γ and δ phases obtained via ammonolysis of molybdenum oxides, provides an essential grounding for

understanding the structure-property relations in this widely employed material, therefore having wide implication beyond just the solid acid electrochemical cells.

Chapter 5, is again an application focused study, wherein Tantalum and Molybdenum Oxynitride phase samples synthesized and characterized above in chapter 3 and 4, were tested as electrocatalysts for proof of concept Solid acid electrolyzer cells (SAEC) cells based on CDP electrolyte, operating at 250^{o}C. Just like SAFC, by operating at intermediate temperatures, SAEC enjoy improved kinetics and lower electrical energy requirement for water splitting compared to commercialized alkaline water and PEM electrolyzer cells (<100oC operating temperature). At the same time, SAEC are do not suffer from the cycling issues and high-cost requirement for thermal components as in the case of SOEC (>600^{o}C operating temperature). Several phases of these oxynitrides were evaluated for both of these systems. Ta-O-N phases are demonstrated as effective Oxygen evolution reaction catalyst in SAEC anodes, with upto 2.5 mmol $O_2/cm_2/h$@1.5V rate, higher than reported Ir-RuO_2 based PEM cells. Phase sensitivity and performance stability with time was also evalated by comparing performance of mixed and phase pure oxynitride based SAEC cahodes. Increased initial performance by using nano sized TaON powder is also discussed, along with the concerned stability issues of these nano-TaON based SAEC cells. In contrast, Molybdenum oxynitrides were realized to be unstable in oxidative conditions, however auxillary experiments demonstrated their good stability under reducing conditions. Therefore, molybdenum oxynitrides were evaluated as HER catalysts for proof of concept SAEC study. Excellent HER performance with good stability was observed using Mo-O-N based SAEC cathodes, with all phases giving, upto >10 mmoles of $H_2/hr/cm_2$ @0.75V. Performance was found to be phase sensitive, with hexagonal phase pushing the HER rate upto 15.8 mmoles of $H_2/hr/cm_2$.@0.75V. Chemical and structural information of these molybdenum oxynitrides determined via detailed characterizations in Chapter 4 were revisited to hypothesize the reasons for such performance difference. Finally, the chapter ends with future outlook on how thin films of these oxynitrides can be used in make next generation SAEC cells. Motivated from results in Chapter 1, ideas prosing ALD films of these oxynitrides for SAEC electrode fabirication is discussed. Advantage of such thin film approach, in improving catalysis is discussed proposing schematics of expected OER and HER evolution reaction pathways in such a SAEC cell. As an appendix

study, successful ALD of Molybdenum oxynitride films are also demonstrated. As a bonus content, yet another future outlook, of extending the application of SAEC to SAPEC. SAPEC stands for Solid acid photoelectrolyzer cells, which are conceptualized as new devices for high temperature solar steam splitting. Such a system would enjoy all the thermodynamic and electrocatalytic advantages of SAEC system, however instead of using electrical energy to drive electrolysis, solar energy will be used.

Chapter 2 ALD for Solid Acid Fuel Cell (SAFC) Cathodes

2.1 Introduction

Hydrogen economy is the only long-term sustainable renewable fuel-based energy alternative, and fuel cells are a key part of it.[1, 13] Fuel cells provide a way for using hydrogen as a clean energy vector for portable applications releasing water as the only by product into the environment.[30-35] Fuel cells have different operating temperature ranges. Operation at high temperatures (example: solid oxide fuel cells (SOFCs) and molten carbonate fuel cells (MCFCs)) improves fuel flexibility, kinetically favored higher efficiency, however, difficult thermal cycling, and costly supporting components are key issues, limiting their application in stationary power generation. Lower temperature fuel cells on the other hand offer rapid thermal cycling (example: polymer electrolyte membrane fuel cells (PEMFCs)) but requires the use of expensive and higher loadings of noble metal catalysts.[33, 36, 37] By operating at intermediate temperatures, Solid Acid Fuel Cell (SAFC) system are unique in bringing the best of the two worlds[18-20, 38-42]. In SAFC, protons are transported across the electrolyte while electrons are transported through an external circuit as the oxidation reduction reaction (ORR) occurs at cathode (working electrode) and hydrogen oxidation reaction (HOR) occurs at the anode (counter electrode), where the fuel (H_2) is fed as shown in Figure 2.1-1. More detailed discussion on SAFCs can be found in multiple thesis from our Haile Group, who work on the forefront of SAFC research.[16, 22, 27, 38, 43]

Half Cell Reactions

CE : Anode :

Hydrogen oxidation reaction (HOR)

$H_2 \rightarrow 2e^- + 2H^+$

WE : Cathode :

Oxygen reduction reaction (ORR)

$1/2O_2 + 2H^+ + 2e^- \rightarrow H_2O$

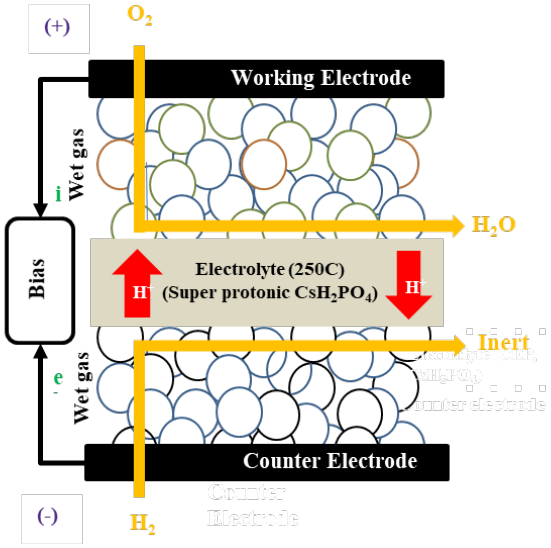

Figure 2.1-1 Schematic of SAFC with HOR and ORR half cell reactions shown.

SAFC commercialization faces several challenges, including pushing peak power output close to competitive PEMFCs or SOFCs, lowering the Pt loading requirement, overcoming high over-potential losses specially at the electrodes and maintaining the high catalytic activity. Figure 2.1-2a shows that the ohmic losses at the electrolyte (which can be reduced by making electrolyte thinner) or the electrode thickness have a small effect on polarization losses in comparison to slow electro-catalysis at the electrodes.[20, 44] Figure 2.1-2b shows that the activation polarization at the cathode for ORR is much higher than for the HOR at the anode (~ 2 orders of magnitude larger). Thus a standard half-cell is used comprising of (1) a support microporous layer formed from a mixture of acetylene carbon black (Alfa Aesar, 99.9%), naphthalene (Alfa Aesar, 99.8%), and CDP (in a 3:1:2 mass ratio), (2) an electrocatalyst layer formed of high surface area Pt on C (Alfa Aesar, 99.9%) and CDP (in a 1:6 mass ratio), and (3) an electrolyte layer, of 50 μm thick CDP resulting in pretty good HER and HOR catalysis, while avenues for improving the ORR catalysis have been explored in this work.

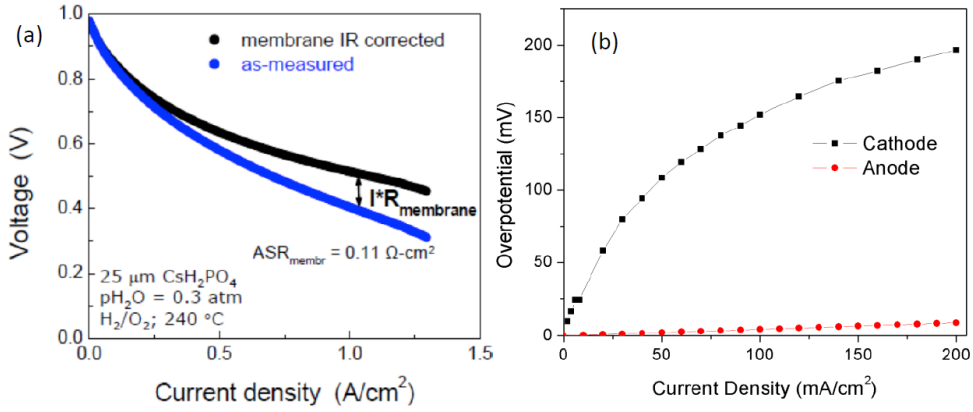

Figure 2.1-2 (a) IR corrected solid acid fuel cell polarization plot showing small ohmic losses in comparison to other sources of overpotential loss.[20] (b) Cathode (2 order higher) and anode contributions to the overpotential of a SAFC (Courtesy : Sasaki).[44]

2.2 Atomic Layer Deposition (Platinum thin films) for SAFC Cathodes

2.2.1 Motivation for thin films in SAFCs

Preliminary SAFCs electrodes including cathode, employed mechanical mixtures of ionic (the electrolyte) and electronic (Pt black and Pt on carbon) components.[18, 42] While essential at that time for demonstrating proof-of-concept with an easily fabricated cell, the approach resulted in excessive Pt loadings, ranging from 8 to 18 mg/cm^2 in the cathode alone. Recently, Papandrew et.al recognized that Pt connectivity and utilization in SAFC cathodes could be dramatically enhanced by application of a thin film of Pt onto fine CDP particles.[45] These coated particles (Pt@CDP) were then lightly pressed to generate a porous structure with an interconnected electronic conduction pathway. Such an approach results in reduced Pt loading.

As seen in Figure 2.1-1 reaction schematic, for a Pt/C based mechanically mixed electrode, the ORR on the catalyst is limited by the limited triple phase boundaries, where the e- from Pt/C catalyst (typical for mechanically mixed SAFC cathodes) can interact with both O_2 in gas phase and protons from the CDP based protonic pathway. Such boundaries are limited given the irregular shape of these catalyst

powders and different surface areas, and depends on how well the mixing was performed, adding to reproducibility issues in performance often. However much of the bulk catalyst is not effectively used for reaction activation, and merely provides the requisite e- conductivity. In contrast, in case of thin films based SAFC cathode, such active area/ active ORR catalysis sites are theoretically maximized by an ideal conformal thin film catalyst as shown schematically in Figure 2.1-1, with the entire double phase boundary between Pt-CDP being active. Since the active region is often small, very thin films can be used (thick enough for mechanical stability, and good electronic conductivity), thereby resulting in better catalyst utilization. Also, such thin films can allow the proton to pass through, thereby making the reaction happen and enhanced by the active sites throughout Pt-air double phase boundary. Metal organic chemical vapour deposition (MOCVD) and Atomic Layer deposition are two potential techniques, that can be used to fabricate Pt thin film based SAFC cathodes.

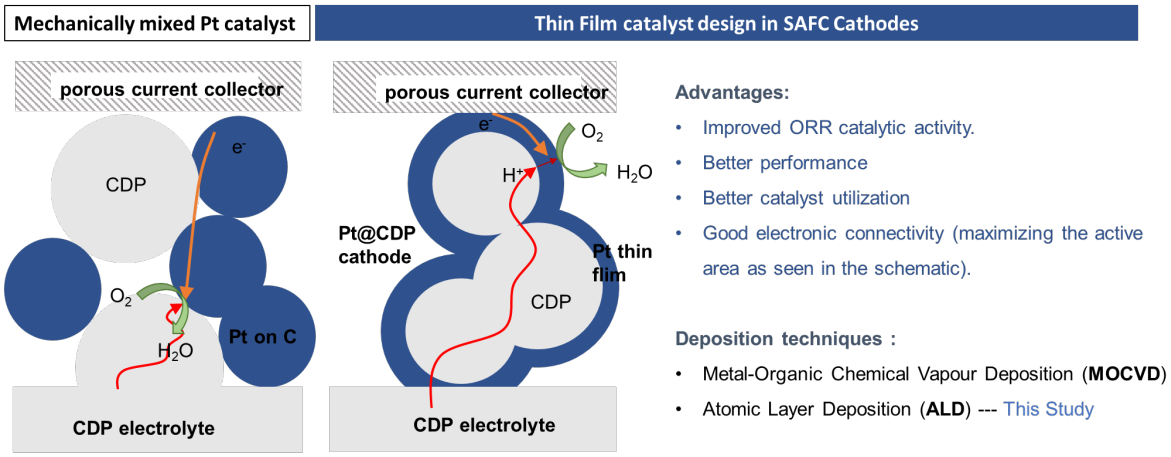

Figure 2.2-1 Reaction pathway for ORR reaction on SAFC cathodes, comparing the mechanically mixed vs thin film-based cathode fabrication approach. Several advantages offered by the Thin Film SAFC design are listed. The two common techniques applied for SAFC in Haile Group at Northwestern University for Pt deposition are MOCVD and ALD, with this work highlighting the use case of ALD.

2.2.2 MOCVD for SAFC Cathodes

Application of the Pt coating by MOCVD on SAFC have been pursued in the literature. MOCVD based SAFC cells were also studied for SAFC cathode (not discussed in this thesis). Typically, in-house MOCVD Pt deposition involves, milling platinum acetylacetonate ($Pt(acac)_2$), the Pt precursor, together with CDP, and then heating the mixture to a temperature (210°C) high enough to induce vaporization of the precursor and its decomposition on the CDP surface, with the precursor relative amount to CDP. The procedure generates a thin Pt coating on the CDP particles, the approximate thickness of which was controlled sim- ply by controlling the relative amounts of $Pt(acac)_2$ and CDP. A schematic of Pt MOCVD on CDP powder is shown in

While attractive in terms of low cost and ease of implementation, MOCVD does not lend itself to precise control of Pt morphology. In turn, this suggests challenges in tuning the process for optimal Ptutilization and in using such structures for elucidating the critical factors determining the oxygen reduction rate in SAFC. Furthermore,degradation of the cathode created by this process was noted as aremaining challenge in literature and in our in-house tested MOCVD based cells,[42] motivating us to try ALD which as discussed below has several advantages over MOCVD.

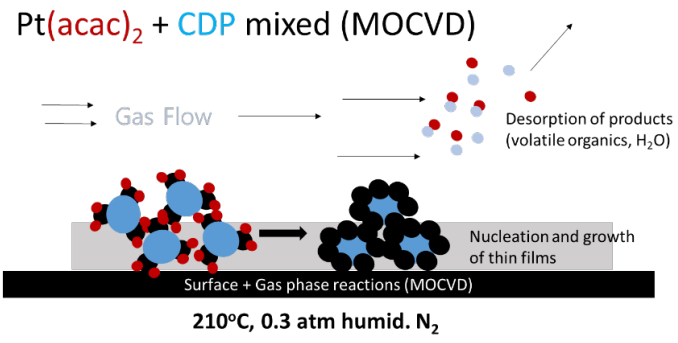

Figure 2.2-2 : MOCVD of Pt thin films on CDP powder.

2.2.3 Atomic Layer Deposition for catalysis (advantages over MOCVD)

Atomic layer deposition (ALD) has emerged as a remarkable process for deposition of conformal films of a wide variety of materials specially focused on catalysis.[46, 47] In case of MOCVD as seen in cartoon Figure 2.2-2, gaseous (or in our case mixed $Pt(acac)_2$ powder with CDP substrate) precursor reactants are co-introduced into a heated reaction chamber. At the requisite temperature, simultaneous homogeneous reactions, in the gas phase and heterogeneous reactions on and near the substrate (CDP powder surface in our case, and all around the chamber on hot surfaces) take place resulting in a film deposition.[46, 48]

ALD in principle is like CVD, except those precursors are separated from instant interaction, by sequentially introducing them into the reaction chamber with inert gas purge in between, and the deposition is achieved through self-limiting sequential chemical reactions between precursor vapors and the surface. Such “isolated” exposures of precursors and their subsequent purge, shown as “half cycles” in Figure 2.2-3 effectively inhibit the homogeneous gas phase reactions between precursors, making the deposition in a more controlled manor. Within the “self-limited window”, the idea is that the precursors diffusion time is enough to cover one monolayer of the precursors at least on entire substrate where the excess precursor is purged out completely by sufficient purge time after each precursor pulse, in each half cycles. Adequate presence of surface of substrate – precursor interaction is necessary for adequate precursor adsorbtion to cover the whole substrate or lead to complete conversion of Precursor A to final product film after reacting completely with Precursor B. Often the Silicon chips are pretreated in the electronics industry where ALD is often used for coating thin films oxides. Success of saturation withing each half cycles, depends on the number of reactive surface sites and steric hindrance of precursor ligands.[49] For our case, the CDP surface is expected to be populated with terminating hydroxyl groups, which should be such reactive site for bonding with precursor. Several other parameters such as precursor bottle temperature, delivery line temperature reaction pressure also dictate the success of having the adequate

precursor pressure for adequate time to achieve self-limiting growth. In general, Finally, for each ALD process, there is usually a temperature regime within which self-limiting growth can be achieved. This temperature regime is often called the “ALD process window”.[46, 47, 49-51] No growth due to nucleation barrier, or on the other side uncontrolled growth via condensation, or thermal decomposition of precursors must be avoided to achieve conformal deposition on substrates, especially in the case of catalyst synthesis. More details on mechanisms of ALD for catalysis can be found in review article by Luet.al from Stair group, Northwestern University,[25] and several other reviews.[47, 52-55]

Therefore, a typical ALD cycle consists of 2 half cycles **(**for depositing one monolayer of film), which usually have two steps in each. A 4-step simple binary ALD cycle (schematic shown in Figure 2.1-1) can be written as:

Half Cycle 1 (Precursor A → Purge) → Half Cycle 2 (Precursor B → Purge)

longer precursors dose times are required to achieve saturation on high surface area substrates, and powder materials.[56, 57]

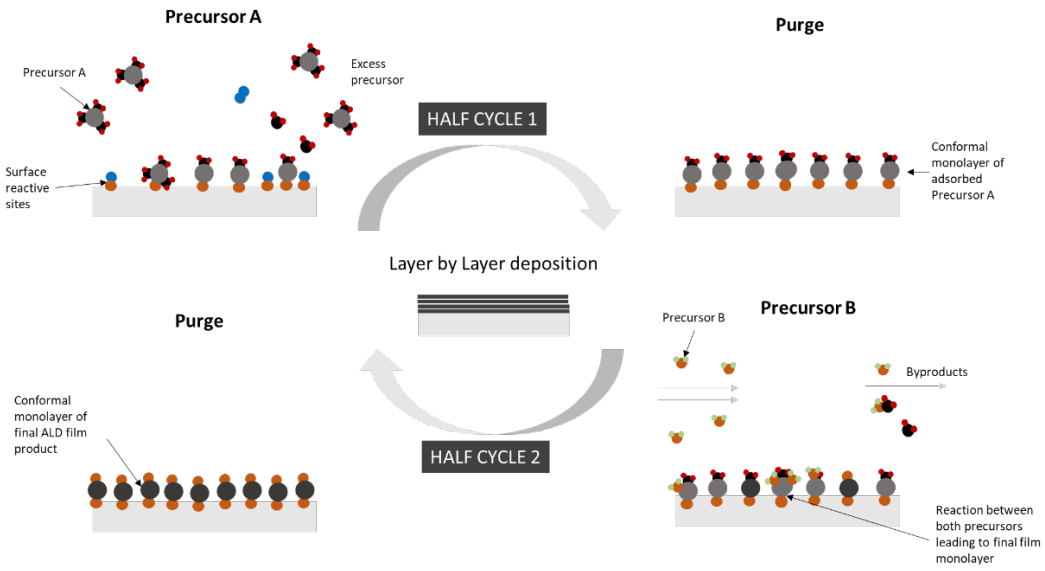

Figure 2.2-3: Cartoon schematic of a generic binary ALD process.

For the reasons discussed above, this self-limiting mechanism of ALD makes it possible to achieve uniform deposits on high surface area, high aspect ratio and porous solids, making it much more suitable to fabricate precise cathode architectures in comparison to MOCVD. While broadly used, MOCVD (and CVD in general) can lack the degree of conformality and digital thickness control that makes ALD so critical for applications in catalysis.

2.3 ALD of Platinum thin films for SAFC cathodes

2.3.1 Experimental Details

ALD of Pt on CDP powder

Several initial development ALD recipes were attempted to finalize the required precursors, purge times, temperature variables on precursor and delivery lines, to enable successful CVD at 150°C on the thermally fragile CDP powders, before finalizing the recipe discussed below. Details of this are discussed in Appendix B.1.

Powders of CDP with specific surface area of 2.4 m^2/g were prepared in-house by aqueous routes using cesium carbonate (Alfa Aesar, 99.9%) and phosphoric acid (Fisher Scientific, 85%) as the starting materials[14]. ALD preparations were carried out using a pulse type Savannah 100 reactor (Cambridge Nanotech, Inc.) with 80 mg of CDP powders loaded into the reactor for each deposition. Prior to the delivery of reactant gases, the CDP was vacuum heat-treated for 30 min at 150°C to remove any physisorbed water. The CDP powder was then held at 150°C for the subsequent deposition. The solid platinum precursor was pulsed at a temperature of 75 °C, using ultra-high purity nitrogen as the carrier, which also served as the purge gas. Each deposition cycle consisted of the following five steps: (1) 1 s pulse of $MeCpPtMe_3$; (2) 220 s hold to provide time for the precursor to diffuse throughout the powder; (3) 220 s N_2 purge; (4) 45 s pulse of O_3; (5) 45 s N_2 purge. This sequence of ALD steps was then repeated,

between 100 and 450 times. Sample nomenclature hereafter follows the system Pt-xxx, where xxx is the number of cycles. The Pt-100 and Pt-200 preparations were duplicated to evaluate reproducibility.

ICP for Ptwt%

The quantity of Pt deposited onto the CDP powders was deter- mined using Inductively Coupled Plasma Optical Emission Spectroscopy (ICP-OES, Thermo iCAP 7600) with sub ppm detection levels. Samples of the Pt@CDP material were placed in a 10% vol/vol acid solution with a 1:1 vol ratio of trace metal grade HCl: HNO_3 in Millipore water, with a solid's concentration of 10 mg of solids in a 10 ml solution. Complete digestion, yielding a clear, pale-yellow solution, was achieved after sonicating the solution for 15 min at room temperature and then holding it at 60ºC for 48 h.

Structural Characterizations

The surface morphology of the CDP powders before and after Pt coating was examined by field-emission scanning electron microscopy (FE-SEM; Hitachi SU8030 and Hitachi S-4800). In some cases, for direct visualization of the morphology of the Pt layer, the underlying CDP was dissolved away in water. The residual Pt films so obtained were imaged by FE-SEM (as above) and/or by trans- mission electron microscopy (TEM; Hitachi HD2300 and Hitachi H8100). The Pt@CDP powders were further characterized by X-ray diffraction (XRD; D/MAX Ultima, Rigaku) using Cu Ka radiation at a scan rate of 5º/min. Diffraction data were collected from both as-prepared powders and powders extracted from fuel cell cathodes after prolonged electrochemical measurements.

SAFC Button Cells Fabrication based on ALD Pt@CDP particles

Anode-supported electrochemical cells, 1.9 cm in diameter, were prepared using the Pt@CDP powders in the cathode following procedures similar to those described elsewhere.[42, 45] In brief, the anode electrocatalyst layer is 25 mg of a mixture of CsH_2PO_4 + Pt on carbon (20 mass% Pt on carbon black, HiSPEC® 3000, Alfa Aesar) in a 6:1 mass ratio. This layer is supported on 75 mg of a mixture of CsH_2PO_4 + carbon black acetylene (Alfa Aesar, 99.9%) þ naphthalene (Alfa Aesar, 99.8%) in a 3:1:2 mass ratio, where the naphthalene serves as a fugitive pore former. The anode bilayer, in turn, supports a ~50 mm

thick dense electrolyte layer. Complete fuel cells were prepared by spreading between 33 and 50 mg of the cathode powder over the entire area of a half-cell, and then applying a top layer of carbon paper (TGP-H-120 Toray paper) to serve as a gas diffusion layer and cathode-side current collector. The entire structure was lightly pressed to adhere the layers to one another without closing the electrode porosity. Pt loadings in the cathode ranged from 0.1 to 4.1 mg/cm^2, as described below.

SAFC Electrochemical characterization

For electrochemical characterization, cells were sealed into an in-house constructed fuel cell test station[42]. Fuel cell polarization curves and impedance spectra were collected at 250^{o}C after thermal equilibration. Cathode and anode were respectively supplied with humidified (pH_2O = 0.38 atm) high purity hydrogen at a flow rate of 30 sccm and with humidified synthetic air at a flow rate of 75 sccm. Data were recorded using a BioLogic SP-300 potentiostat configured with an integrated frequency response analyser. Impedance spectra were collected over the frequency range 0.1e10^6 Hz without and with a bias of 200 mA/cm^2. Without bias, the spectra were recorded using a voltage amplitude of 20 mV; with bias, they were recorded using a current amplitude of 10mA. Polarization curves were obtained every hour over a period of 100 h, by scanning the voltage from 1 to 0 V at a rate of 10 mV/s; the open circuit voltage (OCV) was in all cases below 1 V and thus the full range of cell voltages was captured. Between measurements, cells demonstrating high current densities were held at a fixed bias of 200 mA/cm^2, whereas those of low performance were held at OCV. The electrode overpotential was determined from the raw polarization curves by subtraction of the ohmic loss determined from impedance spectroscopy and the measured voltage from the expected Nernst potential of 1.116 V. The latter is computed on the basis of the fuel cell measurement conditions. Impedance measurements of symmetric cells with anode components on both sides and exposed to hydrogen at both electrodes showed negligible electrochemical resistance to the hydrogen electrooxidation reaction (~0.05 Ωcm^2 per electrode), and thus the entirety of the electrode overpotential was assigned to the cathode (i.e., the anode serves as a pseudo-reference).

2.3.2 Results and Discussions

Deposition of Pt on CDP powders were successfully achieved at 150C using a combination of $MeCpPtMe_3$ and ozone, with amounts ranging from 0.6 to 30 wt% Pt for the range of cycle numbers utilized, as summarized in Table 2.3-1. The variation of Pt loading on the CDP with the number of ALD cycles is shown in Figure 2.3-1a). The Pt deposition graph can be divided into two regimes: before 84 ± 20 cycles marking the nucleation delay regime (based on linear regime fitting extrapolation), while after 84 cycles marking the linear growth regime as expected in self- limited ALD growth. The linear fit in later region suggests Pt deposition rate of 0.09 ± 0.01 wt%/cycle, which corresponds to ~ 0.02 nm/cycle, as estimated based on the CDP specific surface area of 2.4 m^2/g. The complete calculated Pt thickness variation with ALD cycles is summarized in Table 2.3-1. The zero-growth intercept based on linear fit is 84 ± 20 cycles. SEM images were taken, to look at the Pt film coating on Pt coated CDP particles. It was observed that for the first stage of about 80 cycles, minimal deposition occurred. Specifically, after 100 ALD cycles an average of only 1.5 wt% Pt was deposited. Moreover, for the Pt-100 materials with 0.56 wt% Pt, the metal was essentially undetectable in the X-ray diffraction pattern (Figure 2.3-1b)), and the SEM image, Figure 2.3-2b), reveals the presence of isolated Pt nanoparticle clusters on the surface of the large CDP particles. For the linear region, the deposition behavior was found to be reasonably reproducible, as indicated by the low scatter in the data (R^2 = 0.93). Unless stated otherwise, the samples with lesser Pt amounts from the two duplicated depositions, Pt-100 and Pt-200, were used for subsequent studies, including the SEM im- aging and diffraction analysis. Papandrew et al.,[45] have suggested that Pt film thickness is an important parameter in defining the polarization behavior of SAFC cathodes prepared using such powders. For a specific surface area of CDP of ~2.4 m^2/g, the average Pt thickness implied by the Pt deposition amounts are between 0.1 and 5.9 nm (summarized in Table 2.3-1), and the value for each of the cathode catalyst powders is also included in the table.

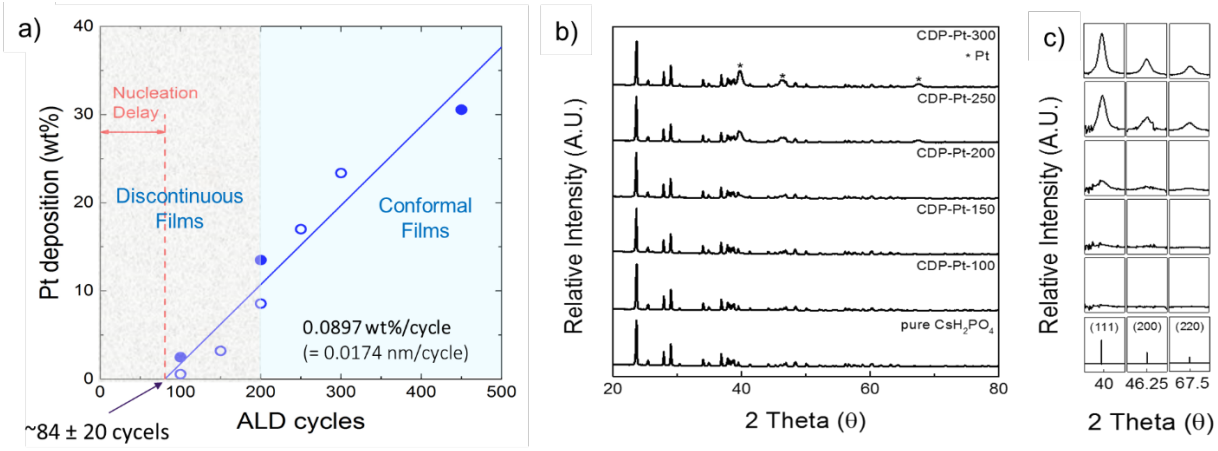

Figure 2.3-1 *(a).* Pt loading on CDP powder as a function of ALD cycles as measured by ICP -OES. (b) X-ray diffraction pattern of CDP and Pt coated CDP cathodes. (c) Prominent Pt FCC peaks after subtracting pure CDP peak contribution for crystallite size calculation

Table 2.3-1 Summary of Pt ALD runs

Sample	Deposition (wt%)	Thickness (nm)	Crystallite size (nm)[#]	Cathode mass (mg)	Pt loading (mg/cm^2)
Pt-100*	0.56	0.1	not detectable	50	0.1
Pt-150	3.20	0.6	not detectable	40	0.5
Pt-200*	8.56	1.8	7.8	33	1.0
Pt-250	17.00	4.0	10	36	2.2
Pt-300-1[§]	23.17	5.9	11.9	37	3.0
Pt-300-2[§]				50	4.1
Pt-450	29.90	8.3	Not pursued for application		

* using Pt-100 and Pt-200 depositions that resulted in lower Pt yields.

[§] prepared from the same Pt@CDP batch

[#] number in parentheses indicates crystallite size as measured after 100 h of electrochemical measurement.

Such overall non-ideal Pt growth via ALD has been reported earlier in general for metal catalysts ALD due to their high surface energy, wherein the extent of such nucleation delay is said to depend on the nature of substrate materials and the nucleation site of the surface such as hydroxyl group and ionic species.[19, 20, 39, 40] During the incubation period (nucleation delay prior to the onset of layer-by-layer growth), rather than the deposition of uniform, monoatomic layers of the metal, isolated nanoparticles, as exemplified in Figure 2.3-2b), are formed as a result of the high surface energy between substrate and deposit. These nuclei undergo very slow lateral growth (or additional nuclei are formed at a slow rate), until a continuous film is eventually attained which here occurs for the Pt-200 sample as seen in Figure 2.3-2d). This suggests that the transition between films with discontinuous and continuous morphology as a function of number of ALD

cycles would not have been sharp. However rough transition region from discontinuous to continuous region in terms of films that happen around 200 cycles, is marked on Figure 2.3-1a), and also expressed schematically in the form of cartoon on SEM figures left top (Figure 2.3-2). Specifically, the SEM image of the Pt-150 material, with a Pt content of 3.2 wt%, reveals a Pt film that is generally interconnected, though clearly not yet continuous (Figure 2.3-2c, h). After 200 cycles, the resulting film is entirely continuous (Figure 2.3-2d); a large defect in the free-standing Pt-200 film (Figure 2.3-2i)) is a result of the handling involved in removal by dissolution of the underlying CDP. Because of limited thickness of the films (seen in Figure 2.3-2i)), the micron scale surface morphology of the Pt@CDP is largely unchanged from that of the neat CDP material (shown in Figure 2.3-2a)). The slight variation in the deposition efficiency observed in the Pt-100 and Pt-200 experiments could be attributed to variations in the nature of the CDP surface (different humidity can affect too), which would have impacted the nucleation characteristics, along with precursor vapor pressure variation due to depletion over period at source.

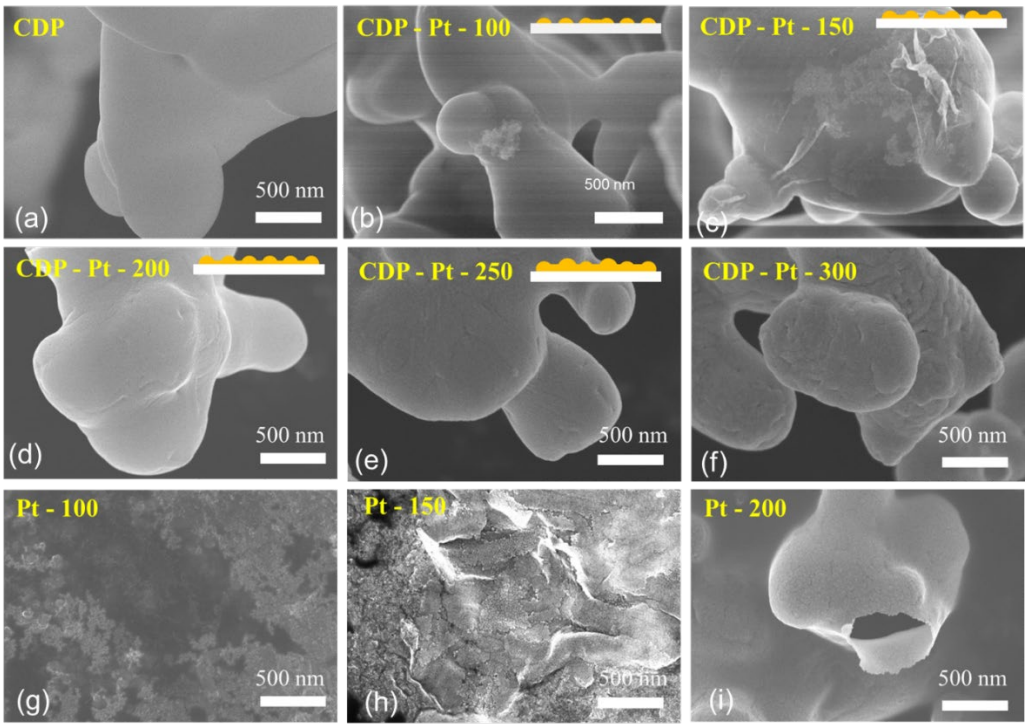

Figure 2.3-2 High resolution SEM images of Pure CDP and ALD Pt coated CDP particles: (a) CDP; after ALD cycles (b) CDP-Pt-100, (c) CDP-Pt-150, (d), CDP-Pt-200, (e) CDP-Pt-250, (f) CDP-Pt-300; and after dissolved in water (g) CDP-Pt-100, (h) CDP-Pt-150, and (i) CDP-Pt-200

To check for any detrimental effect of using powerful oxidant such as ozone on CDP, SEM, XRD and XPS analysis were performed. Figure 2.3-3a) and b) show SEM images of electrolyte CDP powder showing ozone based ALD doesn't cause any morphology changes. Crystalline Pt film boulders can be seen in Figure 2.3-3c) after dissolving CDP in water, which are shaped in triangles. The polycrystalline nature is further confirmed by both XRD patterns in Figure 2.3-1 b) and c) and TEM images shown in Figure 2.3-4a), with SADP indexing (Figure 2.3-4 b)) confirming FCC Pt (after dissolution of CDP from Pt-200 sample). Diffraction peaks of CDP essentially were unchanged for all samples, indicating CDP powders were not structurally damaged during ALD process at 150 °C with ozone. The Pt peak can be hardly observed for CDP-Pt-100, due to low Pt loading. The Pt (111), (200), and (220) diffraction peaks in Figure 2.3-1 c) indicate that Pt film was polycrystalline, and its peaks positions match well with that of the XRD pattern for Pt in the literature (JCPDS, No. 87-0646). The average Pt particle was calculated by Scherrer equation,[5837] to be, 7.8, 10.0, and 11.9 nm for CDP-Pt-200, CDP-Pt-250 and CDP-Pt-300 respectively. XPS analysis reveals that the Cs peaks were unchanged, suggesting ozone did not affect CDP chemically. Additionally, XPS analysis of Pt ALD films on CDP is shown in Figure 2.3-5. Pt4f XPS signal reveals the presence of primarily Pt metal signal (Pt^0) with some contribution from Pt^{2+} and Pt^{4+} signals on surface. However, upon etching to reveal relatively bulk information in the case of Pt -ALD does not remove the oxidized species (Pt hump), nor do the O1s or C1s signal disappear completely, suggesting possible oxygen incorporation throughout the film in case of ALD, rather than just on the surface. This is expected from the Pt ALD mechanism reported in literature.[59] The other possibility is that the surface oxide film was thicker than the 3-4nm etching done in the study, or complexity in XPS depth profiling reliability due to the powder samples based surface (signal collected from multiple powder particles).

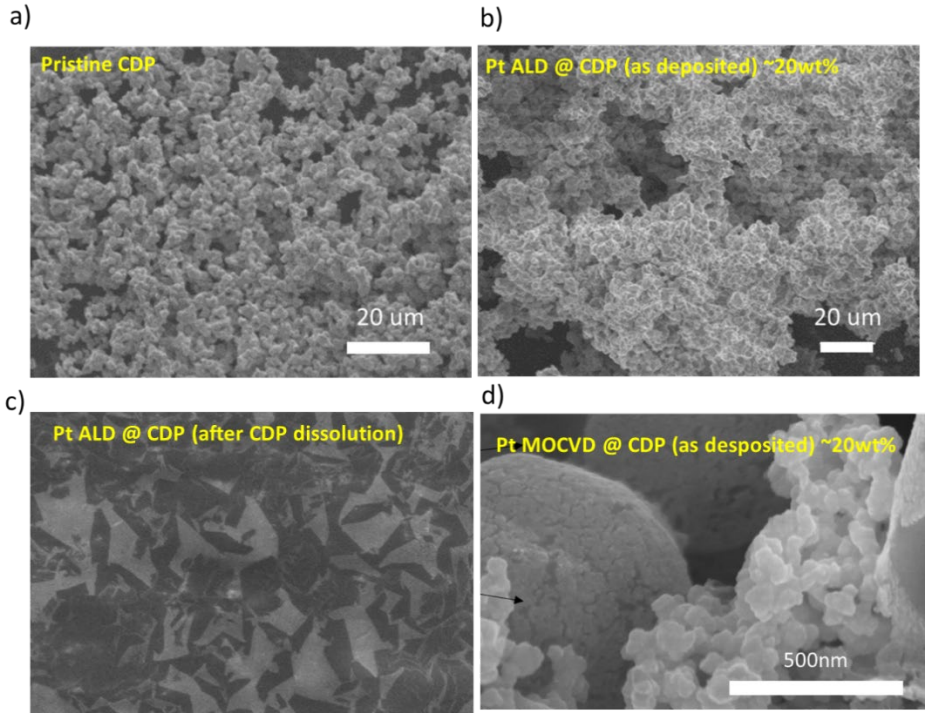

Figure 2.3-3. SEM images of CDP particles (a) before and (b)after Pt ALD Ozone (Pt -150) showing the smooth conformal coating from ALD. SEM images of c) Pt single crystal sheets from ALD after CDP dissolution, broken along a cleavage plane and d) CDP after Pt MOCVD deposition on CDP showing the agglomeration of secondary particles unlike ALD.

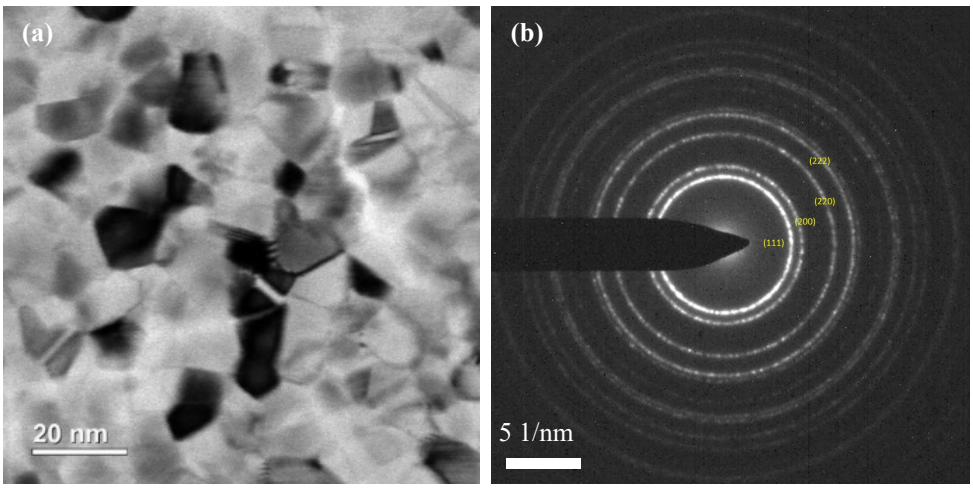

Figure 2.3-4 : (a)Transmission Electron microscopy images of Pt ALD (Pt-200) material after dissolution of the underlying CDP. Variations in darkness of different grains in the TEM images are largely due to variations in grain orientation (b) selected area diffraction pattern (SADP), indexed to FCC Pt.

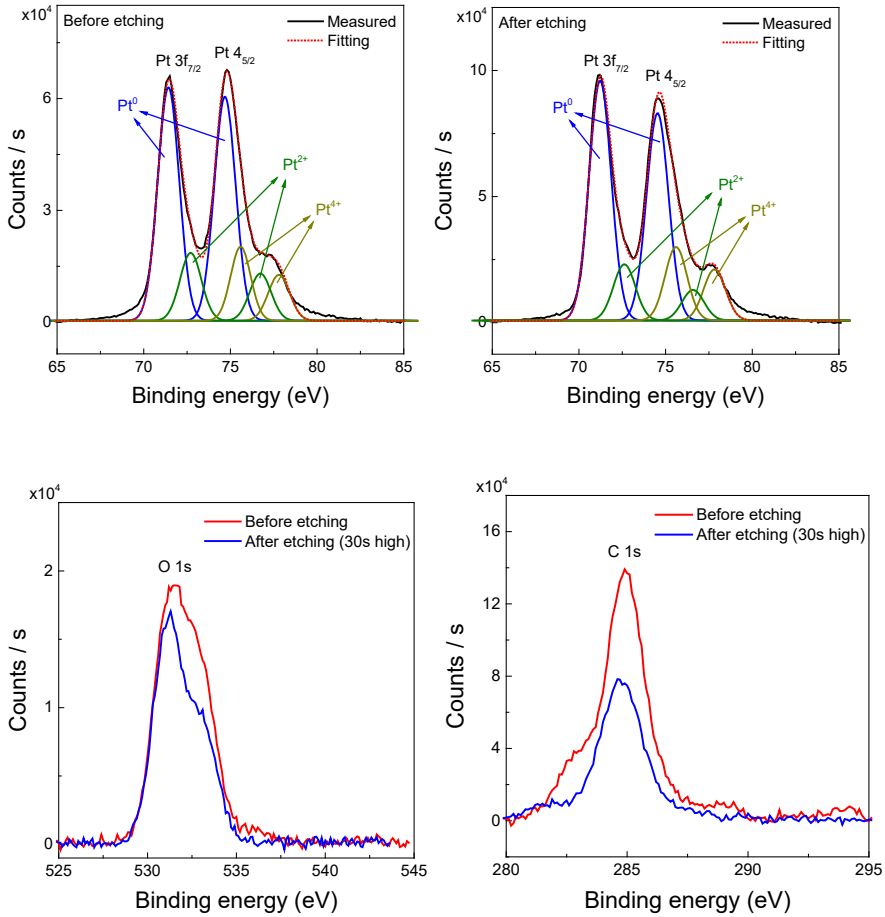

Figure 2.3-5 XPS spectra of Pt ALD films on CDP. Pt4f spectra (a) before and (b) after etching to remove surface layer withing XPS. (c) O1s and (d) C1s spectra again before (red) and after (blue) etching.

The cathode overpotentials, as recorded after 100 h of operation, are shown in Figure 2.3-6, were found to be remarkably similar for the cells incorporating Pt-200, Pt-250, and Pt-300 powders in the cathode (Figure 2.3-6 b). In contrast to cells prepared from Pt@CDP powders of 200 or more ALD cycles, those prepared from Pt-100 and Pt-150 displayed extremely high overpotentials (Figure 2.3-6 a), consistent with the poor continuity of the Pt films obtained from these depositions as seen in SEM micrographs and also having low Pt loadings. Similar results of Pt-300#1 and Pt-300#2 suggests that even a substantial variation in cathode mass (see Table 2.3-1) was found to have no significant impact on cathode overpotential, one prepared using 37 mg and the other using 50 mg of Pt@CDP. This suggests that the

active region lies well within 80 microns of the electrolyte-cathode interface (where 80 micron is the thickness of the 37 mg cathode). It is further noteworthy that the overpotential is insensitive to the Pt crystallite size, which spans from 8 nm in Pt-200 to 12 nm in Pt-300 as also summarized in Table 2.3-1. Comparison of cathode overpotentials of various Pt ALD@CDP based SAFC cells at 200mA/cm^2 and 50mA/cm^2, processed in this work, and Papandrew's MOCVD work is shown in Figure 2.3-6 c). The overpotentials are plotted against Pt content (measured by ICP), area normalized Pt loading calculated (mg/cm^2), crystallite size (Lab XRD), while showing the rough division of continuous vs discontinuous flims as found from SEM. Overall, the cathode overpotential trends with Platinum loadings are in general agreement with those of Papandrew *et al.*, who also observed poor activity from Pt@CDP powders with 5 wt% Pt, powders while 9 wt% Pt and higher displayed approximately fixed activity (i.e., independent of Pt wt%), and in further analogy to the present results, the electrocatalytic behaviour was insensitive to Pt crystallite size too. Those authors attributed poor oxygen electroreduction rates at low Pt loadings to discontinuity of the Pt films resulting in poor electronic connectivity, a feature also evident in the low Pt content films prepared here.

A proposed electrochemical reaction pathway in which protons or atomic hydrogen species migrate through the Pt film and undergo reaction with oxygen at the Pt-air interface, is shown in Figure 2.3-7c). It is motivated from the slightly higher cathode overpotential observed in this work in comparison to similar Pt loading in Papendrew's MOCVD based cell. It suggests that in the case of oxygen electro-reduction, loss of CDP surface area would result in loss of active area, and loss of Pt grain boundaries (higher crystalline size) would result in loss of possible hydrogen diffusion pathways or surface reaction sites, both leading to decreased performance. This explains why ALD coated cells here with crystalline size range (8-12nm) could have lesser active area in comparison to Papendrew's MOCVD cells with much smaller crystalline size (2-4nm), although performance is insensitive internally in these ranges. Alternatively, the difference in overpotentials may be due to the speculated loss in CDP surface area during ALD processing. Both possibilities are consistent with the proposed mechanism.

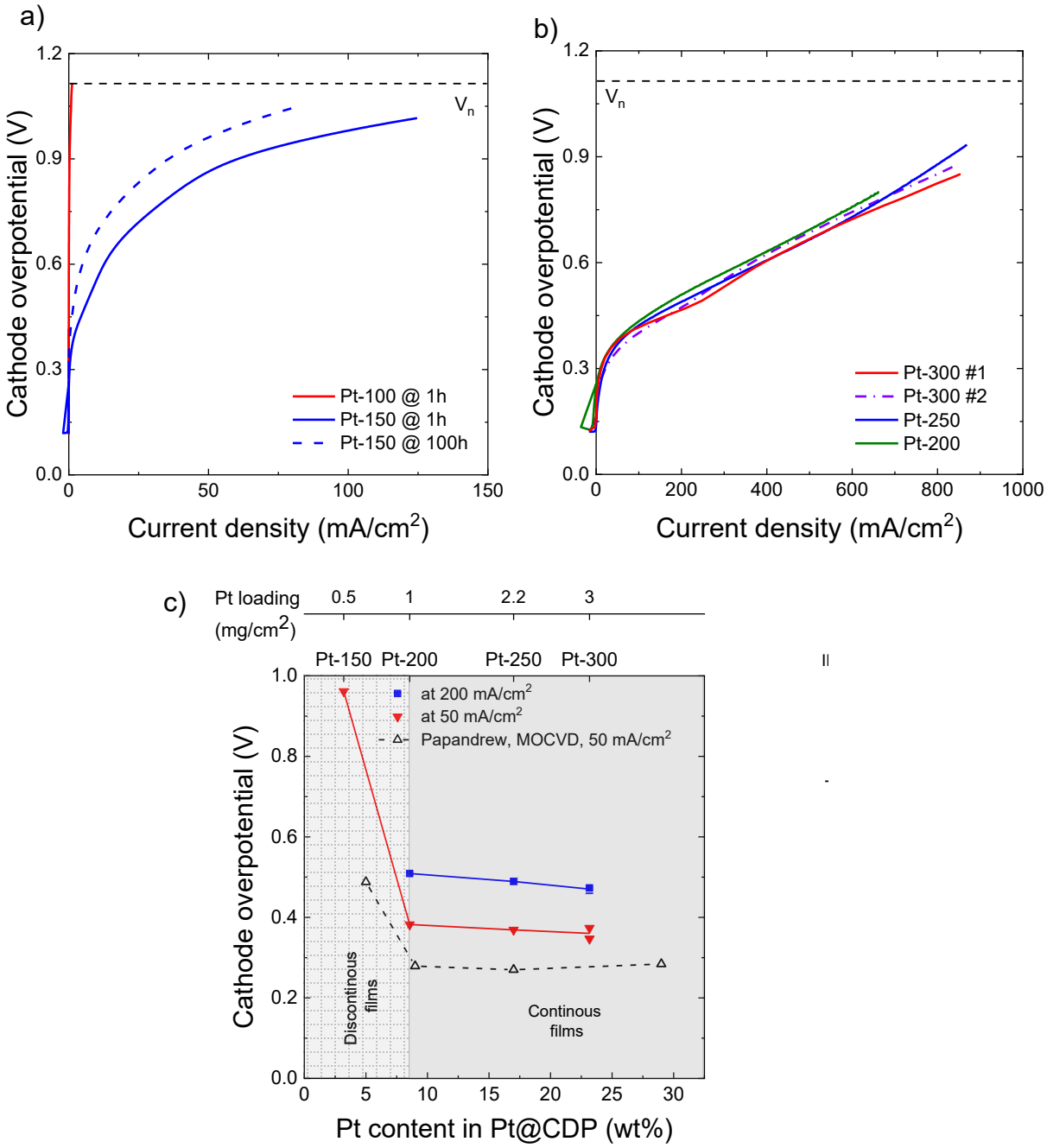

Figure 2.3-6 a) High cathode overpotentials curves in SAFCs for Pt-100 (operated for only 1hr) and Pt -150 having discontinuous Pt films. b) Similar cathode overpotential curves for Pt-200, Pt-250, Pt-300#1, Pt-300#2 with continuous Pt films after 100hr operation. c) Cathode Overpotential values after 100hrs operation @50mA/cm^2 and @200mA/cm2 for different platinum loading (both wt% relative to electrode) and (mg Pt/cm^2). (Courtesy : SAFC electrochemical measurements by Daekwang Lim, Haile group, Northwestern University).

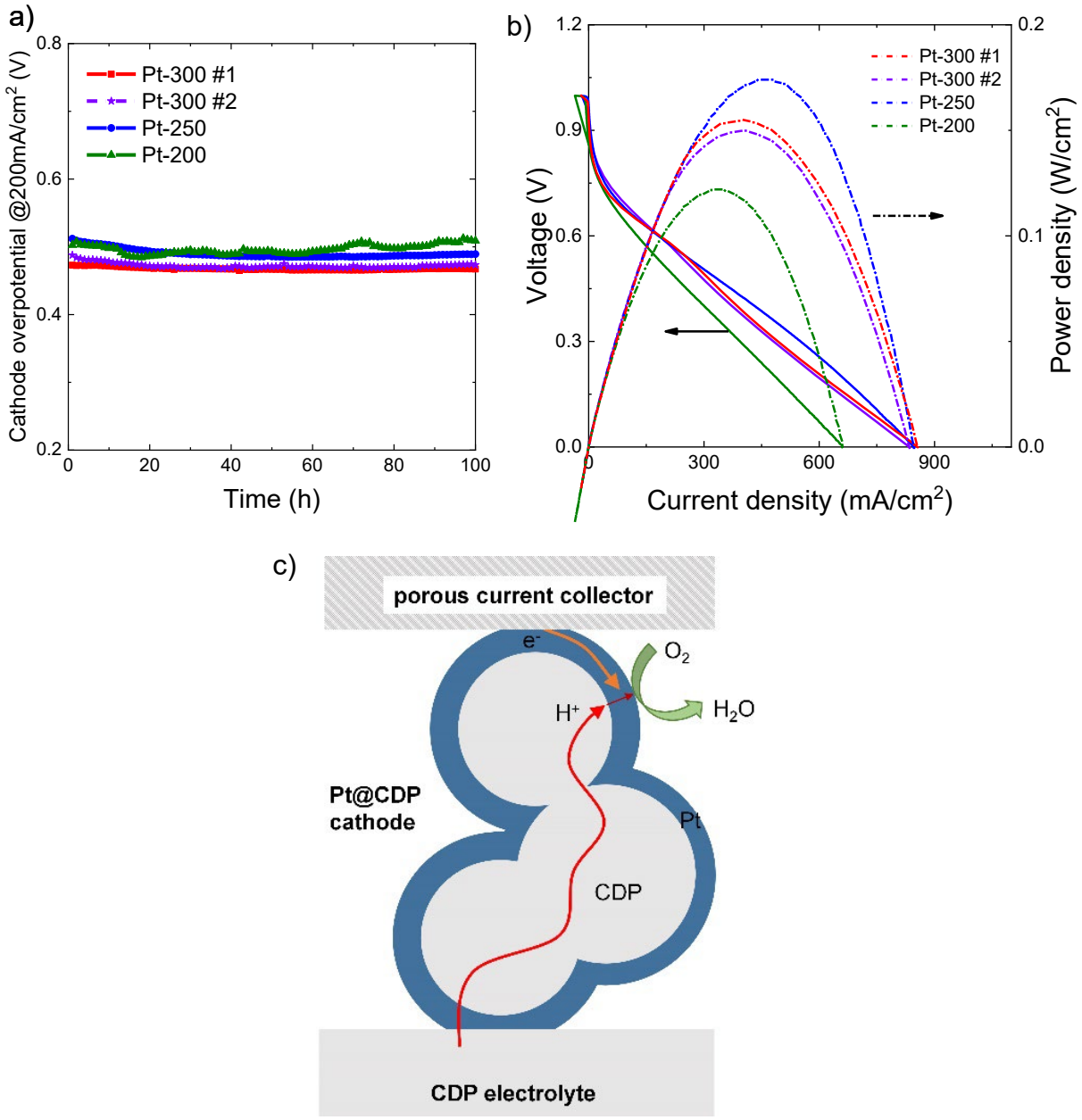

Figure 2.3-7 (a) Temporal evolution of the cathode overpotentials at 200 mA/cm^2 for cells (b) Polarization curves and power densities for cells (not IR corrected) (c) Schematic illustration of the proposed reaction pathway for oxygen electrooxidation on Pt@CDP

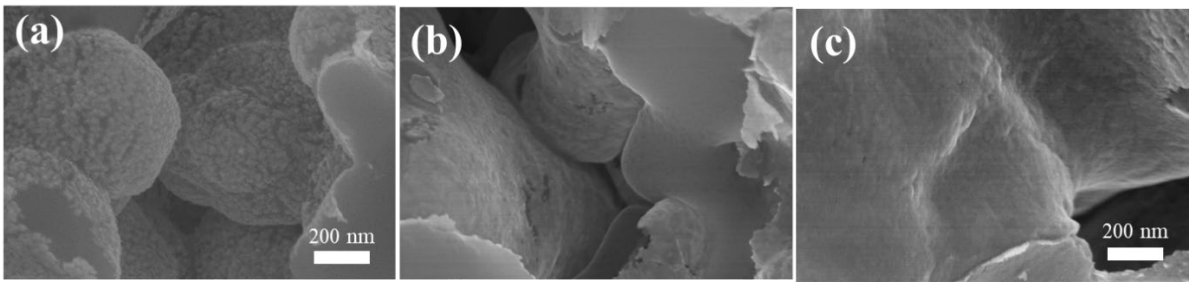

Figure 2.3-8 SEM image of cross section of SAFC Cell after 100 hr operation a) Pt – 200 b) Pt – 250 c) Pt – 300 cells

Despite the slightly higher overpotential, ALD along with good performance brings the benefits of high Pt utilization and great durability. Pt utilization here is defined as $(1/\eta@50mA.cm^{-2})$ *$(1/mg_{Pt}cm^{-2})$ where $\eta@50mA.cm^{-2}$ is the cathode overpotential at a current density of 50 mA·cm^{-2}, which is higher for the ALD processed cathode in comparison to MOCVD. For example Pt-200 (2.6 cm^2·V^{-1}·mg_{pt}^{-1}) has better Pt utilization than the best MOCVD processed cathode (2.0 cm^2·V^{-1}·mg_{pt}^{-1}), calculated from the data reported by Papandrew *et al*).[45] Yet another exciting feature of ALD processed cathodes is their excellent stability, as shown in the evolution of the cathode overpotential over time at a current density of 200 mA/cm^2, Figure 2.3-7a). The Pt-300-#1 sample is particularly stable, undergoing a very slight decrease in cathode overpotential in the first 50 h of measurement, then remaining within 1 mV of 0.466 V for the subsequent 50 h. The Pt-250 and Pt-300-#2 samples similarly show initial slight improvements of about 10 mV followed by stable performance. In contrast, fluctuations in voltage are evident for the Pt-200 sample, which furthermore shows a slightly more pronounced average improvement in the first 50 h followed by a slightly more pronounced degradation in the latter 50 h. Over the entire 100 h measurement, the cathode overpotential of this sample increases by only 6 mV, but over the last 50 h the increase is 21 mV. These differences in voltage stability appear to be due to differences in the morphological evolution of the Pt coatings as shown in the post-measurement electro interfaces high resolution SEM images in Figure 2.3-8. In particular, coarsening is evident in the case of the Pt-200 powder, whereas negligible morphological changes occur for Pt-250 and Pt-300.

Comparing Pt ALD to Pt MOCVD (in-house)

The recipe for MOCVD is discussed earlier in this chapter. To probe the difference in Pt films deposited by ALD vs in-house MOCVD of Pt films on CDP, some additional characterizations were done. Figure 2.3-9 and Figure 2.3-10 compare the XPS signals for Pt, O and C scans taken on as deposited samples from MOCVD, ALD and Sputtering, and then again after etching with Argon to remove ~2-3 nm of surface species, respectively. Pt films from Sputtering (30nm on "Flat CDP" electrolyte pellet) were also studied as reference. Flat here is an exaggeration, as recent lab studies show these Flat CDP

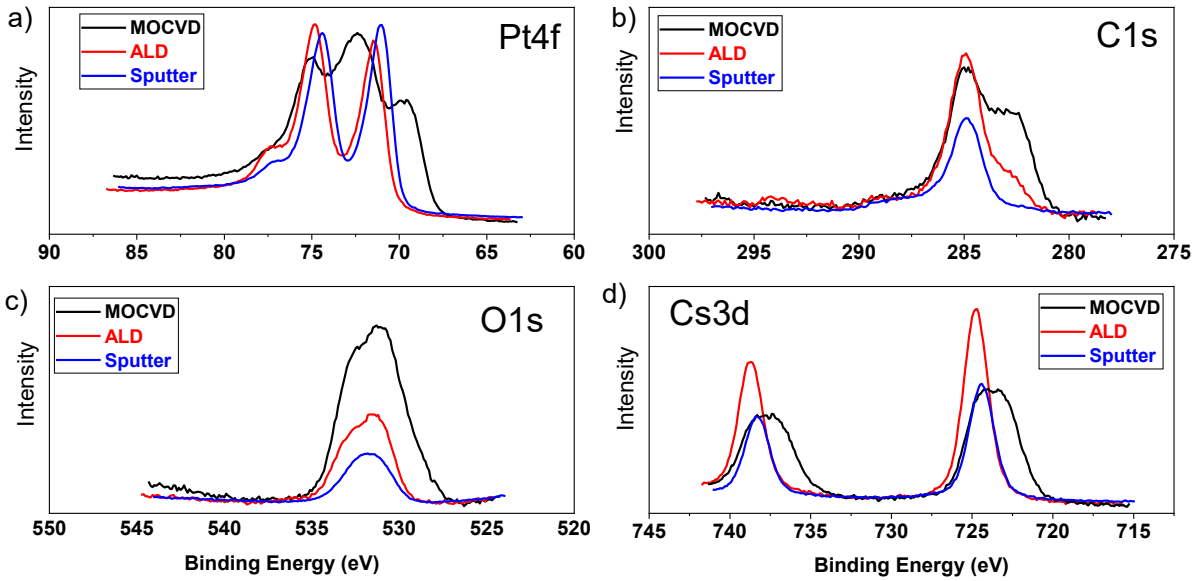

Figure 2.3-9 Before Etching Pt deposition XPS comparison: ALD (red), MOCVD (black) and Sputtering (blue)

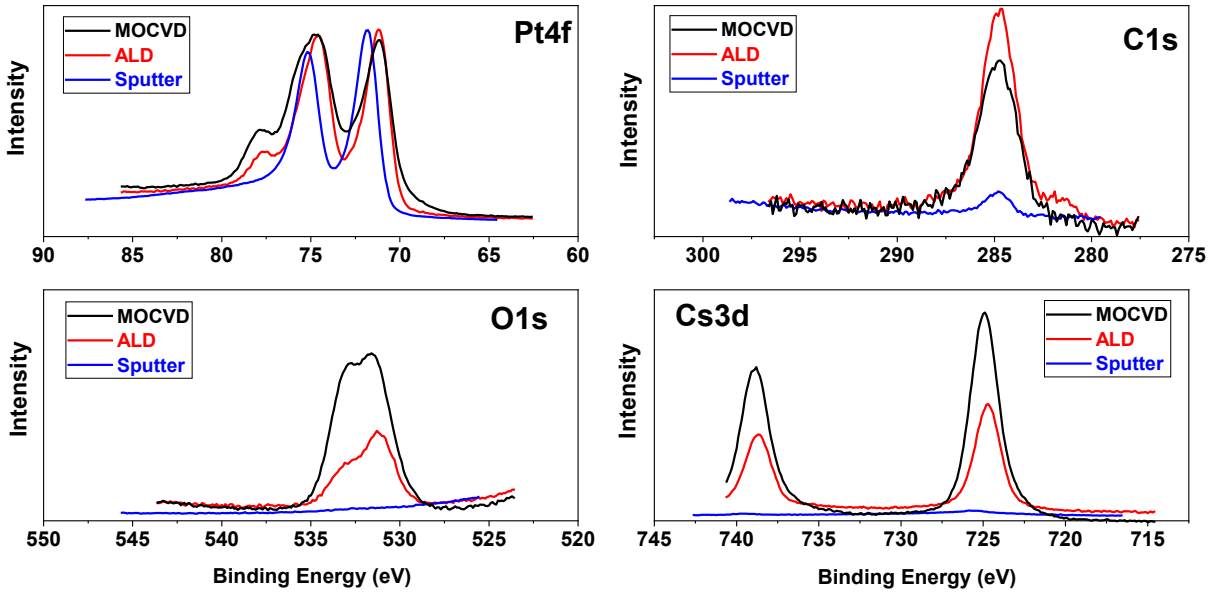

Figure 2.3-10 After Etching Pt deposition XPS comparison: ALD (red), MOCVD (black) and Sputtering (blue). Etching gets rid of Pt shoulder peak in the case of sputtering (possibly nm thin oxide layer, resulting in PtO_2 bond XPS shoulder peak). However, shoulder peaks for Pt remain in the case of ALD and MOCVD.

electrodes have quite a rough surface compared to thin films that are processed on these, more discussion can be found in Louis Wang's PhD Thesis, Haile Group, Northwestern University. Note that intensity of the Pt peaks were first normalized for all deposition types, so that the biggest Pt4f scan peak have approximately same relative intensity across all techniques. The same multiplicity factor obtained from Pt plots, was then used to plot C and O plots for all the techniques, to ensure relative % of these impurities can be directly compared to each other and to Mo content.

Pt XPS signal of all techniques, contain primarily Pt metal signal (Pt^0) with some contribution from Pt^{2+} and Pt^{4+} signals on surface. However, upon etching to reveal relatively bulk information in the case of Pt -ALD does not remove the oxidized species in contrast to sputtered Pt, suggesting oxygen incorporation throughout the film in case of ALD, rather than just on the surface as for the sputtered Pt case. This is expected from the Pt ALD mechanism reported in literature.[59] The same is true for the MOCVD case, in which case the shoulder Pt4f peak (probably due to residual Pt^{2+}, Pt^{4+} due to surface

oxides or organic precursor/ derivatives of reaction) is even more apparent than ALD. However, C on as deposited and after etching XPS scans were found in much higher relative quantity in MOCVD compared to ALD, with these elements being almost absent after etching for the case of pristine sputtering which is expected to carry least impurity.

Additionally, Figure 2.3-3b) and d) compared CDP SEM images of as deposited Pt films using ALD and MOCVD, and it can be seen that the chunks of bright agglomeration seen in the case of MOCVD, which could potentially be excess Pt agglomeration, based on EDS(not shown here) are absent in the case of Pt ALD coated CDP, where are the brightness of particles is uniform suggesting much uniform thickness films coated via ALD compared to MOCVD. This again highlights the advantages of ALD over MOCVD, for not only getting conformal, smooth, continuous, controlled thickness films, but also films that are lower in C and O impurity, specially the carbon,which can otherwise react with oxygen and result in cell degradation.[16]

One of the key challenges of MOCVD Pt based SAFC cathodes is their irreproducibility and often rapid degradation. ALD based SAFC cathodes, as discussed turn out to be stable when continuous Pt films-based cells were tested (Pt-200 and beyond). Comparative SEM study was performed on Electrolyte-Cathode interface of SAFC cells processed via ALD (left panel, Figure 2.3-11) and that via MOCVD (right panel, Figure 2.3-11). At low magnification Figure 2.3-11a) and b) both the interfaces look smooth, however at higher magnification, chunks of agglomerates around the interface, and coarsened disintegrated films can be clearly seen in the case of MOCVD Figure 2.3-11d) , whereas the post operation interface is much more smoother, and still well connected for the case of ALD processed cells Figure 2.3-11c). The Pt content of both these cells was similar (~20wt%), probably resulting close to same thickness

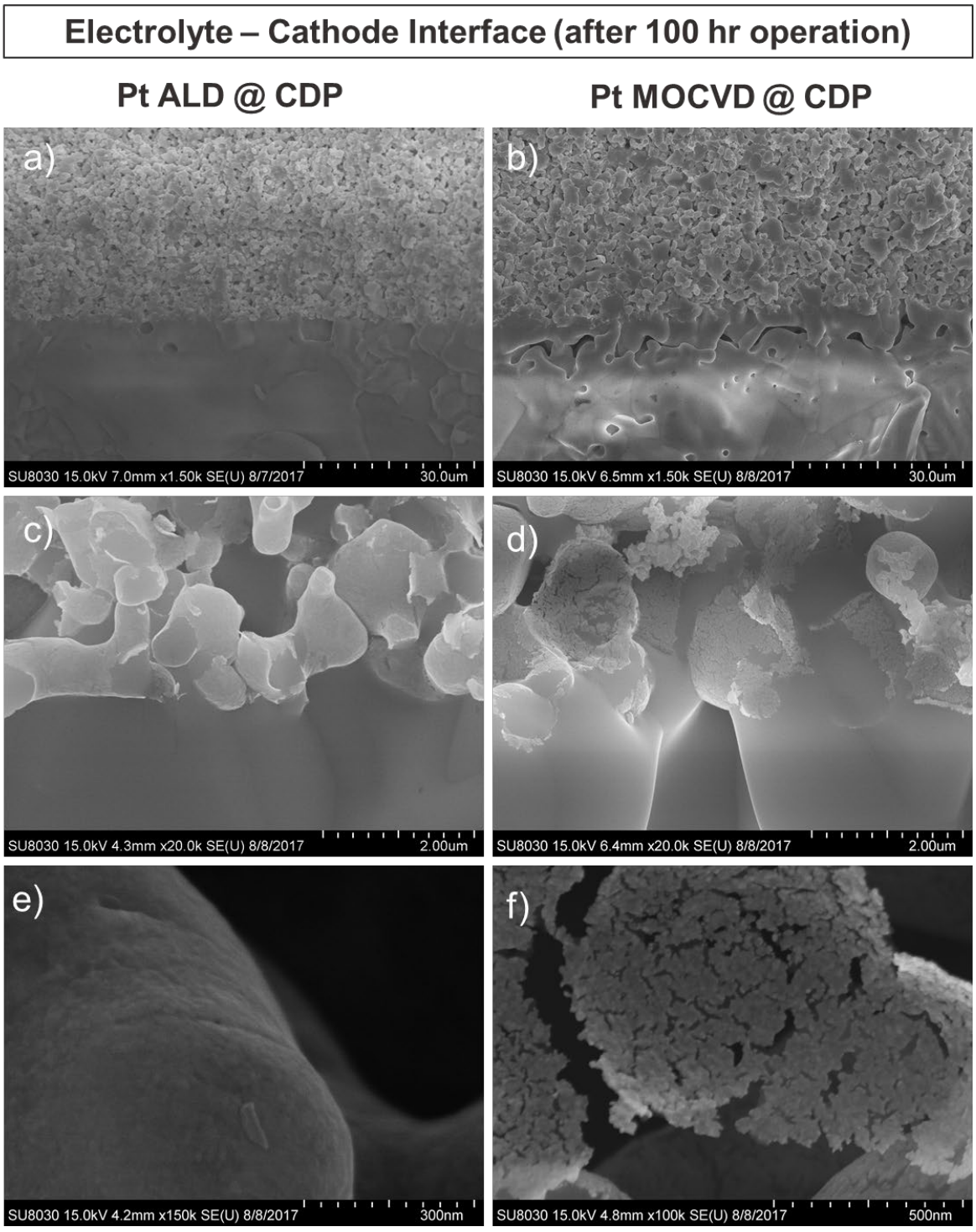

Figure 2.3-11 ; SEM images of Electrolyte -Cathode interface of SAFC cells after 100hr of operation processed via (a),(c),(e) ALD and (b),(d),(f) MOCVD for comparison.

2.4 Conclusions and Future Outlooks : Thin Flims for SAFC Cathodes.

Growth of Pt thin films by atomic layer deposition on CDP for application in SAFC cathodes was studied. ALD was performed using trimethyl(methylcyclopentadienyl) platinum ($MeCpPtMe_3$) and ozone as the reagents. The growth occurs by a two-stage process. In the first 80 cycles, slow nucleation and limited lateral growth occur, resulting in almost negligible deposition. Subsequently, after a continuous film is formed, conventional layer-by-layer growth occurs at a growth rate of 0.09 ± 0.01 wt%/cycle, which corresponds to approximately 0.02 nm/cycle. Fully continuous films were obtained after 200 deposition cycles (8.6 wt% Pt). The cathode overpotential in cells prepared using these Pt@CDP powders was relatively insensitive to the Pt loading on the CDP powders, measuring ~0.5 V for a current density of 200 mA/cm^2, so long as Pt film continuity was achieved. The overpotential as also largely insensitive to Pt crystallite size. Significantly, these cells demonstrated excellent stability as measured over a 100-h period, despite increases in Pt crystallite size by 50-65%. The general characteristics of these Pt@CDP powders are like those reported previously for analogous powders prepared by unconventional MOCVD methods. The results support the proposal that hydrogen migrates through the Pt film and that the rate-limiting step in the overall electrochemical reaction occurs at one or both double-phase boundaries, the Pt-CDP and Pt- air interfaces, justifying fabrication strategies that aim to maximize the (Pt-coated) electrolyte specific surface area rather than the CDP-Pt-air triple-phase boundaries. In comparison to Pt thin films coated in-house using MOCVD, ALD films are much more smooth, conformal and do not show presence of agglomerated Pt chunks as observed in the case of MOCVD coated films. ALD processed SAFC also have a much uniform and Pt debris free electrolyte -cathode interface before and after SAFC operation, as probed under SEM.

As discussed, ALD of Pt thin films offers several advantages for SAFC cathode fabrication. Without cost limitations, such a process can be scaled up using recent developments of commercial ALD reactors, however both <1% yield and Pt being expensive, in future alternate thin film catalysts for SAFC cathode should be explore. For example, Pd and even better its alloys with Pt-Pd have been shown to

have good ORR activity in SAFC cathodes, even better than Pt, however degradation occurs fast due to Pd reacting with CDP. ALD can be used to coat an atomically thin oxide layer onto the CDP before employing the Pd catalyst. Such oxide-metal nanoparticles bilayer using multi-step ALD processed all under one reactor, has been a recent topic of interest recently. In addition to physically inhibiting the reaction between CDP and Pd, the oxide can also act as a catalyst support for the ORR. Such collaborative efforts building on the ALD study here are being actively pursued in Haile Lab, Northwestern University.

Chapter 3 Oxynitride Materials: Synthesis and Stability with CDP

3.1 Introduction

Metal oxynitrides are increasingly investigated because of their emerging applications as photocatalysts, pigments, phosphors, dielectrics, and magnetic materials.[60-65] Fundamental similarities and differences in the properties of nitrogen and oxygen allows oxynitrides to form a wide range of N/O solid solutions (ex Ti-O-N system) or completely result in new phases (ex Ta-O-N system). Phases could be both stoichiometric (example: β-TaON) or largely non-stoichiometric phases, (example: TiO_xN_y, γ-Mo_2N). Due to the difference in the anionic charge of nitrogen and oxygen changes in the N/O ratio (even at the doping level) for constant cationic composition helps modulate oxidation state of cations, thereby modifying the physical, chemical and opto-electronic properties.[60-62, 66] Figure 3.1-1 shows some examples from literature how optical band gap, catalytic response and thermal conductivity can be tailored by introduction of N in bulk and form oxynitrides. Nitrogen's less electronegativity, more negative charge and more polarizability than oxygen increases the covalency of bonding, resulting in larger crystal field splitting.[61] For instance doping of Nitrogen in Tantalum oxide, results in band gap decrease with formation of new oxynitride and nitride phases, explained by the formation of hybridized orbital at valence band with introduction of N in bulk.[67] While oxynitrides research in both bulk and thin films applications is a hot topic of the decade, for this work, we will stick our discussion to Bulk powder oxynitrides.

Figure 3.1-2 shows the overview of Bulk oxynitrides synthesis work summarized in this Chapter. Overview of Synthesis of Oxynitride, Type of Oxynitrides with examples shown specific to the ones synthesized in this work, and finally potential applications chart where these oxynitrides can be used as a catalyst. Mo-O-N and Ta-O-N would be identified as the two key oxynitride system in this Chapter, with a plethora of potential applications shown on the Figure 3.1-2 *Applications* flow chart. Out of the many applications that are collaboratively pursued (beyond the scope of this thesis), the case of novel Solid

Acid Electrolyzer Cells (SAEC) catalyzed by Mo-O-N and Ta-O-N oxynitride systems for HER and OER respectively as discussed in Chapter 5.

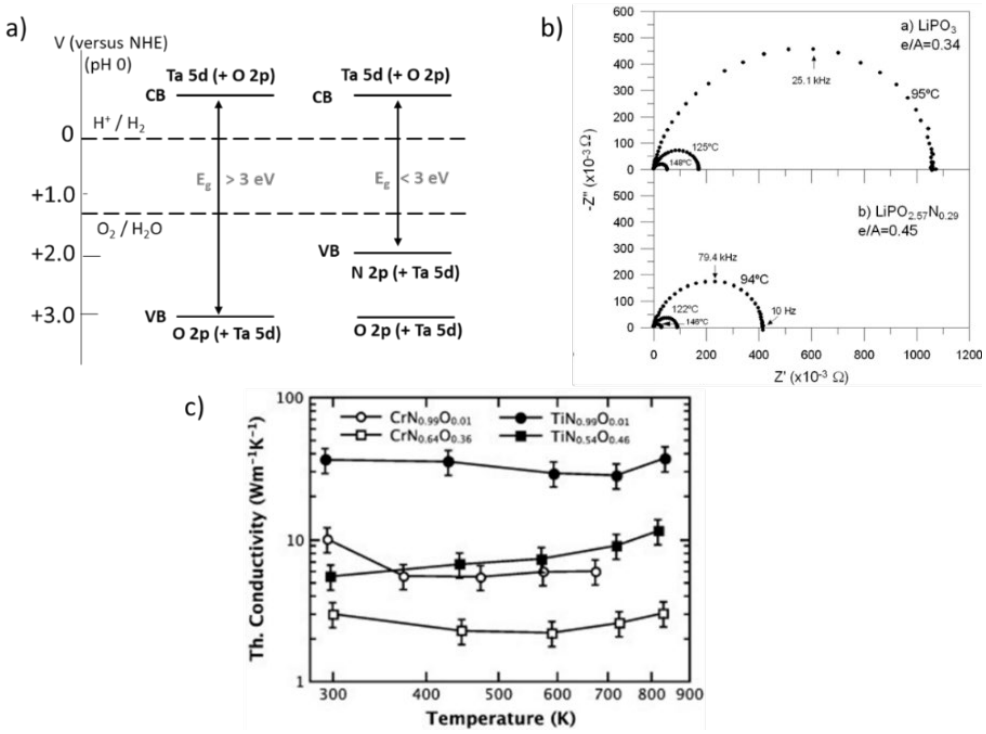

Figure 3.1-1: Some examples from literature for tailoring fundamental properties by forming oxynitrides. (a) Lowering of Tantalum oxide band gap with the introduction of N resulting in either Tantalum oxynitride or Nitride phases. Figure cited from Chun et.al work.[67] (b) Increase in conductivity, and therefore the Catalytic response of its devices of $LiPO_3$ electrolyte (decrease in impedance arc) formation of oxynitride via introduction of N in bulk.[68] (c) Modification of thermal conductivity plotted against temperature by changing N/O ratio in Chromium and Titanium oxynitride thin films. By introducing more Oxygen in bulk, thermal conductivity can be reduced.[6910]

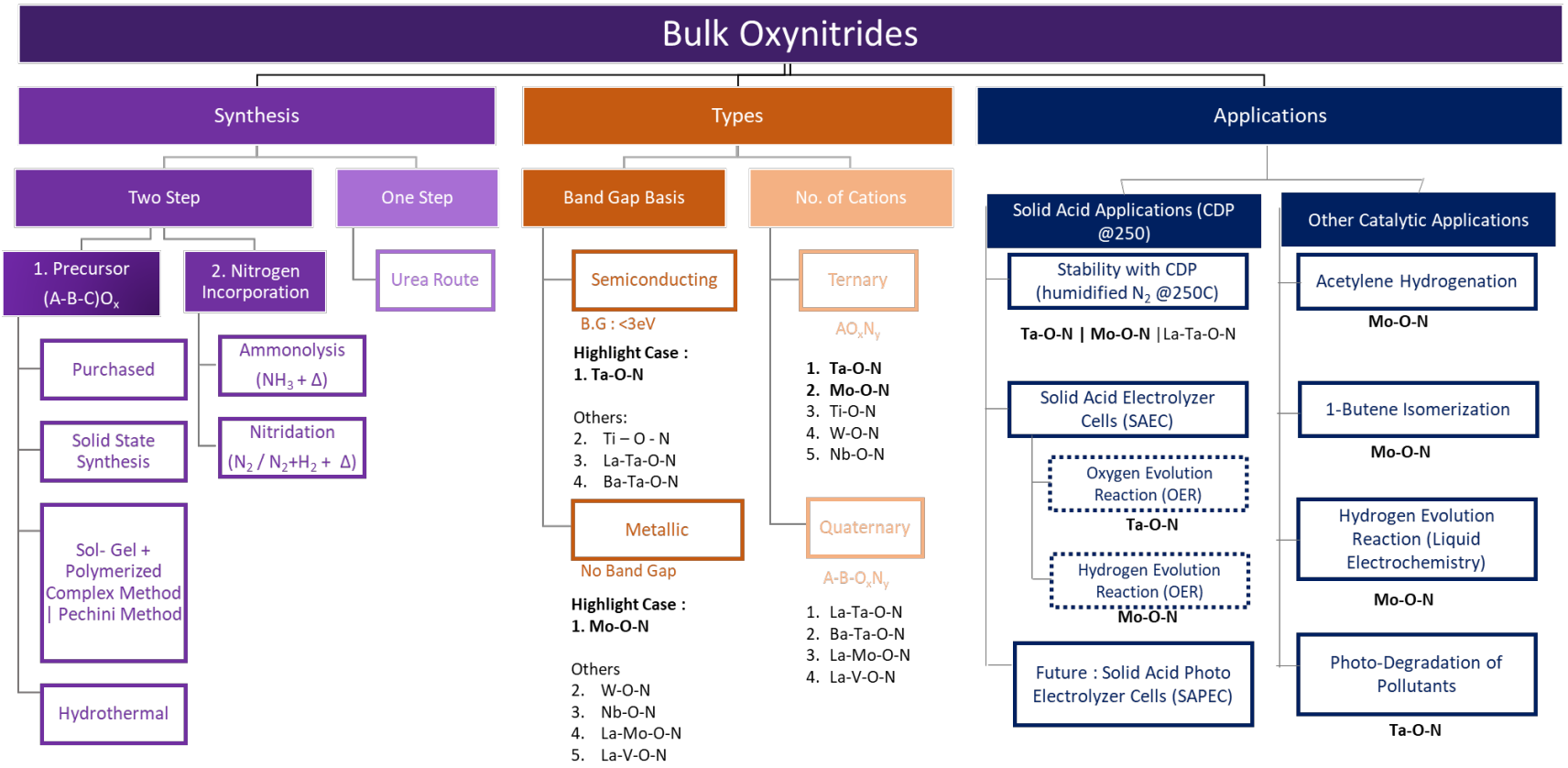

Figure 3.1-2 : Overview of Synthesis, Type and Applications of Oxynitrides. The examples in Types are the 9 oxynitride candidates that were attempted to synthesize and tested for stability with CDP under steam @250°C. Two key oxynitride systems: Mo-O-N and Ta-O-N were identified as potential candidates stable with CDP. Detailed synthesis (this Chapter) and characterizations studies (Chapter 5 for Mo-O-N) were performed to synthesize various phases of these two oxynitride systems. Applications tree covers the different in-house (CDP based applications) and collaborative applications across various labs being performed on Ta-O-N and Mo-O-N synthesized in this chapter.

3.2 Types of Oxynitrides

Since photo-active property of many of these bulk semiconductive oxynitrides is often a hot topic in the literature, one way to divide oxynitrides can be based on whether they are low band gap "Semiconducting" oxynitrides which are potentially photoactive (colorful powders) or are "Photo-absorbing" oxynitrides which do not have an optical band gap. These are mostly black looking powders, which have either or multiple attractive metallic, mechanical, electronic, thermal, or magnetic properties.[61, 62, 66, 69-72] This makes *Photo-absorbing* oxynitrides potential catalysts for non-solar based applications, for example electrocatalysis. Highlight case for *Photo-absorbing* oxynitrides synthesized in this work is Mo-O-N system. All the phases (Cubic γ, Hexagonal δ, and Tetragonal β) of Molybdenum oxynitrides synthesized in this Chapter are shown as potential catalysts for Hydrogen evolution reaction by steam splitting at 250^{o}C using solid state electrocatalysis in novel Solid acid electrolyzer cells based on super protonic CDP electrolyte, discussed in Chapter 5.

Whereas, "Semiconducting" oxynitrides have band gaps that are often in the visible range, making them potential catalysts for various photocatalytic applications, where their ability to absorb greater part of the solar spectrum thereby producing more reaction driving force.[60, 61, 73-75] These types of Semiconducting candidates would be Photo-active Semiconducting oxynitrides.[60, 75-77] Several of these semiconducting oxynitrides are also used as co-catalysts and supports where their ability to lower the activation barrier of the electrocatalytic reaction owing to their electronic properties is utilized. These may or may not be photo-active. Highlight case in this case is Ta-O-N system. Different tantalum oxynitride mixture phases (β-TaON, γ+ β-TaON, Ta_3N_5, and also nano-TaON powders) synthesized in this Chapter are shown as potential catalysts for Oxygen evolution reaction by steam splitting at 250^{o}C using solid state electrocatalysis in novel Solid acid electrolyzer cells based on super protonic CDP electrolyte, discussed in Chapter 5.

These oxynitrides can also be categorized based on number of cations, for example Ternary oxynitrides (A-O-N, with A in this work = Mo, Ta, Ti, W, Nb), or multiple cations like Quaternary oxynitrides (A-B-O-N, in this work A = La, Ba; B = Ta, V). Several of the quaternary oxynitrides are

perovskites oxynitrides. with formula $ABO_{2-x}N_{1+x}$ where B site: early transition metals Ti^{4+}, Nb^{5+}, and Ta^{5+} (12-fold cuboctahedral coordination) and A site: Alkaline Earth elements^{2+} (Ca^{3+}, Sr^{2+}, Ba^{2+}) and Ln^{3+} (La^{3+}, Nd^{3+}) (6 fold octahedral coordination). Different crystal symmetries from cubic *Pm*.3*m* to tetragonal, orthorhombic or monoclinic superstructures as a consequence of varying level of less understood anion ordering is reported in literature.[78, 79]

3.3 Oxynitride synthesis: overview and challenges

High temperature ammonolysis of precursor oxides is the most common synthesis route for bulk or powder form synthesis of these oxynitrides.[60-62, 66] This is a two-step process, wherein first the requisite oxide needs to be procured/ synthesized, followed by high temperature ammonolysis. Alternatively, instead of doing ex-situ ammonolysis using NH3 as nitrogen, a one-step oxynitride synthesis route is also discussed in literature which involves a urea-based sol gel one step route, for the tantalum oxynitride system. Some of this work has been followed for TaON nanoparticles synthesis in this work later in the respective section.

3.3.1 Oxide precursor synthesis: Overview and Challenges

The two-step ammonolysis of oxide-based precursors is the most common process and has been applied the most while exploring synthesis of different oxynitride systems studied in this work. For the synthesis of ternary oxynitrides, mostly the precursor of these ammonolysis reactions are binary metal oxides, that can be directly purchased in high purity. For example, Ta_2O_5, MoO_3, MoO_2, WO_3 were purchased (details of vendor and purity in respective sections) for their respective oxynitride synthesis work. However, sometimes to achieve advanced morphologies or target specific oxynitride phases during ammonolysis, these binary oxides are synthesized in-house. For example, in one of the collaborative works (*Elise and Jill, Haile Group, Northwestern University*) hydrogen molybdenum bronzes synthesized in this work (refer

Appendix B.3), were used to produce highest surface area Cubic γ-phase Molybdenum oxynitrides at lower reported temperatures. In general, when more than one cation based oxynitride phases are required (example quarternary oxynitrides A-B-OxNy), complex precursors need to be synthesized. Depending on the complexity of the oxynitride system, several synthesis protocols are used including solid and liquid chemistry-based approaches.[80-83] As shown in Figure 3.1-2, three such synthesis approaches were used in this work for precursor synthesis:

3.3.1.1 Solid State Reaction

This is the conventional ceramic route, in which appropriate amounts of metal oxides or carbonates are mixed, and then the mixture is heated for a long period at high temperatures to allow interdiffusion of the cations. This method is often scalable, simple, and cost effective, however, sometime in difficult to diffuse cations inhomogeneous product can form, and often very high temperature and pressure is required in this approach. Therefore, preparing oxides in their pure form at relatively low temperatures is mostly the bottleneck in this approach.[84] An example form this work is the synthesis of Lanthanum Vanadium Oxide precursor.

$$La_2O_3 + V_2O_5 \xrightarrow[900C,\ 15\,hrs]{} LaVO_4$$

3.3.1.2 Sol Gel | Polymerized Complex | Pechini –Solution chemistry.

Above disadvantages can be taken care by pursuing Sol–gel process, which is a chemical solution route often involving alkoxide precursors[85, 86]. It enables shorter heating time at relatively low temperatures, while support multi-cations easily for homogenous products at the end. This method has excellent control over the texture and surface properties of the materials[87], often producing small particle size resulting in

good surface area for catalysis[65, 80, 88]. Nanostructures are often reproducibly synthesized using Sol gel approaches, and so are films and fibres[84, 89]. However, the method is often very messy, difficult to scale up reproducibly, and can be complex if the nominal choice of conditions cannot avoid the insoluble hydroxide formation.

In general the Sol gel process involves three major progressions (more detail by Parashar et.al[84]) :

(1) Hydrolysis: Precursor hydrolysis in water (aqueous sol–gel method) or in a alcohol (nonaqueous sol–gel route). In addition to water and alcohol, an acid or a base also helps in the hydrolysis of the precursors. The general chemical reaction for the hydrolysis process is given below:

$$M - OR + H2O \rightarrow MOH + ROH(Hydrolysis), where\ M\ =\ metal, R\ =\ alkyl\ group\ (CnH2n + 1)$$

The amount of water strongly influences the gel formation; a higher water content facilitates the formation of a higher ratio of bridging to nonbridging oxygens, thus yielding a more polymerized and more branched structure during the condensation.[90]

(2) Gelation: Condensation of adjacent molecules, where water/alcohol are eliminated and metal oxide linkages are formed, and polymeric networks grow to colloidal dimensions in the liquid, increasing its viscosity leading to the gel formation. [89, 91] The general chemical reaction (effected by pH and alcohol precursor choice, [89] but esterification often supports long pH ranges as one of the strengths of Sol Gel techniques) for the condensation process is given below[89]:

$$M - OH\ + XO - M \rightarrow M - O - M\ +\ XOH(Condensation), where\ M\ =\ metal, X$$
$$=\ H\ or\ alkyl\ Group\ (CnH2n + 1)$$

(3) Drying and Heat treatment: As the gel dries, it ultimately leads to decrease in porosity and increasing thickness between colloidal particles. Heat treating the porous gel at high temperature causes densification, and crystallization. Lastly, thermal treatment/calcination is performed to

drive off the residues and water molecules from the desired sample, where the temperature plays a key role in controlling the pore size, crystallite size, crystallinity and phase purity, surface area loss (due to sintering) and the density of the material

A further famous subset of the Sol Gel family of reactions, is the polymerized complex (PC) method, a gel technique, known as the Pechini method,[92] where the polymerization between ethylene glycol (EG) and citric acid (CA) in the presence of soluble metal−CA complexes; wherein mixing happens at the molecular level.[85, 93-95] Various oxide precursors synthesized in this work using Sol Gel approach, is shown schematically in Figure 3.3-1, with the progressive stages of hydrolysis, gelation and drying+heat treatment

3.3.1.3 Hydrothermal Synthesis

Hydrothermal synthesis is another process, that offers uniform size and morphology of products, and using which nanostructures with complex morphologies are often synthesized. However, large difference of the ionic radii and chemistry of rare earth ions and transition metal ions is a challenge sometimes, and the technique's biggest drawback is scalability. Typical hydrothermal synthesis involves, heating a mixture of precursors in some solvent (often aqueous based), above the boiling point of water, and consequently, the pressure within the reaction autoclave is dramatically increased above atmospheric pressure. in an autoclave. Autoclave used in this work is Teflon based, however in literature higher pressure and temperature experiments (>250^{o}C) call for stainless steel autoclaves. Combined high temperature and pressure provides a one-step process to produce highly crystalline materials without the need of post annealing treatments, provided parameters such as precursor concentration, fill of autoclave (dictating pressure), temperature, stabilizing agents if any, and the time of synthesis. [81, 96-100]

In our studies, MoO_2 nanoparticles were synthesized in this work, following reported strategies,[101-103] to support a collaborative in-situ study (*Elise and Jill, Haile Group, Northwestern University*) where studying

the ammonolysis of these nanoparticles helps reveal key insights in ammonolysis of MoO_3 reaction pathway to form either γ or δ phase, as discussed later in results and discussions below.

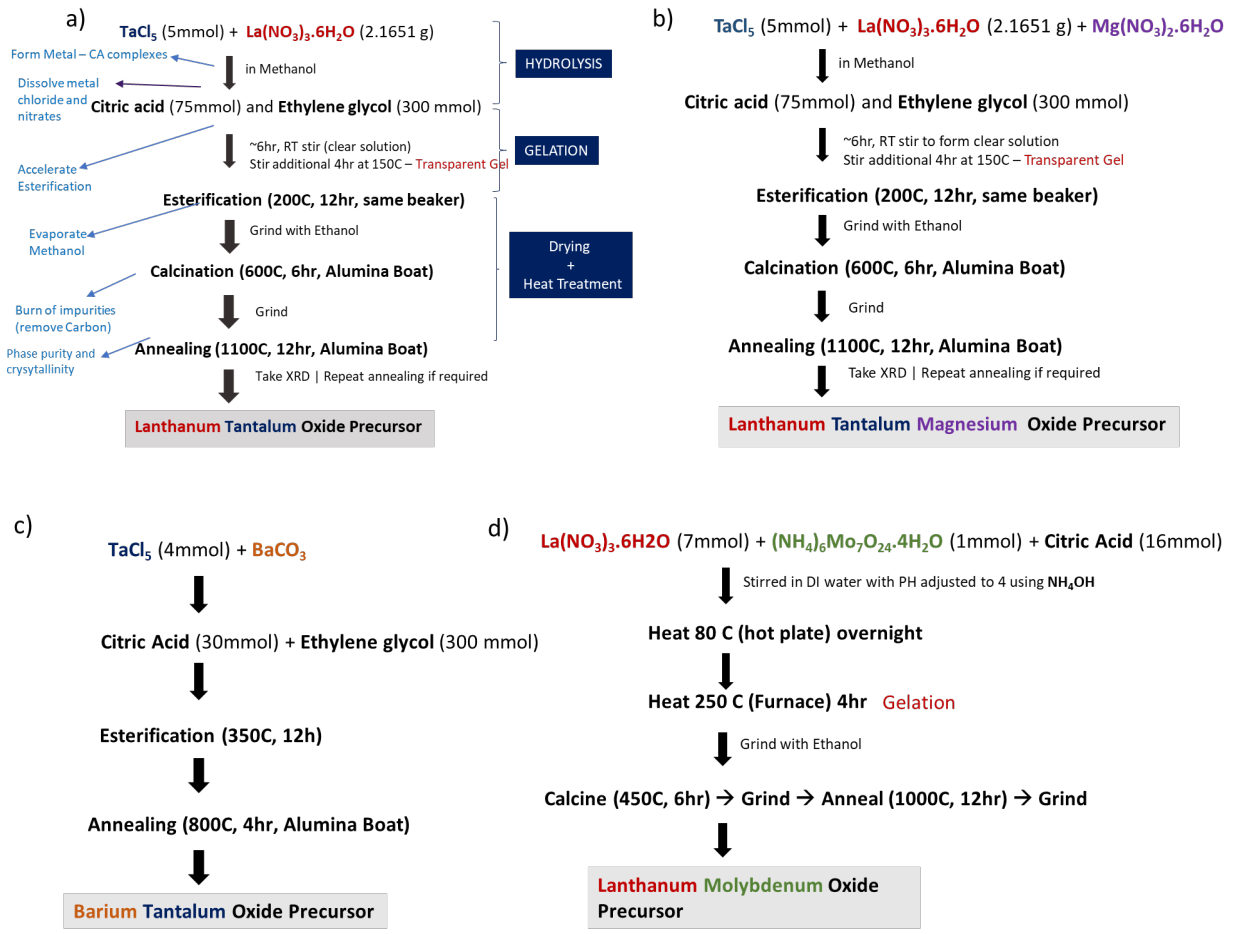

Figure 3.3-1 : Various oxide precursors synthesized in this work using Sol Gel/ Polymerized Complex approach

3.3.2 Ammonolysis for Oxynitrides synthesis: Overview & Challenges

High temperature ammonolysis of precursor oxides is the most common synthesis route for bulk or powder form synthesis of these oxynitrides. Ammonia thermodynamically would be expected to dissociate appreciably into N_2 and H_2 at temperatures higher than 500°C, however the kinetics of the dissociation is

slow, and its extent is often influenced by the flow rate along with reactor geometry, sample placement. It should be acknowledged based on the flow rates we used it should be the undissociated ammonia,[104] that does the nitridation, as shown in Figure 3.3-2b). Details on apparatus used to determine actual %ammonia decomposition can be found in Appendix B.2. Typical experiments involve greater than 20sccm NH_3 flow rate (commonly close to 100sccm) where considerable ammonia (mostly all of it) is in undissociated, yet in active state at high temperatures. It is important to however acknowledge that this estimate is based on empty reactor, and we know the ammonia decomposition could be accelerated in the presence of catalysts.[105] Finally, the ammonia dissociation equilibrium and the simultaneous nitridation reaction of the oxide is sensitive to the presence of pH_2O, for example look at the simultaneous equilibria (Figure 3.3-2c) involved in ammonolysis of simple binary Ta_2O_5.

A schematic of the available ammonolysis system setup at Haile Lab, Northwestern university is show in Figure 3.3-2 a). High temperature nitridation of oxide precursors can be performed either by either using ammonia mixture or nitrogen mixture. For example, for phase pure synthesis of tetragonal β-phase Molybdenum nitride, N_2+H_2 gas mixture (1:3 volume ratio) was necessary, as using dry ammonia for same ammonolysis temperature profile, results in cubic γ-phase molybdenum nitride (Details in Appendix C.1). Therefore, the reactor is equipped with NH_3, N_2 and H_2 lines as reducing gases. However, except for the above special case of β-phase Molybdenum nitride, most phases require flowing dry ammonia (couple hundred sccm over 0.1-1 g precursor sample) over oxide-based metal precursors at high temperatures (500 – 1000^{o}C depending on oxynitride system). This is terms as "Dry ammonolysis" in this work. This Argon (shared with Nitrogen line) is used for purging the reactor before and after synthesis. Nitrogen is often used for purging during pre-synthesis prep for cost effectiveness. This dependence of nitridation potential of the ammonia gas with the introduction of water vapor (bubbled using either Argon or Nitrogen line with separate mass flow controllers for each compared to their dry counterparts on the reactor), can often be used to achieve phase sensitivity. This technique is referred to as "Wet Ammonolysis" in this work. For example, as shall be discussed in their respective sections, even a little

amount of pH_2O with ammonia can help target β-TaON and δ-MoN while suppressing there competing tantalum and molybdenum (oxy)nitride phases for the respective oxynitride systems.

Although, oxynitrides synthesis, focusing on constant improvement in surface area and morphologies of products, have been studied for many years now, less emphasis, however, has been given on understanding the rather complex phase space of these oxynitrides. Reproducibility, phase -pure synthesis , controversial or lack of synthesis pathways knowledge for commonly used ammonolysis recipes to synthesis oxynitrides, lack of proper chemical and structural characterization protocols due to difficult to distinguish N and O, unavailability of complete phase diagrams, little understanding of the N-O ordering (could be completely disordered or ordered) in the structure of these oxynitrides are some of the major challenges in this field limiting the potential of these oxynitrides applications.

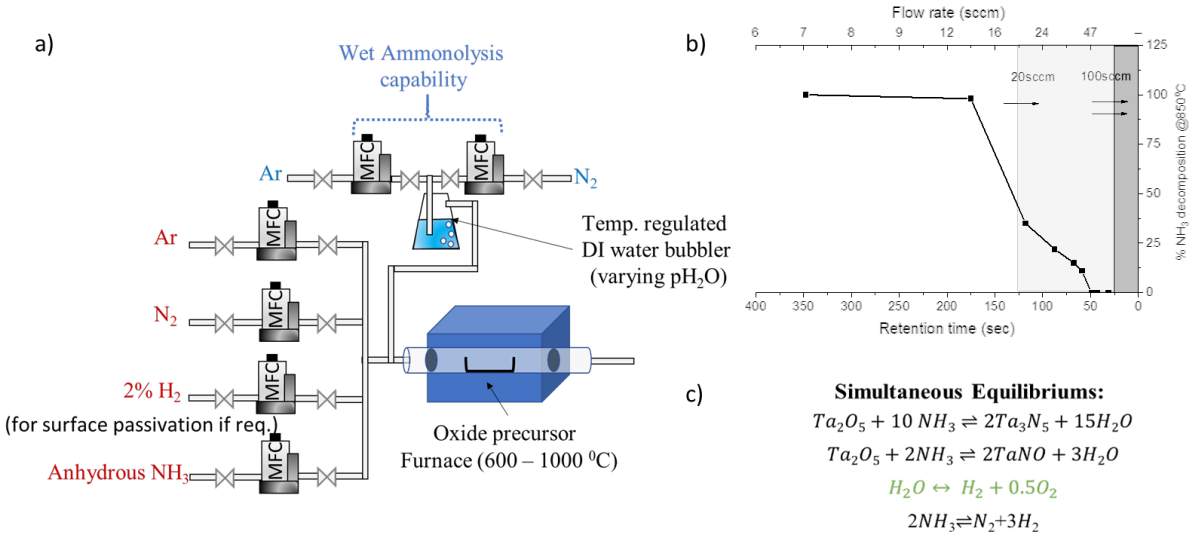

Figure 3.3-2. (a) Ammonolysis reactor schematic (b) Effect of retention time (dependent on flow rate) on actual decomposition of anhydrous ammonia, for Haile Lab ammonia reactor (calibrated using ammonia dissociation measuring burette). c) Example reaction showing the presence of pH_2O (wet ammonolysis) in the system directly effects the simultaneous equilibriums of water dissociation, ammonia dissociation, and nitridation of the oxide. This makes Wet Ammonolysis a phase sensitive process, offering selective phase targeting.

3.4 Oxynitride Candidates in this work

Several oxynitrides systems were worked with in this work in order to screen them for potential catalysis applications. One of the key applications (discussed in detail in Chapter 6) is Solid Acid Electrolyzer Cells (SAEC) where steam splitting happens using super protonic solid acid CDP as electrolyte, and oxynitrides are used to catalyze the hydrogen evolution and oxygen evolution reaction. Simultaneously band gap of all Semiconducting oxynitrides synthesized was measured with DR UV-VIS. By having band in the visible range, some of the discussed oxynitrides can be potential candidate for photocatalysis applications.

For CDP based applications, it is critical for these oxynitrides to show good stability by itself and with CDP under the operating conditions of solid acid-based devices. For this Stability tests (discussed in experimental section 3.5) were carried out to screen the as synthesized oxynitride samples. In total 9 oxynitride systems were evaluated, where the choice of metals was broadly based on their oxide reported to be stable with CDP at operating temperature of 250 °C under required humidity (0.48 atm pH_2O).

5 out of total 9 synthesized oxynitrides in this work were *Photo-absorbing* (as seen in Figure 3.1-2):

(1) Highlight Case: Molybdenum Oxynitride system (Mo-O-N)
(2) Tungsten Oxynitride system (W-O-N)
(3) Niobium Oxynitride (Nb-O-N)
(4) Lanthanum Molybdenum Oxynitride (La-Mo-O-N) | Never reported before
(5) Lanthanum Vanadium Oxynitride (La-V-O-N)

The remaining 4 oxynitrides are *Semiconducting* (as seen in Figure 3.1-2):

(1) Highlight Case: Tantalum Oxynitride (Ta-O-N)
(2) Titanium Oxynitride
(3) Lanthanum Tantalum Oxynitride (La-Ta-O-N)
(4) Lanthanum Barium Oxynitride (La-Ba-O-N)

Additionally, for a separate collaboration (Jaye Harda, Rondinelli Group, Northwestern University), Strontium Tantalum Oxynitride, specifically the $SrTaO_2N$: Ruddlesden-Popper compound, which is difficult to synthesize phase pure, was achieved through iterative ammonolysis process, on in-house synthesized precursor. Details in Appendix C.4.

3.5 Experimental details

3.5.1 CDP synthesis

All the synthesis details of oxides and oxynitrides are integrated into their respective sections, excluding generic experimental details which are mentioned in this section.

Coarse CDP was made through a co-precipitation method. 14.19 g H_3PO_4 (o-phosphoric, 85 wt%, Fisher Chemical) was slowly added to 20.00 g Cs_2CO_3 (Cs_2CO_3, 99.99%, Alfa Aesar) powder with Pasteur pipette. After that, 10 ml DI water was added to the suspension while stirring under 333 K until all the solid was completely dissolved. Then, the mixture was poured into 200 ml methanol and massive precipitation was formed. CDP was obtained by filtering the powder and drying overnight under 353 K.

3.5.2 High temperature stability tests with CDP under steam @250^{o}C

In order to probe oxynitrides for their potential for being a catalyst in CDP based applications, or in general their own stability under steam at 250^{o}C several tests were done following below standard protocol.

Oxynitride – Steam test: To test the stability in the steam, oxynitride powder was first heated to 150^{o}C under N_2 flow (flow rate: 40 ml/min) with negligible humidity. After that, the powder was heated to 250^{o}C

under humidified N_2. The condition was achieved by flowing the N_2 through a bubbler kept at 80°C , to ensure the partial pressure of steam was over 0.4 atm. Then, the powder was kept at 250°C for 24 h and allowed to cool down to 150°C. The atmosphere was switched to dry N_2 again in order to prevent water condensing when the temperature drops below 423 K.

Oxynitride-CDP stability test: To test the reactivity between oxynitride and CDP, a disk sample was prepared by pressing the mixing powder of oxynitride and CDP, in 1:1 wt ratio (~300mg total). The pellet was first heated to 150°C under N_2 flow (flow rate: 40 ml/min) with negligible humidity. The pellet was then heated to 250°C under the atmosphere of N_2 and H_2O. The condition was achieved by flowing the N_2 through a bubbler kept at 80°C , to ensure the partial pressure of steam was over 0.4 atm. Then, the powder was kept at 250°C for 48 h and allowed to cool down to 250°C . The atmosphere was switched to dry N_2 again to prevent water condensing when the temperature drops below 150°C.

3.5.3 Characterization Details (XRD, UV-VIS and XPS)

Powder X-ray Diffraction (PXRD) patterns were recorded by a powder diffractometer (Rigaku Ultima IV) using Cu Kα radiation, and zero background Si-C holder to avoid any peaks from holder. For post reactivity tests, disk samples were broken and carefully ground in a mortar before each Lab XRD measurement.

Diffuse Reflectance Ultraviolet-visible Spectroscopy (DRUV-vis) measurements was performed on a spectrophotometer (Perkin Elmer LAMBDA 1050) equipped with an integrating diffuse reflectance module. The powder sample was carefully sandwiched between two quartz slides to make an area without any crack and exposed to the aperture. Quantitative analysis of band gap energy is carried out through Tauc method.[106] Firstly, relative reflectance R is transferred to F(R) based on the following equation:

$$\mathrm{F(R)} = \frac{(1-R)^2}{2R}$$

According to K-M (Kubelka-Munk) mode, F(R) is proportional to extinction coefficient α for scattering particles in a matrix. Then, the relation between electronic transition behavior and α can be described as the following expression proposed by Tauc and co-workers: [106]

$$(\alpha h\nu)^{1/n} = A(h\nu - E_g)$$

where h is the Planck's constant; ν is the frequency of light; A is the proportional constant; E_g is the band gap; n = 1/2 for semiconductors with direct band gap and n = 2 for those with indirect band gap. Since, indirect band gaps for photoactive materials are often reported, the value of 2 was used. Finally, the raw data were re-depicted by plotting [F(R) $h\nu$]^2 versus $h\nu$. The energy of band gap can be reported by extrapolating the linear part to F(R) = 0.

X-ray Photoelectron Spectroscopy (XPS) data was collected on a spectrophotometer (Thermo Scientific ESCALAB 250Xi) by applying the Cu tape to stick the powder sample. The position of C 1s line was set to 284.6 eV for charge correction.

3.6 Highlight System : Molybdenum Oxynitride

3.6.1 Mo-O-N phase space and synthesis challenges

Although not comprehensive, molybdenum nitride system phase diagram is reported in literature.[107] Apart from the solid solution (α phase) which contains about 1.8 at. %N, molybdenum nitrides are known to crystallize in two non-stoichiometric crystal systems and one stoichiometric crystal system. The tetragonal β phase is a non-stoichiometric phase and is a face centered tetragonal structure of metal atoms with an ordered array on nitrogen atoms. Existing at higher temperature, the cubic-γ phase is also non-stoichiometric with molybdenum in weird partial positive state stabilized by vacancy while oxygen and nitrogen occupying similar sites and is thermodynamically less stable than both the α and β phases. The

cubic phase is reported in both Fm-3m (225 sg),[108, 109] and Pm-3m (221 sg) space group.[110] The hexagonal-δ (MoN) phase is the only stoichiometric phase, of which also several different space groups have been reported lately.[111]

Preliminary experiments, show that mixture of γ-Mo_2N (matching with Cubic 225sg, PDF# 04-018-6868) and δ -phase (matching with hexagonal 186sg, PDF#04-003-5713) is obtained, on ammonolysis of as purchased molybdenum oxide, 0.25g MoO_3 *(XRD Orthorhombic, Pbnm (62)*, PDF#04-007-0887) at 700oC, for 5 hrs following a constant heating rate of 5°C/min and natural cooling to room temperature all under 100sccm of dry ammonia (C. Upon subjecting the γ+δ mixture to CDP-Oxynitride stability test, the ammonolysis mixture remained stable with no new Lab XRD peaks apart from CDP and ammonolysis phases could be seen as shown in Figure 3.6-1. More stability tests of Molybdenum nitride in contact with CDP under humidified oxygen rather than nitogen, and also conductivity properties, are discussed in Appendix B.9.

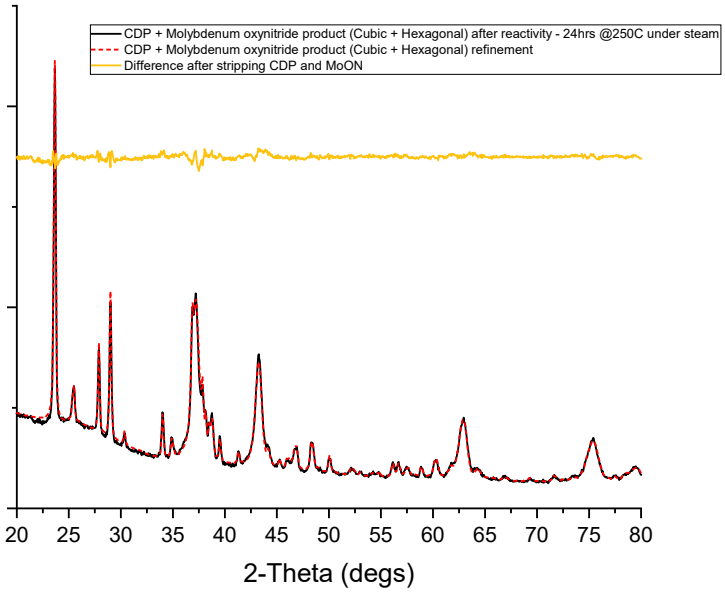

Figure 3.6-1 : After reactivity product XRD (black solid line) can be completely refined by CDP + γ-Mo_2N (Cubic, sg: Fm-3m (225)) and δ-MoN (Hexagonal, sg: P63mc (186)), and upon stripping these phases, only noise remains (yellow line), suggesting no reaction of Molybdenum nitrides with CDP under humidified N2 (0.4 pH_2O) @250°C.

3.6.2 Phase pure synthesis of Cubic γ-phase(s) via MoO_3 ammonolysis .

3.6.2.1 Optimizing Ammonolysis recipe for phase pure Cubic F (γ-Mo_2N) and Cubic P (γ'-Mo_3N_2)

Aiming for phase pure cubic γ-Mo_2N product, several dry ammonolysis conditions on MoO_3 precursor, were attempted, as summarized in Table 3.6-1 below (Lab XRD not shown). These conditions leading to γ phase via dry ammonolysis of MoO_3, are acronymed as DA-MoO3-#. To maximize the cubic phase, increased flow rate in Condition DA-MoO_3-2 vs preliminary analysis above done using DA-MoO_3-1 (used for CDP stability test) was used, followed by increased ammonolysis time (DA-MoO_3-3), decreased sample size and more extended ammonolysis time (DA-MoO_3-4) were attempted, which did help maximize cubic phase. Phase pure cubic- Mo_2N was obtained upon following an alternative approach reported by Sayag et al,[112] wherein a slow ramp rate of 0.6 °C/min in the temperature range of 300 – 500° C was reported to synthesize the cubic γ-Mo_2N phase. No reason was given for the slower ramp rate in the literature, however in-situ studies done in collaborative MRSEC IRG2 project, helps understand the role of intermediates and slow ramp rate, discussed in brief in this chapter later. This was used for Condition *DA-MoO_3-5*, wherein initially temperature was ramped to 350ºC @5ºC/min, from 350-500ºC @0.6ºC/min and 500-700ºC @3ºC/min, hold for 3hrs before cooling down naturally. Higher hold times were tried, but 3 hrs was found enough to achieve complete mass loss within the sensitivity of lab microbalance within experimental error. Synthesized γ-Mo_2N, rietveld analysis shows that the lattice parameter in the cubic γ-Mo_2N phase has been determined to be 4.187 Å. Finally, the same heating profile from above is extended in Condition *DA-MoO_3-6* to 800ºC, and this results in the primitive cubic Pm-3m space group molybdenum nitride pattern reported as γ'-Mo_3N_2 phase[51], differentiated by the presence of superstructure peaks for the Cubic P phase, with a larger lattice constant of 4.129 Å .

Note to reader: For simplicity, these two important phase pure samples synthesized by DA-MoO_3-5 and DA-MoO_3-6 conditions will here on be referred as phase pure C700 and C800 samples respectively, where C refers to the Cubic crystal system, and following number represents the ammonolysis synthesis temperature

for these important sample. Later these samples are characterized in detail as an oxynitride hydride both of which have the same 221sg, therefore both are Cubic P with different compositions as confirmed from Neutron and Xray corefinements in Chapter 4. However, for the purpose of this thesis these two products, are referred interchangeably to as γ-Mo_2N ↔ γ-phase ↔ Cubic F ↔ C700); and γ'-Mo_3N_2 ↔Cubic P ↔ C800 samples for the sake of simplicity, just because their Lab XRD at first pass would match well with Fm-3m (γ-Mo_2N) and Pm-3m (γ'-Mo_3N_2). These are also referred to as A700 and A800 in published article on this work.

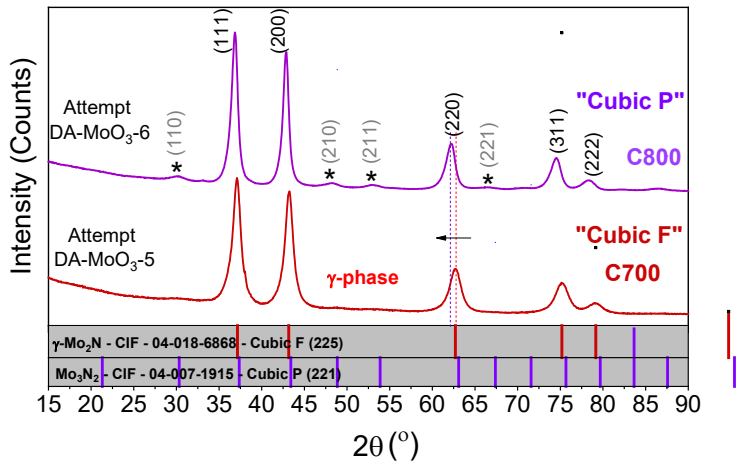

Figure 3.6-2. Representative lab XRD patterns of Cubic F (lower) and Cubic P (upper) collected with Cu Kα radiation (λ = 1.5406 Å). Diffraction peaks of mixed *h k l* parity, required to be absent for a face-centered cubic lattice, have finite intensity in the pattern of Cubic P. The patterns are further differentiated by the narrower peaks, indicative of a larger crystallite size, and by the larger lattice constant of the Cubic P material

3.6.2.2 MoO_3 Dry Ammonolysis reaction pathway to Cubic γ-phase

In order to understand how the intermediates in the phase pure formation of these Cubic phases (C700 and C800 samples) via MoO_3 ammonolysis, several *Ex-situ* (where samples are synthesized and then evaluated with XRD), followed by *In-situ Lab XRD* (where continuous Lab XRD scans are taken while the ammonolysis happens inside the XRD chamber) ammonolysis were done.

Note to reader : In Chapter 4, it is shown that the sample to sample variation was observed in cubic γ-phases (Cubic F and Cubic P) that were synthesized via dry ammonolysis of MoO_3 coming from different precursor bottle. Differences were observed between Sigma Aldrich vs Alfa Aesar MoO_3 bottles, and even between different bottles from same vendor (see Appendix B.8). However, for all the cubic samples synthesized in this chapter, only single precursor bottle (Alfa Aesar – Original, see Appendix B.8 for details)

For the set of *Ex-situ* experiments, MoO_3 was subjected to ammonolysis at various temperatures, following different heating profiles. Heating profiles of these 4 ex-situ synthesized samples via Dry ammonolysis of MoO_3 is shown schematically in Figure 3.6-3. For the low temperatures (Region 1 : 350ºC, 425ºC and 500ºC), where intermediates were expected mostly based on prior literature,[113, 114] the ammonolysis of MoO_3 was stopped at these temperatures without any hold and the ammonia was turned off and switched to equal flow (100sccm) of Argon to preserve the intermediates and stop any further nitridation during cooling step. These samples are called MoO_3-350, MoO_3-425 and MoO_3-500. For the high temperature case of 650ºC , where ammonolysis is expected to be close to completion, a 3 hr hold was introduced. This sample is called MoO_3-650. Lab XRD analysis of above 4 Ex-situ synthesized MoO_3 ammonolysis samples at different temperatures, along with phase pure C700 and C800 Cubic phase samples, and MoO_3 was performed using Rietveld refinement in JADE, with phase fractions, lattice constant, and crystallite size were determined and summarized in Figure 3.6-4. Phase fraction plot, Figure 3.6-4a), starting from phase pure precursor (MoO3), shows the presence of MoO_2 and bronze as intermediates in mid temperatures. The identified bronze matches with Orthorhombic (Cmcm), with lattice constant suggesting $H_{0.3}MoO_3$ composition (detailed discussion on Bronze in Appendix B.3). The presence of bronze in MoO_3-350 and MoO_3-425 (progressively decreasing), and the appearance of the γ-phase nitride as major product (remainder being unreacted MoO_2) in MoO_3-500, suggests that the MoO_3 proceeds to the final cubic phase via orthorhombic bronze and monoclinic MoO_2, however it's unclear if the bronze entirely converts to nitride only or goes through MoO_2. This is where literature is also split in terms of reaction pathway. The two possible reaction pathways from MoO_3 to γ-phase nitride are shown in Figure 3.6-6a) and Figure 3.6-6b). The bronze is known to form via hydrogen intercalation in layered

MoO_3 resulting in lattice expansion along b axis, where its overall structure is same as the starting precursor MoO_3, with its lattice slightly expanded (Figure 3.6-4b)) compared to MoO_3. Such pseudomorphic transformation is accompanied by a rapid drop in crystal size of the MoO_3, apparent with the lower crystallite size of remaining MoO_3 in ex-situ synthesized products (Figure 3.6-4c)).[114-117] The bronze and MoO_2 form of similar crystallite size range in intermediate samples, with the bronze retained in MoO_3-425 being of lower crystallite size compared to MoO_3-350, suggesting overall the average crystallite size of products keeps dropping, towards the Cubic phase which only have 5-9nm size crystallite size.

In order to clarify the complete synthesis pathway and to build on to the Ex-situ ammonolysis analysis discussed above, a series of in situ PXRD measurements were carried out to understand phase evolution from MoO_3 to phase pure Cubic γ-phase. Details of this collaborative work, and in general, on the reaction pathway study of molybdenum and tantalum oxynitrides can be found in Elise Goldfine's thesis, Haile Group, Northwestern University. Replicating the ex-situ γ-phase synthesis condition (*DAG-MoO_3-5)* as much as possible (note some time was involved in taking in-situ periodic scans which made the effective ramp rates slightly different), in-situ PXRD runs of MoO_3 ammonolysis was performed. To understand the role of intermediates, in situ PXRD measurements were also carried out on MoO_2 and in-house synthesized orthorhombic bronze (details on Blue Orthorhombic $H_{0.3}MoO_3$ bronze is in Appendix B.3). Phase evolutions (intermediates and products) are shown with time on x-axis, and temperature overlayed on alternate axis in Figure 3.6-5. The resulting reaction pathway from MoO_3 to phase pure Cubic nitrides derived from combined observations of these three in-situ experiments in shown in Figure 3.6-6.

Table 3.6-1. MoO_3 Dry Ammonolysis runs leading to Cubic F (γ-Mo_2N) and Cubic P (γ-Mo_3N_2) phase pure cubic samples synthesized at 700C and 800C using slow ramp rate intermediate temperatures.[113, 116]

Condition	*Precursor amount (g)*	*Dry ammonolysis Experimental Condition*			*γ-Mo_2N (Space group: Fm-3m(225))*		*δ-MoN (Space group : P63mc (186))*		
			Temp/ Time	*Gas Composition*	*Phase %*	*Lattice (A)*	*Phase %*	*a*	*c*
DA-MoO_3-1	0.25	Heating	25 to 700C @5C/min	50 sccm NH_3 VF: (178 cm^3/min)	94.5	a = 4.18507 <2>	5.5	a = 5.73309 <2>	c = 5.61031 <2>
		@700C	5 hrs.						
		Cooling	Furnace Cooling						
DA-MoO_3-2	0.25	Heating	25 to 700C @5C/min	100 sccm NH_3 VF: (356 cm^3/min)	97.4	a = 4.18511 <2>	2.4	a = 5.73313 <2>	c = 5.61026 <2>
		@700C	5 hrs.						
		Cooling	Furnace Cooling						
DA-MoO_3-3	0.25	Heating	25 to 700C @5C/min	100 sccm NH_3 VF: (356 cm^3/min)	97.9	a = 4.18509 <2>	2.1	a = 5.73325 <2>	c = 5.61029 <2>
		@700C	10 hrs.						
		Cooling	Furnace Cooling						
DA-MoO_3-4	0.1	Heating	25 to 700C @5C/min	100 sccm NH_3 VF: (356cm^3/min)	95.7	a = 4.18477 <2>	4.3	a = 5.73310 <2>	c = 5.61086 <2>
		@700C	20 hrs.						
		Cooling	Furnace Cooling						
DA-MoO_3-5	0.25	Heating	25 C to 350 C @5C/min, 350C to 500C @0.6/min, 500C to 700C @ 3C/min	100 sccm NH_3 VF: (356cm^3/min)	**100% Cubic** F	a = 4.18317 <2>	-	-	-
		@700C	3 hrs.						
		Cooling	Furnace Cooling						
DA-MoO_3-6	0.5g	Heating	25 C to 350 C @5C/min, 350C to 500C @0.6/min, 500C to 800C @ 3C/min	100 sccm NH_3 VF: (356cm^3/min)	**100% Cubic P**	4.22577<2>	-	-	-
		@800C	3 hrs.						
		Cooling	Furnace Cooling						

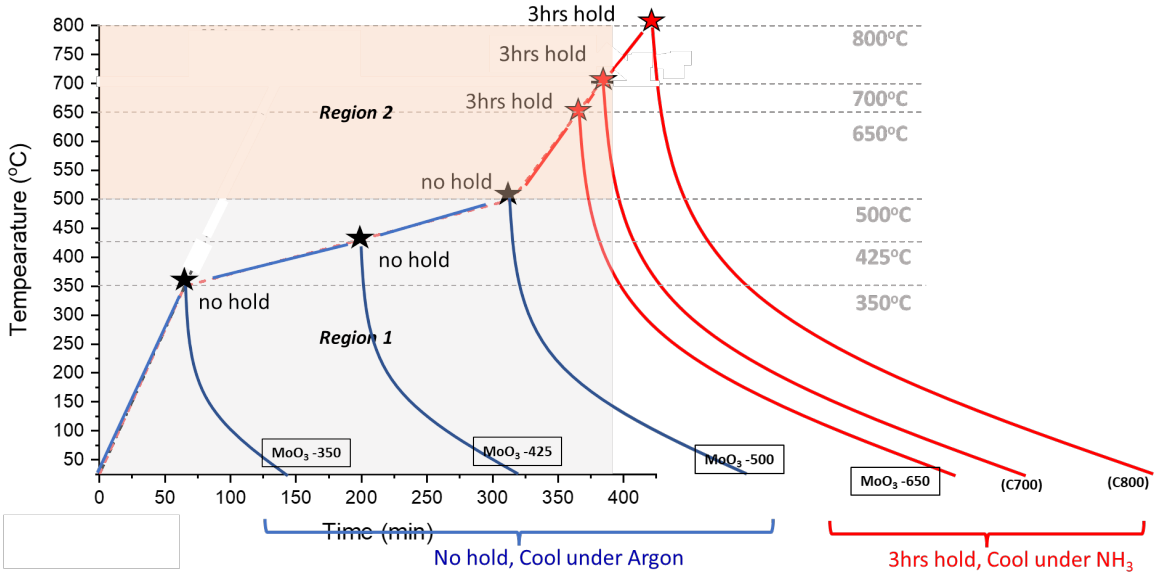

Figure 3.6-3 Ex-situ experiments layout showing the various heating profiles used for performing MoO_3 Dry ammonolysis at various temperatures, producing sample that are analyzed ex-situ post synthesis.

Figure 3.6-5a), shows in-situ phase evolution plot for MoO_3 (orthorhombic, space group Pbnm) ammonolysis to 700C. Agreeing with what was observed from ex-situ samples, two intermediates are observed, (1) MoO_2, with space group $P2_1/c$, and (2) orthorhombic hydrogen molybdenum bronze, $H_{0.3}MoO_3$, with space group Cmcm, both of which convert to cubic nitride product finally (γ-phase). However, given the bronze/ MoO_2 appearance and disappearance happens in short span of time, it's unclear from just MoO_3 ammonolysis in-situ experiment, if the bronze also converts to MoO_2. It should be noted that a small amount of secondary nitride phase hexagonal δ-phase (186 sg), appears at mid temperatures, which seems to go away if the reaction temperature is raised to ~750C. This could be due to slight differences in average heating profile and gas flow velocities between in-situ and ex-situ runs as δ-phase was not observed in ex-situ synthesis using DAG-*MoO_3-5* recipe at 700°C hold and cooldown.

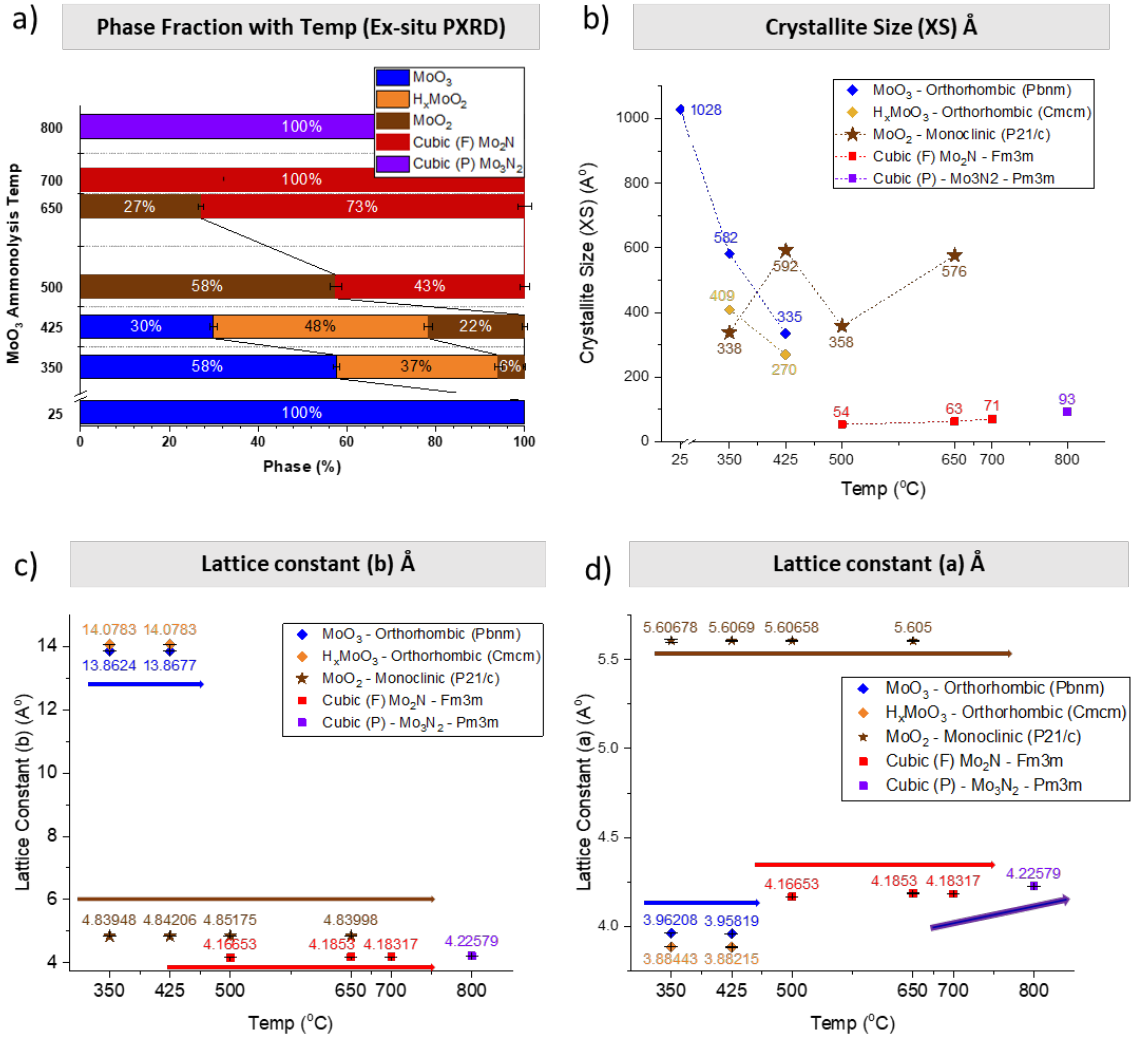

Figure 3.6-4 Lab XRD analysis of Ex-situ synthesized MoO_3 ammonolysis samples at different temperatures. (a) Phase fraction, b) crystallite size, (c)&(d) lattice constants for these ex-situ ammonolysis products. Starting from phase pure precursor (MoO3), intermediate samples show the presence of MoO_2 and bronze as intermediate, and finally phase pure synthesis of small crystalline sized Cubic F (C700) and Cubic P (C800) samples obtained at 700 and 800C.

Noting that the two intermediates (MoO_2 and $H_{0.3}MoO_3$) coexist for about ~60 °C, and to clarify the disputed MoO_3 ammonolysis pathways in Figure 3.6-6a) and b), to understand if the bronze transforms to MoO_2 during the ammonolysis reaction of MoO_3, in situ PXRD was utilized to monitor the ammonolysis reactions of commercial MoO_2 and in-house synthesized $H_{0.3}MoO_3$ under the same reaction conditions as those with MoO_3 as the precursor.

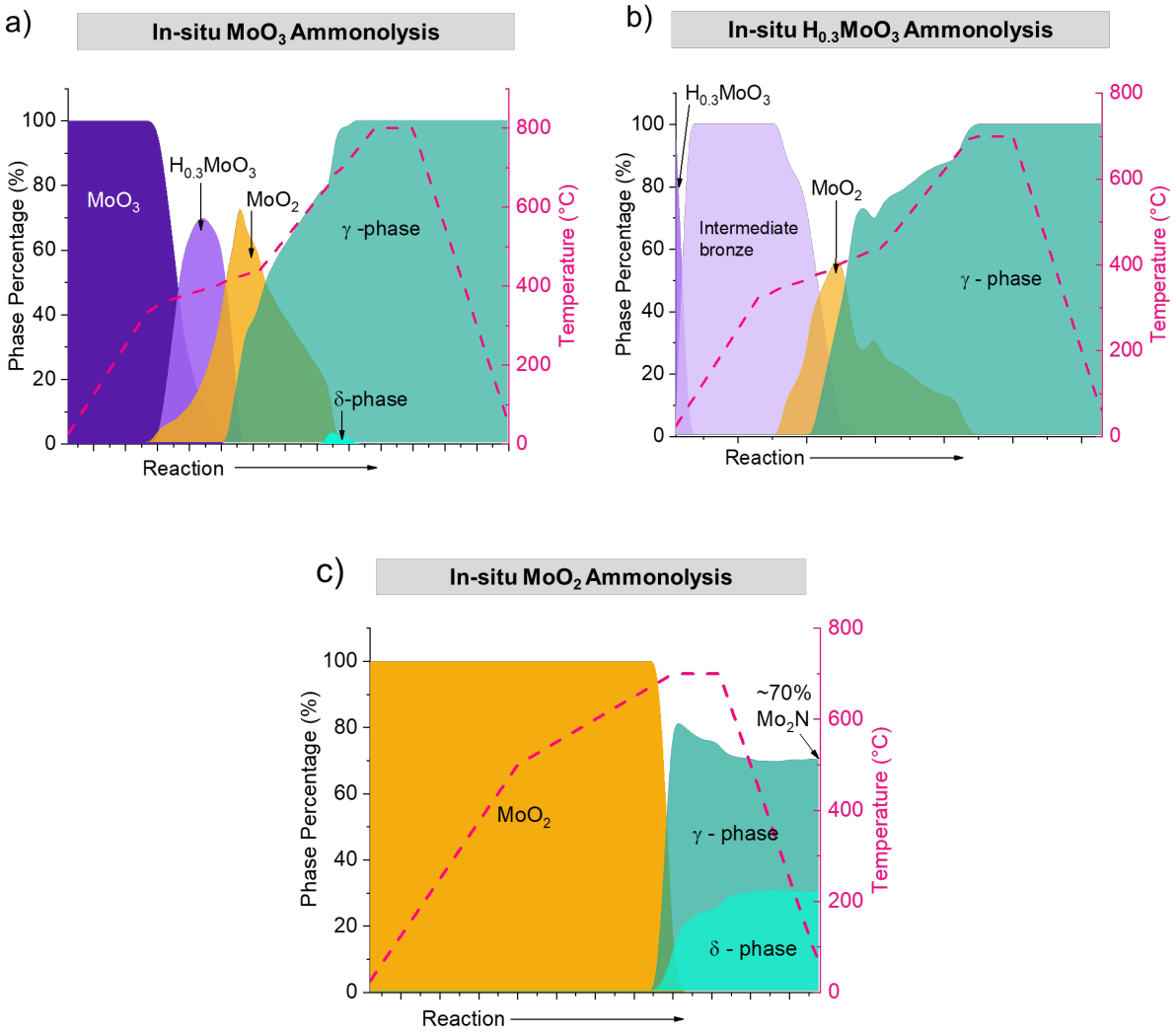

Figure 3.6-5 : Phase evolution with time based on in-situ Lab XRD dry ammonolysis studies starting with (a) MoO_3, (b) Bronze and (c) MoO_2 (Courtesy : Elise Goldfine and Jill Wenderott, Northwestern University, Haile Group)

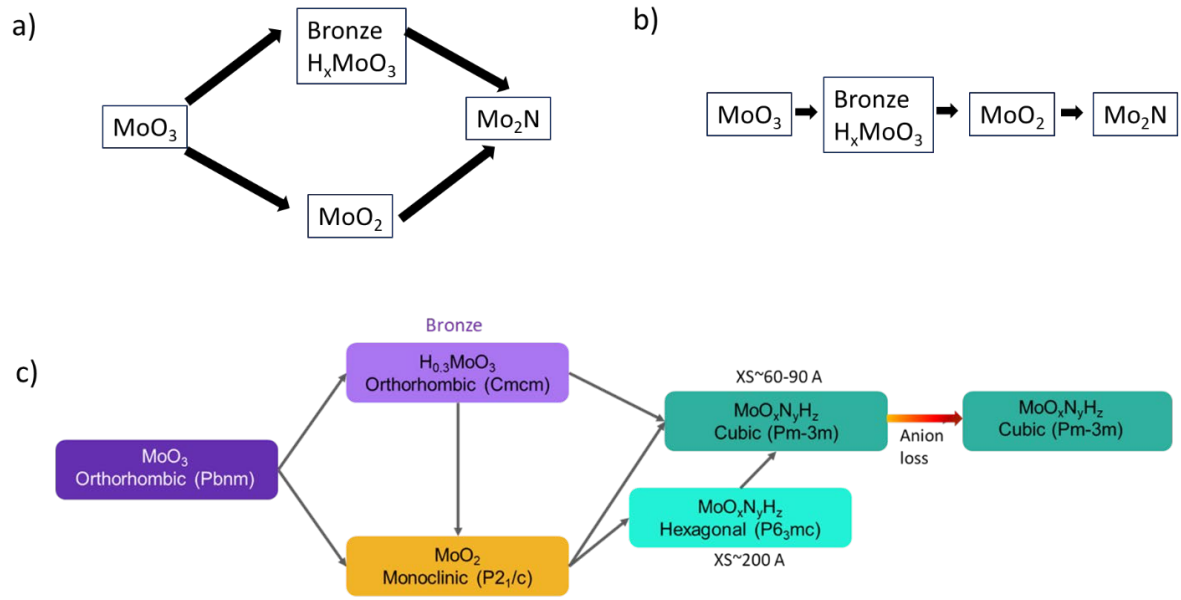

Figure 3.6-6 (a) and (b) Literature suggested reaction pathways for MoO_3 ammonolysis resulting in γ-phase via high temperature dry ammonolysis.[55, 58-60] (c) Actual MoO_3 reaction pathway determined by combination of ex-situ and in-situ studies in this work.

As a precursor, $H_{0.3}MoO_3$ in-situ studies Figure 3.6-5b), shows erratic intermediate bronzes formation at lower temperatures that quickly dissipates in rapid formation of MoO_2 first, then quickly followed by appearance of γ-phase, whose phase fraction kept increasing, with intermediates rapidly converting to phase pure γ-phase. It is noteworthy that the bronze, does not lead to the formation of any amount of competing hexagonal δ- phase. This is in good agreement with several ex-situ studies (not discussed here), that show that bronze (irrespective of type of bronze with various crystal systems and space group) when subjected to dry ammonolysis resulted in γ-phase only at temperatures beyond 500°C, with no hexagonal δ-phase formation. However, in-situ studies on MoO_2, Figure 3.6-5c) shows that unlike bronze, MoO_2 is indecisive under dry ammonia resulting in considerable (~30wt%) fraction of secondary hexagonal δ- phase, however no bronze formation was observed, confirming that transformation of bronze to MoO_2 was a one way reaction. DFT studies in collaboration with Wolverton group, Northwestern University (Courtesy : Jiahong Shen, Christopher Wolverton Group, Northwestern University) were performed, that corroborate these in-situ results, showing that with higher temperatures, both the

competing γ and δ phases share phase boundary with MoO_2, supporting the above observations. This study however are just preliminary calculations as this used literature reported Mo_2N and MoN composition for γ and δ phase respectively, and therefore some changes are expected if true oxynitride compositions were used which were determined later in time. It is interesting to note that micron crystallite sized commercially brought MoO_2 powders, are not a good representative of the MoO_2 that had formed in ex-situ MoO3-350, MoO3-425 and MoO3-425 samples, as a result of MoO_3 ammonolysis, as these had much smaller crystallite size (~0.3-0.5 micron). Such a MoO_2 intermediate results in mainly γ-phase (if not phase pure C700, C800), which raises the question of what factors causes this ambiguous behavior of MoO_2. More in-situ studies were performed starting with MoO_2 nanoparticles synthesized in this Chapter above with small (more relevant to inform synthesis pathway of MoO_3 ammonolysis) crystallite size. The in-situ studies comparing dry ammonolysis of commercial MoO_2 and MoO_2 nanoparticles, revealed that crystallite size of MoO_2 does play a role in the final product formed, as it seems the nanosized powder favors the formation of γ-phase, but δ-phase is still present in considerable amount in the final nitride product.

Final reaction pathway, visualized after above ex-situ and in-situ studies discussion is shown in Figure 3.6-6c). This collaborative study (Courtesy : Elise Goldfine and Jill Wenderott, Haile Group, Northwestern University), clarifies the debated pathways in Figure 3.6-6a) and b), and establishes a critical understanding that the bronze does convert to MoO2 in some amounts irreversibly, and the fact that MoO_2 plays a critical role in determining if we see the presence of secondary δ- phase or not, when aiming for phase pure γ product.

3.6.3 Hexagonal δ-Phase via Wet ammonolysis of oxides

In comparison to Dry ammonolysis, which favored Cubic γ- phase, it was observed that Wet ammonolysis favored the formation of Hexagonal δ- phase nitride. Wet ammonolysis was realized as a novel synthesis protocol to synthesize phase pure hexagonal δ-phase nitride, starting from MoO_2. As discussed in the

introduction, δ-phase hexagonal molybdenum nitride (often written as stoichiometric MoN phase), is mostly never synthesized via ammonolysis of oxide precursors, as that usually results in mainly competing cubic γ-Mo_2N phase. It was realized that irrespective of precursor choice, introduction of small % of pH_2O along with ammonia during high temperature ammonolysis results in formation of considerably δ-phase in the final product.

The key sample called as the “Delta Phase”↔δ-phase↔δ-MoN↔H700 in this work was synthesized using an optimized wet ammonolysis reaction, wherein MoO_2 precursor was heated to 973K and held for 12 hrs and then furnace cooled to room temperature, all under the mixture of anhydrous NH3 and humidified Argon, with 2% pH_2O (details in Table 3.6-2, Sample ID : “Delta Phase”). However, to reach this optimized recipe, several dry and wet ammonolysis were carried out to understand the effect of different partial pressure of pH_2O, heating rate and precursor choice. For the precursors, MoO_3 (99.9995% metals basis) and MoO_2 (99% metal basis) were purchased from Alfa Aesar, while H_2MoO_5 Molybdenum bronze was synthesized in-house as described earlier (discussed in detail along with other bronzes in Appendix B.3).[118, 119] Figure 3.6-8 shows Lab XRD of as purchased MoO_2 (Monoclinic), MoO_3 (Orthorhombic) and as synthesized H_2MoO_5 bronze (monoclinic). Molybdenum oxynitride samples were prepared by temperature programmed ammonolysis of various Molybdenum based precursors either with (wet ammonolysis) or without (dry ammonolysis) the presence of steam. In case of wet ammonolysis, steam was introduced using Argon flowing through a water bubbler kept at room temperature (~0.0313 atm vapor pressure 25^oC), where the relative flow rate of dry ammonia and Argon through water bubbler dictates the final partial pressure of NH_3 (pNH_3) and steam (pH_2O) in the gas stream. Detailed summary of synthesis conditions including actual flow rates, sample mass and temperature profile for all the ammonolysis synthesized samples for this section 3.6.3 are provided in Table 3.6-2.

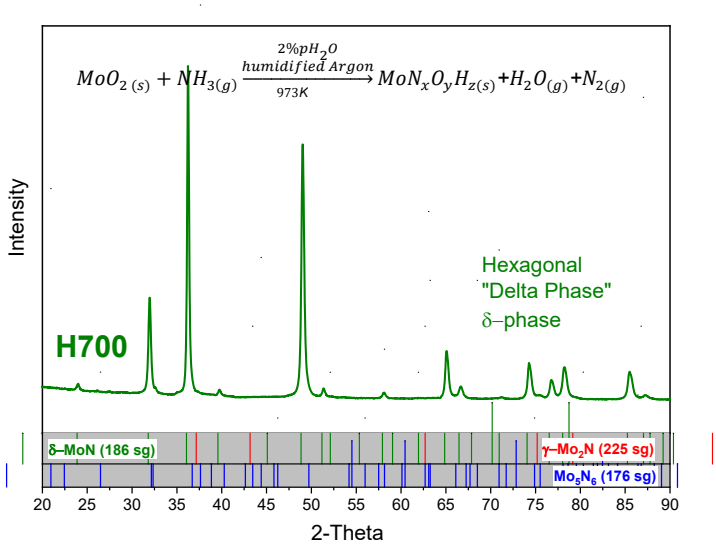

Figure 3.6-7 : Representative lab XRD patterns of as synthesized “Delta Phase” by wet ammonolysis (2% pH_2O) of MoO_2 at 973K collected with Cu Ka radiation (I = 1.5406 Å). The pattern shows no presence of competing y-phase. Later in Chapter 5, this hexagonal wet ammonolysis product (H700) is characterized as an oxynitride hydride with $MoN_xO_yH_z$ type composition, just like cubic phases C700 and C800.

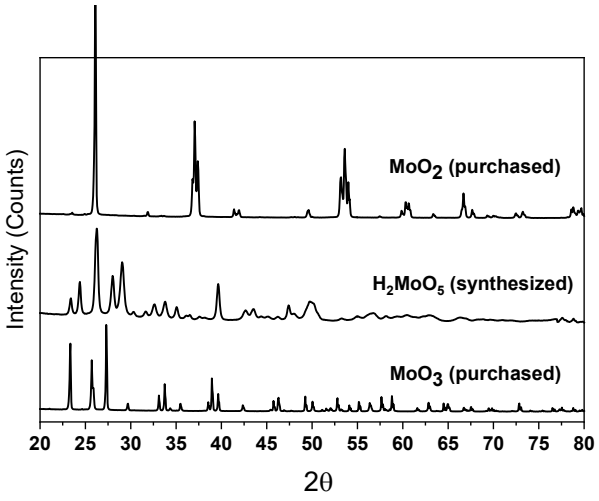

Figure 3.6-8 Lab XRD of precursor materials MoO_3, MoO_2 and H_2MoO_5

Table 3.6-2 Detailed synthesis parameters for various Dry and Wet ammonolysis recipes for Molybdenum nitrides used in the discussion of this section 3.6.3

Sample ID	Precursor (Crystal system)	Precursor amount (g)	Ammonolysis Type	Heating Protocol	Partial pressure of Gases			Flow rate of Gases (sccm)			Net Flow (sccm)	Flow Velocity (cm/g) @25C	Flow Velocity (cm/g) @700C
					pNH3	pAr	pH_2O	NH3	Ar	H_2O			
MoO_3 - Dry	MoO_3 (Orthorhombic)	0.125g	Dry	HP1	1.000	0	0	100	0	0	100	7	21
MoO_2 - Dry	MoO_2 (Monoclinic)	0.125g	Dry	HP1	1.000	0	0	100	0	0	100	7	21
H_2MoO_5 - Dry	H_2MoO_5 (Monoclinic)	0.125g	Dry	HP1	1.000	0	0	100	0	0	100	7	21
MoO_3 - Wet (1.5%)	MoO_3 (Orthorhombic)	0.125g	Wet	HP1	0.493	0.492	0.015	100	100	3.1	203	13	43
MoO_3 - Wet (2%)	MoO_3 (Orthorhombic)	0.125g	Wet	HP1	0.328	0.652	0.020	100	200	6.2	305	20	65
MoO_3 - Wet (2.5%) – slow ramp	MoO_3 (Orthorhombic)	0.125g	Wet	HP3	0.328	0.652	0.020	100	200	6.2	305	20	65
MoO_3 - Wet (2.5%)	MoO_3 (Orthorhombic)	0.125g	Wet	HP1	0.189	0.786	0.025	100	415	13	528	34	112
Delta phase (δ-phase)	MoO_2 (Monoclinic)	0.125g	Wet	HP1	0.328	0.652	0.020	100	200	6.2	305	20	65
H_2MoO_5 – Wet (2%)	H_2MoO_5 (Monoclinic)	0.125g	Wet	HP1	0.328	0.652	0.020	100	200	6.2	305	20	65

For Dry ammonolysis 0.125g of precursor (MoO_3, MoO_2 or H_2MoO_5) was placed inside a tube furnace at ambient temperature and subjected to 100sccm of dry NH3 (7 cm/g flow velocity) with HP1 heating profile: RT to 700ºC at 3K/min; hold for 12 hrs, and cooldown to ambient temperature under ammonia. The Sample ID for these ammonolysis products are *MoO_3 – Dry*, *MoO_2-Dry* and *H_2MoO_5 – Dry* depending on the choice of precursor. For Wet ammonolysis, same sample mass (0.125g) of MoO_3 precursor was subjected to HP1 heating profile, however in addition to 100sccm of NH_3, humidified Argon was introduced to obtain 1.5%, 2% and 2.5% partial pressure of H_2O (pH_2O) in the ammonolysis stream. The samples obtained were called *MoO_3-Wet(1.5%)*, *MoO_3-Wet(2%)* and *MoO_3-Wet(2.5%)* respectively, depending on pH_2O levels. Details of exact flow rates can be found in Table 3.6-2. Additionally, MoO3 was also subjected to a step wise slower ramp rate heating profile HP2: RT to 350ºC at 5 ºC /min; 350 to 500ºC at 0.6 ºC/min ; 500 to 700ºC at 3 ºC /min ; hold 12 hrs, and cooldown to ambient temperature. The obtained product was called *MoO_3-Wet(2%)-slow ramp*. Wet ammonolysis under 2% pH_2O was also performed starting with MoO_2 and H_2MoO_5 precursors, where the product from H_2MoO_5 is referred as *H_2MoO_5 – Wet(2%),* and that from MoO_2 simply as the "*Delta phase (δ)"* (XRD pattern in Figure 3.6-7). All samples synthesized by ex-situ Wet or Dry ammonolysis was evaluated by laboratory XRD (Ultima, Rigaku) using Cu Kα radiation at a scan rate of 2.5°/min, with a step size of 0.05°. The sample was ground and then placed on a zero background SiC holder and rotated at a speed of 3.1 rad/s during measurement.

The ammonolysis of molybdenum oxides using anhydrous ammonia at high temperatures (700-800ºC) are known to result mostly in γ-phase, however, a competing delta phase can often be found in final products in varying amounts[113, 116, 120, 121]. Lab XRD of resulting in *MoO_3 – Dry*, *MoO_2-Dry* and *H_2MoO_5 – Dry (details* Table 3.6-2*)* ammonolysis nitride mixtures, are shown in Figure 3.6-11a), and resulting phase fractions in Figure 3.6-11b), after heating them under NH_3 to 700ºC at a constant ramp rate of 3ºC/min (heating profile HP1), and holding them there for 12hrs, followed by cooldown all under constant 100sccm anhydrous NH_3 flow. At 700ºC, dry ammonolysis of as synthesized monoclinic H_2MoO_5 phase results in phase pure γ-phase, consistent with what was observed by Panda et.al[119], whereas 3%

and 29% phase fraction of secondary delta phase was observed when the precursor was MoO_3 and MoO_2 respectively, depicted by the hexagonal peak observed as the left shoulder on cubic peak around 36° (marked in green *). MoO_3 ammonolysis as discussed in section 3.6.2.2, proceeds through two parallel reactions through $HxMoO_3$ bronze and MoO_2 intermediate. While the reaction through bronze is considered topotactic in nature, often resulting in high surface area γ-phase (reported as γ-Mo_2N), the simultaneous reaction through MoO_2 is known to result in MoN as secondary product with low surface area products.[113, 114] Heating profile of MoO_3 is known to impact both the final gamma: delta ratio, and the surface area of final products. Slower heating rates in intermediate temperature to favor the formation of bronze intermediates, whereas faster heating profile during high temperature to avoid sintering is often used to produce high surface area γ-phase.[117, 121] We had earlier synthesized phase pure γ products in section 3.6.2.1 by applying heating profile HP2, to MoO_3 precursor, wherein slower intermediate temperature (0.6°C/min from 350-500°C, followed by 3°C/min up to final ammonolysis temperature), allowed formation of bronze intermediates properly (as observed in-situ Lab XRD studies), leading to the formation of phase pure gamma phase (Cubic 'γ-phase') within 3 hrs. Even here, upon subjecting MoO_3 under this slower ramp rate, leads to favoring the γ-phase slightly, even though the effect of pH_2O on favoring δ-phase is still dominant, as seen in the Lab XRD patterns and phase fraction bar plot in Figure 3.6-10 of Slow vs Fast ramp samples with IDs *MoO_3 - Wet (2%)* and MoO_3 - Wet (2%) in Table 3.6-2 respectively. Fast ramp here just means the normal HP1 for most runs in this Wet ammonolysis study.

Interestingly, it was observed that Wet ammonolysis favored the formation of δ-phase rather than γ-phase. For wet ammonolysis, MoO3 was subjected to same heating profile HP1, but this time wet Argon was introduced with dry ammonia. Figure 3.6-9a), shows the Lab XRD pattern post wet ammonolysis runs on MoO_3 under various partial pressures, and Figure 3.6-9b) shows the resulting phase mixture as stacked bar plots. Wet ammonolysis at 700°C with 1.5%, 2% and 2.5% pH_2O in the ammonolysis gas mixture was performed on MoO_3 (details in Table 3.6-2), and it was observed that even 1.5% pH_2O was enough to result in quarter of the product as δ-phase, which increase quickly to ~ 97wt% delta phase at 2% pH_2O. An incrementally higher 2.5wt% however was high enough to result in retained dioxide

intermediate in the final product. Therefore, to maximize δ-phase formation, 2% pH_2O was chosen and wet ammonolysis was performed using MoO_2 and H_2MoO_5 precursors following the same heating profile HP1, to understand the effect of precursor on phase selectivity of δ-phase vs γ-phase in final product. The resulting Lab XRD patterns and phase fractions are shown in Figure 3.6-11c) and d). Surprisingly, H_2MoO_5, which is not expected to form δ-phase based on prior ammonolysis studies on it,[119] and in our analogous dry ammonolysis here, also results in ~30wt% δ-phase, again highlighting the mysterious yet strongly phase selectivity role of humidity in ammonolysis of these Molybdenum oxide precursors. As expected, MoO_2 favored the delta phase the most, and resulted in nearly phase pure delta phase, as shown in Figure 3.6-11c) green curve with space group $P6_3mc$ (186 sg), same as the Lab XRD pattern for Delta phase shown earlier.

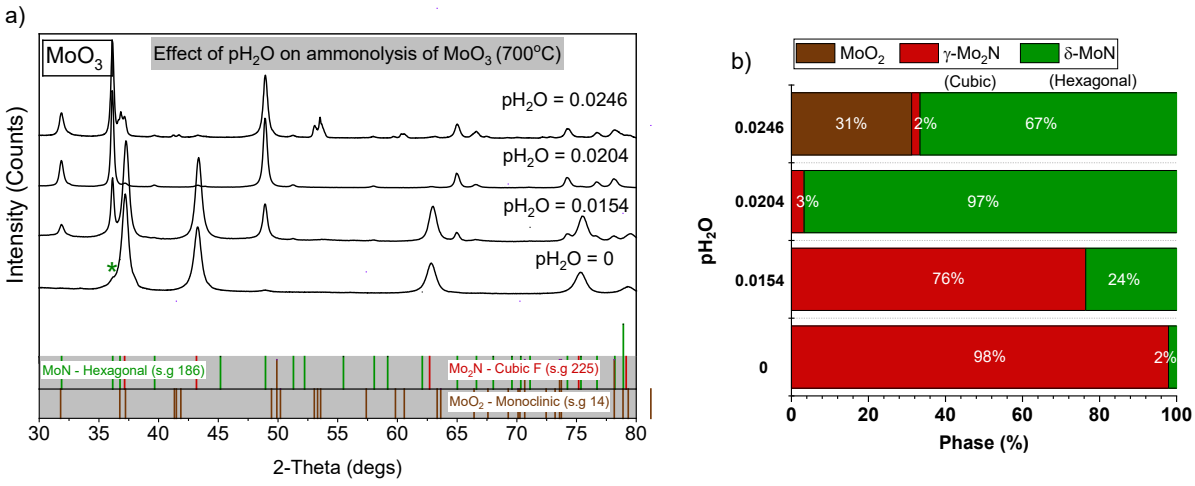

Figure 3.6-9 Outcome of ammonolysis reactions conducted using the steam partial pressures indicated, wherein the sample under desired ammonolysis gas mixture is heated to 700°C at constant ramp rate of 3 °C /min and held for 12hrs prior to cooldown. a) Ex situ Lab XRD of products, and b) Stacked bar plot showing resulting phase fractions. The presence of a minor amount of δ-MoN is evident in the product of dry ammonolysis from the presence of a shoulder on the main (111) peak of "γ-Mo2N".

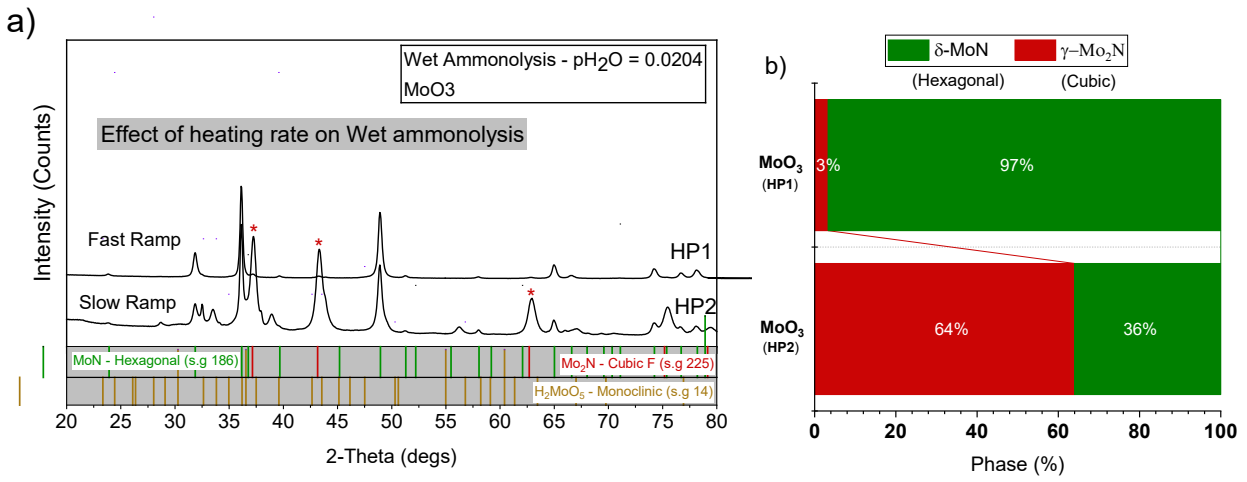

Figure 3.6-10 Influence of heating protocol on the outcome of wet ammonolysis reactions using MoO_3 as the precursor. HP1 = heat from RT to 700ºC at constant ramp rate of 3 ºC /min and hold for 12 h prior to cooldown. HP2 = heat from RT to 350ºC at a ramp rate of 5 ºC /min, then heat to 500ºC at 0.6 ºC /min, then heat to 700ºC at 3 ºC /min , then hold for 12 h prior to cooldown. a) Ex situ Lab XRD of products, and b) Stacked bar plot showing resulting phase fractions.

To understand the phase evolution of MoO_2 wet ammonolysis with 2% pH_2O at 973K to produce the delta phase, in situ PXRD in collaborative MRSEC IRG2 project effort (Courtesy: Elise Goldfine and Jill Wenderott, Haile Group, Northwestern University) was performed in an Anton Paar XRK 900 reactor chamber on a 9 kW Cu rotating anode Rigaku Smartlab with a D/TEX Ultra 250 1D silicon strip detector. Measurements were taken in θ/2θ geometry over the angular range 11°-82° with a scan speed of 50°/min to minimize dwell time at each temperature. MoO_2 (vendor, purity) was placed inside the reactor chamber at ambient temperature, purged with N_2, and subjected to a flow of anhydrous NH_3 and He bubbled through a room temperature water bath to get 2% pH_2O in wet ammonolysis stream. The material was then subjected to the following thermal profile: heat to 700 °C (3 °C/min, 12 hr hold) and cool to ambient temperature (10 °C/min) while still under gas flow. The chamber was purged with N_2 for 30 minutes before exposing sample to air. An analogous experiment was performed to study the Dry ammonolysis of same MoO_2 precursor under same heating and scan profile.

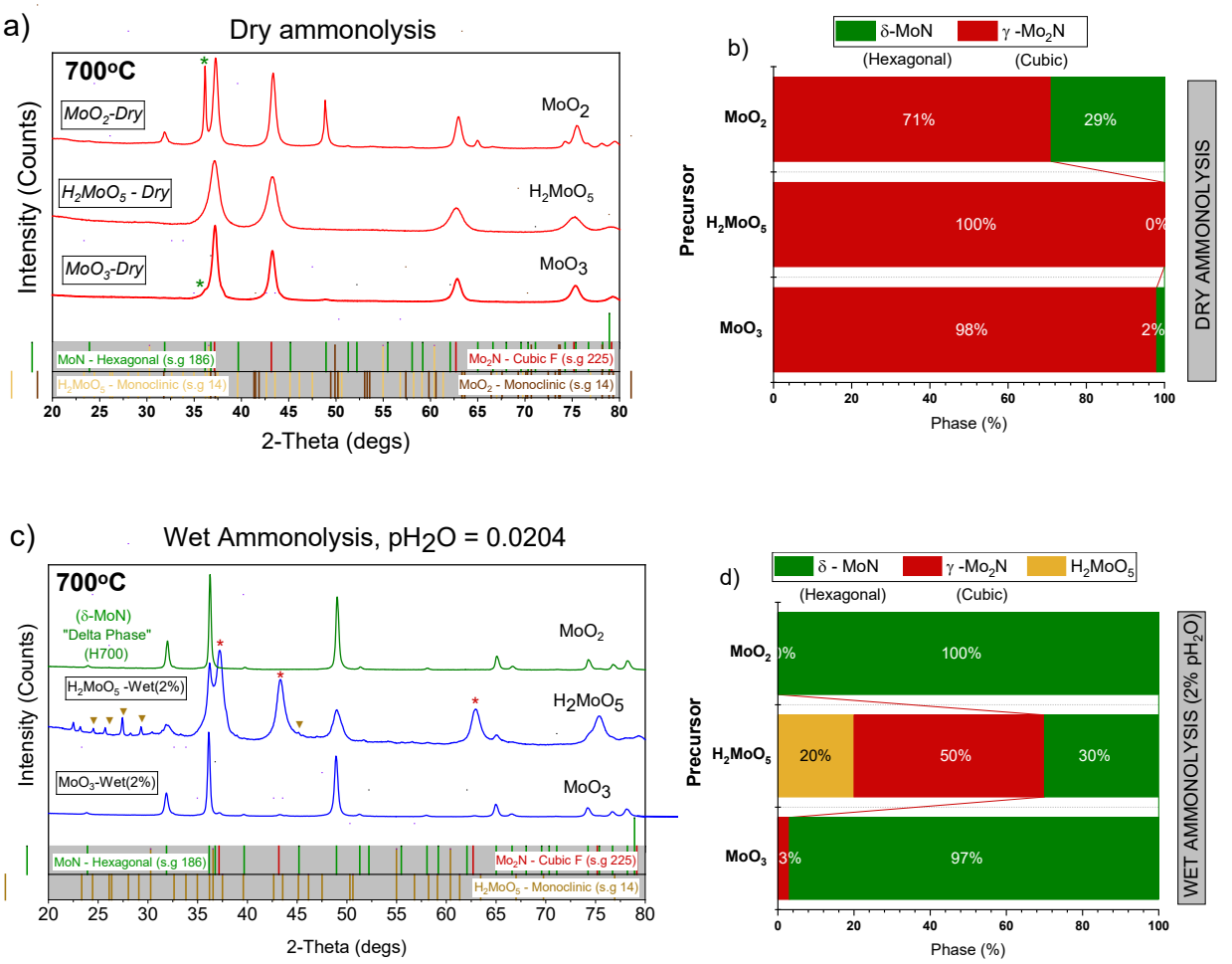

Figure 3.6-11 Influence of precursor and humidification on the outcome of wet ammonolysis reactions. a), c) Ex situ Lab XRD of products of Dry and Wet ammonolysis (2% pH_2O) of MoO_3, MoO_2 and H_2MoO_5 precursors at 700°C , and b), d) their corresponding stacked bar plot showing resulting phase fractions. Sample ID from Table 3.6-2 shown in boxed text. MoO_3 results in nearly δ-phase product with 3wt% γ-phase. Even with γ-phase favoring bronze, under wet ammonolysis upto 30% δ-phase was seen in product. Wet ammonolysis of MoO_2 at 700°C following Heating Profile HP1, under 2% pH_2O ammonolysis mixture results in only "δ-phase" (green curve marked δ-MoN based on literature reported stoichiometry for sg 186, with no γ-phase peaks marked by red star (*) on the curves resulting from MoO3 and Bronze wet ammonolysis

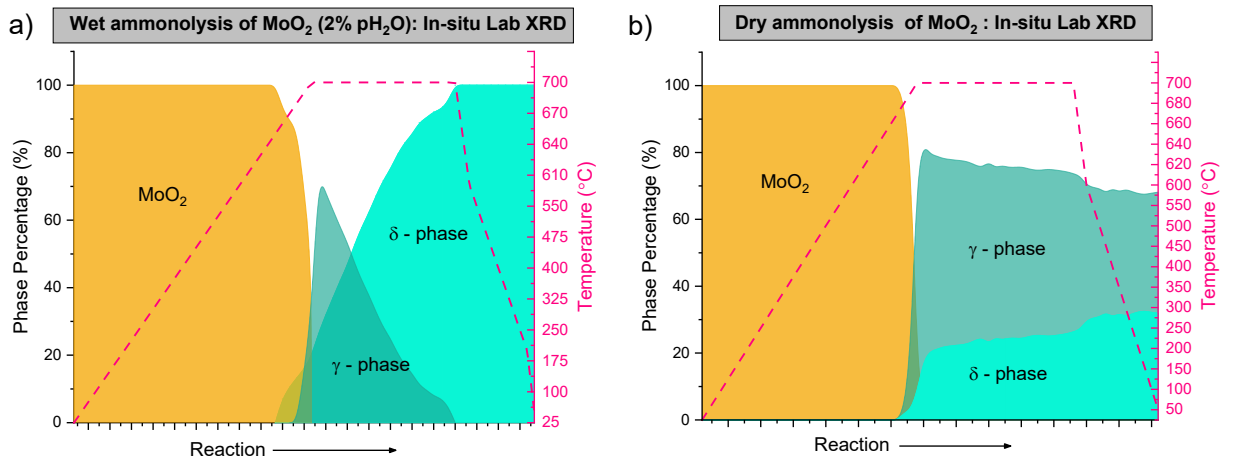

Figure 3.6-12 In-situ XRD plots for (a) wet ammonolysis of MoO_2 at 700°C under 2% pH_2O wet ammonolysis mixture of humidified helium and anhydrous ammonia, and same in-situ reaction under b) dry ammonolysis at 700°C. (Courtesy : Elise Goldfine and Jill Wenderott, Northwestern University, Haile Group)

The phase evolution from in-situ wet ammonolysis of MoO_2 is shown in Figure 3.6-12, the gamma and delta nitride phases formed directly from MoO_2 at 660 °C. The gamma phase rapidly became the majority phase during the continued heating to 700 °C, peaking at 74%. The MoO2 precursor was fully reacted by 700 °C leaving only the nitride products. During the hold at 700 °C, the phase fraction of delta gradually increased until it surpassed the gamma phase at 2.5 hrs. By the end of the 12-hour hold, the sample was phase pure delta. In contrast, during dry ammonolysis the gamma phase remained the majority phase during the entire hold at 700 °C and the phase fraction of delta reached a steady value of 25%. The cross-over during hold when compared neck to neck in reaction progress for wet (Figure 3.6-12a) vs dry (Figure 3.6-12b)) MoO_2 ammonolysis only happens for the wet ammonolysis, indicating the critical yet unclear role of external H_2O in ammonolysis mixture.

3.7 Highlight System : Tantalum Oxynitrides (Ta-O-N)

3.7.1 Phases of Tantalum (Oxy)nitride - Introduction

In general, at least three stoichiometrically similar TaON oxynitride phase (bulk oxynitrides studies) have been reported. δ-TaON (tetragonal, sg: I41/amd)[122], β-TaON phase (monoclinic, sg: P21/c),[67, 74, 123-125] and γ-TaON (monoclinic, sg: C2/m)[73, 126-128] are the 3 oxynitride phases. Often β and γ have been reported to co-exist but are often very difficult (nearly impossible in case of γ) to be synthesized in phase pure form and are many a times obtained along with the nitride Ta_3N_5 as a result of ammonlysis of Ta_2O_5. Also, at least three phases of tantalum nitride, each with a different stoichiometry have been reported, namely Ta_3N_5 (monoclinic, sg: C2/m),[124, 129-132] TaN (hexagonal, sg: P62-m),[133-135] and Ta_4N_5 (tetragonal, sg: I4/m)[136, 137]. Out of these, the phases that we observe while performing various Dry and Wet ammonolysis experiments discussed below, include the β-TaON, γ-TaON, Ta_3N_5 and sometimes δ-TaON, as discussed below.

3.7.2 Controlled ammonolysis for Tantalym (Oxy)nitride synthesis: Wet vs Dry ammonolysis.

Ammonolysis produces substantial changes in the crystallographic properties of tantalum oxide. First pass ammonlysis @850C based on literature, which resulted in a mixture of Ta_3N_5, β -TaNO and γ -TaON, confirmed by Lab XRD in Figure 3.7-1a). Before doing the CDP-Oxynitride test, the oxynitride mixture by itself was exposed to steam @250^{o}C which left the phase mixture essentially unchanged (confirmed by XRD, Figure 3.7-1b), compared green and red curves) showing the nitridation was irreversible. Next, the stability of mixture of tantalum (oxy)nitrides against reaction with CsH_2PO_4 was evaluated, by conducting the CDP-Oxynitride Stability test. No change in the diffraction patterns is evident between the before and after samples, Figure 3.7-2, indicating negligible reaction between CsH_2PO_4 and

each of the phases (both oxynitride and nitride phase) in the tantalum oxynitride mixture. This makes Ta-O-N system as a potential candidate for CDP electrolyte bases applications, as will be shown for Oxygen Evolution Reaction catalysis in Solid Acid Electrolyzer Cells in Chapter 5.

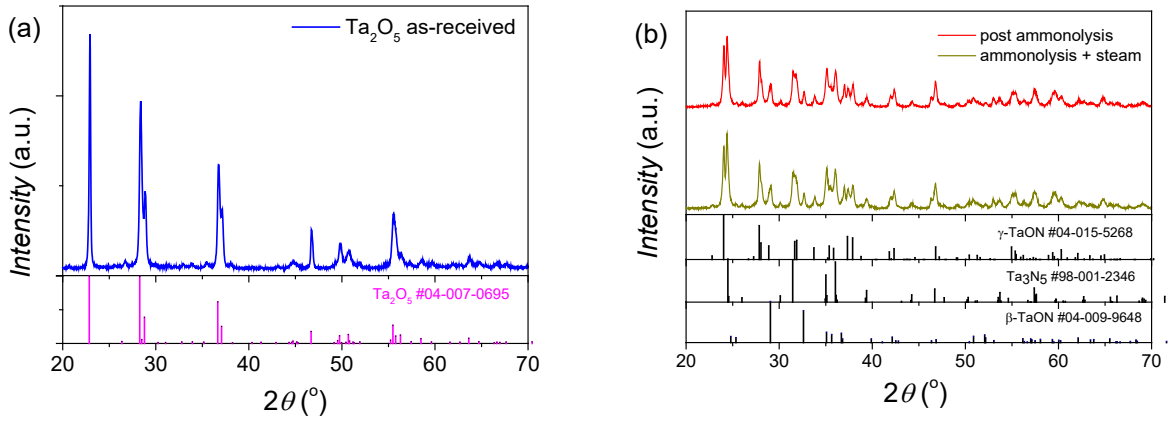

Figure 3.7-1 : X-ray powder diffraction patterns of (a) as-received Ta_2O_5, and (b) the product after ammonolysis (exposure to NH_3) and after ammonolyzed material is exposed to steam. The ammonolyzed and steam treated powders are mixtures of Ta_3N_5, γ-TaON and β-TaON. (Lab XRD courtesy : Kaiyang Wang, Summer visiting undergraduate student, Haile Group, Northwestern University)

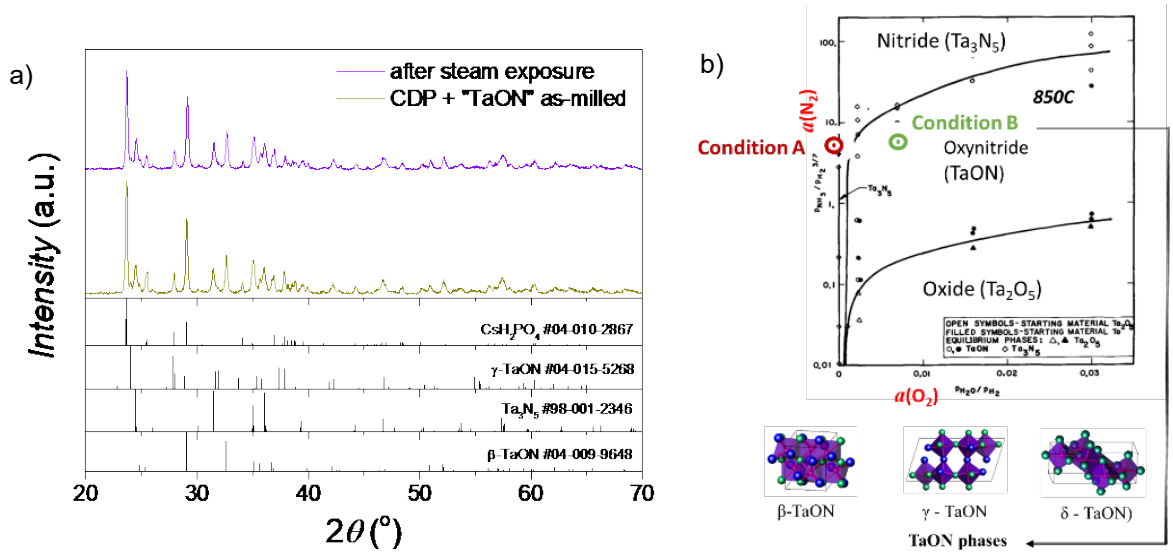

Figure 3.7-2 : a) Tantalum (oxy)nitride mixture shows stability with CDP @250 under 0.4atm steam (N2 carrier) for 24hrs. b) Dry ammonolysis (Condition A) vs Wet Ammonolysis (Condition B) to favor nitride or the oxynitride phase during ammonolysis of oxide @850C based on Ta-O-N phase diagram proposed by Swisher et. Al.[67]

In order to probe the potential of these oxynitride for various applications and potentially compare for phase sensitivity in catalysis, it was important to obtain phase pure tantalum (oxy)nitride phases and understand the phase-space of Ta-O-N system first. Referring to phase diagram of Ta-O-N by Swisher *et. al*, shows that either the oxynitride (Condition B) or the nitride (Condition A) can be selectively favored, by changing the nitrogen and oxygen potential in the ammonolysis gaseous mixture, by effecting the 4 simultaneous equilibria reactions occurring at 850°C, namely ammonia decomposition, water decomposition, and competing ammonolysis of oxide to form nitride or oxynitride phases. Thus, controlling relative nitriding and oxidative potential by varying the pH_2O in the ammonolysis gaseous mixture could allow the phase space of Ta-O-N to be explored effectively.

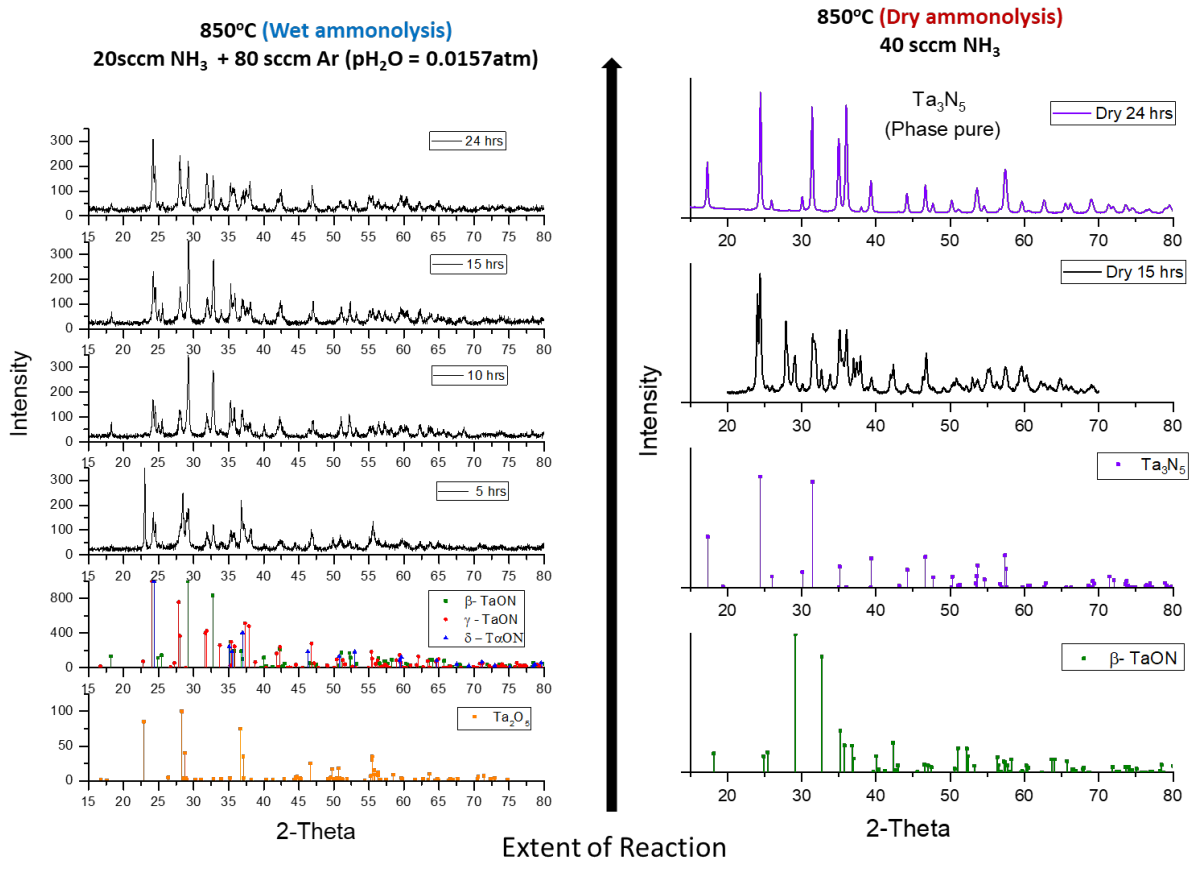

Figure 3.7-3 : Lab XRD patterns of Wet (1.5% pH_2O) and Dry ammonolysis products of Ta_2O_5 at 850°C, for different extents of time (5-24 hrs). Top right plot in purple solid curve is the Lab XRD pattern for phase pure Ta3N5 nitride product as a result of dry ammonolysis for 24hrs.

Figure 3.7-4, shows the phase composition results obtained from powder XRD whole pattern fitting patterns on as collected Lab XRD patterns (Figure 3.7-3) for different ammonolysis conditions. Following 'Condition A' path, dry ammonolysis of Ta_2O_5 @850C results in mixture of β –TaON and Ta_3N_5 phases initially (15hrs), however increasing the extent of reaction, results in phase pure Ta_3N_5 nitride (monoclinic, sg: C2/m, PDF#04-009-5976) as the final product. Slight introduction of steam (achieved by bubbling Ar through DI water at room temperature, picking up 2% pH_2O) effects the simultaneous equilibrium to completely suppress the nitride phase as expected from the phase diagram, resulting in various mixtures of the three TaON phases depending on extent of reaction. Additionally, the effect of different pH_2O on ammonolysis of Ta_2O_5 was studied at 850ºC, Figure 3.7-5a), where ammonolysis on these samples were carried out for the same amount of time (15hrs). It was realized that lower level of pH_2O favored the formation of β-TaON over the metastable γ –TaON polymorph, during wet ammonolysis of Ta_2O_5 at 850ºC . Capitalizing on this, an even lower pH_2O in the chamber and extended time of reaction was used to obtain phase pure *β* –TaON (XRD pattern shown in Figure 3.7-5b).

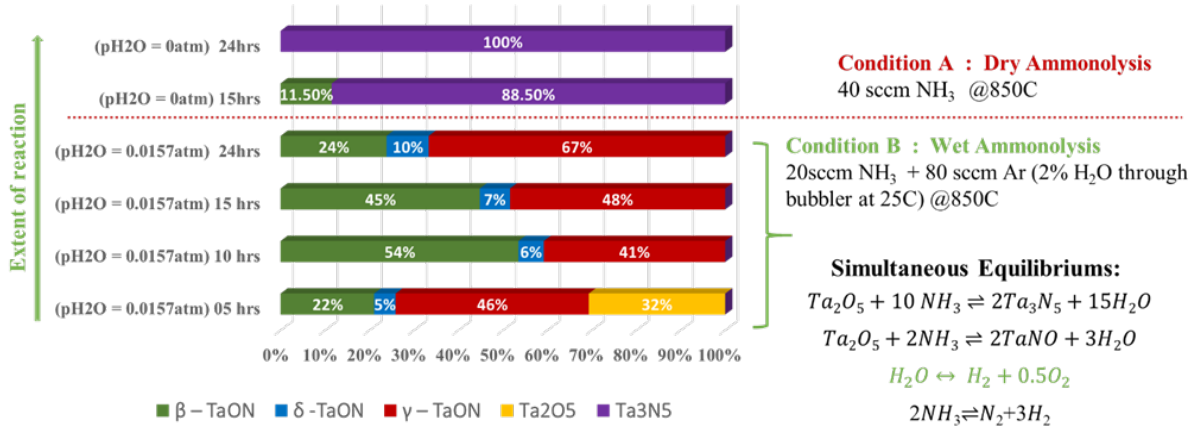

Figure 3.7-4 : *Synthesis of Tantalum (oxy)nitrides via dry and wet ammonolysis route. Positive pH_2O in the system favour oxynitride phase over the nitride, while different extent of reaction results in different oxynitride phase mixtures.*

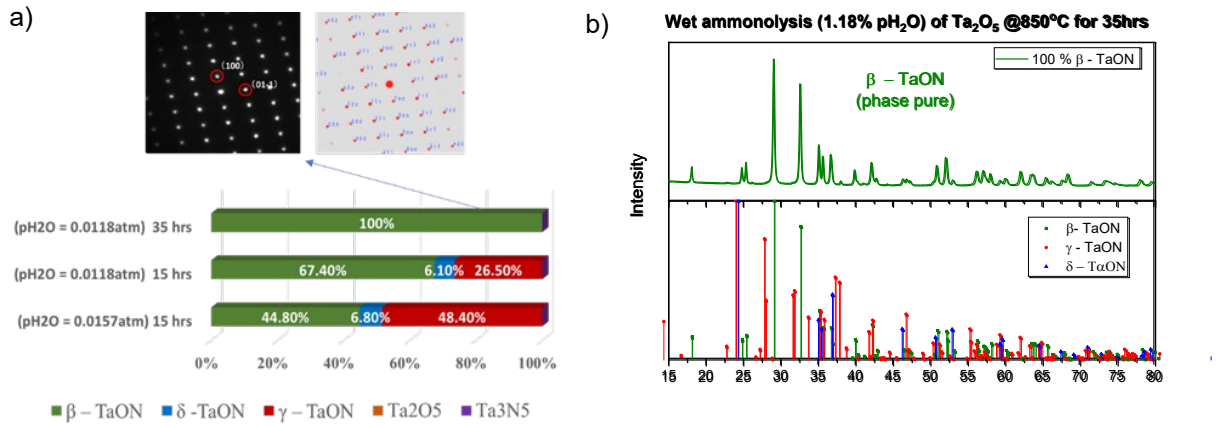

Figure 3.7-5 : a) Favoring of β-TaON phase upon decreasing pH_2O in the system, leading to successful phase pure-β-TaON synthesis. TEM SADP in inset (Courtesy: Vinayak P. Dravid Group, NU). b) XRD pattern of phase pure β-TaON, prepared by wet ammonolysis (1.18% pH_2O) of Ta_2O_5 at 850°C for 35hrs.

Nano-beam TEM Diffraction pattern of *β*-TaON particle was further used to confirms the N and O ordering in the phase pure tantalum oxynitride, leading to a monoclinic crystal system with space group $P2_1/c$ (inset in Figure 3.7-5a) inset, along with simulated pattern). Additionally, the stoichiometry of the synthesized β-TaON was determined by CHNS elemental analysis (error <0.4%), which indicated as synthesized β-TaON to have stoichiometric formula of $TaO_{0.94}N_{1.04}$. Within instrumental error, this implies a 1:1 atomic ratio of N and O in the sample as expected. The band gap of all these tanatalum (oxy)nitrides were measured using DR-UV VIS spectroscopy (not shown here) ranging from 2.37eV (for β-TaON) to as low as 1.92eV (for nitride), which agrees with those observed in literature.

3.7.3 Ta-O-N Nanoparticles synthesis (Urea Synthesis Route)

Since the Ta-O-N phase space was found to be stable with CDP under steam at working temperatures, it was considered a great candidate for CDP based catalysis applications. In Chapter 5, the potential of Ta-O-N powders synthesized in this work are used for catalyzing oxygen evolution reaction in solid acid electrolyzer cells operating at 250°C. Since nanoparticles of oxynitrides due to their increased surface area

are shown to improve OER catalysis, attempts to synthesize Ta-O-N nanoparticles using urea-based calcium-assisted preparation method described by Gao, et al.[138]. A key advantage of this technique is that the oxynitride phase is directly synthesized, without recourse to high temperature ammonolysis that inevitably results in large particle size. Desired quantities of $TaCl_5$, $CaCO_3$ and urea were added to methanol, the solutions of which formed gels at room temperature. In one series of synthesis experiments, the urea:Ta mole ratio was fixed at 2.0 and the Ca content varied (Ca/Ta = 0, 0.5, 2). In a second series, the Ca content fixed at a Ca:Ta mole ratio of 1.0, whereas the urea:Ta ratio was varied (1, 2, 4, 6). Calcination of the semi-solid gel product was performed under dry N_2 @775C for 2 h, following which the product was treated in HCl overnight to remove calcium.

A summary of the outcome of these synthesis experiments is provided in Figure 3.7-6. Consistent with the literature, we observe a strong influence of the Ca and urea concentrations on the nature of the product phases. For example, with urea:Ta fixed at 2.0, Figure 3.7-6a), we find that that Ca is required in order to prevent formation of the nitride, Ta_3N_5 and the oxide, Ta_2O_5, phases. Specifically, these undesired phases are observed in the absence of Ca or when the Ca:Ta ratio is 0.5. In contrast, when the Ca:Ta: ratio is 1, only oxynitride phases, β-TaON (monoclinic, sg: $P2_1/c$) and γ-TaON (monoclinic, sg: C2/m), are observed. The influence of further increases in the Ca content has not been explored but could possibly be used to influence the β to γ ratio in the TaON product. Alternatively, the nature of the oxyntride phase may be amenable to control via manipulation of the calcination temperature. With the Ca:Ta ratio fixed at the desirable value of 1, variation of the urea:Ta ratio, Figure 3.7-6b), has a somewhat predictable influence on the outcome. Too much urea results in a product that is extremely rich in Ta_3Na_5, whereas too little urea results in a product containing a significant fraction Ta_2O_5. Significantly, with respect to (photo)electrochemistry, the wet chemical synthesis route indeed produces oxynitride material with much smaller particle size and much higher surface area than traditional, high-temperature ammonolysis of the precursor oxide, Figure 3.7-6c) and d) , as evident from the scanning electron microscopy images of TaON phases obtained from high temperature ammonolysis and from the urea-based wet chemical method (urea/Ta = 2.0 and Ca/Ta = 1.0). Analysis of the XRD pattern obtained from the latter indicated a crystallize size of ~ 6 nm.

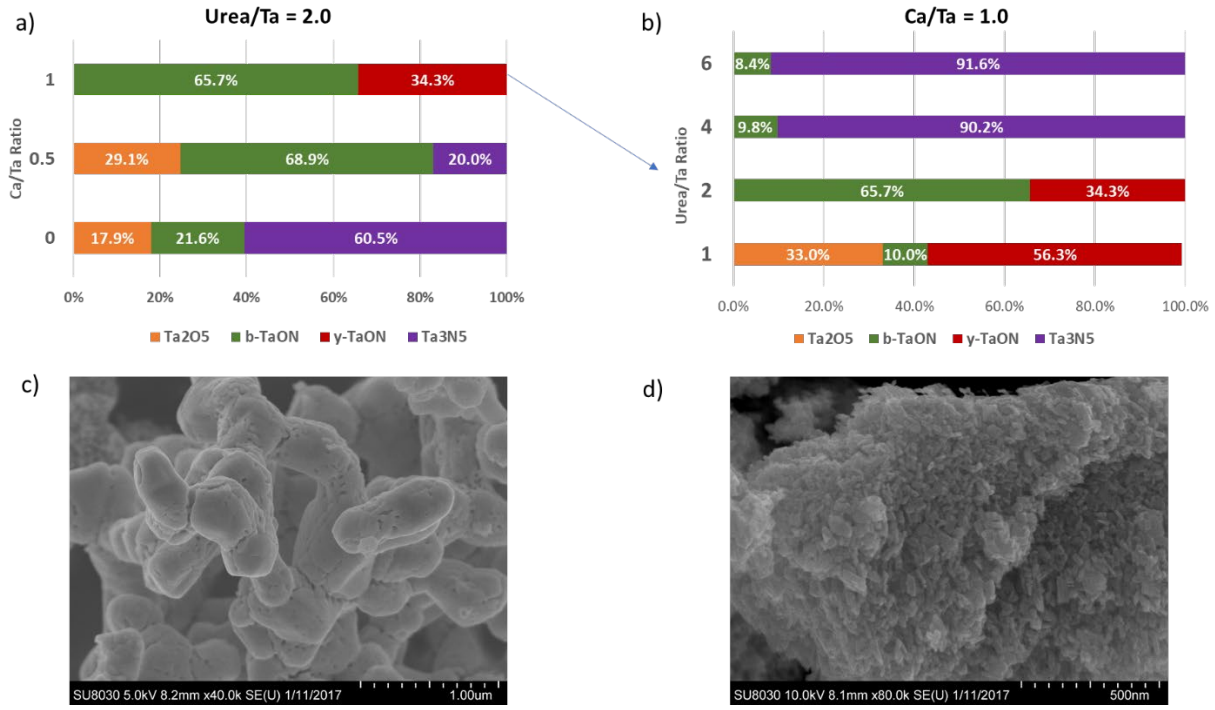

Figure 3.7-6 : Characteristics of the urea-based calcium-assisted synthesis of TaON: (a) Product phase fractions as a function of Ca/Ta ratio at fixed urea/Ta ratio = 2.0; (b) product phase fractions as a function of urea/Ta ratio at fixed Ca/Ta ratio = 1.0; c) SEM micrograph of TaON phases obtained from urea-based calcium-assisted synthesis using urea/Ta = 2 and Ca/Ta = 1; and (d) SEM micrograph of TaON phases obtained from typical high-temperature ammonolysis of as purchased micron sized oxide precursors.

3.8 Other - Photo-Absorbing Oxynitrides

3.8.1 Tungsten Oxynitride (W-O-N)

Synthesis of tungsten oxynitride was pursued by ammonolysis of tungsten oxide.[65, 70, 116] Typically, 0.5 g of WO_3 (Alfa Aesar, 99.99%, light green color, nano-powder, matched to PDF #01-083-0950, Monoclinic, space group P21/n, Figure 3.8-1a) was put under the flow of anhydrous NH3 100 sccm at 700 °C for 3 hrs. The ammonolysis transformed the material to a black powder, with a diffraction pattern, Figure 3.8-1b), matching that of a single-phase material of the fluorite structure (space group Fm-3m), with lattice constant 4.142 Å. It has been reported in the literature that tungsten oxynitride adopts such a structure.[65, 70] The XPS spectrum, Figure 3.8-2, indicates an elemental composition of O (30.4%) and N (32.3%), balance W. Thus, the ammonolysis successfully produced $WO_{1-x}N_x$ with a nearly equal atomic percentage of oxygen and nitrogen.

Absorption spectra using DR-UV VIS for both the oxide (light green) and the resulting oxynitride (black) are shown in Figure 3.8-3. Tungsten oxide, has an absorbtion edge at around 535 nm with a band gap of 2.31 eV, whereas the oxynitride absorbs light throughout the visible range, consistent with its black color. The stability of the so-synthesized W(O, N) was assessed with the *CDP-Oxynitride stability test* The post-treatment diffraction pattern (Figure 3.8-4) indicated a slow reaction between the two materials, despite the absence of a visible color change. Accordingly, further examination of this material as an electrode catalyst for application in CDP-based electrochemical cells was not pursued.

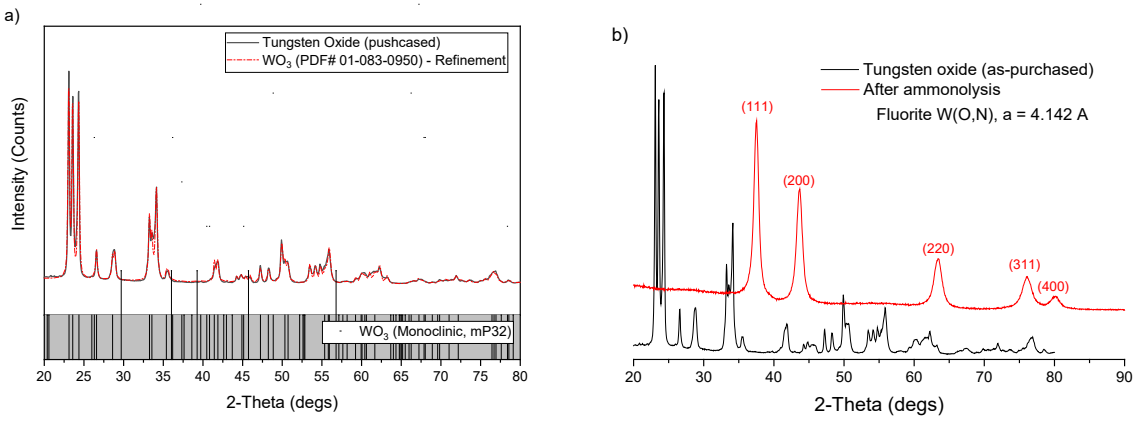

Figure 3.8-1 : a) Lab XRD pattern confirming monoclinic phase of purchased WO_3 (black solid line), confirmed by refinement overlayed (red dash curve) matching with PDF#01-083-0950. b) Resulting Cubic (Fm-3m) Tungsten oxynitride post dry ammonolysis at 973K, compared with oxide.

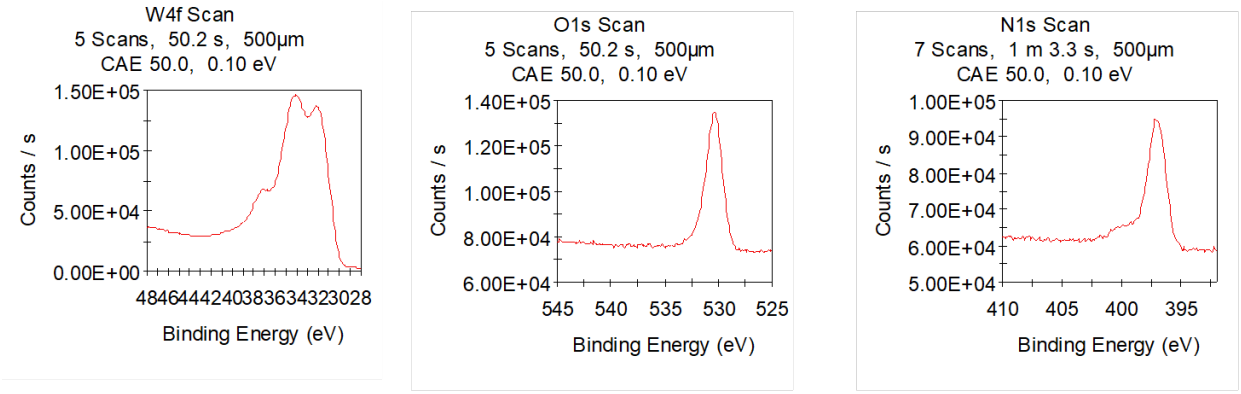

Figure 3.8-2: XPS spectrum of $W(O_{1-x}N_x)$ showing the presence of W and anions O and N in almost equal atomic amounts.

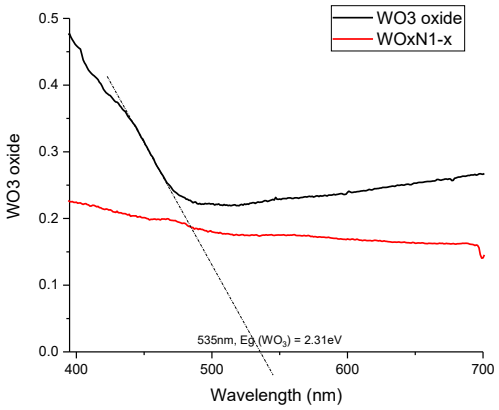

Figure 3.8-3 : DR UV-VIS spectrum of tungsten oxide and of $W(O_{1-x}N_x)$, showing that the oxynitride is light absorbing throughout the visible region, whereas the oxide has a clear adsorption edge at 535 nm.

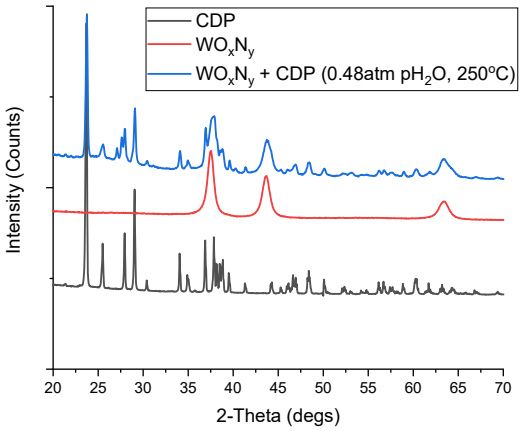

.

Figure 3.8-4 : Lab XRD of CDP (black curve), as synthesized Tungsten oxynitride (red curve) and post CDP-Oxynitride Stability test mixture (blue curve).

3.8.2 Niobium Oxynitride (Nb-O-N)

For oxynitride synthesis, 0.4gm of as purchased Nb_2O_5 *(Alfa Aeser, 99.9985%, white color, matched to PDF #04-007-0450, Monoclinic Crystal system, Lab XRD not shown)* was put under the flow of anhydrous NH_3 + 37.5 vol% H_2 (total flow rate: 130 sccm) @ 900K for 12 hrs. The results comfirmed the formation of

62.5 wt% Tetragonal niobium oxynitride (PDF# 04-011-6182, $Nb_{3.49}N_{4.56}O_{0.44}$), with the balance being monoclinic Nb_2O_5, as seen in Figure 3.8-5. Stability of the oxynitride against oxidation and its stability against reaction with CsH_2PO_4 were evaluated simultaneously, for which the *CDP-oxynitride stability test* was performed. Surprisingly, the diffraction pattern of the mixture (prior to high temperature steam exposure), Figure 3.8-5, shows very few peaks that can be assigned to the otherwise prominent peaks of the "NbON" phases detected in the absence of CsH_2PO_4. On the other hand, the diffraction patterns reveal very little change between the as-milled and heat-treated mixtures, indicating negligible evolution in phase distribution as a consequence of the annealing. The reason of the almost immediate elimination of the "NbON" peaks on mixing with CDP is unclear. Because the resulting composite is black and therefore unsuitable for photocatalysis, efforts to understand this are behavior are not a priority currently.

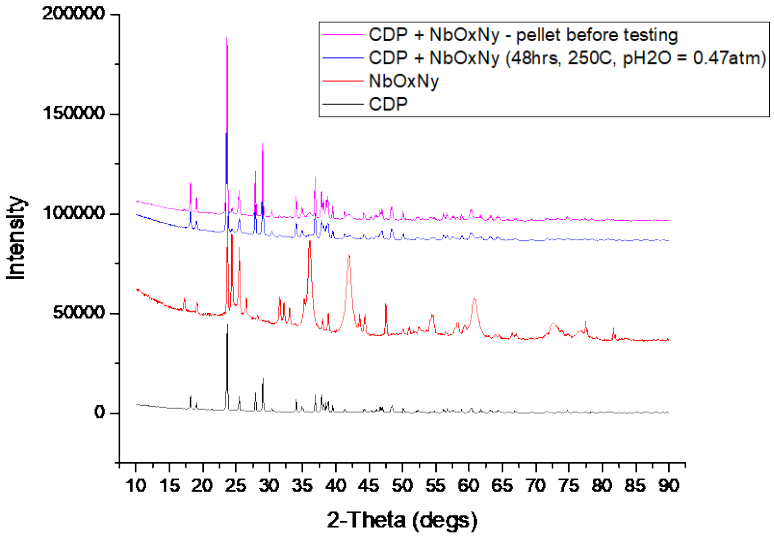

Figure 3.8-5 : Lab XRD patterns of CDP electrolyte (black curve), Niobium oxynitride mixture (red curve), CDP + oxynitride mixture prior to CDP-Stability test, and the mixture pellet after steam exposure (pink).

3.8.3 Lanthanum Molybdenum Oxynitride (La-Mo-O-N)

Synthesis of barium tungsten oxynitride was pursued by ammonolysis of lanthanum molybdenum oxide, $La_2Mo_2O_9$, a procedure which has not previously appeared in the literature. The precursor oxide is not available commercially; its synthesis was pursued according to the following chemical solution method. 7 mmol of $La(NO_3)_3.6H_2O$ *(Sigma Aldrich, 99.9%)* was added to ~40 ml DI water, followed by addition of 1 mmol $(NH_4)_6Mo_7O_{24}.4H_2O$ *(Alfa Aesar, 99.999%)* and 16 mmol citric acid. While stirring this solution, NH_4OH was added dropwise to adjust the pH to ~4. The solution was then heating, under continued stirring to 80 °C to yield a transparent gel. This product was subsequently held at 250 °C for 12 h, producing a black char. After grinding, the powder was heat-treated at 450 °C for 6 h, ground again, then heat-treated at 1000 °C for 5 h, generating the desired oxide in phase pure form (cubic $La_2Mo_2O_9$ *P213, - PDF#00-061-0510)*, Figure 3.8-6, which shows Lab XRD of synthesized oxide in black curve and refinement based on cubic $La_2Mo_2O_9$ overlayed in blue curve.

With the goal of producing the oxynitride, 0.5 g of $La_2Mo_2O_9$ was subjected to the flow of anhydrous NH_3 150 sccm at 800 °C for 12 hrs. The ammonolysis transformed the color of the powder from white to black. The XRD pattern of the ammonlysis product, Figure 3.8-6, indicates that the material amorphized, showing diffraction peaks that are extremely broad. While some of the peaks could be weakly attributed to hexagonal MoO_2 (PDF#00-050-0739), the majority of the peaks could not be attributed to any particular phase. XPS data in Figure 3.8-7 shows that the weakly crystalline ammonolysis product consisted of Nitrogen and Oxygen along with Lanthanum and Molybdenum, with the elemental composition analysis based on peak fitting suggesting 11% Nitrogen and 49% Oxygen by atomic %. Preliminary reactivity studies with CDP were inclusive, with the diffraction pattern of the reaction product revealing only peaks from the electrolyte phase (not shown). For future project, this work motivates to optimize ammonolysis to avoid the little impurity phase, and also the product could be heat treated under ammonia or Argon to increase its crystallinity to a point where a new oxynitride phase can be indexed.

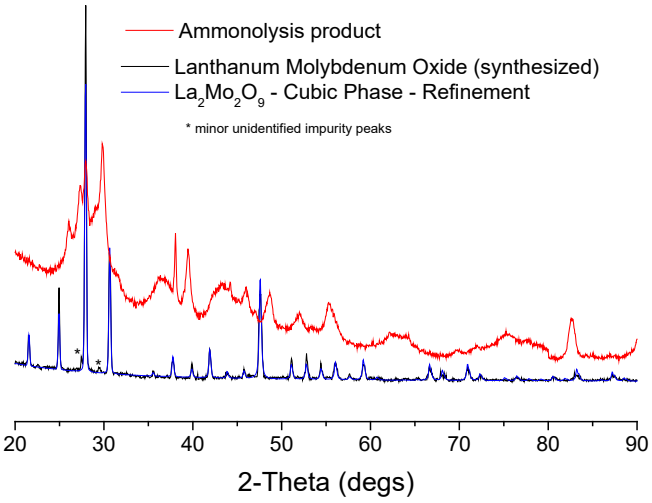

Figure 3.8-6: X-ray powder diffraction patterns of as prepared lanthanum molybdenum oxide, matching the simulated patterned of $La_2Mo_2O_9$, and of the product of ammonolysis of this oxide.

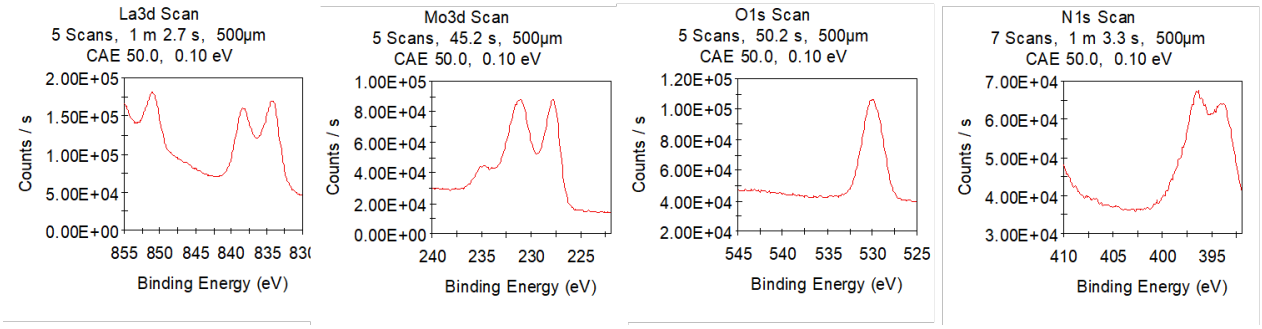

Figure 3.8-7 : XPS spectrum of the product of ammonolysis of $La_2Mo_2O_9$ showing the presence of La, Mo, O and N

3.8.4 Lanthanum Vanadium Oxynitride (La-V-O-N)

Synthesis of lanthanum vanadium oxynitride was pursued by ammonolysis of lanthanum vanadium oxide, $LaVO_4$, as reported previously by Fuertes et al.[139] The lanthanum vanadate precursor oxide is not available commercially, and it was accordingly synthesized in-house, using a solid state reaction route. Lanthanum oxide (La_2O_3, *Alfa Aesar, 99.9%)* was first heat-treated at 900 C for 12 hr to remove surface carbonates and hydroxides. It was subsequently combined with vanadium oxide *(V_2O_5, Alfa Aesar, 99.2%)*, and the composite was formed into a dense compact, which was then annealed at 900 °C for 15

h. The grinding and annealing steps were repeated a second time to obtain the final form of the precursor oxide. The XRD pattern of the oxide, Figure 3.8-8, matches that of monoclinic $LaVO_4$ (Space group, $P2_1/c$ (PDF#04-006-7044).

To produce the oxynitride, 0.6 g of $LaVO_4$ (*orthorhombic, bright yellow*), was subjected to the flow of anhydrous NH_3 2000 sccm at 700 °C for 24 h. The ammonolysis transformed the color of the powder from bright yellow to black. The diffraction pattern, Figure 3.8-8 matches closely that of orthorhombic $LaVaO_{3-x}N_x$, reported by Fuertes et al.[139] The structure crystallizes in space group Pnma, with lattice constants (as determined from the diffraction analysis) of a, b, and c equal to 5.5287, 7.8163 and 5.5585 Å, respectively. Two very minor unidentified peaks were observed. Based on the unit cell dimensions and the study of Fuertes et al., the value of x in the oxynitride prepared here is estimated at 0.5. The DR-UV VIS spectrum, Figure 3.8-9, shows that the oxynitride absorbs light throughout the visible region, consistent with the black color. In contrast, the yellow oxide precursor has a band edge of around 398 nm, indicative of a band gap of approximately 3.11 eV.

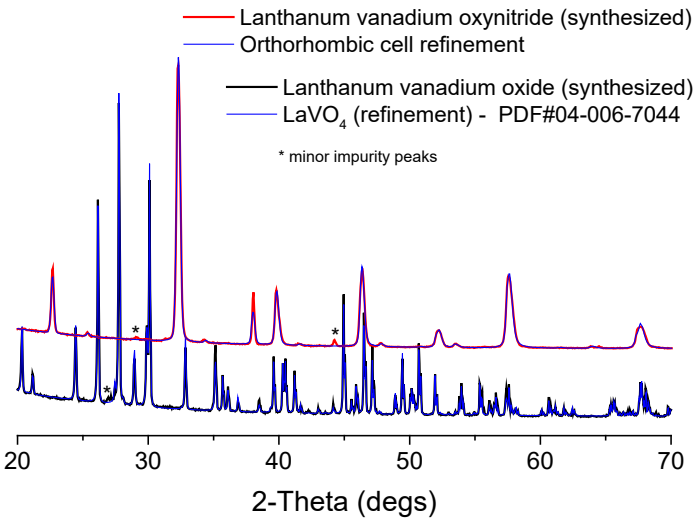

Figure 3.8-8 : X-ray powder diffraction pattern of the oxide precursor $LaVO_4$, matching with Monoclinic $LaVO_4$ with space group P21/c(14) [PDF#04-006-7044]

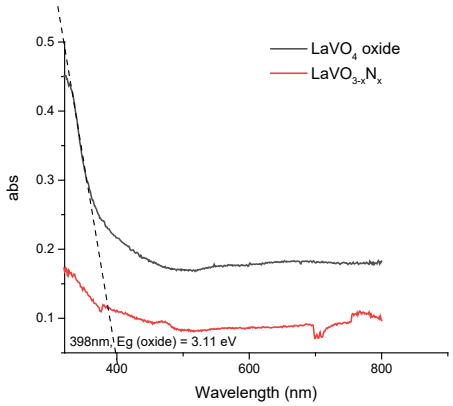

Figure 3.8-9 : DR-UV Vis spectrum of LaVO4 and of La-V-O-N, showing that the oxynitride is light absorbing throughout the visible region.

3.9 Other Photo-Active (Semiconducting) Oxynitrides

3.9.1 Titanium Oxynitride (Ti-O-N)

Titanium oxynitride was prepared by heating the 0.8 g as-received TiO_2 anatase powder (TiO_2, Anatase, 99.9%, 32nm APS powder, Alfa Aesar) under a flow of NH_3 (flow rate: 50 ml/min) at 823 K for 10h in a tube furnace. The temperature was raised at a heating rate of 10 K/min and the nitride powder was allowed to cool down to room temperature automatically

To test the stability of Nitrogen incorporation at high temperature under steam, the *Oxynitride-Steam test* was done. Titanium oxynitride powders were exposed to 0.4 atm pH_2O (balance N_2) at 250°C for 24 h. The as-received oxides, the ammonolysis products, and the steam-treated oxynitride powders were characterized by X-ray powder diffraction, DRUV-vis and XPS.

The XRD patterns of the titania-based materials suggest little change upon exposure to ammonia and subsequent exposure to steam, Figure 3.9-1. The as-received material, though sold as 100% anatase, contains detectable quantities of rutile. Neither the phase fractions nor the lattice constants of the two

components change as a result of the treatments (as determined by Rietveld refinement, not shown). At first glance, the result suggests negligible interaction between TiO_2 and the gas phase species. However, clear changes in optical properties are evident from the DRUV-vis spectra and the direct optical images, Figure 3.9-2. Exposure to ammonia darkens the material, and subsequent exposure to steam returns it to a pale yellow. These features suggest modification of the electronic structure as a result of nitrogen incorporation upon exposure to NH_3, induced by N exchange with O upon exposure to H_2O.

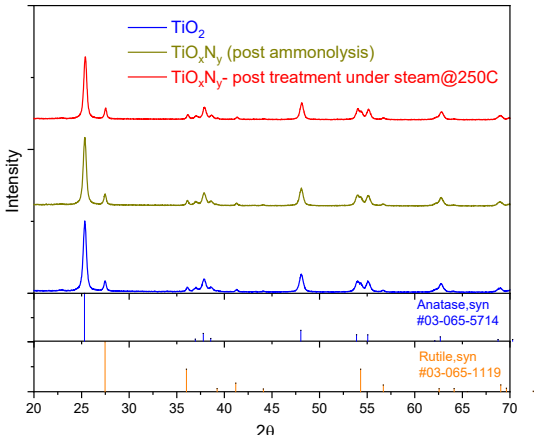

Figure 3.9-1 : X-ray powder diffraction patterns of as-received TiO_2, after ammonolysis (exposure to NH_3) and after ammonolyzed material is exposed to steam. The as-received material is largely anatase but contains detectable quantities of rutile. No apparent changes in crystal structure occur as a result of either high temperature gas exposure, under ammonia @550ºC or subsequent treatment under steam @250ºC (red curve) (Lab XRD courtesy : Kaiyang Wang, Summer visiting undergraduate student, Haile Group, Northwestern University)

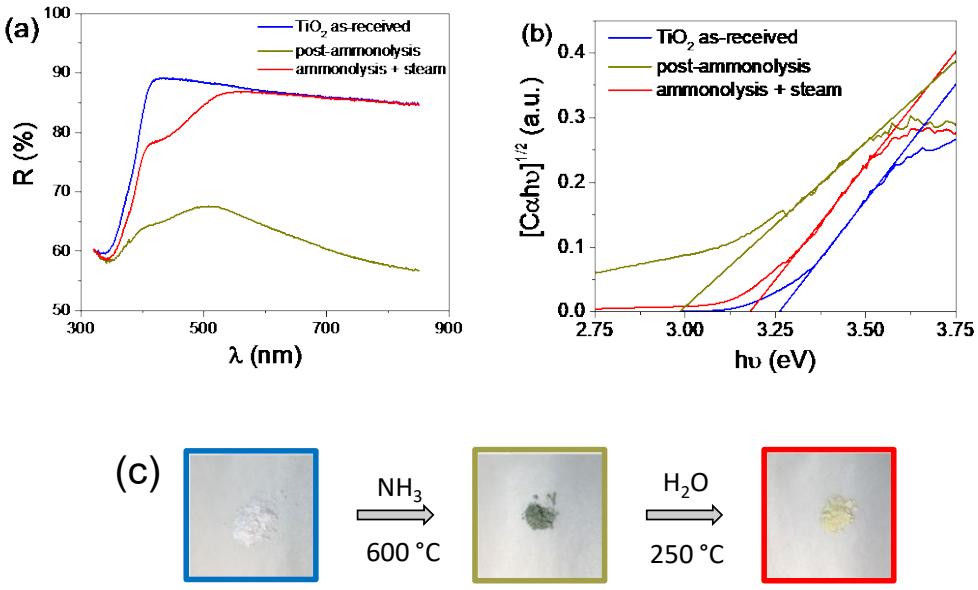

Figure 3.9-2 : Evolution of optical properties of TiO_2 upon sequential exposure to NH_3 and H_2O: (a) Raw DRUV-vis spectra; (b) band gap analysis from optical spectra; and (c) optical images of as-received and treated powders. In (a) R is the reflectance of the material in comparison to a standard. Exposure to NH_3 darkens the material and decreases the bandgap, whereas subsequent exposure to steam returns it to a lighter state and widens the gap. (UV-VIS results in a) and b) courtesy of Kaiyang Wang, Summer visiting undergraduate student, Haile Group, Northwestern University)

Table 3.9-1 Optical band-gaps of titiania based materials deduced from DRUV-vis spectra, Figure 2. (r is the correlation coefficient of linear fitting)

Sample	TiO_2 as-received	post-ammonolysis	steam treated
r^2	0.9972	0.9941	0.9938
E_g (eV)	3.26	2.98	3.18

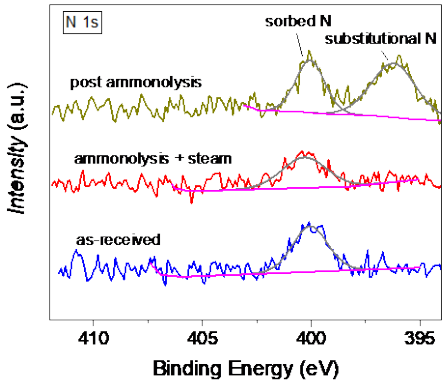

Figure 3.9-3 : XPS spectra in the N 1s region for titania-based powders. Only the powder exposed to ammonia shows a peak due to substitution N. All three materials show a peak attributed to surface sorbed nitrogen species.

XPS spectra, Figure 3.9-3, reveal the presence of molecularly chemisorbed N on each type of titania-based powder (peak centered at 400 eV in the N1s spectra). In contrast, only the powder exposed to ammonia but not treated further displays a peak at 396-397 eV, a peak position that is characteristic of substitutional nitrogen. The spectra in the region of Ti (not shown) were unchanged with gas treatments and hence there is no direct evidence of changes in concentration of Ti^{3+} species. Together with the XRD and DRUV-vis data, we conclude that ammonolysis indeed produces N-doped titania (with N incorporating substitutionally for O). Subsequent exposure to steam largely reverts the material to an undoped state, but residual defects, perhaps oxygen vacancies, may leave the material with a slightly modified electronic structure. It can be concluded that TiO_xN_y is not stable under the conditions relevant to CsH_2PO_4-based devices, and the material was not considered further.

3.9.2 Lanthanum Tantalum Oxynitride (La-Ta-O-N)

Synthesis of lanthanum tungsten oxynitride was pursued by ammonolysis of lanthanum tantalum oxide, $LaTaO_4$. This oxide is not available commercially. Accordingly, it was synthesized in-house following the polymerized complex method reported by Zhang et.al.[140] Typically, 5 mmol $TaCl_5$ *(Sigma Aldrich, 99.99%)* and 5 mmol $La(NO3)_3.6H_2O$ *(Sigma Aldrich, 99.9%)* were dissolved together in methanol, followed by the

addition of 75 mmol of citric acid, along with an excess of ethylene glycol (300 mmol). The solution was stirred at room temperature for ~4.5 h, followed by stirring at 150 °C for 4 h, yielding a transparent gel. This product was then held at 200 °C for 12 h, producing a black char. The mixture was ground and calcined at 600 °C for 6 h to completely remove the carbon. The calcined product was ground and annealed at 1100 °C for 10 h, multiple times, until phase pure $LaTaO_4$ was obtained.

To produce the oxynitride, 0.5g of $LaTaO_4$ (*orthorhombic, light yellow*), was subjected to the flow of anhydrous NH_3 150 sccm @ 900 °C for 20 hrs. The ammonolysis transformed the material to a red powder, and the XRD pattern, Figure 3.9-4, changed from that of phase pure $LaTaO_4$ to that of a mixture of predominantly (94.6%) monoclinic $LaTaON_2$ (PDF #04-012-2451) and a small amount of Ta_2O_5 (PDF #01-070-4775). Such phase separation with the formation of tanalum oxide has also been reported in the literature.[83] In addition, two very minor unidentified impurity peaks appeared, the origin of which remains uncertain. Surface sensitive XPS survey and elemental scans, in Figure 3.9-5 revealed an atomic composition of Ta (17.19%), La (19.66%), O (52.11%) and N (11.04%). The implied O:N ratio of 4.72:1, being much greater than the ratio of 0.5:1 expected based on the structure, suggests that the Ta_2O_5 may be concentrated on the surfaces of the powders, and probably a surface passivation would be good to minimize the surface oxide formation.

The DR UV-VIS spectrum of the composite [predominantly $LaTaON_2$ (red color)] resulting from the ammonolysis is shown in Figure 3.9-6. An absorption edge at around 670 nm is evident, implying a band gap of 1.85 eV. This is close to the value reported in the literature for $LaTaON_2$,[140-142] and is the basis for expecting that the material will absorb and permit utilization of a signficant part of the solar spectrum, if used for any photo-active catalysis applicatoins.

CDP-Oxynitride stability test was performed on La-Ta-O-N phase (94.6 % monoclinic $LaTaON_2$ + balance Ta_2O_5). The post-treatment diffraction pattern, Figure 3.9-7, suggests negligible interaction between La-Ta-O-N oxynitride and CsH_2PO_4; the pattern is fully as a combination of the starting materials, CDP and the La-Ta-O-N mixture. In addition, the color of the pellet was unchanged, suggesting no electronic structure change.

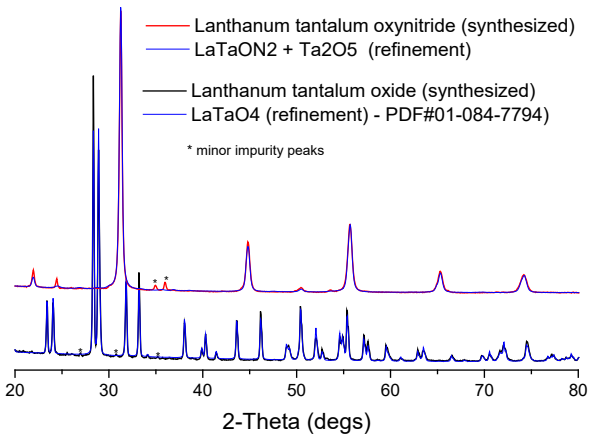

Figure 3.9-4 : X-ray diffraction patterns of lanthanum tantalum oxide and lanthanum tantalum oxynitride, as indicated. ~5% of Ta_2O_5 impurity was found in the synthesized $LaTaON_2$.

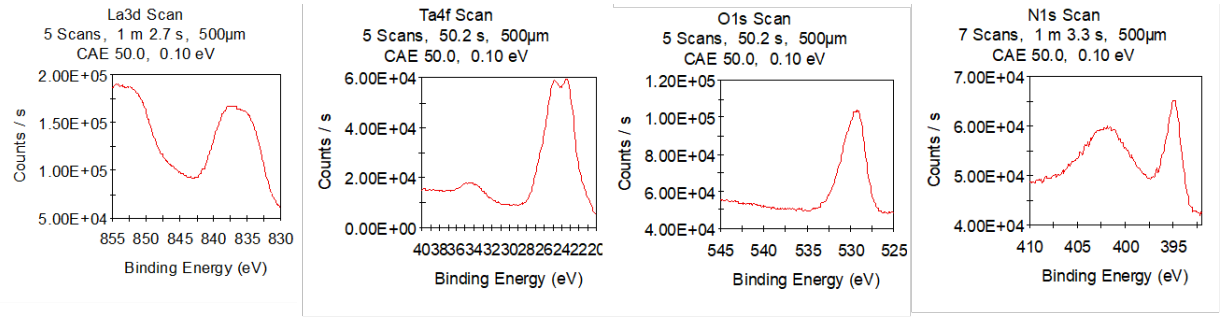

Figure 3.9-5 : XPS for $LaTaON_2$

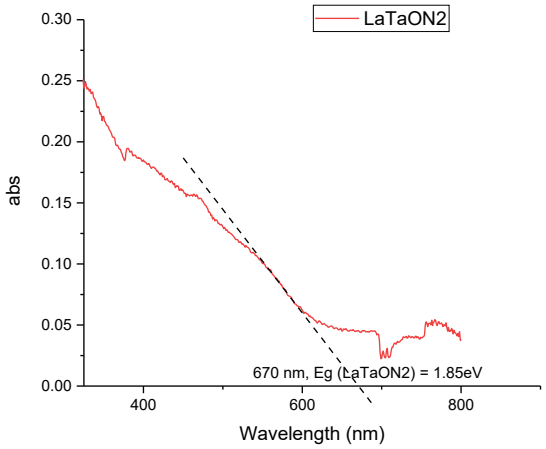

Figure 3.9-6 : DR-UV-VIS spectrum of “La-Ta-O-N” formed predominantly of $LaTaON_2$ (94.6 %).

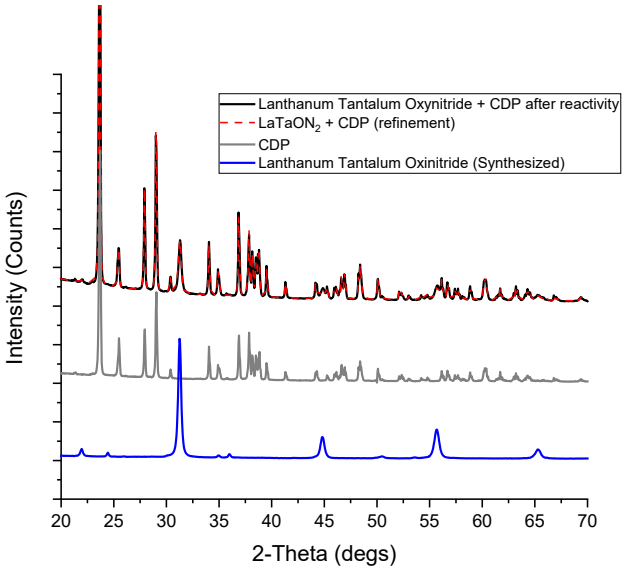

Figure 3.9-7 : Lab XRD pattern for as synthesized Lanthanum Tantalum Oxynitride (blue curve), CDP (grey curve) and their mixture post CDP-Oxynitride reactivity test (black curve) overlayed with refinement based of $LaTaON_2$ + CDP.

3.9.3 Barium Tantalum Oxynitride (Ba-Ta-O-N)

Synthesis of barium tungsten oxynitride was pursued by ammonolysis of barium tantalum oxide, $Ba_2Ta_2O_7$. This oxide is not available commercially; its synthesis was attempted following the polymerized complex route reported by Domen et al.[143], a method similar to that used here for the synthesis of $LaTaO_4$. In a typical synthesis, 4 mmol $TaCl_5$ *(Sigma Aldrich, 99.99%)* and 4 mmol $LaCO_3$ *(Alfa Aesar, 99.95%)* were dissolved in 30 ml plus 30 ml deionized (DI) water, followed by the addition of 30 mmol of citric acid, along with an excess of ethylene glycol (300 mmol). The solution was stirred at room temperature for ~6 h, followed by stirring at 150 °C for 4 h, yielding a transparent gel. This product was then held at 350 °C for 12 h, producing a black char. The mixture was ground and calcined at 800 °C for 4 h to completely the carbon. No further heat treatment was applied. The resulting oxide was found by X-ray diffraction, Figure 3.9-8, to be a mixture of three phases: 28.6% $BaTa_2O_6$ (Orthorhombic, PDF#00-020-0146) + 51.4% $Ba_5Ta_4O_{15}$ (Hexagonal - P3m1, PDF#04-007-8955) + 20.1% $Ba_3Ta_5O_{15}$ (Tetragonal - P4/mbm - PDF#04-012-1438).

Perhaps not surprisingly, ammonolysis of this mixed oxide yielded a mixed product, but which did include a large fraction of the target oxynitride, cubic $BaTaO_2N$ (Figure 3.9-9). Preliminary reactivity studies with CDP suggested no instability but were not entirely conclusive (not shown). For future, more comprehensive evaluation of this material should be pursued to first achieve phase-pure synthesis, by both optimizing phase pure oxide synthesis and an optimized ammonolysis procedure.

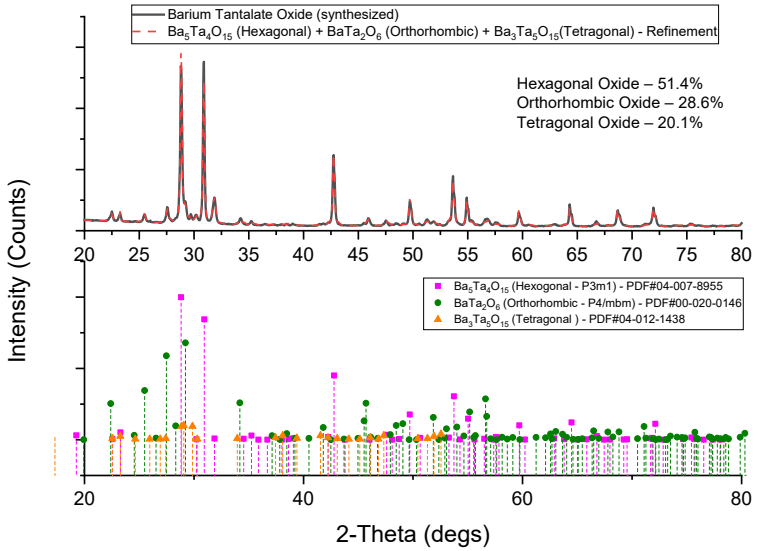

Figure 3.9-8 : X-ray diffraction pattern of the oxide resulting from chemical solution attempts to prepare $Ba_2Ta_2O_7$

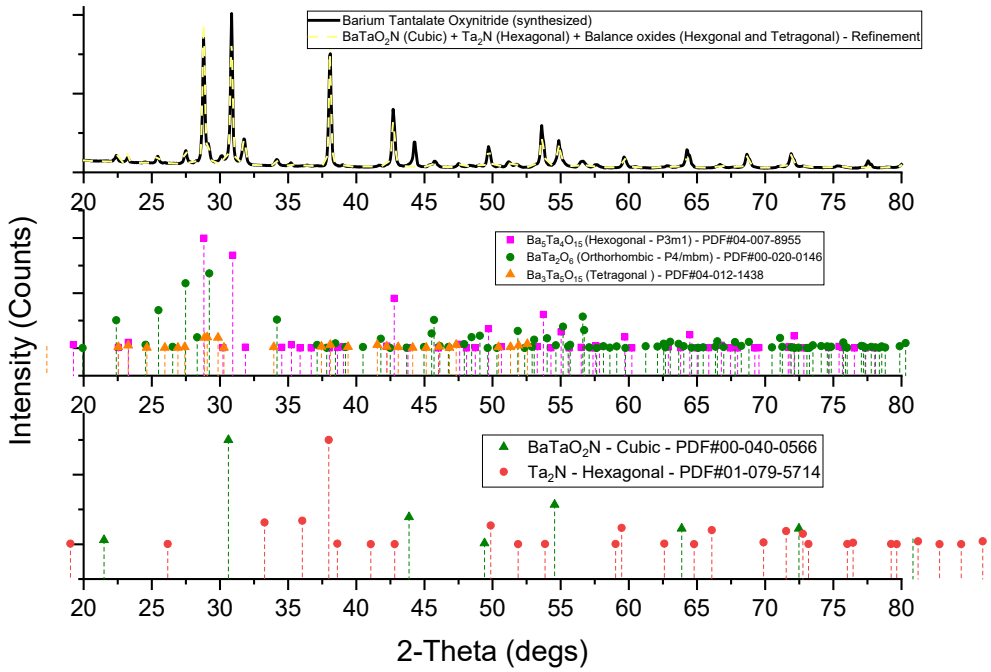

Figure 3.9-9: X-ray diffraction pattern of the Barium Tantalum oxynitride mixture resulting from ammonolysis of oxide mixture as precursor. A combination of oxynitride ($BaTaO_2N$), nitride (Ta_2N) and some oxides were best model for their refinement overlayed in yellow dash curve on the black curve showing as synthesized oxynitride Lab XRD curve.

3.10 Conclusions and Future Prospects.

Several oxynitride systems were potentially screened for future catalyst application in Solid acid applications. The 9 oxynitride systems screened were categorized as photo-absorbing and semiconducting oxynitrides.

Photo-absorbing oxynitride systems: Mo-O-N | W-O-N | Nb-O-N | La – Mo-O-N | La-V-O-N

Photo-active oxynitride systems: Ta-O-N | La -Ta - O -N | Ba-Ta-O-N

Summary of Lab XRD patterns showing the transitions from oxide to corresponding oxynitride mixtures used for oxynitride systems studies of stability against reaction with CDP under device-relevant conditions is shown in Figure 3.10-1.

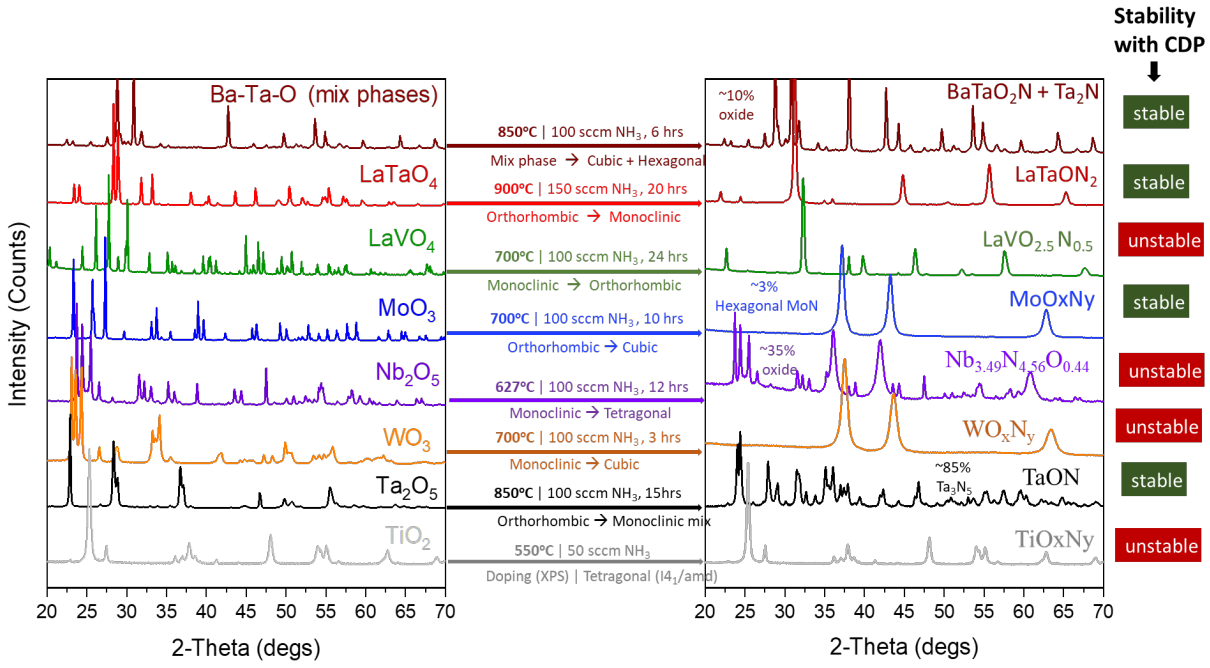

Figure 3.10-1 Lab XRD of precursor oxide and post ammonolysis (oxy)nitride products for various oxynitride systems studied in this work. Also indicated is the stability of these ammonolysis products with CDP under humidified N_2 at 250°C for 48hrs

Molybdenum Oxynitride (Mo-O-N) and Tantalum oxynitride (Ta-O-N) were recognized as highlight systems as initial reactivity test suggest stable performance under operating conditions with CDP under humidified nitrogen at 250^{o}C. Dry vs Wet ammonolysis, wherein in the later along with dry ammonia some humidity (through carrier gas Argon) is introduced, were performed to explore the phase space of these two oxynitride systems.

Mo-O-N

- Dry ammonolysis of MoO_3 was optimized (sample mass, flow rate, heating profiles) to result in phase pure Cubic F and Cubic P nitride samples, where in the key experimental factor was determined to be the heating protocol.
- Reaction pathway for γ-phase synthesized via MoO_3 ammonolysis (700^{o}C) was studied, and the discrepancies in literature regarding the complete reaction pathway via bronze and MoO_2 was resolved.
- Wet ammonolysis was discovered as a novel method favoring hexagonal phase over the competing γ-phase.
- Optimization of wet ammonolysis (pH_2O, precursor choice, heating rate) was performed to obtain phase pure δ-phase, wherein 2% pH_2O, MoO2 as precursor and longer reaction time (compared to cubic phase synthesis) were combined to obtain the δ-phase at 700C.
- Reaction pathway of wet ammonolysis of MoO_2 to obtain δ-phase.

Phase pure synthesis protocol of all four molybdenum nitride phases (determined to be oxynitrides in Chapter 4) is present in detail in Appendix C.1. These phases synthesized through this work are also being used for collaborative applications, some of which are displayed in Figure 3.1-2. These applications can be broadly categorized into those that would be based on solid acid electrolyte CDP with 250^{o}C being the operating temperature and those that are non-CDP focused. These Molybdenum oxynitride phases are shown as potential hydrogen evolution reaction catalyst for Solid Acid Electrolyzer Cells in Chapter 5. As a small side study (Appendix C.3), γ-phase synthesized here were also combined with Ruthenium nanoparticles and preliminary characterization of these composited was conducted using XRD, and later

evaluated as positive electrocatalyst for ammonia decomposition reaction (using CDP as electrolyte). It is to be noted, that Cubic P phase (C800 sample) was also tried for Solid Acid Fuel Cell cathode, however it resulted in rapid performance degradation. Similarly attempts to use these for Oxygen evolution reaction catalysts both at mid temperature SAEC and low temperature water electrolysis resulted in rapid degradation. The overall unsuitability of Molybdenum oxynitrides application in oxidative conditions is studied in Appendix B.9, where degrading conductivity and structure under humidified air at 250^{o}C is shown, whereas these are stable under reducing conditions. Realizing that these are best suited for applications with non-oxidizing operating conditions, collaborative applications such as catalyzing isomerization and hydrogenation reactions, which often involve reducing working gas atmosphere, are being pursued as subsequent projects, to continue capitalizing on our ability to synthesize all the four phase of these Molybdenum nitrides and characterize their chemistry and structure (in Chapter 4 for Cubic and hexagonal phases, and Appendix C.1 for tetragonal phase) as a part of MRSEC IRG 2 project effort.

Ta-O-N

Dry and Wet ammonolysis of Ta_2O_5 at 850^{o}C was explored to explore the phase space of Ta-O-N system, with following conclusions:

- Dry ammonolysis of Ta_2O_5 @850C results in mixture of β –TaON and Ta_3N_5 phases were increasing the extent of reaction, results in phase pure Ta3N5 nitride (monoclinic, sg: C2/m, PDF#04-009-5976) as the final product.
- Wet ammonolysis however, completely suppresses the nitride phase resulting in various mixtures of the three TaON phases (δ, β and γ-TaON) depending on extent of reaction.
- While more studies, especially in-situ XRD based are needed, preliminary exploration of pH_2O showed, that lower pH_2O levels favored β-TaON formation over the higher energy metastable

(and viceversa), which was capitalized to phase pure β –TaON, which was confirmed stoichiometric with chemical analysis, and characterized using several other techniques.

- Additionally, nanoparticles of TaON (β-TaON, γ-TaON and/or Ta_3N_5mixtures) were synthesized using Urea based Sol Gel route. While uniform nanoparticles can be synthesized this way, no phase pure product was obtained suggesting further optimization of recipe is required or alternate methods need to be explored.

Unlike, Molybdenum nitride which are black powders, Ta-O-N samples are colorful (shades of dark yellow, green, brown, and red depending on the phase mixture) as these are known photo-active oxynitride materials. These Ta-O-N samples synthesized in this Chapter, are used for catalyzing Oxygen Evolution Reaction (OER) in Solid Acid Electrolyzer Cells at 250^{o}C using CDP electrolyte in Chapter 5. While SAEC utilize the electrocatalytic catalyzing potential of Ta-O-N system, a whole untapped potential offered by these well synthesized and characterized Ta-O-N samples, is their active optical band gap. Collaborative efforts are already being pursued for several such applications shown in Figure 3.1-2, including photo-catalytic pollutant degradation. A yet another proposed application that harnesses both the optical and electrocatalytic potential of these compounds, is Solid Acid Photo Electrochemical Cell (SAPEC). Such a proposed device would perform high temperature solar based steam electrolysis. Such a device would benefit from high temperature steam electrolysis advantages that SAEC possess, but additionally, the band gap of Ta-O-N (1-9-2.4eV) is enough to drive the electrochemical steam splitting reaction. In this sense SAEC which form prequal system to SAPEC, would suggest that current densities (proportional to O_2 evolution) an order to magnitude higher than those observed in room temperature solar water splitting could be achieved. Such a system would require a transparent electronic conductor at the photo-anode, and also a transparent current collector electrode that allows light through it. For this purpose, a side project to sputter ITO films onto glass substrate was pursued, wherein using sputtering, various thickness ITO films were coated, and measured for absorption, smoothness and thickness using Ellipsometry. A smooth 16nm ITO film on glass substrate was measured to be 90% transparent to visible

light radiation. Details of this preliminary study can be found in Appendix C.5. A schematic of such a system is shown in Figure 3.10-2.

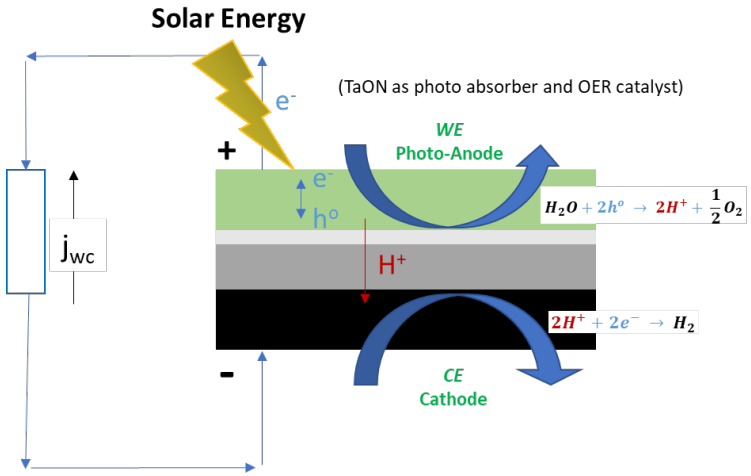

Figure 3.10-2 Concept of Solid Acid Photo-Electrolyze Cell utilizing CDP as electrolyte and Ta-O-N as both photo absorber (for photo-voltage generation) and electrocatalyst for catalyzing the OER reaction on the photo anode side. The counter electrode can simply be a well-studied Pt on C that is known to work good for HER reaction in CDP based solid acid systems.

Yet another stable photo-active oxynitride system that has been synthesized, but not used in applications is La-Ta-O-N:

- Prepared phase pure oxide precursor $LaTaO_4$ by chemical solution routes
- Prepared oxynitride product (red) consisting of 96% $LaTa(O_{3-x}N_x)$, balance Ta_2O_5 , where repeating the ammonolysis for longer time almost achieves phase pure oxynitride. More optimizations might be needed for reproducibility.

Absorption edge of $LaTaON_2$ lies at 670 nm, implying a band gap of 1.85 eV, which is suitable for photo-catalytic applications, and probably a competing candidate for Ta-O-N in SAEC and SAPEC, as it passed the CDP reactivity test.

Several other oxynitride systems were explored (in various capacities) and characterized specially using DR UV-VIS, Lab XRD and XPS occasionally, with the following key conclusions:

- Ti – O – N
    - Nitrogen was successfully doped into TiO2 using high temperature ammonolysis confirmed by XPS and reduced bang gap (<3 eV) (without any phase change in XPD).
    - However, the N doping is reversible at high temperature under humidity, where a blue shift B.G shifts back to 3.19 (that of TiO_2) was observed from the steam treatment.
- W – O – N
    - Prepared phase-pure oxynitride $WO_{1-x}N_x$ (black) with ~ 1:1 O: N (literature rock salt Cubic F structure)
    - Oxynitride absorbs light throughout the visible regime
    - Oxynitride reacts weakly with CDP
- Nb – O – N
    - Oxynitride synthesis was attempted, however phase pure product needs more optimization.
    - Multiphase ammonolysis product however reacts with CDP under humidity@250^oC
- Ba – Ta – O – N
    - Attempts to prepare phase pure oxide precursor $BaTa_2O_7$ by chemical solution routes unsuccessful; many avenues remain for addressing this synthesis
    - Oxynitride product of multiphase oxide is also multiphase.
- La – V – O – N
    - Prepared phase pure oxide precursor $LaVO_4$ by solid state reaction
    - Prepared oxynitride $LaVaO_{3-x}N_x$ (black) with x ~ 0.5; composition as estimated on the basis of unit cell parameters
    - Oxynitride absorbs light throughout visible regime.
    - Fails the CDP-Oxynitride reactivity test.

While the above oxynitrides are reported in literature, an attempt to synthesize La-Mo-O-N oxynitride was conducted, which has not been reported before. Phase pure ammonolysis oxide precursor candidate $La_2Mo_2O_9$ was synthesized by chemical solution routes was successfully prepared, and exposure to ammonia induces amorphization of this oxide and material becomes black. XPS does show detectable but limited nitrogen incorporation, suggesting the possibility of an oxynitride phase in the making. More studies are needed to reproduce this work, and to apply post ammonolysis heat treatments to crystallize the new oxynitride phase, on which Xray/Neutron diffraction along with chemical analysis techniques can be used to determine the complete phase. Although, this oxynitride phase in its present form does react with CDP, making it unattractive for Solid Acid based applications using CDP as electrolyte.

Chapter 4 Hidden Complexity in the Chemistry and Structure of Ammonolysis-Derived “γ-Mo2N” and “δ-MoN”: Overlooked Oxynitride Hydrides.

4.1 Molybdenum Nitrides via ammonolysis of oxides (Nitride or Oxynitrides?)

4.1.1 Introduction

Molybdenum nitrides have received significant attention due to their excellent and tunable mechanical, electronic, thermal, catalytic, and magnetic properties.[144, 145] A range of synthetic approaches has been employed to produce materials within this class. In studies in which the physical and electronic properties are of interest, thin film approaches such as sputtering and physical vapor deposition are common.[145] When the catalytic,[146-150] electrocatalytic,[151-158] and electrochemical[71, 159, 160] properties are instead targeted, temperature programmed reaction of oxide precursors with ammonia (ammonolysis) is often pursued to generate materials with high specific surface area.[113, 118, 120]

Although not comprehensive, experimental molybdenum nitride system phase diagram (Mo + S_2 study) is reported in literature.[107] Apart from the solid solution (α phase) which can contain about 1.8 at. %N, molybdenum nitrides are known to crystallize in two non-stoichiometric crystal systems and one stoichiometric crystal system. The tetragonal β phase is a non-stoichiometric phase and is a face centered tetragonal structure of metal atoms with an ordered array on nitrogen atoms. Existing at higher temperature, the cubic-γ phase is also non-stoichiometric, but is often reported with Mo_2N nominal composition, crystallizing in rock salt Fm-3m space group.[108, 109] Additionally, a nitrogen rich primitive Cubic P with nominal composition Mo_3N_2 is also reported, which can be called as γ’-phase.[110] The

hexagonal-δ (MoN) phase is reported as a stoichiometric phase, of which also several different space groups have been reported lately.[111]

4.1.2 Cubic γ-Mo_2N phase – Curious case of oxygen & characterization challenges

Successful synthesis of the target molybdenum nitride phase, most commonly the B1-type γ phase, from the ammonolysis reaction is typically presumed on the basis of the agreement of the experimental X-ray diffraction pattern with that in the ICDD (International Center for Diffraction Data) database.[161] In a handful of studies, it has been recognized that, despite displaying a readily recognized diffraction pattern, the product of this reaction can, in fact, retain a substantial oxygen content such that the material may be more appropriately considered a molybdenum oxynitride.[112, 162-164] In particular, Lyutaya[164] reported that, of the anions in a Cubic γ-Mo_2N sample produced by ammonolysis of MoO_3 at 700°C, ≈ 28 mole % were oxygen atoms, whereas Gouin *et al*.[162] reported that 17 mole % of the anions were oxygen atoms after synthesis under similar conditions.

A rather intriguing feature of the crystal chemistry of the γ-phase of molybdenum nitride is the apparently high concentrations of anion vacancies. The phase is typically described as having a stoichiometry of Mo_2N, with nitrogen atoms randomly distributed over one-half of the available octahedral anion sites of the B1 structure.[165] Although deviations from the 2:1 stoichiometric ratio are rather widely recognized,[107] the extent to which the true stoichiometry may differ from this idealized value is not well-established. From an electron-counting perspective, there is little reason to expect a stoichiometry of Mo_2N, and indeed atomistic computational studies have suggested the existence of several ordered phases across the Mo-N system.[166] Troitskaya and Pinsker[110] reported the existence of Mo_3N_2 (obtained from ammonolysis of Mo films), a phase richer in anions than the standard Mo_2N stoichiometry. This phase is distinct from the conventional γ phase due to the presence of vacancies on *both* anion and cation sites, with cation site vacancies ordered such that the symmetry was lowered from $Fm\bar{3}m$ to $Pm\bar{3}m$. The occurrence of a

molybdenum nitride phase of space group *Pm*$\bar{3}$*m* that is similarly rich in anions relative to "Mo_2N" has also been reported from ammonolysis of MoO_3. Specifically, Tagliazucca *et al.*[115] reported a primitive cubic phase of stoichiometry of $Mo_{3.2}N_{2.7}$ when the synthesis was carried out at 800°C. The conventional *higher* symmetry *Fm*$\bar{3}$*m* phase was obtained from ammonolysis at a *lower* reaction temperature of 923 K. This surprising behavior (of a decrease in symmetry on increasing synthesis temperature) was not explained. Overall, these factors indicate that, while the stoichiometry and chemistry of "γ-Mo_2N" are at first glance rather simple, the material is in fact chemically quite complex, with variable anion:cation stoichiometry, possible ordering at high temperature, and unknown solubility of oxygen and hydrogen.

Furthermore, as shown by Kreider *et al.* for the example of oxygen reduction activity, the extent of oxygen uptake can profoundly impact properties.[167] In parallel, some studies have revealed that bulk hydrogen uptake can also occur in these materials, either during the ammonolysis itself[109] or by post synthesis treatment.[108, 150] Alternative synthesis routes, such as direct reaction of Mo and N_2 or nitride film growth under high vacuum conditions, may inherently limit, without entirely precluding, the possibility of incorporation of foreign species (O and H).[111]

Note to reader: Cubic F (γ-phase) and Cubic P (γ'-phase) molybdenum nitride samples synthesized in Chapter 3, referred to as C700 and C800 respectively are extensively characterized in this study.

4.1.3 Hexagonal δ-MoN phase

While γ-phase synthesized via oxide ammonolysis have been studied the most for a plethora of catalytic applications as highlighted above, the hexagonal δ-phase has recently garnered a lot of attention owing to several unique properties attributed to this phase over recent years. Chen, et.al showed that δ-MoN samples were more active for HER catalysis compared to γ-Mo_2N.[168] Couple of years later Cao et.al evaluated various molybdenum nitride phases for ORR activity, and observed that all the hexagonal phases (δ-MoN, Mo_5N_6) were more active than the γ-Mo_2N.[155] Recently hexagonal molybdenum nitrides

have also been applied for Li-S batteries,[169] SERS applications,[170, 171] supercapacitors and more hydrogenation catalysis.[172]

In the original phase diagram for Mo-N system by Jehn et.al,[107] δ-phase hexagonal molybdenum nitride was reported as a stoichiometric δ-MoN. Originally synthesized by Hagg et.al (later called as the δ_3-MoN variant), in 1930 by reaction Mo foil with ammonia at 973K, more recently, several space groups for these δ-phase hexagonal molybdenum nitrides are suggested in the literature. Ganin, et.al have described the main four hexagonal molybdenum nitrides variants δ_1-MoN, δ_2-MoN, δ_3-MoN and finally a nitrogen rich Mo_5N_6 phase, reported in literature.[111]

δ_1-MoN, was originally synthesized by reacting $MoCl_5$ with NH_3 between 790-910K in 1980s by Lengauer,[173] crystallizing in WC-type structure with $P\bar{6}m2$ (187 sg) space group. While high temperature ammonolysis of chloride with ammonia still remains the only used method for the synthesis of bulk δ_1-MoN, the structure however has been updated over years.[111]

δ_2-MoN was originally reported by Schonberg in 1950s, synthesized using PECVD via MoCl5 and N2 reaction at 1003K.[174] It is known to crystallize with a NiAs-type structure with $P6_3/mmc$ (194 sg) space group. Complex synthesis routes,have been used recently to synthesize 194 sg MoN bulk samples, for example sequential ammonolysis of $Mo(NH_2O)n$ complex at 873 and 923K by Gajbhiye.[109]

δ_3-MoN is the phase that can be called the original δ-phase, synthesized by Hagg,[175] by simple ammonolysis of Mo foil at 973K. These crystallize in modified Ni-As type structure (FeS type), with $P6_3mc$ (186 sg) space group. Both disordered and ordered versions are reported for this 186sg MoN. The usual route to get the 186sg MoN is to perform ammonolysis of $MoCl_5$ at temperature around 900 K (upto 1100K), [15, 111, 120] which usually results in low surface (<10 m^2/g) area but phase pure 186sg MoN (δ_3-MoN). The product of above reaction is usually disordered, however most structural studies perform a high T and high-pressure post treatment to convert these to ordered δ_3-MoN phase. This method was originally described by Behzinga, who applied 6GPa of pressure at 1800K on disordered 186MoN to obtain the δ_3-MoN, where they characterized this phase properly for the first time. In this structure, N atoms site on every second trigonal prismatic void built by Mo atom layers. Such a clustering of Mo atoms

and ordering of N atoms best describes the structure being a slightly deformed 2X2X1 superstructure of the NiAs type. Recently, other high P and T routes using Na_2MoO_4 and hBN as precursors at ~1700K and 3.5-5GPa pressures, have been reported, for δ_3-MoN synthesis.

Finally, Mo_5N_6 is a nitrogen rich hexagonal phase reported in addition to the three variants discussed above. Originally these were synthesized in 1963, by Troitskaya and Pinsker, via ammonolysis of Mo flims at 1023K,[176] who described these to crystallize in 186sg with $Mo_{0.82–0.85}N$ composition, however later Marchand et.al highlighted these as Mo_5N_6 with the structure similar to an intergrowth product of the WC- and NiAs-type structures. However, only recently Ganin et.al clarified the true space group of this Mo_5N_6 phase as centrosymmetric $P6_3/m$ (176 sg), where the this MoS_2 type filled 176sg model when refined suggested a anion rich chemistry with two out of the 5 Mo sites being approximately half vacant, with no anion vacancy.[111]

While several variants as discussed above are reported, δ_3-MoN are unarguably is the most reported phase in literature, and also the phase that we synthesized in Chapter 3 as H700 sample. Recently these 186sg MoN have been explored a lot for their superconducting and mechanical properties. The phase exhibits superconducting transition at the Tc of 12–14 K,[29, 111, 177] which is the second highest among the known the metal nitrides (lower than γ-phase) after γ –NbN. More recently a nature article crowned this phase as the hardest superconduting material (Vickers hardness ~30GPa)[177], and the hardest metal nitride. It should be acknowledged that these δ_3-MoN are either prepared by ammonolysis of MoCl5 which in general results in low surface area products, or complex multistep synthesis is required to produce high surface area materials.[170, 171, 178, 179] Unlike, γ-phase, simple ammonolysis of MoO_3 (or other oxides) cannot be used to make these with high surface are, as competing γ-phase dominates the final product. In this way wet ammonolysis discussed in Chapter 3, can be considered as a novel route for preparing these compounds starting from oxides.

Note to reader: Hexagonal (δ-phase) synthesized in Chapter 3, referred to as H700 is extensively characterized in this study. The specific variant based on literature for H700 would be δ_3-MoN as the sg determined for H700 is 186, however for simplicity these are only referred to as δ-phases in the rest of the thesis.

4.1.4 Advanced characterization approach (true structure and chemistry determination)

The crystallographic features of the molybdenum nitride phases resulting in literature from nominally oxygen-free synthesis conditions and from bulk ammonolysis are surprisingly similar. This similarity is likely the reason the products of ammonolysis, have often been judged to be strictly nitrides, however, as shown below, ammonolysis of MoO3 derive y-phase nitrides are hydrogen incorporated Molybdenum Oxynitrides with generic formula $MoN_xO_yH_z$.

In this work, we undertake a comprehensive chemical, crystallographic, electronic, and morphological study of both Cubic and Hexagonal molybdenum nitride phase samples (C700, C800 and H700) synthesized in Chapter 3, via ammonolysis of precursor oxides either under dry (for Cubic samples C700 and C800) or humidified NH3 gas (for hexagonal H700 sample). We first characterize the products using electron energy loss spectroscopy (EELS) in a scanning/transmission electron microscope (S/TEM), X-ray photoelectron spectroscopy (XPS), X-ray adsorption spectroscopy (XAS), thermogravimetric analysis (TGA), prompt gamma-ray neutron activation analysis (PGAA), and combustion analysis to establish the chemical compositions of all 3 samples. Using these compositions to inform models, the structure of each phase is determined by Rietveld refinement using combined synchrotron X-ray diffraction (XRD) and neutron diffraction (ND) data. ND is particularly well suited to the study of molybdenum oxynitrides because N and O, with respective scattering lengths of 9.36 fm and 5.803 fm,[180] can be differentiated, and the pattern is not dominated by Mo (with a neutron scattering length of 6.715 fm), as it is in XRD and electron diffraction. The crystallographic characterization is supplemented by electron microscopy, surface area analysis, and pycnometry for morphological and physical evaluation. These studies reveal

that all of these phases, including the hexagonal phase (reported to be stoichiometric MoN) contain considerable concentrations of oxygen, along with some hydrogen, in addition to the primary molybdenum and nitrogen components. Furthermore, differential fourier maps are used to estimate the hydrogen position while performing the co-refinement, as hydrogen has a negative neutron scattering factor. both C700 and C800 samples obtained via MoO3 dry ammonolysis at 700ºC and that at 800ºC, crystallize in a structure of space group $Pm\bar{3}m$, and both contain substantial concentration of cation vacancies. They are readily distinguished by the nonnegligible x-ray and electron diffraction intensities of peaks with mixed even and odd *h*, *k*, *l* indices in the compound synthesized at 800ºC, peaks which are expected to be absent due to lattice centering in space group $Fm\bar{3}m$.

The clarification provided here of the true composition and crystal chemical features of the product of these heavily studied γ and δ phases obtained via ammonolysis of molybdenum oxides, provides an essential grounding for understanding the structure-property relations in this widely employed material.

4.2 Experimental Methods and Materials

4.2.1Synthesis of phase pure Cubic F, Cubic P and Hexagonal Molybdenum Oxynitride

Cubic and Hexagonal Molybdenum nitrides synthesis protocols were discussed in detail in Chapter 3. Brief recall of recipes for the 3 key ammonolysis derived molybdenum oxynitride samples, which were labelled as C700, C800 and H700, corresponding to phase pure Cubic F, Cubic P and Hexagonal samples in Chapter 4:

Cubic Molybdenum Oxynitride synthesis recipe (Cubic F | C700 and Cubic P | C800 samples): Temperature programmed ammonolysis of MoO_3. 0.25 g MoO_3 (99.9995% metals basis, Alfa Aesar or 99.97% metals basis, Sigma Aldrich) was placed inside a tube furnace at ambient temperature and immediately subjected to a flow of 100 mL/min (space velocity of 1.65 cm/s) of anhydrous NH3. The material was then subjected to the following thermal profile: heat to 350°C (5 °C/min, no hold), heat to 500°C (0.6 °C/min, no hold), heat to either 700°C or 800°C (3°C/min, 3 h hold), and finally furnace cool to ambient temperature while still under ammonia flow. The samples obtained from ammonolysis at 700°C and 800°C , are hereafter referred to as C700 and C800, respectively in this work. The majority of the experiments were performed using the higher purity Alfa Aesar precursor. As described below, some sample-to-sample variations in physical characteristics were observed. Because of the limitations of the sample mass in the synthesis, not all characterization studies could be performed on a single batch of material and in some cases, multiple batches were combined. It was realized that precursor vendor (Sigma Aldrich vs Alfa Aeser) and even individual bottles of purchased MoO_3 could result in some sample-to-sample variation, which is why several analysis were repeated on samples synthesized from different precursor bottles. Results of this supplementary study are included in Appendix B.8, and has been cross-referenced in this chapter wherever appropriate.

Hexagonal Molybdenum Oxynitride Sample recipe (Hexagonal | H700 sample): "Delta Phase" in this work was synthesized using an optimized wet ammonolysis reaction, wherein MoO_2 precursor was heated to 700°C and held for 12 hrs and then furnace cooled to room temperature, all under the mixture of anhydrous NH3 and humidified Argon, with 2% pH_2O. The sample is referred as H700

4.2.2 Characterization Details

Most characterizations were identically performed on both Cubic Phases (C700 and C800) and Hexagonal Phase (H700) oxynitride samples. Wherever required, specific extra information on characterization parameters dependent on the specific sample is provided.

4.2.2.1 SEM, BET and Lab XRD

For all samples (C700, C800 and H700), morphology was studied by scanning electron microscopy (SEM) in secondary electron imaging mode using a Hitachi SU8030 equipped with a cold field emission source operating at 15 kV and 10 μA. No prior coating was necessary given the conducting nature of the samples. BET (Brunauer–Emmett–Teller) surface areas and pore(s) size were determined from nitrogen physisorption isotherms measured at liquid nitrogen temperature using a Micromeritics 3Flex instrument (50 mg to 200 mg for C700 and C800 samples, and ~200mg for H700). Data were analyzed using the MicroActiv software package, which provides quantitative uncertainty estimates for the surface area. Phase formation was evaluated by laboratory XRD (Ultima, Rigaku) using Cu Kα radiation at a scan rate of 2.5°/min, with a step size of 0.05°. The sample was ground and then placed on a zero background SiC holder and rotated at a speed of 3.1 rad/s during measurement. The commercial software package, JADE (MDI, Inc.) was used for whole pattern fitting to determine the lattice constant and the crystallite size, along with their uncertainties. For the purposes of this analysis, the entirety of the peak broadening was attributed to size effects. A Micromeritics AccuPyc II 1340 pycnometer was utilized for the density determinations of all samples.

4.2.2.2 TEM and EELS

For TEM and EELS studies, powder products (C700, C800 and H700) were lightly ground, sonicated in ethanol, and dropped on ultrathin carbon-coated Cu grids. Conventional TEM images and selected area electron diffraction (SAED) patterns were obtained using a JEOL Grand ARM 300F operated at 300 kV. STEM images and EELS spectra were acquired at 200 kV using a Cs-corrected JEOL ARM 200CF equipped with a Quantum Dual EELS system. EELS spectra of the two samples were obtained from areas with similar thickness. The thicknesses were estimated from the zero-loss spectra, which showed t/λ values of 0.45 (~45nm), 0.40 (~40nm) and 0.5 (~50nm) for the C700, C800 and H700 samples, respectively.

Core-loss and low-loss EELS spectra were collected using an entrance aperture of 5 mm and energy dispersion of 0.25 eV/channel, which resulted in a 1.5 eV energy resolution. The convergence angle was set to 20.6 mrad, and the probe size was ≈ 2 Å. STEM/EELS datasets were collected using the commercial software package Gatan Microscopy Suite (GMS). The simultaneous acquisitions from multiple channels were synchronized using the Gatan Digiscan system. Final EELS spectra were obtained by averaging the signal across different areas within the sample. Simultaneous acquisition of core-loss spectra and low-loss spectra enabled accurate measurement of absolute chemical shifts and energy differences.[181] Data analysis was performed with GMS and the commercial software package Origin. For EELS analysis, core-loss spectra were aligned using simultaneously acquired low-loss spectra. Background subtraction was then performed on both spectra using a power law expression, AE^{-r} where E is energy and A and r are constants, in the pre-edge energy window 180 eV to 220 eV. Multiple scattering effects were removed by Fourier-ratio deconvolution following methods described by Egerton.[182] The $Mo_{M2,3}$ and N_K edges overlap at around 400 eV, and the features were thus deconvoluted by peak fitting to obtain peak energies. The uncertainty in the energy onset position in EELS is reflected in the nature of zero loss peak (ZLP), which embodies the point-spread-function of the EELS spectrometer, all instrument/acquisition instabilities, and related perturbations to the energy onset

position. As a result, some fraction of the width of the ZLP is often considered as the uncertainty in EELS. That fraction is, in turn, determined by the ability of modern curve-fit software and other methods to discriminate or identify overlapped edges, which is conservatively 1/3 of the ZLP width (and optimistically 1/5).[182] Thus, with ZLP of about 1.5 eV (with sample in the beam), the energy uncertainty is ≈ 0.4 eV.

4.2.2.3 Thermal XPS

Qualitative chemical analysis was performed by XPS using a Thermo Scientific ESCALAB 250Xi instrument, equipped with an aluminum anode (Al Kα= 1486.6 eV) X-ray source, an electron flood gun, a scanning ion gun, and a heating stage. Samples (C700, C800 and H700) were prepared by pressing the ammonolysis products into a disc, 3.2 mm in diameter. Because Ar etching, which is typically used to remove surface species, is known to modify the Mo oxidation state in molybdenum bearing compounds,[54] the contribution of adsorbed gases to the signal (potentially N_2, H_2O, NH_3, H_2) was minimized by performing measurements at elevated temperature. Once inside the preparation chamber, the sample was slowly heated to 250^{o}C K and held until the vacuum stabilized at ≈ 1.3×10^{-5} Pa, approximately 45 min. Following an initial survey scan (not shown), which revealed the presence of Mo, N, and O in the oxynitride samples, high resolution data were collected in the Mo3d (220 eV to 240 eV), C1s (279 eV to 298 eV), and O1s (520 eV to 545 eV) regions, using a step size of 0.1 eV with a dwell time of 50 ms and integrating over 10 scans. Due to significant peak overlap, results in the N1s-Mo3p region (380 eV – 405 eV) are not reported. Charging effects were corrected by referencing to the adventitious carbon Cls binding energy at 284.8 eV. The commercial software package Thermo Scientific™ Avantage was used for data processing. The instrument energy resolution of 0.10 eV was taken as the uncertainty in the binding energies determined by this analysis. The attributes of the Mo3d XPS peaks were established by fitting doublets with standard constraints ($Mo3d_{5/2}$ and $Mo3d_{3/2}$ with intensity ratio 3/2 and ΔBE ≈ 3.15 eV). Peaks due to three species were resolved: Mo^{6+} at a BE of ≈ 232.6(1) eV, Mo^{4+} at a BE of ≈ 230.1(1) eV

and $Mo^{\delta+}$ at a higher binding energy, with the assignments based on literature studies of molybdenum oxides.[160, 181, 182]

4.2.2.4 TGA, Combustion and PGAA

Quantitative and semi-quantitative chemical analyses were performed using a combination of TGA, combustion analysis, and PGAA. Uncertainty in the analysis stems from the variable extent of surface oxidation/hydration.[112] To mitigate against this factor, characterization experiments were generally performed within a few days of sample synthesis. TGA was used in complete reduction experiments to reveal the total mass of Mo in the materials and thereby provide an estimate of the anion to cation ratio. Data were collected using a Netzsch STA F3, using 50 mg to 75 mg of ground powder in each measurement (~72 mg for H700). The sample was loaded into a Pt pan, heated to 900°C under 3 % H_2 (balance Ar) and held for 3 h. Laboratory XRD was performed after completion of the TGA experiment to confirm, within detection limits, the presence of only Mo metal in the reduction product. The uncertainty in the TGA mass measurements was determined from the manufacturer reported instrument drift (5 μg/h), in combination with the sample mass and the total measurement time. This uncertainty was smaller than the sample-to-sample variation in mass loss. Specially for the Cubic samples (C700 and C800), additional TGA reduction measurement under 7% H_2 (balance He) at a rate of 2°C/min, was performed (hold for 3 hrs). Simultaneously, the onset of bulk mass loss was tracked by in situ XRD under flowing 7 % H_2 (balance He) using an Anton Paar XRK 900 reactor chamber mounted on a 9 kW Cu rotating anode Rigaku Smartlab diffractometer.

Determination of the nitrogen and in some cases hydrogen content was performed by microchemical combustion analysis using the commercial service of Midwest Microlabs. The materials were examined in either the as-synthesized state or after heat-treatment under Ar at 400°C to remove surface adsorbed species, a step that typically resulted in a 2-3 % decrease in mass for C700 and C800 samples, however much lower (~1%) for the hexagonal H700 sample. For the analysis, samples were combusted at 1000°C K under ultra-pure oxygen and the effluent stream was evaluated to determine the nitrogen and steam content. In principle, the absolute oxygen content can be determined through an

analogous pyrolysis approach, but the facility was unable to perform such a measurement. Uncertainties in the N and H mass fractions so determined are as provided by Midwest Microlabs.

PGAA measurements were carried out at the cold neutron PGAA instrument at neutron guide D at the NIST Center for Neutron Research. A pressed pellet weighing approximately 300 mg was prepared from as-synthesized samples of each material (C700, C800 and H700) using a 13 mm diameter die and a hydraulic press. Calibration standards were prepared from mixtures of MoO_3 (99.9995% metals basis, Alfa Aesar) with urea (SRM 912b) and graphite (Spectrographic Services, 100 mesh), MoO_2 (99% metal basis, Alfa Aesar) with the afore mentioned urea and graphite, and from ammonium molybdate tetrahydrate (ACS reagent grade, 81.0 % to 83.0% MoO_3 basis, Fisher Scientific), with the mixture or compound being pressed into a 300 mg pellet to give the same geometry as the C700 and C800 samples. For PGAA analysis, samples and standards were packaged in Al foil. and were irradiated in vacuum inside a ^{6}Li-aluminum lined sample box. The Prompt gamma-ray emissions at 778 keV (Mo), 2223 keV (H), and 10830 keV and its two escape peaks at 10318 keV and 9807 keV (N) were detected using an n-type, closed-end, coaxial high-purity germanium (HPGe) detector (41% efficiency) surrounded by a bismuth germanate Compton shield.[183-185] Oxygen has an extremely low prompt gamma-ray cross section, rendering quantification of this element by PGAA unfeasible. Mass ratios (mg:mg) for Mo:N and Mo:H were calculated using count rates from gamma rays measured in sample spectra and element sensitivities (counts s^{-1} mg^{-1}) calculated from gamma ray count rates in standards spectra and from standards preparation data. These were converted to molar ratios using atomic mass data for Mo, N, and H. Relative 2σ uncertainties for the resulting Mo:N and Mo:H ratios were estimated at 2.5 % based on the following (with approximate 1σ contribution): counting statistics (1 %), standards measurement replication ($\sigma/\sqrt{n} = 0.7/\sqrt{3}$ for the average Mo/N sensitivity ratio calculated for the three standards and $0.5/\sqrt{3}$ for the Mo/H ratio), purity of standards (estimated at 0.5 %), and target positioning in the beam (estimated at 0.5 % from repeated measurements of the gamma ray count rate of a Ti flux monitor).

4.2.2.5 Neutron and Synchrotron Co-refinement

Cubic Phases (C700 and C800)

ND data were collected using the POWGEN instrument of the Spallation Neutron Source at Oak Ridge National Laboratory. Powder samples were loaded into vanadium cans, and diffraction patterns were measured from two detector banks at ambient temperature. Neutron Bank 1 (NB1) offers a higher time-of-flight (TOF) range (with moderate resolution), whereas Neutron Bank 2 (NB2) offers better resolution (with shorter range). The data from NB1 were analyzed over the TOF range from 8×10^3 μs to 76×10^3 μs, corresponding to a q range of 1.87 $Å^{-1}$ to 17.73 $Å^{-1}$ (d-spacing ≈ 0.35 Å to 3.36 Å). NB2 data were analyzed in the TOF range of 11.6×10^3 μs to 76×10^3 μs corresponding to a q range of 1.87 to 12.22 $Å^{-1}$ (d-spacing ≈ 0.51 to 3.36 Å). X-ray synchrotron powder diffraction patterns were collected at beamline 11-BM of the Advanced Photon Source at Argonne National Laboratory. The measurements were performed at ambient temperature using an X-ray wavelength of 0.457876 Å, with the sample placed in a capillary spun at ≈ 90 Hz. For C700 data were analyzed from 7.96 ° to 46 °in 2θ, implying a q range of 1.90 $Å^{-1}$ to 10.65 $Å^{-1}$. For C800, the corresponding ranges were from 7.44 ° to 46 ° in 2θ and from 1.73 to $Å^{-1}$ to 10.65 $Å^{-1}$ in q. The d-spacing ranges were thus 0.59 Å to 3.30 Å (C700) and 0.59 Å to 3.52 Å (C800). Lattice parameters, atomic coordinates, and atomic isotropic thermal parameters were obtained by combined Rietveld refinement of XRD and ND patterns using the General Structure Analysis System II package.[58] The backgrounds in the ND patterns were fitted with 6^{th}-degree Chebyschev and Chebyschev-1 polynomials, respectively, for C700 and C800, whereas for the XRD patterns, 7^{th}-degree Chebyschev and 5^{th}-degree Chebyschev-1 polynomials were used for C700 and C800, respectively. Scale factor, sample absorption, sample displacement perpendicular to the beam, crystallite size (isotropic for C700, uniaxial for C800), and microstrain (uniaxial) parameters were sequentially refined for each material. In the final respective final refinement cycles, 7 independent crystal structure parameters refined for C700 and 8 for C800. In principle, hydrogen, which is entirely invisible to X-rays (and electrons) in the presence of Mo, is also detected by ND due to its negative scattering length of -3.7390 fm.[180] However, inclusion of

this species at sites identified by difference Fourier maps produced only marginal improvements to the refinement statistics and thus hydrogen was omitted from the final refinements. The reported uncertainties are the statistical uncertainties obtained from the GSAS refinements and, for derived quantities, from numerical propagation of such uncertainties.

Hexagonal Phase (H700)

ND data were collected using the POWGEN instrument of the Spallation Neutron Source at Oak Ridge National Laboratory. Powder sample was loaded into a vanadium can, and a diffraction pattern was measured at ambient temperature using the Bank 1 detector. The data were analyzed over the TOF range from 4×10^3 μs to 67×10^3 μs, corresponding to a q range of 2.11 $Å^{-1}$ to 35.5 $Å^{-1}$ (d-spacing ≈ 0.177 Å to 2.967 Å). X-ray synchrotron powder diffraction data were collected at beamline 11-BM of the Advanced Photon Source at Argonne National Laboratory. The measurement was performed at ambient temperature using an X-ray wavelength of 0.457876 Å, with the sample placed in a capillary spun at ≈ 90 Hz. The data were analyzed from 5.88 ° to 46.00 °in 2θ, implying a q range of 1.41 $Å^{-1}$ to 10.72 $Å^{-1}$. The d-spacing ranges was thus 0.59 Å to 4.46 Å. Lattice parameters, atomic coordinates, and atomic isotropic thermal parameters were obtained by combined Rietveld refinement of XRD and ND patterns using the General Structure Analysis System II package.[186] Hydrogen, which is entirely invisible to X-rays (and electrons) in the presence of Mo, can be detected by ND due to its negative scattering length of -3.7390 fm. A difference Fourier map was computed to identify the positions of hydrogen atoms. The background in the ND pattern was fitted with a 7^{th}-degree Chebyschev-1 polynomial, whereas for the XRD pattern, a 5^{th}-degree Chebyschev polynomial was used. Scale factor, sample displacement perpendicular to the beam, uniaxial crystallite size and microstrain parameters were refined. The fractional occupation of site 2b was initially allowed to refine with N and O anion. It refined to a value close to one with only N. It was then fixed. Site 6c was also allowed to refine with N and O anions but constrained to be fully occupied. The fractions of Mo1 at 2a and Mo2 at 6c were refined. The reported uncertainties are the statistical uncertainties obtained from the GSAS refinements and, for derived quantities, from numerical propagation of such uncertainties.

4.2.2.6 EXAFS analysis

Oxidation state and local structure were further probed by XAS, including both X-ray absorption near edge structure (XANES) and extended x-ray absorption fine structure (EXAFS) measurements. Experiments were performed at beamline 5BM-D at the Advanced Photon Source at Argonne National Laboratory. Data were collected at the Mo K-edge (20000 eV). Powder samples were uniformly spread on tape and measured in transmission mode. All samples were calibrated to a Mo metal foil measured in-line during each sample measurement. Data reduction and analysis were performed using the Demeter software package.[187]

4.3Cubic Molybdenum Oxynitrides | C700 and C800 samples (Results and Discussions)

4.3.1 Physical and Chemical Analysis.

The nitridation process of MoO_3, converted the light green oxide, which consisted of platelet shaped crystallites tens of micrometers in length, into a black powder with metallic luster, consistent with the metallic nature of molybdenum nitrides, Figure 4.3-1. The characteristics of the resulting C700 and C800 materials (prepared by reaction at 700ºC and 800ºC K, respectively) are summarized in Table 4.3-1 , with representative electron microscopy images presented in Figure 4.3-2. In Table 4.3-1 and hereafter, a number in parentheses following a reported measured value indicates the uncertainty in the final digit(s), and is given in the range from 1 to 9, with the exception of crystallographic parameters, for which the uncertainty is reported in the range from 2 to 19. As evident from Figure 4.3-2, the reaction generally preserved the original shape of the micron-sized oxide. Despite the apparently smooth particle morphologies, the specific surface areas of the nitrided products were 135(2) m^2/g and 47.7(3) m^2/g,

respectively, for C700 and C800 (Table 4.3-1), much higher than the 1 m^2/g to 2 m^2/g of the precursor MoO_3. Upon repetition of the synthesis and BET characterization, respective values of 111.9(7) m^2/g and 70.3(3) m^2/g were obtained (Appendix B.8, Table B.8-3). An increase in surface area from precursor to product is common during ammonolysis of MoO_3 at 700°C, and is attributed to the topotactic nature of this pseudomorphic transformation with a concomitant decrease in density.[118, 121, 149] Slight differences in features are evident between the two materials in the SEM images in the form of large pores and depressions on the surface of C800 (Figure 4.3-2b), which are absent from C700 (Figure 4.3-2a).

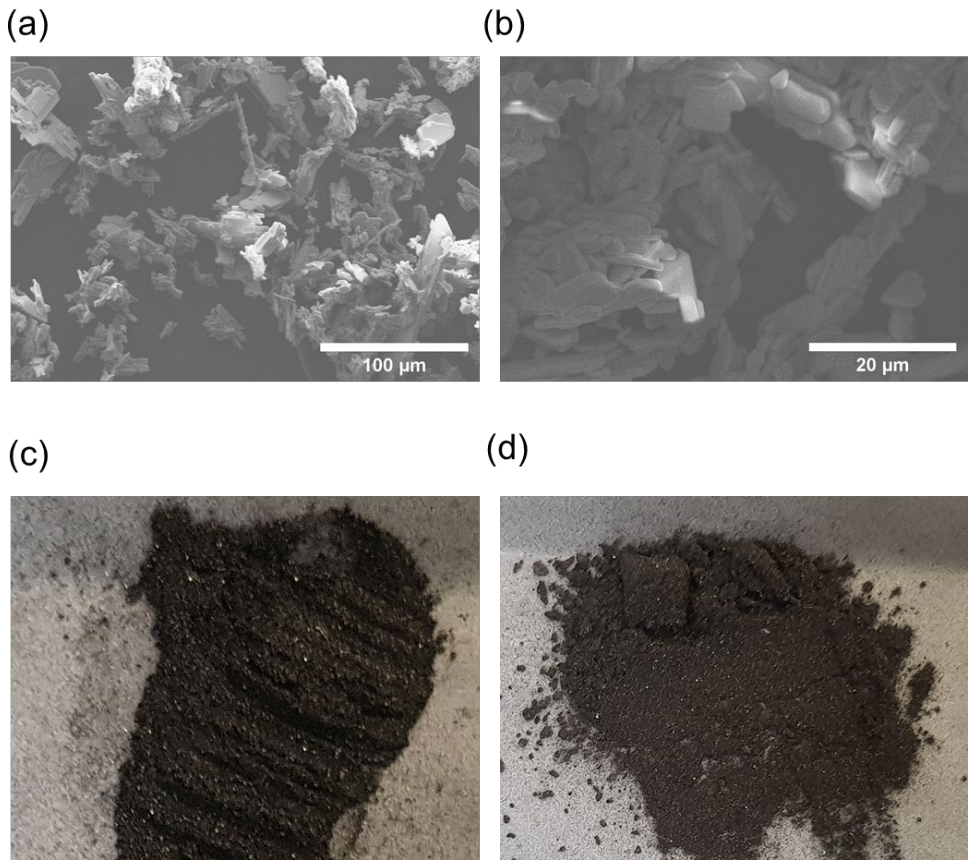

Figure 4.3-1 Images of precursor and product materials: (a,b) SEM images of the commercial precursor MoO_3 used for the preparation of nitrided materials. Due to the non-conductive nature of MoO_3, the image quality is degraded by charging effects. (c,d) Optical images, respectively, of C700 and C800 showing metallic luster of both materials. The edge of each image is ≈ 1cm.

Table 4.3-1 Summary of results of characterization of materials produced by ammonolysis of MoO_3 at 700°C (C700) and 800°C (C800). Estimated uncertainty in the final digit(s) of the reported values are provided in parentheses. See text for methods of uncertainty determination.

	C700	C800
Chemical Analysis		
EELS Analysis		
Elements detected	Mo, N and O	Mo, N and O
Mo edge peak	398.4(4) eV	396.8(4) eV
N edge peak	401.6(4) eV	400.4(4) eV
Thermal XPS spectra		
Elements detected	Mo, N and O	Mo, N and O
Binding Energy (BE) for $Mo^{\delta+}$	229.3(1) eV	228.9(1) eV
Combustion Analysis		
Absolute N content, as-synthesized	11.1(3) mass %	10.1(3) mass %
Absolute N content, surface-desorbed	10.1(3) mass %	9.2(3) mass %
Absolute H content, as-synthesized		
Absolute H content, surface-desorbed	0.8(3) mass %	0.4(3) mass %
	0.4(3) mass %	0.1(3) mass %
PGAA Analysis		
Mo: N atomic ratio	1.05(3)	1.13(3)
Mo: H atomic ratio	1.19(3)	2.53(6)
Deduced from TGA		
Atomic Fraction O/ (O + N)	0.18-0.28	0.13-0.22
Atomic Anion/Cation ratio	0.97-1.14	0.82-0.93
Structural Characterization		
BET Measurement		
Surface Area	135(3) m^2/g	47.7(3) m^2/g
Pore Size(s)	3.6(1) nm	3.4(1) nm, 8.7(1) nm (bimodal)
Pycnometry: Measured density	5.0783(1) g/cm^3	5.6307(1) g/cm^3
Diffraction Co-refinement Results		
Crystallographic formula	$Mo_{0.775(2)}(N_{0.75},O_{0.25})$	$Mo_{0.790(1)}(N_{0.729(5)},O_{0.062(1)})$
Theoretical Density	8.06(2) g/cm^3	7.68(1) g/cm^3
Mo:N molar ratio	1.033(3)	1.084(1)
N	11.82(3) mass %	11.73(1) mass %
Mo	83.7(2) mass %	87.1(1) mass %
Atomic Fraction O/ (O + N)	0.25	0.078(1)
Atomic Anion/Cation ratio	1.290(4)	1.000(1)
Lattice Parameter	4.18426(8) Å	4.22154(7) Å

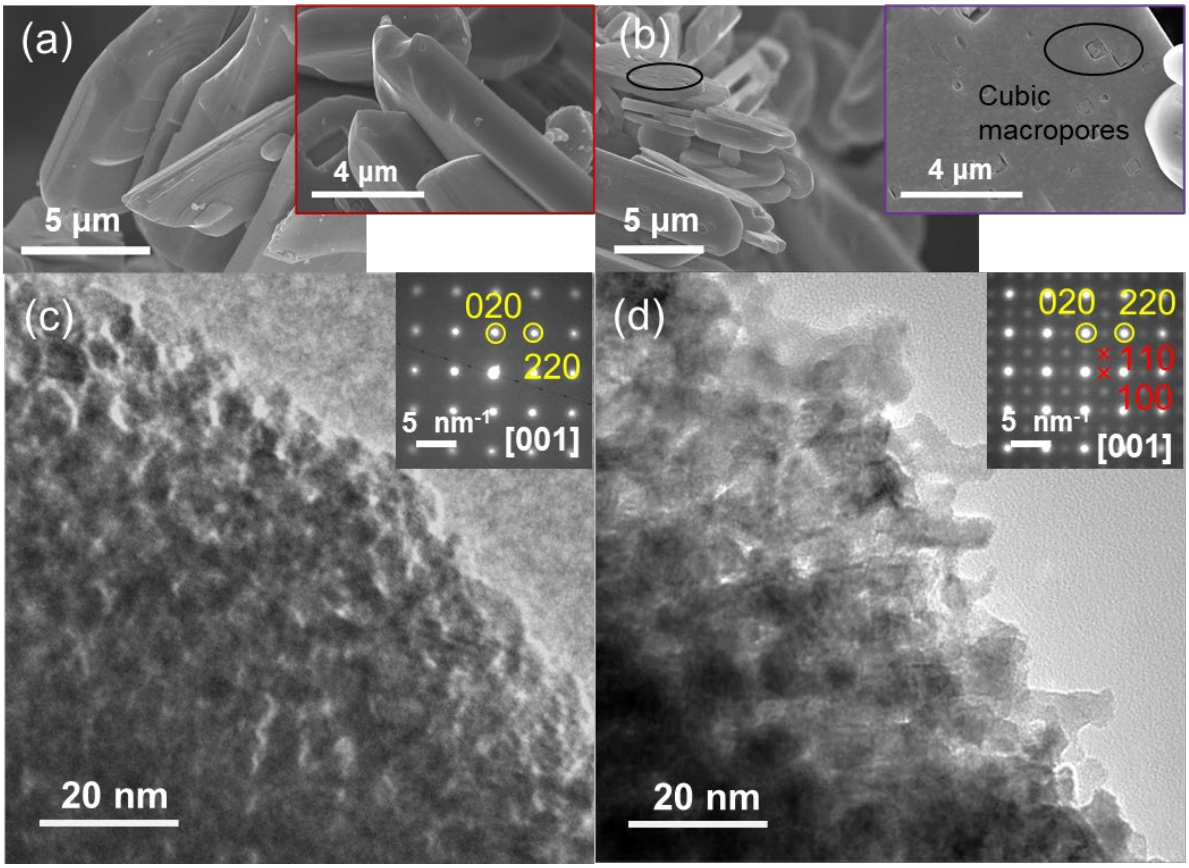

Figure 4.3-2 Electron microscopy images from the products of ammonolysis of MoO_3: (a,c) Scanning and transmission electron images, respectively, of C700; and (b,d) analogous respective images of C800. Insets in (a) and (b) show enlarged SEM images whereas those in (c) and (d) show SAED patterns. Large crystallites in both materials are mesoporous single crystals, with nanoscale crystalline regions (7-8 nm in C700 and 10-15 nm in C800) retaining crystallographic registry over the length scale of the original trioxide precursor particle. The C800 material additional features pores that are tens of nanometers on edge. The SAED indexing and nanoscale features agree with the XRD analysis. (Courtesy: TEM study by Chi Zhang, Dravid Group, Northwestern University)

The TEM images reveal a high level of nanoscale porosity within the macroscopic particles, accounting for the high specific surface area. The images further show C800 (Figure 4.3-2d) to have a generally coarser microstructure than C700 (Figure 4.3-2c). Pores in C700 separate crystalline regions that are 7 nm to 8 nm in size, whereas the crystalline regions between pores in C800 span 10 nm to 15 nm. These dimensions broadly match the crystallite sizes implied from the peak broadening in the diffraction patterns, Figure 4.3-3, 7.1(1) nm and 9.3(2) nm, for C700 and C800, respectively. The values for these specific samples used in structure refinement were in line with the respective averages of 7.2(2) nm and

9.9(6) nm obtained from analysis of multiple syntheses. Overall, no strong effect of precursor choice was observed, with all C700 samples, as shown in Appendix B.8 (Figure B.8-9). Rather remarkably, the large, mesoporous particles visible in the SEM and TEM images of both C700 and C800 are single crystals, as evident from the TEM selected area electron diffraction (SAED) patterns (Figure 4.3-2c, d insets). These were obtained using selected area aperture with an effective diameter up to ≈ 600 nm, and every region within the same particle (several micrometers in lateral dimensions) exhibited the identical diffraction pattern. These patterns reveal the cubic nature of the two materials, and also show the crystal structures to be distinct. Beyond occasional detection of isolated amorphous molybdenum oxide particles, no impurity phases were revealed by the TEM studies.

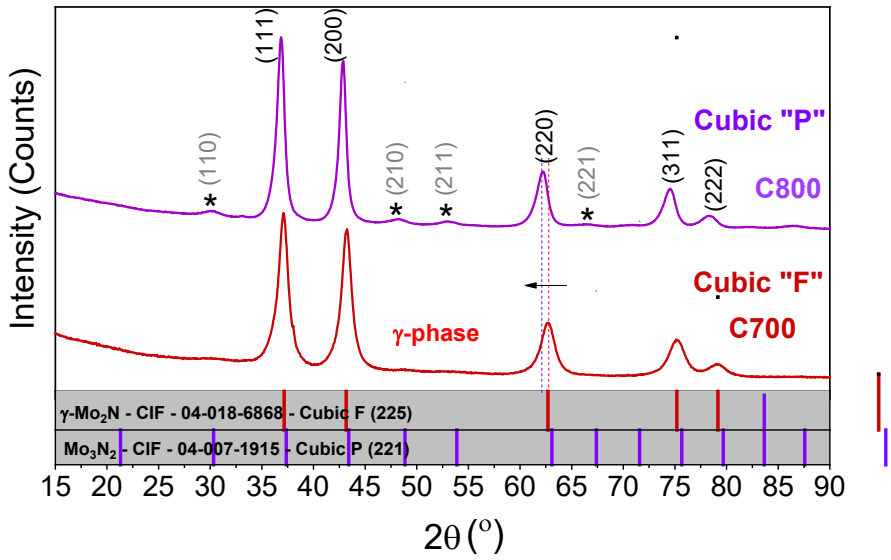

Figure 4.3-3 Representative lab XRD patterns of C700 (lower) and C800 (upper) collected with Cu Kα radiation (λ = 1.5406 Å). Diffraction peaks of mixed *h k l* parity, required to be absent for a face-centered cubic lattice, have finite intensity in the pattern of C800. The patterns are further differentiated by the narrower peaks, indicative of a larger crystallite size, and by the larger lattice constant of the C800 material.

In agreement with the electron diffraction result, the lab XRD patterns, Figure 4.3-3 and few figures in Appendix B.8 (Figure B.8-2, Figure B.8-3 and Figure B.8-4), of the C700 and C800 materials match, at least to a first approximation, the respective patterns reported for γ-Mo_2N (JCPDS No: 04-018-6868, space group *Fm*$\bar{3}$*m)*, and for Mo_3N_2 (JCPDS No: 04-007-1915, space group *Pm*$\bar{3}$*m)*. The peaks that are systematically absent from the pattern of the C700 material (*h*, *k*, and *l* mixed even and odd) are weak in the pattern of C800, but are nevertheless detectable, consistent with the space group characteristics. The SAED patterns collected along the [001] zone axis for both materials similarly show non-zero intensity for peaks of mixed parity in the C800 material (Figure 4.3-2d, inset), whereas this class of peaks is completely absent in the pattern of the C700 material (Figure 4.3-2c, inset). Furthermore, the C800 lattice parameter is measurably larger than that of the C700 material. The present results are in agreement with the observations of Tagliazucca *et al.*,[115] who reported that the *Pm*$\bar{3}$*m* superstructure peaks appear when ammonolysis is carried out at 800ºC . Here, the weak superstructure peaks were always detected in materials synthesized at an ammonolysis temperature of 800ºC, while careful examination of the patterns of several C700 materials, (Appendix B.8, Figure B.8-3), indicated that even after ammonolysis at 700ºC, superstructure peaks can occasionally be detected. In addition to being extremely weak, these peaks were found, in all cases, to be much broader than the substructure peaks, suggesting they could be easily overlooked.

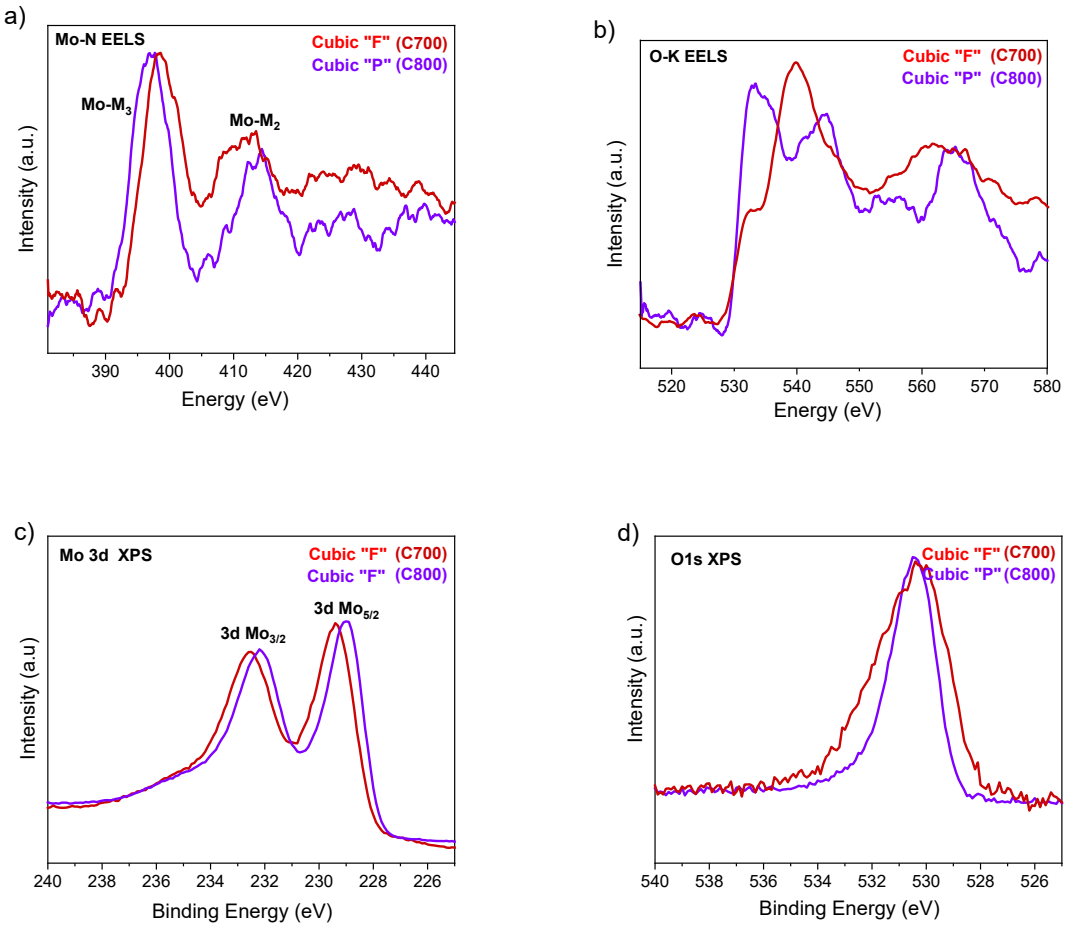

Figure 4.3-4 Spectroscopy studies of the products of ammonolysis of MoO_3: (a,b) EELS measurements; and (c,d) XPS measurements, with spectra for C700 in red and those for C800 in purple. Vertical scales of the C700 and C800 scans were normalized to match the backgrounds and the maximum peak heights. Features of the electronic structure about the Mo $M_{2,3}$ or Mo 3d edge are shown in (a) and (c), whereas those about the O-K or O1s edge are shown in (b) and (d). The oxygen ELNES (b) reveal that bulk oxygen is retained in both materials, whereas the electronic structure about Mo (a,c) reveal that Mo is more reduced after ammonolysis at 800°C than at 700°C. (Courtesy: EELS study by Chi Zhang, Dravid Group, Northwestern University)

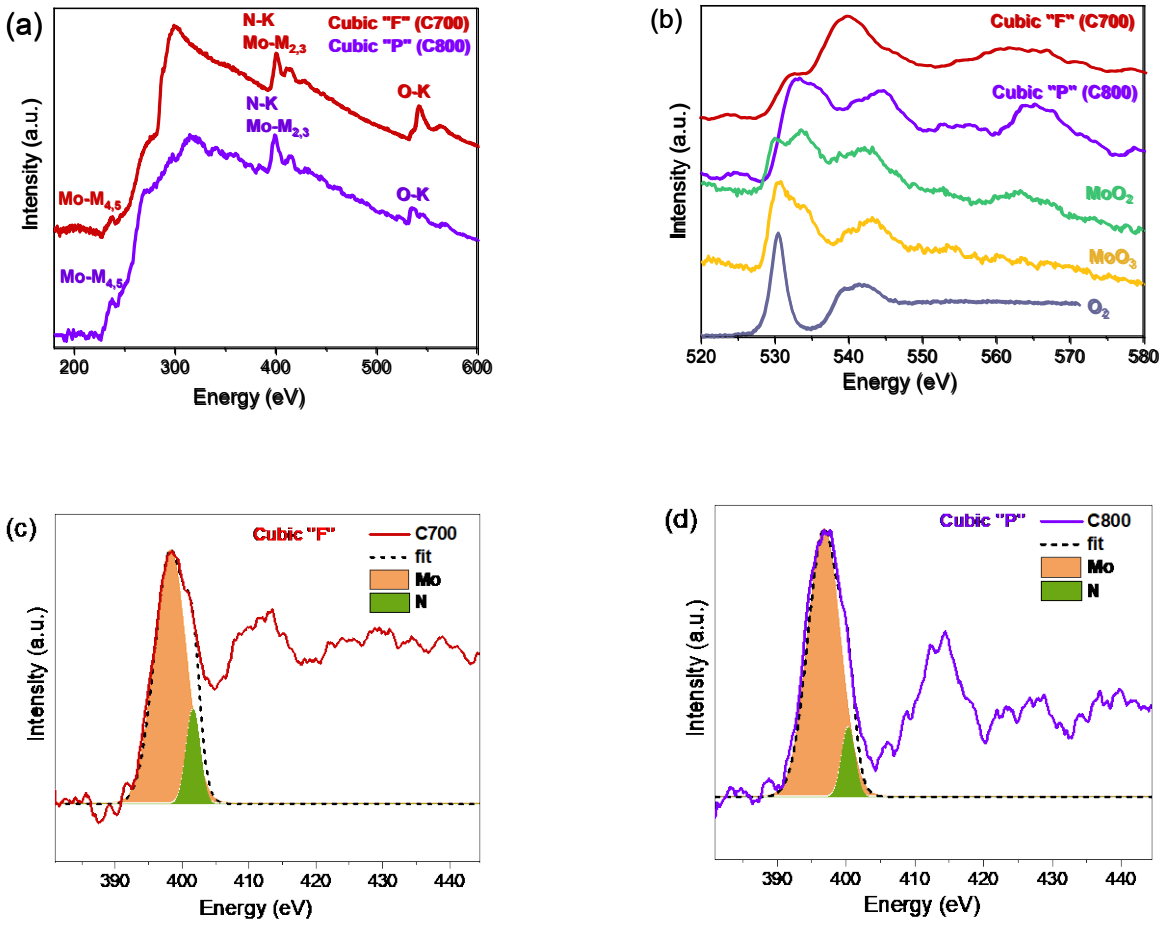

Figure 4.3-5 EELS spectra collected from C700 and C800 materials: a) complete spectra from 190 to 600 eV revealing presence of Mo, N and O; b) spectra in the O-K edge region, shown in comparison to those of oxygen gas, MoO_2 and MoO_3 - distinctiveness of spectra from those of the materials of the present study indicate the presence of oxygen in the bulk of the C700 and C800 materials; and peak fitting of Mo and N ELNES spectra for c) C700 and d) C800. (Courtesy: EELS study by Chi Zhang, Dravid Group, Northwestern University)

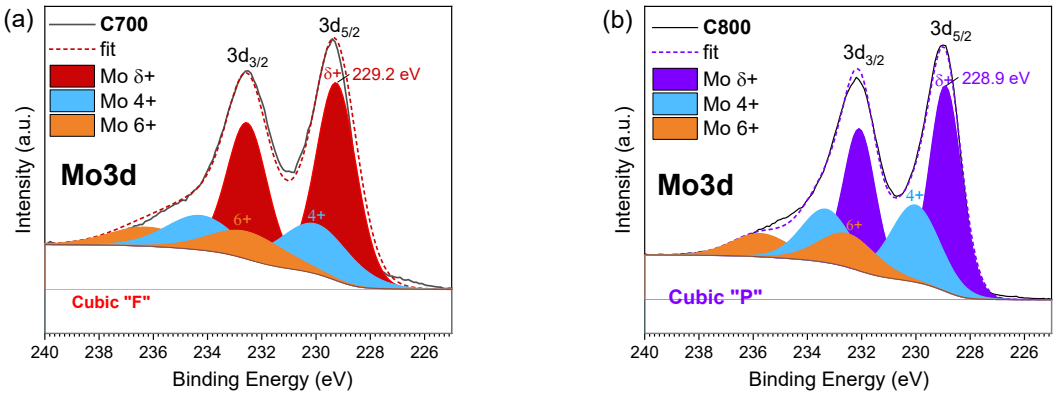

Figure 4.3-6 X-Ray photo electron spectroscopy Mo3d scan collected for a) C700 and b) C800. Peak deconvolution of Mo3d spectra was performed using three sets of doublet peaks corresponding to $Mo^{\delta+}$, Mo^{4+}, and Mo^{6+} (details in Table 4.3-2).

Table 4.3-2 Features of the Mo3d peaks detected by XPS

	C700	C800
BE for $Mo3d_{5/2}$ (eV)		
$Mo^{\delta+}$	229.3(1)	228.9(1)
Mo^{4+}	230.0(1)	230.1(1)
Mo^{6+}	232.5(1)	232.6(1)
Peak Area (Cps.eV)		
$Mo^{\delta+}$	125,018	110,175
Mo^{4+}	32,794	88,865
Mo^{6+}	28,654	29,650

The phase identification based on the diffraction data, which generally indicated consistency with the pattern of "Mo_2N", could easily be interpreted to signify that only Mo and N are present in the materials synthesized here. However, the EELS measurements, Figure 4.3-4, unequivocally revealed the presence of oxygen within the bulk of the ≈ 50 nm thick particles, along with N and Mo. In particular, the distinctiveness of the features of the O_K ELNES (Energy Loss Near Edge Structure) spectra, especially those of the C700 material, demonstrate that the oxygen detected cannot originate from either surface oxides or the gas phase (Figure 4.3-5).[188] Furthermore, as evident from the high resolution TEM imaging and SAED, the particles are free from structurally distinct surface phases (a surface oxide would be

expected to be amorphous[189]). In the case of the XPS data, which unlike EELS, is dominated by the surface region of the material, the possibility of residual surface species of oxygen and/or H_2O remaining after thermal treatment at 250°C and contributing to the response cannot be ruled out. However, the high intensity of the measured O1s signal, with an integrated intensity approximately 1/3 of that of the Mo signal, suggests that bulk oxygen has been detected in addition to that at the surface. Quantification of the composition by XPS was precluded by the presence of surface species (as revealed by the TGA studies), along with the overall roughness of the samples and the overlap of N and Mo peaks.

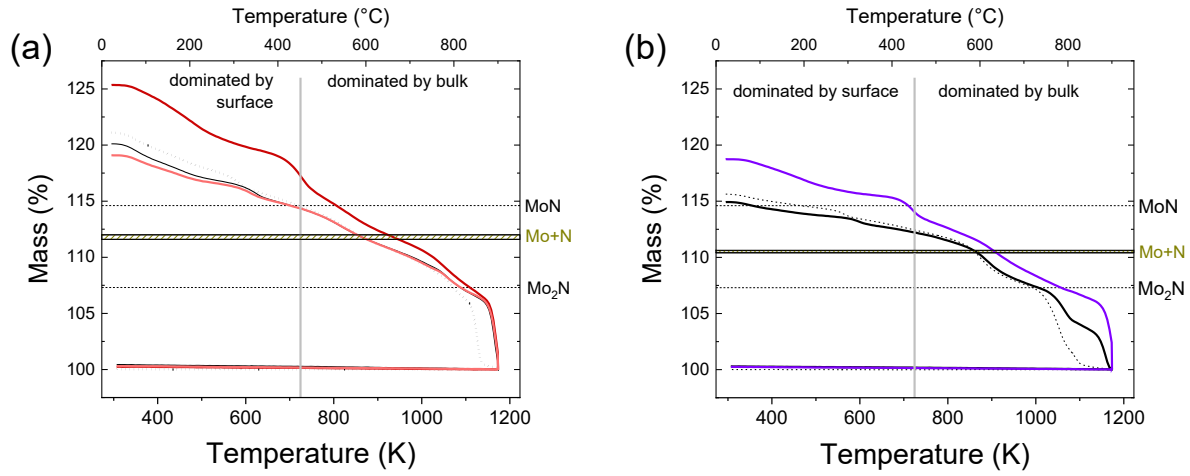

Figure 4.3-7 TGA mass loss profiles under dilute hydrogen (solid lines, 3% H_2; dashed lines, 7% H_2) for (a) C700 and (b) C800 materials obtained using samples 50 mg to 75 mg in mass and a heating rate of 5 K/min. Data shown include those from samples showing maximum and minimum mass losses under 3% H_2. The masses are normalized to 100% upon completion of reduction in recognition of the variable surface mass content. Horizontal lines indicate the masses of ideal Mo_2N, ideal MoN, and the mass range implied by the combustion analysis determination of the N content. A change in gas atmosphere from 3% to 7% H_2 (with profiles recorded using material from the same synthesis batch, black curves) has negligible impact on the mass loss behavior at temperatures below ≈ 1023 K.

Significantly, the electronic states of all three elements, Mo, O, and N, differ noticeably between the two cubic sample materials, as revealed by the EELS edge energies and XPS binding energies summarized in Table 4.3-1. The white line maximum of Mo in the MoM2,3 ELNES spectrum of C800 is shifted to lower energy than in C700 (Figure 4.3-4), as is the doublet peak in the Mo3d region of the XPS spectrum (Figure 4.3-4). These features indicate that the Mo is more reduced after ammonolysis at 800°C than at 700°C. In the XPS results, the $Mo^{\delta+}$ species accounted for 68 % and 50 %, respectively, of the total Mo3d

intensity in the spectra of C700 and C800 (Figure 4.3-6, Table 4.3-2), outweighing contributions from Mo^{6+} and Mo^{4+}. Thus, the $Mo^{\delta+}$ signature was taken to reflect the Mo in the bulk. The $Mo^{\delta+}$ peak positions of 229.3(1) eV (C700) and 228.9(1) eV (C800) correspond in both materials to an Mo oxidation state of ≈ +3, according to the correlation between BE and oxidation state reported by Choi and Thompson.[190] The Mo^{4+} and Mo^{6+} species are attributed to residual surface species, likely trapped at the interfaces between individual particles in the pressed compacts. A very slight shift towards higher energy in the XANES spectra is also visible, Figure 4.3-9, but in this case the effect is almost within the margin of experimental error. For both materials, the position of the adsorption edge indicates an Mo oxidation state lying between the 4+ value of MoO_2 and the 0 value of metallic Mo. In the EELS measurements, which as noted, reflect the oxygen in the bulk, a dramatic difference in spectral features in the oxygen region of C700 and C800 is evident. This result suggests significant differences in the near-neighbor environments about oxygen in the two materials. The EXAFS measurements indicate an analogous dramatic difference in the near neighbor environment about Mo, Figure 4.3-10. In the XPS spectra, Figure 4.3-4, a slight broadening of the O1s peak is evident for the C700 material. However, the overall similarities between the two materials is consistent with an oxygen signal highly influenced by surface species. In sum, the spectroscopic studies reveal the presence of bulk oxygen, demonstrate that Mo in C800 is slightly more reduced than in C700, and that the local structure differs substantially between the two.

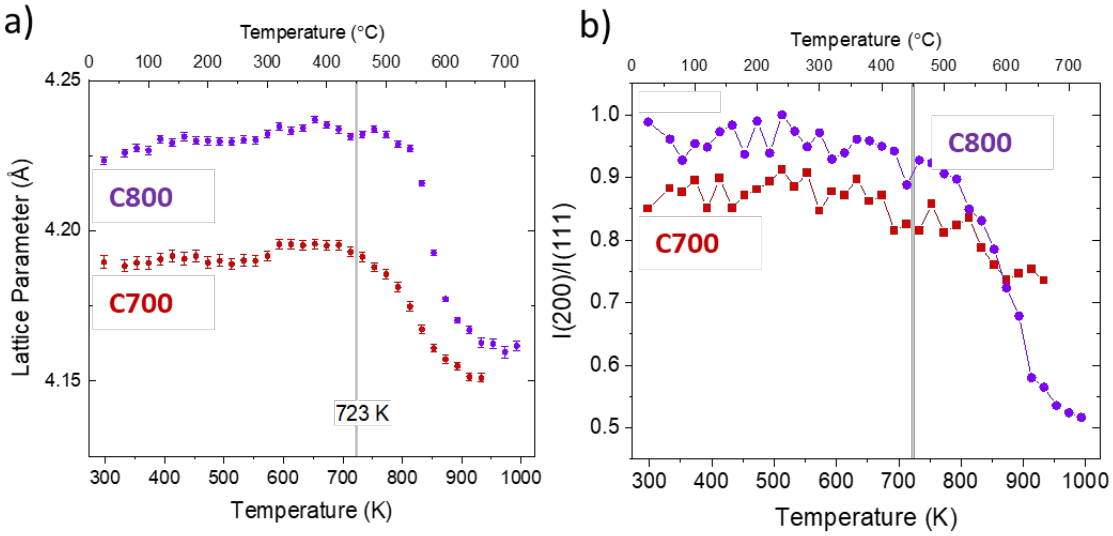

Figure 4.3-8 (a) Lattice constant of C700 and C800 materials (as indicated) upon heating under 7% H_2 (balance He) at a heating rate of 2°C/min. Under these conditions, both materials are fully transformed to Mo at 780°C. The onset of apparent cell contraction at ≈ 450°C is taken to be indicative of bulk changes in composition. This coincides with a slight decline in the (b) intensity ratio of the (200) to (111) peaks

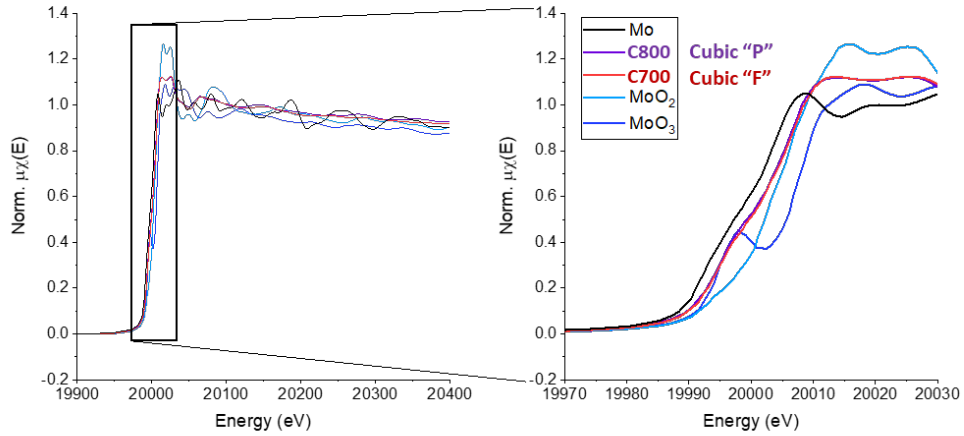

Figure 4.3-9 XANES spectra about the Mo K-edge in C800 and C700 materials, and in several reference materials. A very slight shift towards higher energy in C700 relative to C800 suggests a slightly higher Mo oxidation state in the former. (Courtesy XANES study : Elise Goldfine, Haile Group, Northwestern University)

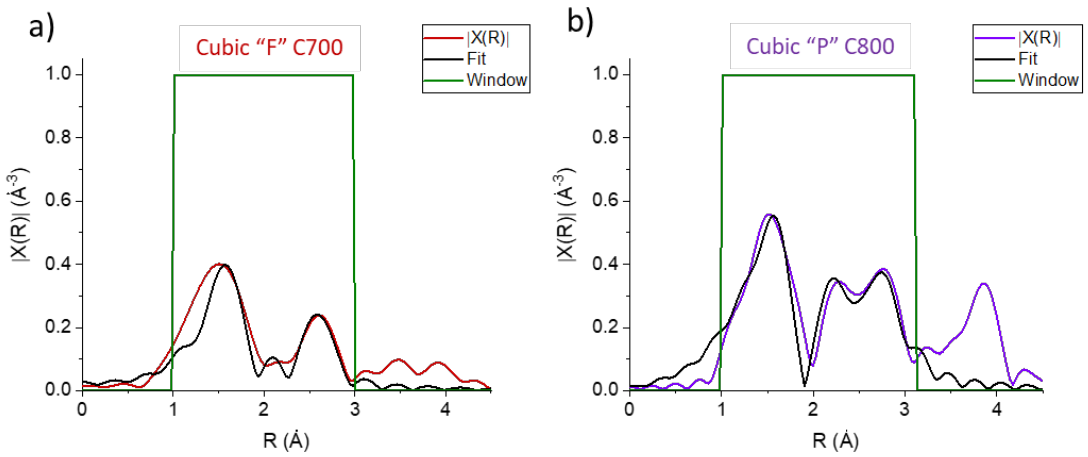

Figure 4.3-10 Fourier transforms of the Mo K-edge EXAFS spectra of the (a) C700 and (b) C800 materials, with crystallographic parameters corresponding to the fit curves summarized in Table 4.3-3. Similarly low coordination numbers of the Mo species in "γ-Mo_2N" have been reported by Pande[191] and by Kreider[167]. (Courtesy EXAFS study : Elise Goldfine, Haile Group, Northwestern University)

Table 4.3-3 Coordination numbers and interatomic distances from Mo as determined by EXAFS

	C700		**C800**	
Nearest Neighbor	**CN**	**Distance, Å**	**CN**	**Distance, Å**
O/N	2.1	2.15(3)	3.5	2.11(3)
Mo	1.4	2.88(12)	2.5	2.64(2)/2.91(7)

The TGA profiles for the complete reduction experiments, can be seen in Figure 4.3-7. More TGA plots categorized by samples synthesized from difference precursor vendors, which seemed to effect the overall mass loss, are shown in Appendix B.8 (Figure B.8-5 and B.8-6 with their analysis summary in Table B.8-1 and B.8-2 for C700 and C800 samples respectively). TGA revealed nearly continuous mass loss from the initiation of the thermal treatment to approximately 850°C, at which a sharp, final mass loss occurred. The representative profiles reflect the span of behaviors observed for the two respective materials. The total mass loss ranged from 19(2) to 25(3)% of the Mo mass for C700 materials, whereas it ranged from 15(2) to 19(2)% for C800. The profiles do not display any obvious plateaus that could enable

definitive distinction between features reflecting loss of mass from the surface vs that from the bulk. Nevertheless, it is immediately evident that the mass loss is inconsistent with materials of ideal bulk composition Mo_2N or even, in the case of C700, MoN. That is, the losses are substantially greater than what Mo_2N or MoN would yield. For example, for the C700 material to correspond to the ideal stoichiometry of Mo_2N, all of the mass loss up to ≈820°C would have to be due to surface species. In the case of C800, this temperature is slightly lower, ≈ 750°C , but is still very high for bulk stability. The in-situ diffraction experiments under 7%H_2/ bal He, Figure 4.3-8a), revealed that changes in bulk diffraction features, beyond simple thermal expansion, initiated at ≈ 450°C, indicating that the bulk is anion-rich relative to Mo_2N. On heating beyond 450°C, cell contraction was observed for both C700 and C800, along with a decline in the I(200)/I (111) peak intensity ratio, Figure 4.3-8b). The significant difference in lattice parameter between C700 and C800, well outside of the range of experimental uncertainty, further underscores the distinction between the two materials. With mass losses below ≈ 450°C attributed largely to surfaces species, it is evident that such species constitute a greater proportion of the mass of C700 than of C800, consistent with the higher specific surface area of the former.

Turning to the quantitative chemical characterization, the combustion analysis indicated absolute N contents in as-synthesized C700 and C800 of 11.1(3) mass % and 10.1(3) mass %, respectively (Table 4.3-1), as averaged over measurements of three distinct samples. After surface desorption, the N contents decreased slightly, to 10.1(3) mass % and 9.2(3) mass %, respectively. The total mass (of Mo and N) implied by the combustion analysis is indicated on the TGA profiles, where the range results from the range in initial masses relative to the final, Mo-only mass. Presuming the treatment under Ar at 400°C has removed the majority of the surface species, the result, along with the total mass change up to indicates that 30 % to 40 % of the mass lost by desorption from C700 is due to nitrogen. In the case of C800, the proportion is 40 % to 55 %. Thus, residual NH_3 accounts for a significant, but not dominant, fraction of the surface species in the as-synthesized material. The PGAA analysis, Figure 4.3-11, Table 4.3-1, revealed Mo:N molar ratios of 1.05:1 and 1.13:1, for as-synthesized C700 and C800, respectively, which are entirely consistent with the combustion analysis. The PGAA additionally revealed high

hydrogen concentrations in both as-synthesized materials, particularly the C700 material. The result is consistent with the combustion analysis, which, although close to the hydrogen detection limit, suggests a higher concentration of H in C700 than C800. While some of difference is likely due to the differences in the quantities of surface adsorbed species, NH_3 and possibly H_2O, (Figure 4.3-7), the difference is too large to be accounted for in this way. Thus, it can be concluded that C700 and likely also C800 retains hydrogen in the structure.

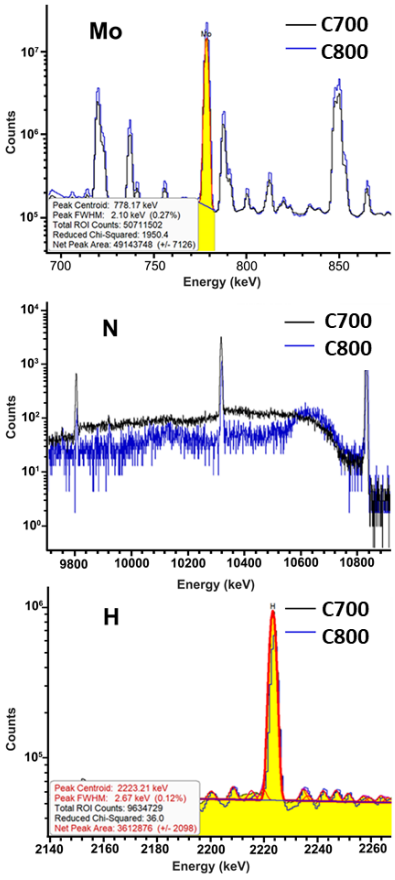

Figure 4.3-11 PGAA spectra in the (a) Mo, (b) H, and (c) N regions from C700 (black) and C800 (blue). For nitrogen, 3 peaks were used (primary photopeak and the two escape peaks) to achieve good statistics. The counting time for C800 was about 4.5 times longer than for C700. (Courtesy PGAA study : Rick L Paul, and Heather Chen-Mayer, NIST)

The most significant feature of the chemical analyses is the clear evidence that the sum of the Mo and N contents do not account for the total sample mass. This can be seen in TGA profiles, in which this sum lies below the measured mass curve until a temperature of about 650ºC in the case of C700 and of

about 600°C for C800, well into the regime at which bulk changes occur. This behavior immediately implies that some other species is present in the materials. This species is presumably oxygen, as the mass of H as determined by PGAA, the only other candidate, is too small to account for this difference. Taking, on the basis of the in situ XRD results, a temperature of 450°C to be a reasonable temperature for delineating between bulk and surface loss and using the nitrogen content measured by combustion analysis of the surface desorbed materials, it is possible to estimate the bulk oxygen content. For C700 the result is 2.5 mass % to 4.5 mass %, whereas for C800 it is 1.6 mass % to 3.0 mass %. These values translate into anion molar fractions (relative to the total anion content) of 0.18 to 0.28 and 0.13 to 0.22, respectively, Table 4.3-1. From this, values for total anion to cation ratios can be deduced and are also provided in Table 4.3-1. Because of the large uncertainty in differentiating between bulk and surface mass loss, more important than the absolute values is the clear evidence that C700 is anion rich relative to C800.

A final piece of chemical information is provided by the measured densities using pycnometry, found to be 5.0783(1) g/cm^3 and 5.6307(1) g/cm^3, respectively, for the specific C700 and C800 samples for which structure refinement was performed. These values are far lower than the expected density of 9.34 g/cm^3 for ideal γ-Mo_2N, and the discrepancy is even greater for ideal rock salt MoN, with an expected density of 9.98 g/cm^3. Furthermore, the measured densities showed a wide range of values, although they were consistently larger for C800 than for C700 materials, and always smaller than the values expected for ideal γ-Mo_2N. The variation (within a given material class, C700 or C800) was found to be correlated to the MoO_3 precursor source, and uncorrelated to the lattice parameter, as discussed in Appendix B.8, Figure C.8-8 b). This result suggests that a large concentration of closed pores or possibly crystallographic vacancies, which would be inaccessible to pycnometry and (in the case of closed pores) highly dependent on the precursor morphology, contribute to the low density. Significantly, although the absolute density of C800 materials are systematically greater than those of the C700 materials, the mass per unit cell volume is greater in the latter as a consequence to the smaller lattice constant. Thus, the internal porosity and/or vacancy concentration must be greater in C800 than C700.

4.3.2 Structure Determination.

With the above insights into the chemical compositions of C700 and C800, in particular the presence of oxygen, structural refinements to simultaneously fit to the synchrotron XRD and time-of-flight ND data were undertaken. A summary of the refinement results is provided in Table 4.3-4, and the measured and final calculated patterns are presented in Figure 4.3-12, with the difference patterns presented in Figure 4.3-13. Direct comparisons of the experimental patterns of the two materials are provided in Figure 4.3-14. Two key features are evident directly from diffraction data. First, the neutron diffraction patterns, particularly those from C700, show significant background intensity, which is readily attributed to incoherent scattering from the hydrogen in the materials. Second, all of the patterns (both X-ray and neutron, and from both materials) indicate non-zero intensity of the (110), (210), and (211) peaks. In the X-ray synchrotron data, these peaks are rather weak and broad, especially in C700, but they nevertheless have non-zero intensity. Detection of these mixed *h k l* parity peaks immediately indicates that the lattice is not face centered cubic for either material. Ultimately, the best fits were obtained using space group $Pm\bar{3}m$ for both materials. The low symmetry of C700 is particularly surprising as this material appeared consistent with space group $Fm\bar{3}m$ by lab XRD and SAED, a typical result in the literature.

The distinction between space groups $Pm\bar{3}m$ and $Fm\bar{3}m$ in the present context lies largely in the chemical identities of the species residing on the pairs of sites, 1a and 3c, and 1b and 3d, Figure 4.3-15. In $Fm\bar{3}m$ the species within each pair are identical such that the translational symmetry of the FCC lattice (+0 +½ +½; +½ +0 +½; and +½ +½ +0) is obeyed. The refinement results, Table 4.3-4, show that while the 1a and 3c sites host the Mo cations, the site occupancies of these two sites differ in both C800 and C700. Analogous distinctions are evident for the 1b and 3d sites, on which the anions reside. In C700 the 1b site is preferentially occupied by oxygen, and the 3d site by nitrogen. Because of the high correlation between site occupancies, chemical identity, and displacement parameters, the final refinement was

carried out assuming complete site differentiation, full site occupancies, and equal displacement parameters at these two sites following refinements results that supported such an assignment. Realistically, some site mixing would be expected, but model insensitivity precluded precise determination of this effect. In contrast to C700, in C800 the 1b site is nearly entirely vacant, and the few anions residing on this site are nitrogen species. The 3d site is predominantly occupied by nitrogen species, and in this feature C800 and C700 are similar. Again because of the high correlation between relevant parameters, the final refinement was performed taking the 3d site to be fully occupied. Free refinement consistently resulted in an occupancy factor exceeding 1. The appearance of X-ray and electron superstructure peaks in C800 and not in C700 reflects the nature of the vacancy ordering on the cation sites. Because of the lower site multiplicity of the 1a sites, the presence of Mo vacancies on this site (C700) does not generate superstructure peak intensity at a level comparable to that generated by vacancies on the 3c site (C800). The NPD patterns, on the other hand, reveal superstructure peaks largely as a result of the anion distribution, with oxygen and nitrogen nearly fully ordered in C700 and vacancies and nitrogen species nearly fully ordered in C800. Although the structure refinement is not particularly sensitive to the low oxygen occupancy on the 3d site, the features of the C800 oxygen ELNES spectrum, Figure 4.3-5b), support the conclusion that bulk oxygen is present in the material. At the same time, the greater similarity of the C800 oxygen ELNES spectrum to those of the molybdenum oxides as compared to C700 suggests a larger relative contribution of surface oxides to the spectroscopy measurement in C800, consist with the low bulk oxygen concentration. The presence of hydrogen, the locations of which were not resolved, also presumably contributes to the NPD superstructure peak intensities, particularly those of C700. The greater breadth of the superstructure peaks compared to those of the substructure suggests the site ordering is spatially limited, and does not extend over the entire length of the crystallites. The final weighted residuals from the refinements (wRp) were 5.95 % and 9.60 %, respectively, for C700 and C800 (Table 4.3-4).

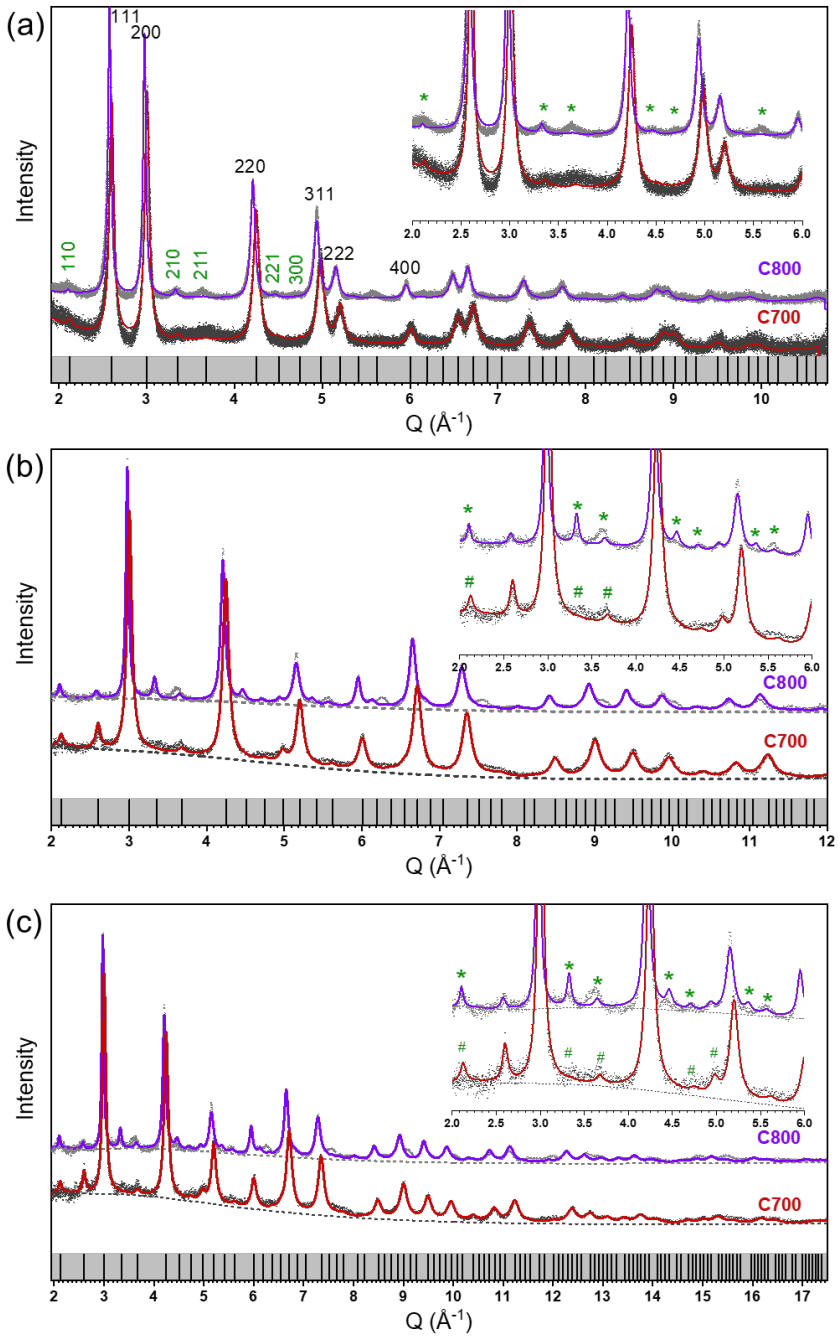

Figure 4.3-12 Measured and calculated diffraction patterns, the latter from co-refinement of the structures of C700 and C800 materials: (a) synchrotron, (b) NB1, and (c) NB2 data. For ease of comparison, data are presented as functions of Q (A$^{o\ -1}$). Measured data are shown as dots and calculations as lines. Insets in each figure shows zoomed in region from 2.0 Q (Å^{-1}) to 6.0 Q (A$^{o\ -1}$), with prominent superstructure peaks in C800 marked in *, and those of C700 marked in #. C700 shows superstructure peaks only in NPD, whereas for C800, superstructure peaks are found in both XRD and NPD patterns.

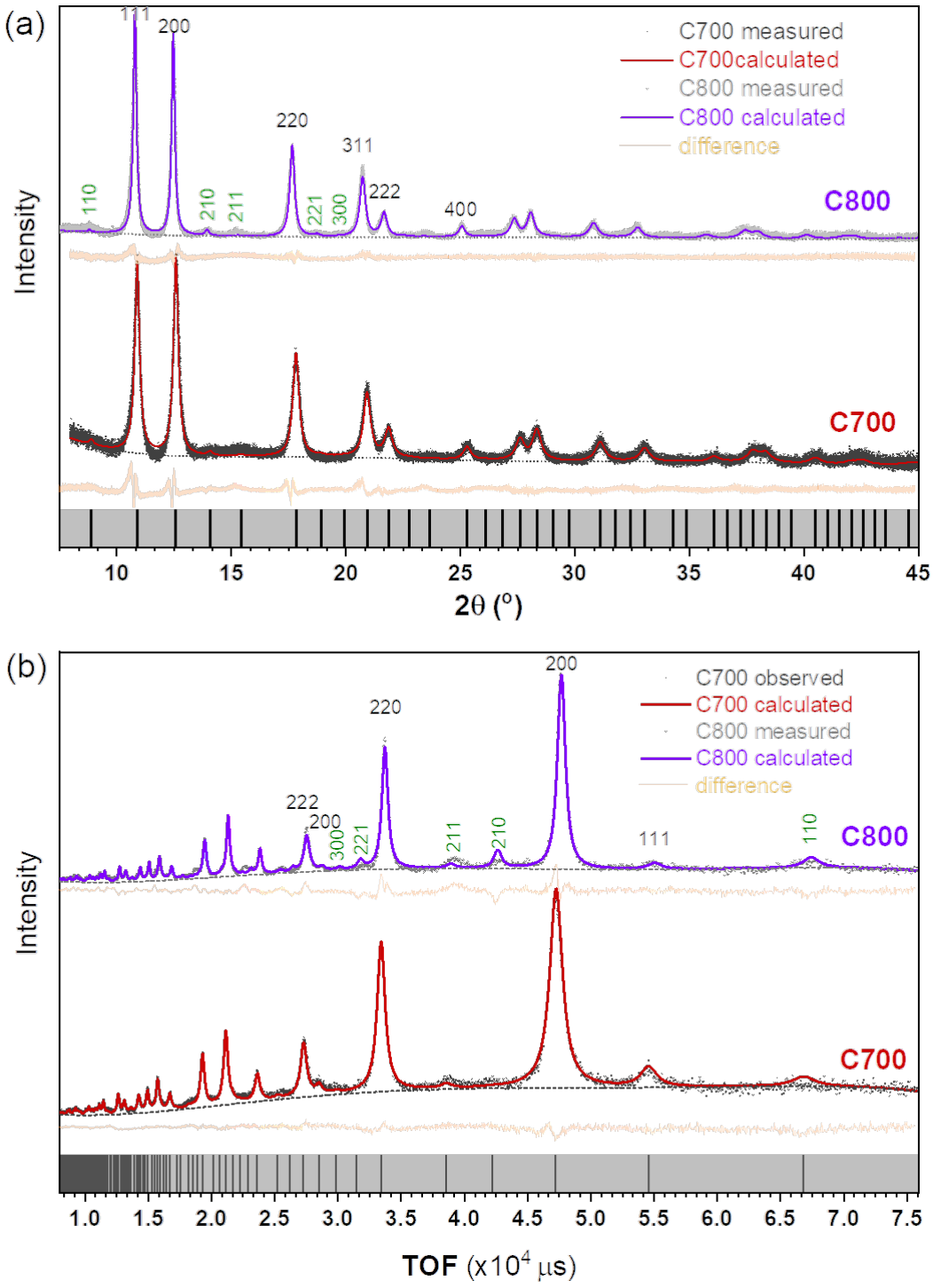

Figure 4.3-13 Measured and calculated diffraction patterns, as well as difference plots for C700 and C800 materials: (a) synchrotron data and (b) neutron data, NB1.

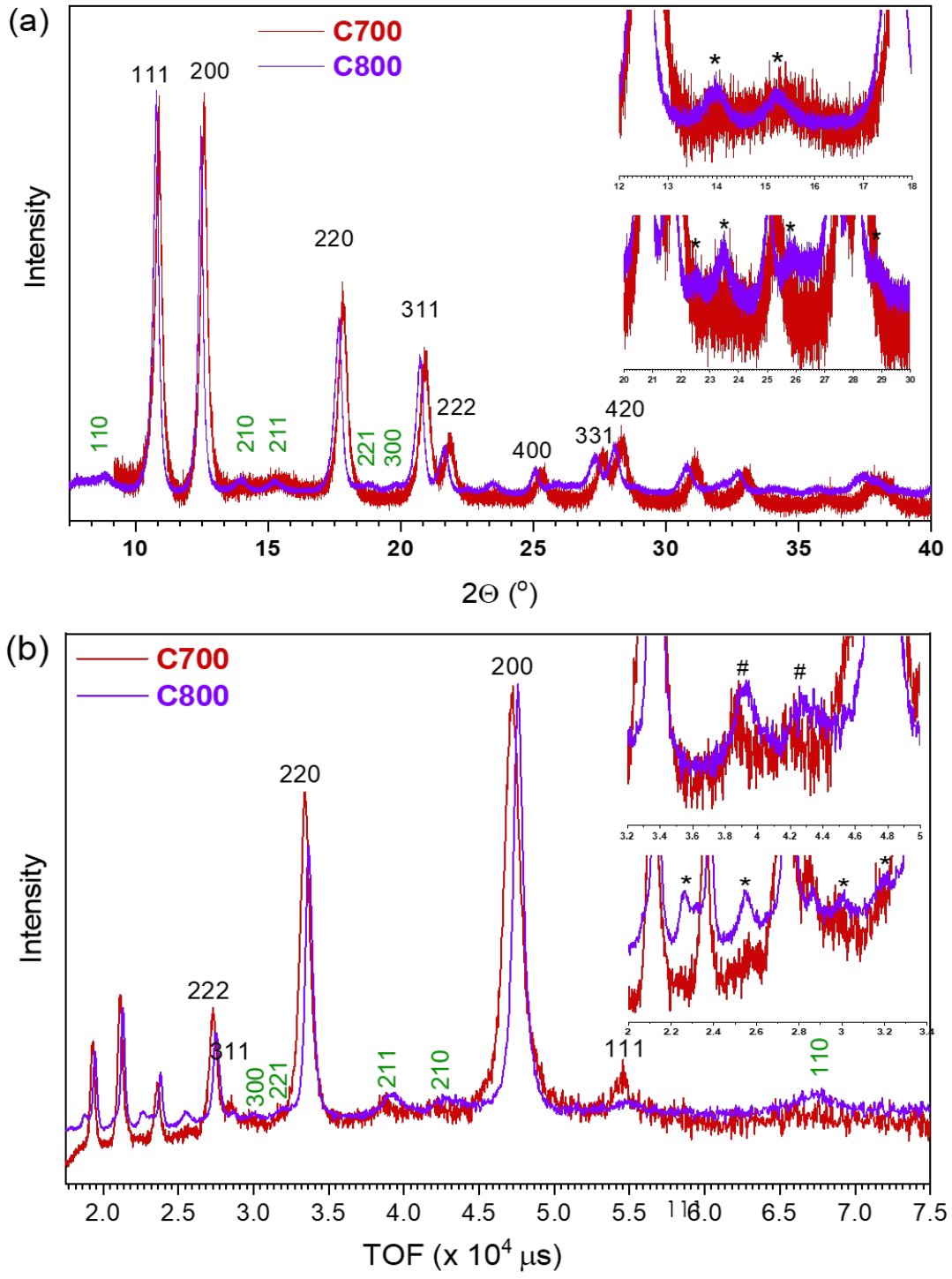

Figure 4.3-14 Direct comparisons of the diffraction patterns of the C700 and C800 materials: (a) synchrotron patterns and (b) neutron patterns (NB2). The insets highlight the regions of the most intense superstructure (mixed h k l parity) peaks.

Table 4.3-4 Atomic coordinates, site occupancies, and isotropic displacement factor coefficients for molybdenum oxy-nitride-hydrides, C700 and C800, obtained from Rietveld Analysis using combined X-ray synchrotron and neutron time-of-flight powder diffraction data. Estimated standard deviation in last digit(s) of refined parameters provided in parentheses. Following recommended practices of the International Union of Crystallographers,[192] uncertainty values are reported in the range from 2 to 19

	C700 $Mo_{0.775(2)}(N_{0.75},O_{0.25})$	**C800** $Mo_{0.790(1)}(N_{0.729(5)},O_{0.062(1)})$
Space group	$Pm\bar{3}m$	$Pm\bar{3}m$
Lattice parameter, Å	4.18426(8)	4.22154(7)
Site 1a, m3m, 0 0 0	Mo(1)	Mo(1)
Occupancy	0.559(4)	1 [fixed]
Uiso, 10^2 Å^2	0.509(8)	0.785(8)
Site 3c, 4/mmm, 0 ½ ½	Mo(2)	Mo(2)
Occupancy	0.8470(15)	0.7206(12)
Uiso, 10^2 Å^2	0.509(8) [constrained]*	0.785 (8) [constrained]*
Site 1b, m3m, ½ ½ ½	O(1)	N(1)
Occupancy	1 [fixed]	0.162(4)
Uiso, 10^2 Å^2	0.781(4)	0.531(6)
Coord. No. (6 × 3c)	5.1	4.3
Site 3d, 4/mmm, ½ 0 0	N(2)	N(2) / O(2)
Occupancy [total fixed to 1]	1 [fixed]	0.918(5) / 0.082(5)
Uiso, 10^2 Å^2	0.781(4) [constrained]*	0.531 [constrained]*
Coord. No. (4 × 3c + 2 × 1a)	4.5	4.9
Goodness of Fit	1.33	1.78
Residual wRp (%)[(a)]		
NB1	3.41 %	6.28 %
NB2	3.82 %	7.40 %
X-ray	12.71 %	14.88 %
Combined	5.95 %	9.55 %

* Displacement parameters of all anions and of all cations in a single structure constrained to equal one another.

In general agreement with the diffraction data, the EXAFS analysis (Table 4.3-3) showed the local coordination environment about the Mo in C700 to be formed of species located at distances of 2.15(3) Å and 2.88(12) Å from the central Mo atom. These correspond to the Mo-O/N and the Mo-Mo distances, determined from the refinement to be 2.09213(4)Å and 2.95872(6) Å, respectively. That the Mo-anion distance is single-valued suggests there are no distinct oxygen-rich or nitrogen-rich regions in the material. In the case of C800, a nearest neighbor distance of 2.11(3) Å is found from EXAFS, again corresponding to the Mo-O/N distance, where the anions in this case are predominantly N. The slight contraction relative to C700, despite a larger lattice constant in C800, suggests local distortions in which the atoms are displaced from the high symmetry positions. Such distortions are strongly indicated by the detection of two apparent Mo-Mo distances in the EXAFS analysis, 2.64(2) Å and 2.91(7) Å. Furthermore, slight discrepancies between the measured and calculated diffraction patterns of C800 indicate shortcomings of the solution to the C800 structure, which implies a single Mo-Mo distance of 2.98508(5) Å. Structure refinements in which the Mo atoms were moved off their respective 1a and 3c sites were attempted, but did not produce satisfactory results. Alternatively, a lower symmetry in this material may be possible, but the narrowing of peaks relative to C700 argues against a lowering of the crystal class. Refinement in space group *P*4/*mmm* (results omitted for brevity) produced only marginally better refinement statistics along with a large disagreement with the measured stoichiometry. Thus, while the general structure of C800 has been captured, resolution of the finer details awaits more focused investigations. Such studies may also explain the surprisingly low coordination numbers determined from the EXAFS analysis for both phases, Table 4.3-3.

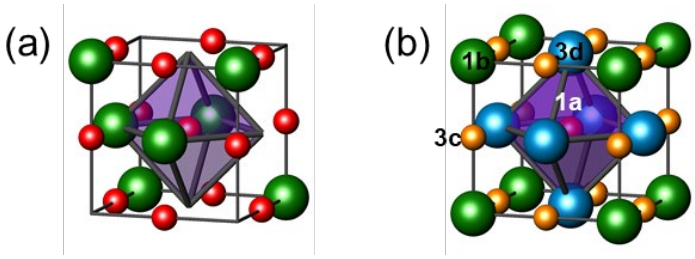

Figure 4.3-15 Structure of (a) conventional "γ-Mo_2N" with space group *Fm*$\bar{3}$*m*, and (b) the Mo-O-N-H materials identified in this work, with space group *Pm*$\bar{3}$*m*. The structures of both the C700 and C800 materials are represented in (b), and for ease of rendition, the unit cell origin is shifted by ½ ½ ½ relative to the coordinates given in Table 4.3-4. In (a), the small red spheres are the Mo atoms and the large green spheres are N atoms, with half of the N sites randomly vacant. In (b), the small central red sphere is the Mo(1) atom on the 1a site, the small yellow spheres are the Mo(2) atoms on the 3c site, the large green atoms are the N(1)/O(1) atoms on the 1b site, and the large blue atoms are the N(2)/O(2) atoms on the 3d site.

The final compositions derived from the refinements were $Mo_{0.775(2)}(N_{0.75},O_{0.25})$ for C700 and $Mo_{0.790(1)}(N_{0.729(5)},O_{0.062(1)})$ for C800, which are in general agreement with the chemical analysis. In particular, the structure analysis captures the higher anion:cation ratio in C700 than C800. Furthermore, taking the nitrogen and oxygen valences as 3- and 2-, respectively, the average oxidation states of Mo in the two materials are ≈ 3.5 and ≈ 2.9, respectively, in good agreement with the oxidation state of ≈ 3 obtained from the XPS analysis, and the conclusion of a higher Mo oxidation state in C700 arrived at from the EELS measurements. The chemical formulae noted above are written to specify the mean vacancy concentrations over the two Mo sites, the absence of vacancies on the anion sites of C700, and their presence in C800. The densities implied by the compositions, 8.06(2) g/cm^3 (C700) and 7.68(1) g/cm^3 (C800) are much larger than measured by pycnometry, Table 4.3-1. The discrepancy suggests that indeed the materials contain a large volume of closed porosity in addition to the vacancies detected by diffraction and EXAFS analysis. The higher diffraction density and lower pycnometry density of C700 suggest this material has higher internal porosity than C800, which is consistent with its higher specific surface area and morphology (Figure 4.3-2).

The overall features of the C700/C800 structures are presented in Figure 4.3-15 along with a comparison to the standard *Pm*$\bar{3}$*m* structure typically reported for "Mo_2N". For clarity, the mixed and partial occupancies are not directly indicated in the figures. Renditions of the structures presenting these details are provided in Figure 4.3-16. As noted above, the Pm$\bar{3}$m space group occurs in C700/C800

because the translational symmetry required of $Fm\bar{3}m$ is lost as a consequence of the distinction of the chemical species residing on the 1a, 3c and 1b, 3d pairs of sites, which respectively, host the cation and anion species. In conventional "Mo_2N" Mo fully occupies the cation sites, creating translational symmetry between 1a and 3c sites, and N partially occupies the anion sites, with randomly distributed vacancies, creating translational symmetry between 1b and 3d sites. The distinction between the C700 and C800 structures arises from the manner in which these pairs of sites are differentiated. In C700, vacancies occur on both of the Mo sites, whereas in C800, the 1a site on which Mo(1) resides is fully occupied and the 3b site of Mo(2) is almost 30% vacant. The distribution of anions differ even more strongly between C700 and C800, than the distribution of cations. In particular, the 1b site is almost entirely unoccupied in C800, whereas it is fully occupied by oxygen in C700. The 3d site, however, is fully occupied in both materials, either entirely or primarily by nitrogen. Notably, oxygen is incorporated into the site of higher coordination number in both materials, Table 4.3-4, where the coordination numbers differ from 6 because of the partial occupancies on the cation sites. The occupancies on the cation 3c sites translate into mean anion coordination numbers on the 1b site of ≈ 5.1 and ≈ 4.3, respectively, in C700 and C800. Analogously, the mean anion coordination numbers on the 3d site, coordinated by Mo atoms on both the 1a and 3c sites, correspond to coordination numbers of ≈ 4.5 and ≈ 4.9, respectively. The large difference in the oxygen ELNES of C700 and C800, Figure 4.3-4b), suggests differences in coordination environment, beyond the moderate difference in coordination number of the oxygen species derived from the refinement (5.1 vs 4.9).

While H atoms could not be reliably located, their presence in the materials was definitively established by the chemical analysis. It is likely these species are present as protons as Pande *et al.* have showed by X-ray absorption near edge spectroscopy (XANES) that electrochemical insertion of H into molybdenum nitride induces a slight reduction of Mo.[191] The source of H in the present materials is assumed here to be the ammonia used in the nitridation. In particular, as seen in Chapter 3 in-situ studies, it was shown that an orthorhombic molybdenum bronze (H_xMoO_3) forms along the reaction

pathway between MoO_3 and NH_3 to produce molybdenum nitrides. Such protons are apparently retained in the cubic phases.

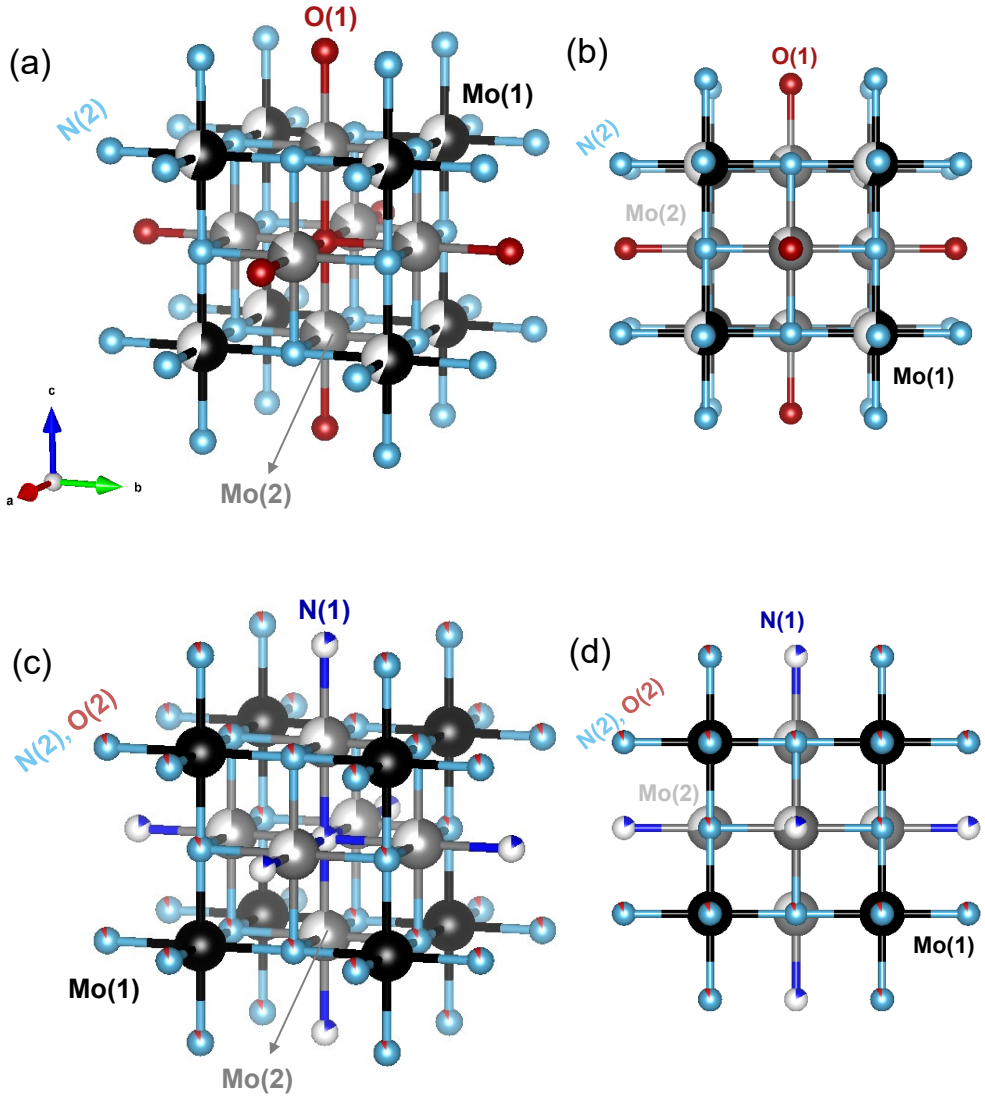

Figure 4.3-16 Ball and stick models of co-refined structures: (a,b) C700, and (c,d) C800 materials, with atom types as indicated. The two structures are differentiated (only) by the site occupancy factors. In both, Mo(1) resides at the order of the cubic unit cell and Mo(2) at the face centers. The N(1)/O(1) anions reside at the body center of the unit cell, and the N(2)/O(2) anions at the edge centers. The strongly differing occupancies at the Mo sites in the C800 structure result in X-ray and electron diffraction patterns in which the absence of face-centered-cubic lattice centering is readily detected.

Beyond a distinction in overall chemistry, the two cubic materials studied here show a slight difference in lattice constant, with that of C700 being somewhat smaller than that of C800. Such a result is also evident in the XRD patterns reported by Tagliazucca *et al.*[115] The difference in cell volumes can plausibly be attributed to the significant presence of oxygen, with a smaller anionic radius than nitrogen, in the C700 material. The decrease in cell volume on heating under hydrogen, Figure 4.3-8, indicates that anions can be lost from the structures without a complete collapse of the framework. The contraction of C700, furthermore, implies a chemical change in this material in a manner that retains its chemical distinction from C800. Thus, loss of oxygen and nitrogen likely occur simultaneously, as opposed to preferential loss of oxygen. It is of some note that Tagliazucca *et al.*[115] also reported a cell contraction at high temperature of their "$Pm\bar{3}m$ Mo_xN_y" but this case upon exposure to NH_3 and with a slightly higher onset temperature of ≈ 823K.

Based on the structure determinations, a hypothesis for the mechanism by which the C800 phase forms emerges. We first presume that the C700 structure appears along the pathway to forming the C800 phase, rather than a direct formation of the C800 material from some other precursor state. The transformation from C700 to C800 then corresponds to a loss of O and H, and to a small extent N, from the structure to generate a near stoichiometric material. The release of oxygen from the structure is accompanied by a shift in Mo position from preferential occupation of the 3c site to preferential occupation of the 1a site, as well as the creation of a notable concentration of anion vacancies. The average cation vacancy concentration, on the other hand, remains relatively unchanged. The loss of surface area and apparent loss of internal porosity in C800 are the result of high temperature coarsening.

The results obtained here for the chemistries and structures of cubic molybdenum nitride materials prepared by ammonolysis of MoO_3 are quite distinct from what is typically reported. In particular, we find that regardless of synthesis temperature (700°C or 800°C), the material is anion rich relative to "Mo_2N," the cation vacancy concentrations are substantial, and the space group symmetry is $Pm\bar{3}m$ rather than $Fm\bar{3}m$. The key chemical distinction imparted by varying synthesis temperature is the extent to which oxygen is retained, which then establishes the overall anion to cation ratio. In prior

studies, the difficulty of distinguishing N and O by XRD and electron diffraction has undoubtedly obscured the anion ordering that gives rise to space group $Pm\bar{3}m$ for materials produced at moderate ammonolysis temperatures of ≈ 700ºC. Furthermore, anion chemical analysis is relatively uncommon when the synthetic goal is the preparation of high surface area materials for catalytic studies, although some authors have detected the presence of residual oxygen.[162, 164] On the other hand, it is likely that small differences in synthesis conditions produce variations in anion to cation ratios, distinct concentrations of residual oxygen, and differing levels of anion ordering, even when the ammonolysis temperature is 700ºC. Cao *et al*., for example, employed NPD to study material similar to the C700 material prepared here and did not detect mixed parity superstructure peaks, although the possibility that the material was anion rich relative to Mo_2N was acknowledged.[155] Furthermore, these authors observed a large incoherent background, attributed, as in this work, to the presence of hydrogen in the material. In contrast to synthesis at 973K, ammonolysis of MoO_3 at higher temperature has been previously recognized to produce materials of space group $Pm\bar{3}m$, specifically, as noted above, by Tagliazucca *et al*.[115] Notably, these authors concluded (apparently from the X-ray structure refinement) that the stoichiometry of their material was $Mo_{3.2}N_{2.7}$. No NPD studies or chemical analysis have been to date reported for this phase.

In general, the perception that the stoichiometry of cubic molybdenum nitride produced from MoO_3 contains more cations than anions is pervasive in the literature. This perception appears to derive from the reported behavior of oxygen free Mo-N compounds, where it is known that stoichiometric MoN is thermodynamically more stable in a hexagonal form, the δ phase, than in the B1 rock salt structure.[107, 193] However, even in true molybdenum nitrides, both computational[193] and experimental[194] studies point towards the presence of vacancies on both cation and anion sites, with cation vacancies displaying more negative defect formation energies, as referenced to the hypothetical perfect B1 structure. Thus, detection here of materials with vacancies on the cation sites is not unreasonable. Most importantly, the comprehensive chemical analysis performed here permits no other conclusion than an anion-rich stoichiometry in materials produced by ammonolysis at the most commonly used synthesis temperature of 700ºC.

4.4 Hexagonal Molybdenum Oxynitride | "Delta Phase" | δ-phase | H700 sample – (Results and Discussions)

4.4.1 Physical and Chemical characterization

Wet ammonolysis of dark brown MoO_2 powder under 2% pH_2O at 700C for 12hrs, converts it into a black conducting delta phase (H700) powder, whose characteristics are summarized in Table 4.4-1i. SEM images in Figure 4.4-1(b), show that the reaction generally preserved the original shape of the micron-sized MoO_2 precursor (not shown here). However wet ammonolysis results in a very porous structure, with macropores visible throughout under the SEM, with surface mimicking that of an alligator skin, a morphology potentially well suited for catalysis. Such a structure could be due to high temperature corrosive action of H_2O on the surface during nitridation.[178] The specific surface area of the H700 product was measured to be 30.1(6) m^2/g, much higher than the 1 m^2/g to 2 m^2/g of the starting precursor MoO_2, however these values are much lower compared to the Cubic C700 (110-135 m^2/g) and C800 (50-70 m^2/g) samples discussed above. As discussed in Chapter 3 via in-situ XRD studies, MoO_2 wet ammonolysis to produce H700 does not produce bronze as an intermediate, which has been known to be the critical intermediate leading to high surface area γ-samples in literature,[108, 117, 121] explaining the overall lower surface area for H700 compared to C700 and C800 samples.

Figure 4.4-3 shows typical TEM images of H700 sample, further confirming a high level of nanoscale porosity within the macroscopic particles, accounting for the increase in specific surface area due to the ammonolysis process. These pores separate crystalline regions that are 33 to 34 nm in size measured from the peak broadening of the the Lab XRD pattern in Figure 4.4-1a), much larger than those observed for the Cubic C700 and C800 samples. Several Lab XRD scans from various batches of H700 used for various analysis techniques is also shown in Figure 4.4-2. Rather remarkably, the large, mesoporous particles visible in the SEM and TEM images of H700 are also single crystals just like C700

and C800 cubic phase, as evident from the TEM selected area electron diffraction (SAED) patterns in Figure 4.4-3a), inset. The selected area electron diffraction (SAED) pattern, can be indexed using the space group *P*6$_3$*mc*. More SAED patterns from different zone axes were obtained to confirm the structure (Figure 4.4-4). These patten were obtained using selected area aperture with an effective diameter up to ~620 nm, and every region within the same particle (several micrometers in lateral dimensions) exhibited the identical diffraction pattern, demonstrating the particle is single crystalline. No extra diffraction spots, spot splitting, or streaking are observed in the SAED patterns. The thickness varies across the sample because of its porous structure. A high-resolution TEM image was taken from a thinner area (marked with a box in Figure 4.4-3a). The measured interplanar d-spacings of $(20\bar{2})$, $(\bar{2}20)$, and $(02\bar{2})$ planes in HRTEM are 1.85, 2.55, 1.85 Å, respectively, as marked on HRTEM Figure 4.4-3. In general the electron diffraction result are in agreement with the lab XRD patterns, that at least to a first approximation, the H700 matches well with reported for δ-MoN hexagonal pure 1:1 stoichiometric nitride phase (JCPDS No: PDF#04-003-5713, *P*6$_3$*mc* space group *)*.

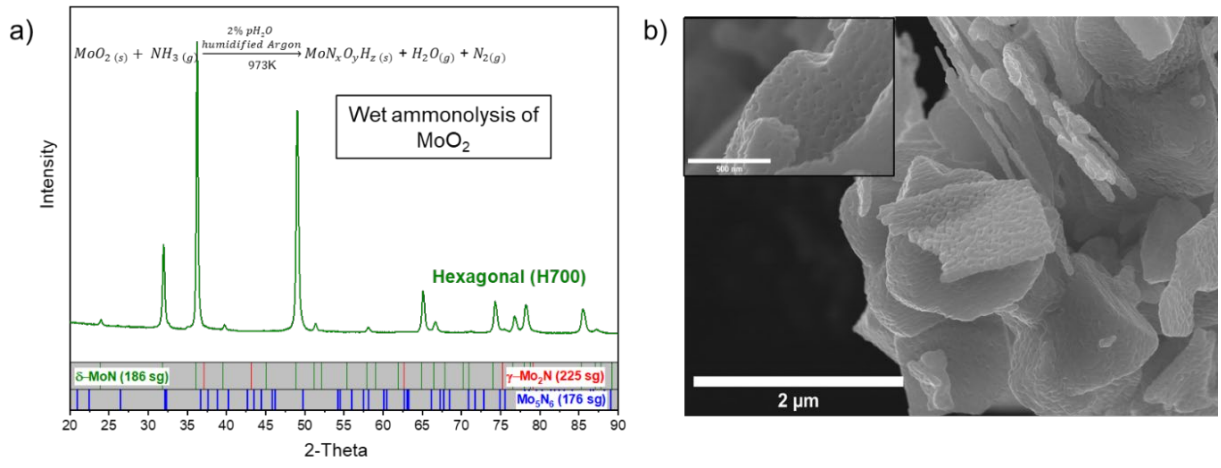

Figure 4.4-1 (a) Representative lab XRD patterns of as synthesized "Delta Phase" (H700) by wet ammonolysis (2% pH_2O) of MoO_2 at 700°C collected with Cu Kα radiation (λ = 1.5406 Å). The pattern shows no presence of competing y-phase. As shown in this study, this hexagonal wet ammonolysis product is an oxynitride hydride with MoNxOyHz type composition. (b) Scanning electron micrographs of H700 sample, showing the uniquely porous 'alligator skin' type morphology.

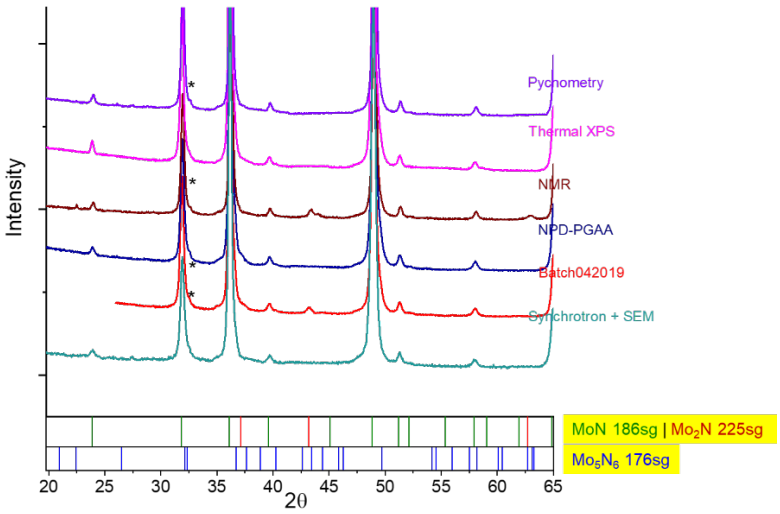

Figure 4.4-2 Lab XRD patterns of various H700 batches that were used for various analysis. Several of these batches consisted of multiple batches of H700 synthesized the exact same way, and subsequently combined together to meet the sample amount requirement for the particular technique).

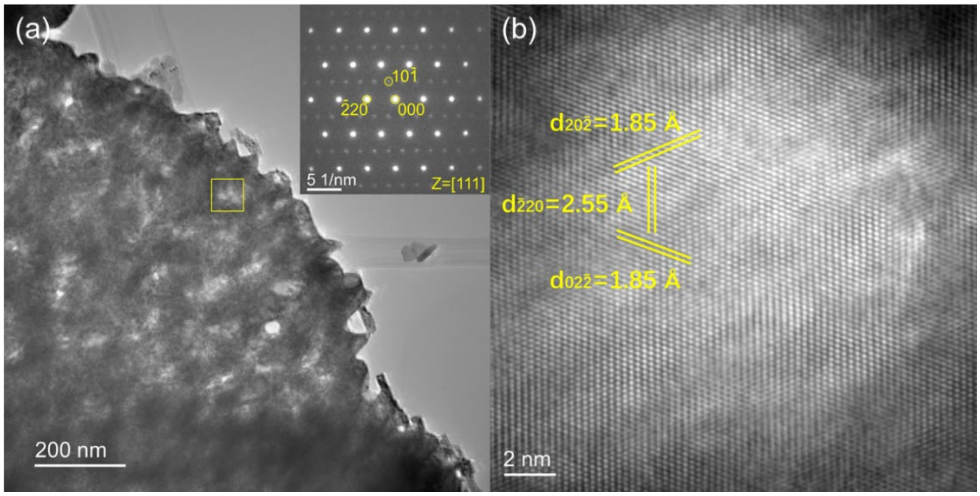

Figure 4.4-3 (a) TEM image of porous structure of the hexagonal molybdenum oxynitride with inset showing SAED pattern confirming 186sg viewed along [111] zone axis. (b) HRTEM zoomed in region circle in (a). Some lattice planes and their corresponding distances are marked in (b). (Courtesy: TEM study by Chi Zhang, Dravid Group, Northwestern University)

Table 4.4-1 Summary of Chemical and Structural Analysis of Hexagonal Molybdenum Oxynitride phase (H700) | Delta Phase

Chemical Analysis	
EELS Analysis	
Elements detected	Mo, N and O
Mo edge peak	396.7 eV
N edge peak	400.9 eV
Thermal XPS spectra	
Elements detected	Mo, N and O
Binding Energy (BE) for $Mo^{\delta+}$	228.7(1) eV
Combustion Analysis	
Absolute N content, as-synthesized | surface-desorbed	11.7(3) | 11.0(3) mass %
Absolute H content, as-synthesized | surface-desorbed	0.4(3) | 0.2(3) mass %
PGAA Analysis	
Mo: N atomic ratio | Mo: H atomic ratio	1.03(3) | 4.05(3)
Chemical Composition	
Pre-desorption :	
Within 5% (TGA + PGAA + CHSN)	$MoN_{[0.92-1.02]}O_{[0.15-0.18]}H_{[0.23-0.26]}$
Post-desorption :	
Deduced from TGA + CHSN	$MoN_{0.88}O_{0.23}$
TGA Results	
Mass loss under Ar TGA @400°C	2.00(1)wt%
Mass loss at 400°C under H_2 TGA (900°C, 3% H_2/Ar)	2.18(1)wt%
Net anion loss H_2 TGA (900°C, 3% H_2/Ar)	16.53(6)wt%
Mo(bulk) using H_2 TGA	85.33(6)wt%
Structural Characterization	
Surface area (BET) | Measured density (pycnometry)	30.1(6) m^2/g | 9.01 g/cm^3

Diffraction Co-refinement Results	
Global Composition[#]	
Composite 'formula'	$MoN_{0.845(3)}O_{0.177(7)}H_{0.137(12)}$
Mo:N molar ratio	1.184(3)
N	10.68(9)wt%
Mo	86.64(8)wt%
O/(O+N) molar ratio	0.173(4)
Anion/Cation molar ratio	1.022(7)
186 sg $MoO_xN_yH_z$ (main phase)	
Crystallographic formula	$MoN_{0.832(3)}O_{0.183(7)}H_{0.142(11)}$
Theoretical Density	9.03 g/cm^3
Mo:N molar ratio	1.203(3)
N	10.52(8) mass %
Mo	86.70(8) mass %
O/(O + N) molar ratio	0.18(4)
Anion/Cation molar ratio	1.015(7)
Lattice Parameter	a = 5.73982(10) Å
	c = 5.61960(6) Å
176 sg Mo_5N_6 (5.46wt%)	
Crystallographic formula	Mo_5N_6
Theoretical Density	8.15 g/cm^3
Lattice Parameter	a = 5.73982(10)
	c = 5.61960(6)

The phase identification based on the diffraction data in Figure 4.4-1a) and those in Figure 4.4-2, which generally indicated consistency with the pattern of "δ-MoN", could easily be interpreted to signify that only Mo and N are present in the materials synthesized here. However, the EELS measurements, Figure 4.4-5, unequivocally revealed the presence of oxygen within the bulk of the ≈ 50 nm thick particles, along with N and Mo. While presence of oxygen in cubic γ-phase has been speculated in literature, the δ-MoN is never reported as an oxynitride, however it should be noted that mostly δ-MoN synthesis do not use the oxide precursor,[29, 111, 170] which unambiguously is the source of oxygen being retained in the structure at the end. In Figure 4.4-5a), $Mo_{M-4,5,}$ $Mo_{M2,3}$, N_K and O_K edges can be observed in the spectra, indicating the presence of Mo, N and O. Noticeably, $Mo_{M2,3}$ and N_K edges were overlapped at around 400 eV. To further investigate the presence of both Mo and N elements and learn more about the Mo and N chemical environment, the ELNES of the Mo-M2,3 and N-K edges was obtained, displayed in Figure 4.4-5b) after alignment, background subtraction and Fourier-ratio deconvolution. Gaussian functions were used to fit the peaks of molybdenum and nitrogen, as shown in Figure 4.4-6a). Peaks at 396.7 eV and 400.9 eV represent Mo and N peaks. Figure 4.4-5c) shows the ELNES of the O_K edge of the hexagonal molybdenum oxynitride. Similar to the ELNES of the Mo_M and N_K edges, O_K ELNES originate from the electron transitions from core orbitals to unoccupied bands, which thus sensitive to the chemical bonding. This helps probe the oxygen source. For example, H700 EELS spectrum differs from oxygen gas shown in Figure 4.4-5c), the split of the O_K edge just above the threshold can be observed clearly in the spectra of the hexagonal molybdenum oxynitride, resulting from the transitions of oxygen s to 2p orbitals hybridized with the Mo 4d orbitals.[195, 196] Therefore the signals of oxygen shown in the EELS spectra are proven to come from the sample instead of the oxygen gas from air. It also show a different shape in comparison to ELNES of O-K edge from both MoO_2 and MoO_3 EELS spectra.[188] Therefore the distinctiveness of the features of the O_K ELNES (Energy Loss Near Edge Structure) spectra and the absence of distinct surface phases in SADP (a surface oxide would be expected to be amorphous[189]), demonstrates that just like the case of C700 and C800, even for the H700 the oxygen detected cannot originate from either surface oxides or the gas phase. However, compared to the Cubic phases the estimated oxidation state of Mo in the hexagonal phase is slightly lower than C800 "Cubic P" sample).

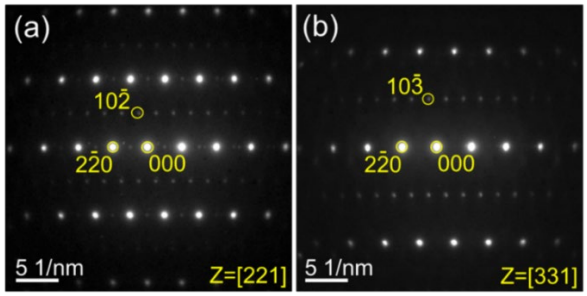

Figure 4.4-4 SAED patterns of the (a) [221] zone and (b) [331] axes for hexagonal molybdenum oxynitride (Courtesy: Chi Zhang, Dravid Group, Northwestern University)

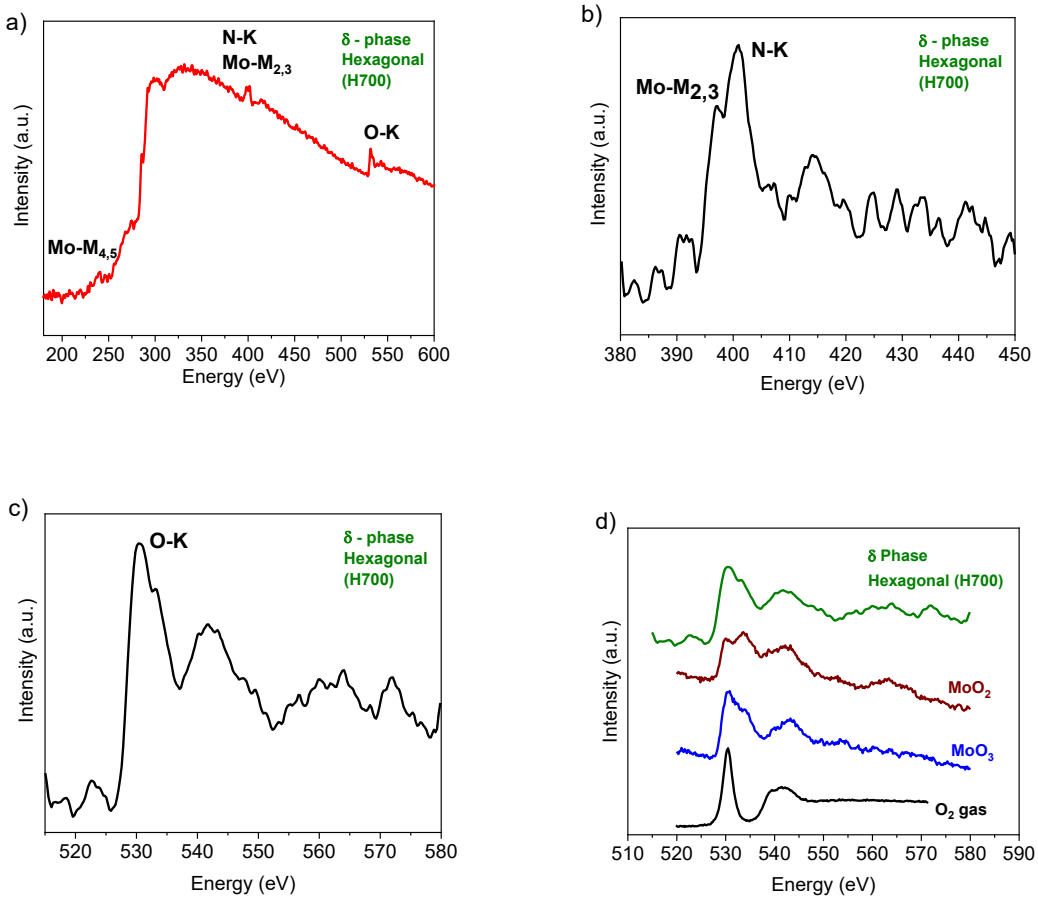

Figure 4.4-5 (a) Core-Loss EELS spectra of hexagonal H700 recorded with a dispersion of 0.25 eV/ch to highlight the peaks position and shape of the Mo-M-4,5, Mo-M2,3, N-K and O-K edges. EELS spectra showing the Electron-energy-loss near edge structures (ELNES) of the (b) Mo-M2,3 edges and (c) O-K edges (d) ELNES of H700 O-K edges compared to oxygen gas[53, 69], MoO_3[61], and MoO_2[61], confirming the signal of O from bulk rather than surface oxide or atmospheric oxygen. (Courtesy: EELS study by Chi Zhang, Dravid Group, Northwestern University)

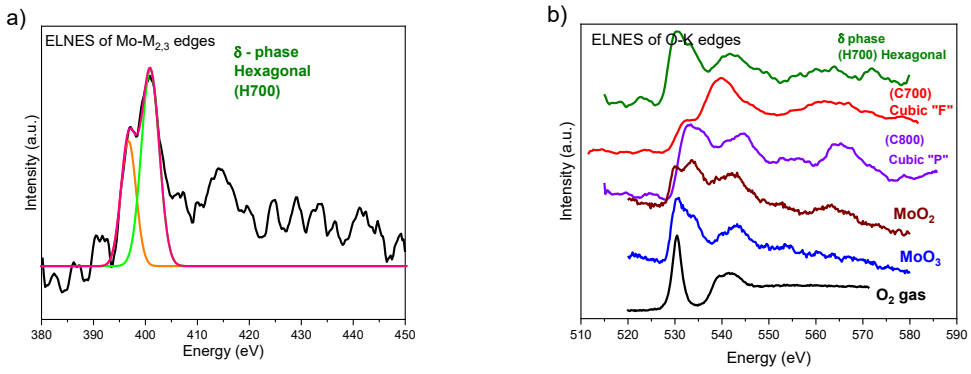

Figure 4.4-6 (a) ELNES of Mo-M2,3 edges of hexagonal molybdenum oxynitride. Gaussian functions were used to fit the peaks of molybdenum and nitrogen. (b) ELNES of O-K edges of hexagonal molybdenum oxynitride comparing oxygen gas[182], MoO_3[188], and MoO_2[188],and Cubic C700 and C800 samples. (Courtesy: EELS study by Chi Zhang, Dravid Group, Northwestern University).

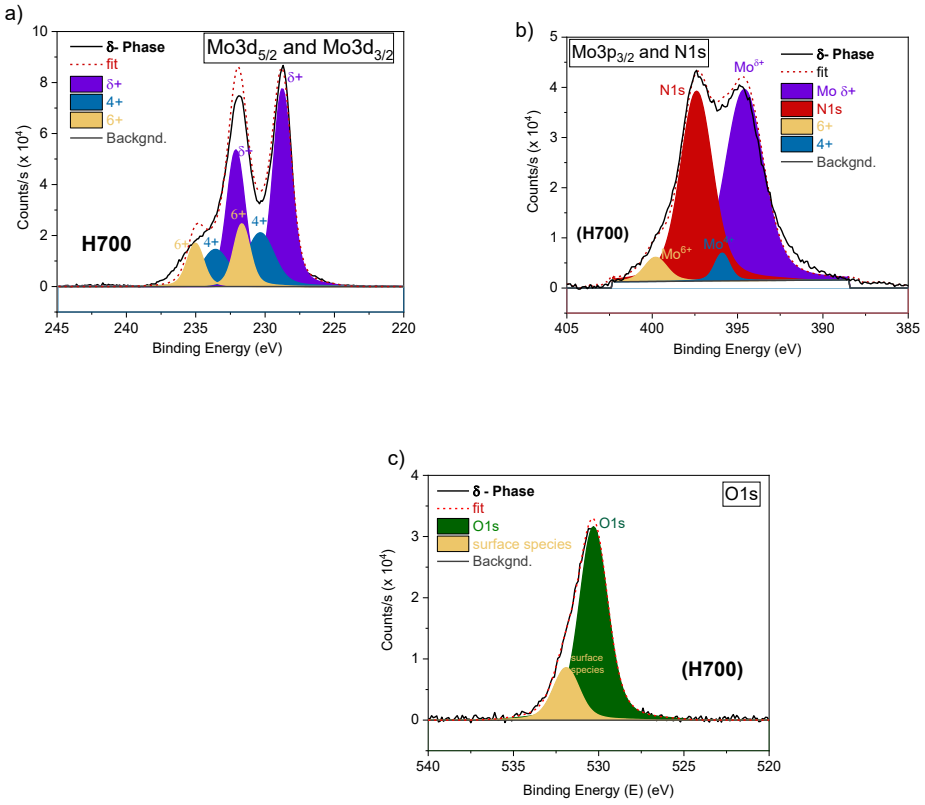

Figure 4.4-7 X-Ray photo electron spectroscopy of (a) Mo3d scan collected for H700. Peak deconvolution of Mo3d spectra was performed using three set of doublet peaks ($3d_{5/2}$ and $3d_{3/2}$) corresponding to $Mo^{\delta+}$, Mo^{4+}, and Mo^{6+} (b) Mo3p overlapped with N1s scan. Peak deconvolution was performed using one N1s and $Mo3p_{3/2}$ divided into $Mo^{\delta+}$, Mo^{4+}, and Mo^{6+}. (c) O1s scan. Peak deconvolution done using one O1s and possible surface species (H2O, hydroxyl group). More details in Table 4.4-2

Table 4.4-2 Features of the Mo3d, Mo3p-N1s and O1s scans peaks detected by Thermal XPS

	Binding Energy (eV)	**Peak Area (Cps.eV)**
Mo3d$_{5/2}$ (eV)	228.7(1)	142744
$Mo^{\delta+}$	230.1(1)	40521
Mo^{4+}	231.5(1)	40939
Mo^{6+}		
Mo3p$_{3/2}$-N1s	394.6(1)	118238
$Mo^{\delta+}$	397.4(1)	98572
N1s	395.9(1)	6742
Mo^{4+}	399.8(1)	8912
Mo^{6+}		
O1s	530.3(1)	73366
O1s	531.9(1)	18298
Surface species		
Cation/ Anion ratio*	0.77	
N/O ratio#	1.34	
Surface Oxide/Bulk ratio&	0.5	
Estimated $Mo^{\delta+}$	2.5(1)	

* - $Area(Mo3p_{3/2}{}^{(\delta+)+(4+)+(6+)}) / (Area(N1s)+Area(O1s))$

\# - $Area(N1s)/Area(O1s)$

& - $Area(Mo3d_{5/2}{}^{(4+)+(6+)})/Area(Mo3d_{5/2}{}^{\delta+})$

Additionally, the difference in O_k spectrums of Hexagonal H700, Figure 4.4-6b) reported in this work compared to the C700 and C800 Cubic samples shows that the molybdenum in the hexagonal phase is likely to be in different coordination of oxygen than both the cubic samples, as expected from different crystal systems.

Thermal XPS results for the H700, can be seen in Figure 4.4-7. Strong O1s spectra signal can be seen in Figure 4.4-7c), however, in the case of the XPS data, as mentioned before the possibility of residual surface species of oxygen and/or H_2O remaining after thermal treatment at 523 K and contributing to the response cannot be ruled out. However, the high intensity of the measured O1s signal, complements the EELS data. Details of all peaks binding energies and their integrated peak areas after peak deconvolution as necessary can be found in Table 4.4-2. Figure 4.4-3a), shows the Mo3d doublet peaks ($Mo3d_{5/2}$ and $Mo3d_{3/2}$), deconvoluted into surface oxide doublets Mo^{6+} and Mo^{4+}, and bulk $Mo^{\delta+}$

peak. Figure 4.4-3b) shows the overlapping Mo3p3/2-N1s region, where the Mo3p is again deconvoluted giving contributions from $Mo^{\delta+}$, Mo^{6+} and Mo^{4+}. Given the strong overlap between Mo and N signals involving complex peak fitting and the possibility of surface species influence, quantitative XPS analysis is always difficult, however some qualitative arguments can be made here based on peak fittings. In the XPS results, being the signature from the bulk, the $Mo^{\delta+}$ species accounted for 50 % of the total Mo3d intensity in the spectra of (Table 4.4-2), nearly equal to combined contributions from Mo^{6+} and Mo^{4+}. The Mo^{4+} and Mo^{6+} species are attributed to residual surface species, likely trapped at the interfaces between individual particles in the pressed compacts. The cation/ anion ratio is ~0.7, possible due to both cation deficient bulk, and presence of any leftover adsorbed NH3 and H2O gases on surface. Combining Mo3d peaks positions of standard Mo^{0}, Mo^{4+}, Mo^{5+} and Mo^{6+},[190] a polynomial curve can be fit to imply the monotonic variation of Mo oxidation state with BE, shown in Figure 4.4-8. With the $Mo3d^{\delta+}$ peak position of 228.7(1) eV, this implies an oxidation state of 2.46+, which makes it more reduced compared to the C700 and C800 cubic phases, in strike contrast to reported compositions of Mo_2N and MoN respectively for cubic γ and hexagonal δ phase.

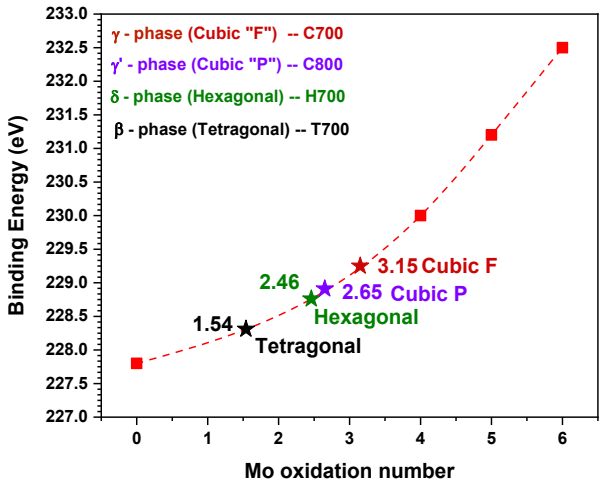

Figure 4.4-8 Estimated oxidation states of different Molybdenum oxynitride phases synthesized at our group including Cubic F, Cubic P, H700 (this work) and Tetragonal phase based on their $Mo3d_{5/2}^{\delta+}$ Binding Energy (eV) from XPS fitting. $Mo3d_{5/2}$ Binding Energies (eV) for $Mo^{0+,}$ Mo^{4+}, Mo^{5+} and Mo^{6+} were obtained from literature. Red line is a polynomial fit for the Binding Energy (eV) = f(Mo oxidation state) hypothetical curve.

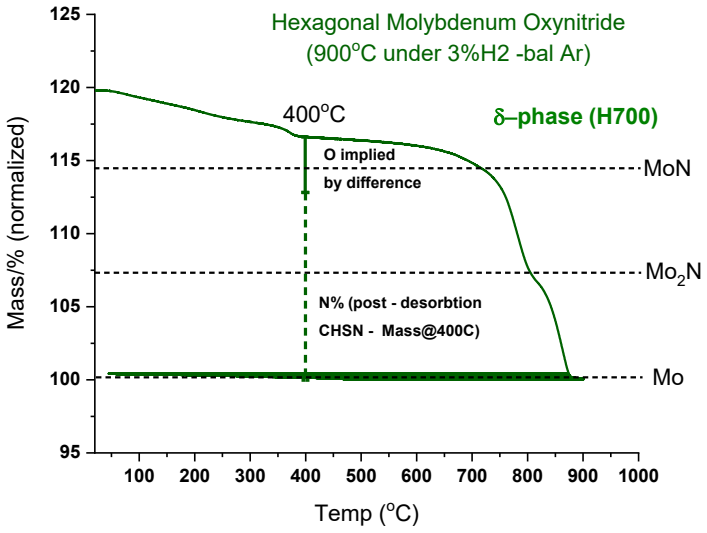

Figure 4.4-9 TGA mass loss profile (solid green line) from as synthesized H700 reduced to Mo metal under dilute hydrogen (3% H2 balance Ar) H2) at 900°C, using a heating rate of 2 °C/min and hold time of 3hrs before cooldown. The masses are normalized to 100% upon completion of reduction in recognition of the variable surface mass content. Horizontal lines indicate the masses of ideal Mo2N, ideal MoN, and the mass range implied by the combustion analysis determination of the N content. Vertical dotted green line indicates contribution of N in the bulk, as obtained from the combustion analysis (N wt%) of H700 sample after desorbing the sample under Argon at 400°C, in attempt to remove as much of surface species, without effecting the bulk. The vertical solid green line implies O content by accounting for the remaining mass (assuming hydrogen as very light).

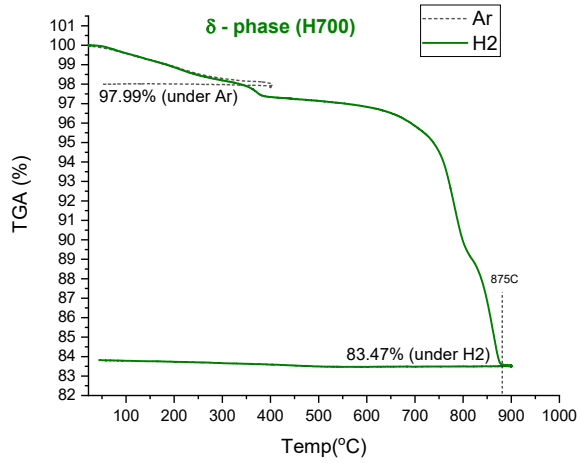

Figure 4.4-10 TGA mass loss profile (solid green line) of as synthesized H700 reduced to Mo metal under dilute hydrogen (3% H2 balance Ar) H2) at 900°C. TGA mass loss showing desorption of as synthesized H700 at 400°C under Argon using TGA in shown (heat to 400C @5C/min; hold 3 hrs and cooldown) in dotted grey line.

TGA mass loss profile, from as synthesized H700 reduced to Mo metal under dilute hydrogen (3% H2 balance Ar) at 900ºC, using a heating rate of 2 ºC /min and hold time of 3hrs before cooldown is shown in Figure 4.4-9 (solid green line). Similar to cubic phases plots, masses are normalized to 100% upon completion of reduction in recognition of the variable surface mass content. The TGA profiles for the complete reduction experiments, revealed nearly continuous mass loss from the initiation of the thermal treatment to approximately 350ºC where first sharp drop occurs possibly due to rapid desorbtion of adsorbed gases such as NH_3, H_2O, N_2 and H_2, with a near plateau region around 673K. Following this, continuous mass loss occurs until 700ºC at which a sharp final mass loss occurs, with total mass loss at 900ºC ~16.53(6)wt%. Interestingly, the mass loss profile of H700, makes it immediately evident that the mass loss is inconsistent with materials of ideal stoichiometric δ- MoN reported for 186sg δ-phase in literature. H700 total mass loss to Mo, is greater than not only Mo2N, but also MoN. With oxygen and nitrogen having similar mass (relative to Mo under first), TGA by itself suggests a non-stoichiometric δ-phase with anions to cations atomic ratio > 1 (for MoN). For example, for the H700 material to correspond to the ideal stoichiometry of MoN, all of the mass loss up to ≈715ºC would have to be due to surface species, which we know isn't the case. Even on repeating the TGA experiment under Argon this time, shown in Figure 4.4-10 (dotted line), by heating the sample upto 400ºC, again resulted in a near plateauted weight loss, suggesting upto ~2wt% desorbed gases on surface. The slightly lower value than observed under Hydrogen can be attributed to sample-to-sample variation, however still suggesting much more weight attributed mainly to N and O in bulk (with H being light) in this hydrogen incorporated Molybdenum Oxynitride Delta phase. While not perfect, the plateau at 400ºC was taken as the approximate end of mass loss from surface, which leads to 85.33(8)wt% of Mo in bulk.

Turning to other quantitative chemical characterization, the combustion analysis indicated 11.7(3) mass % absolute N contents in as-synthesized H700 samples (Table 4.4-1). After surface desorption, the N contents decreased slightly, to 11.0(3) mass. Using this Nwt% information (post desorbtion) and the the bulk Mowt% from TGA analysis, while assigning remainder mass to Oxygen, it was realized that significant mass of the anions can be assigned to O. Vertical dotted and solid green lines in Figure 4.4-9

indicate contribution of N and O in the bulk respectively. This implies that about 30% of the anion weight in bulk is due to Oxygen. Also comparing Nwt% from combustion before and after desorption under Argon at 400°C, and the total wt% of adsorbed species suggested by TGA Ar under same conditions (Figure 4.4-10), it can be said that the about 35% of adsorbed gas species are nitrogen rich (Mainly NH_3 and possibly some N_2), making H_2O the dominant surface adsorbed species. This makes sense given the external introduction of H_2O for the wet ammonolysis.

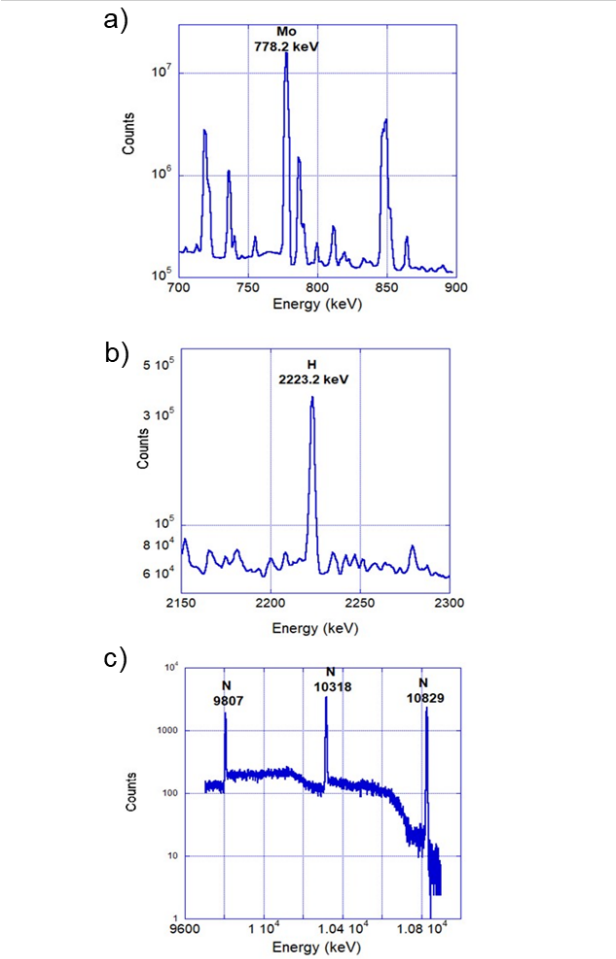

Figure 4.4-11 PGAA spectra of H700 (Delta phase) sample. (Courtesy PGAA study : Rick L Paul, and Heather Chen-Mayer, NIST)

Thus, residual NH_3 accounts for a significant, but not dominant, fraction of the surface species in the as-synthesized materials. Overall, the δ phase (H700) in this study have much less overall surface adsorbed species compared to our Cubic Molybdenum oxynitride samples (C700 and C800) discussed in 4.3, and thus impacts the overall chemical analysis much less, when considering techniques for which as synthesized samples were directly used for analysis. One such quantitative analysis technique is the Prompt Gamma Activation Analysis (PGAA) (Figure 4.4-11) Table 4.4-1, which revealed Mo:N molar ratios of 1.03:1, for as-synthesized delta phase which is consistent with the combustion analysis. The PGAA additionally revealed high hydrogen concentrations in as-synthesized H700, with Mo:H ratio of 4.05:1. The result is consistent with the combustion analysis, which, although close to the hydrogen detection limit, suggests a positive concentration of H in as synthesized H700 and also in post desorption H700, suggesting some hydrogen being incorporate in the bulk of the structure.

All chemical analysis above point to point to H700 sample, as hydrogen incorporated Molybdenum Oxynitrides Using Mo/N and Mo:H directly from PGAA, combined with Mowt% from TGA provides $MoN_{0.97}O_{0.18}H_{0.25}$ as the composition for delta phase suggesting 12wt% N, which is in good agreement with the combustion result of 11.7(3)wt% N in as synthesized powder. The three chemical analysis tools employed here over-define the material compositions, and within 5% error between combined TGA + PGAA + CHSN analysis, an average range of chemical composition for the as synthesized delta phase can be calculated as $MoN_{[0.92\text{-}1.02]}O_{[0.16\text{-}0.20]}H_{[0.23\text{-}0.26]}$. However, this composition slightly overestimates the anions due to the presence of surface adsorbed gases on as synthesized samples. Therefore, a more accurate bulk composition can be determined by assigning 11wt% of bulk weight of delta phase (mass at 400ºC in Figure 4.4-9) to nitrogen with the remainder bulk anion weight being O. Using this case, the bulk composition comes out to be $MoN_{0.88}O_{0.23}$, suggesting about 3.3wt% O of total bulk delta phase, with about 30% of bulk anions being Oxygen, balance being Nitrogen, represented by solid and dashed lines respectively at 400ºC point in Figure 4.4-9. Also going back to surface sensitive Thermal XPS results, which suggests Nitrogen to Oxygen ratio of 1.3, which is much lower than what we find here for the bulk composition again suggesting that the H_2O must be the dominant adsorbed species on the surface of as synthesized delta phase. Note that in above bulk

composition ($MoN_{0.88}O_{0.23}$) , H contribution was ignored, however if this was the case, then the estimated bulk Mo oxidation state would be 3.1+, however as shown in Figure 4.4-8, the estimated Mod+ for delta phase from Thermal XPS is <3+, therefore supporting the PGAA finding of having hydrogen in the bulk of the Dela Phase, making these MoOxNyHz type phase, with anion:cation atomic ratio >1.

A final piece of chemical information is provided by the measured densities using pycnometry, found to be 9.01 g/cm^3 only slightly lower than the theoretical density of 9.2g/cm^3 for ideal δ-MoN. This result suggests that some concentration of closed pores or possibly crystallographic vacancies, which would be inaccessible to pycnometry and (in the case of closed pores) highly dependent on the precursor morphology, contribute to the slightly lower than theoretical density.

4.4.2 Structure Determination of Delta Molybdenum Oxynitride hydride phase.

With the above insights into the chemical composition of H700, δ-phase particularly the presence of oxygen and hydrogen, structural refinements to simultaneously fit to the synchrotron (XRD) and time-of-flight Neutron powder diffraction (NPD) data were undertaken, with appropriate chemical restraints. A summary of the co-refinement results is provided in Table 4.4-3, and the measured and final calculated patterns are presented in Figure 4.4-12 and Figure 4.4-13.

Ultimately, the best fits were obtained using space group *$P6_3mc$ (186) MoOxNyHz* type hexagonal oxynitride phase, however not all peaks (main ones highlighted in yellow * in Figure 4.4-13) could be addressed with just 186sg, and the co-refinement suggests about 5.46% phase fraction of possible Mo_5N_6 as the secondary hexagonal phase with $P6_3/m$ (176) space group. On carefully re-examining, the Lab XRD patterns of several H700 batches Figure 4.4-2, most of the patterns could only be indexed to sg 186, however in few patterns (red and brown curves in Figure 4.4-2) a small peak around 44º was observed, which could be attributed for the detection of Mo5N6 in few of the H700 batches, even under Lab XRD resolution.

Table 4.4-3 Atomic coordinates, site occupancies, and isotropic displacement factor coefficients for δ phase (H700) hexagonal molybdenum oxy-nitride-hydride with space group 186, obtained from Rietveld Analysis using combined X-ray synchrotron and neutron time-of-flight powder diffraction data. Estimated standard deviation in last digit(s) of refined parameters provided in parentheses. Following recommended practices of the International Union of Crystallographers,[cite] uncertainty values are reported in the range from 2 to 19. Note, some secondary phase Mo_5N_6 phase peaks were also present, therefore the corefinement model used both 186 and 176 space group for refinement. For the Mo_5N_6 phase, only the lattice parameter, and phase fraction was refined given its weight raction was <6wt%

Space group	P63mc (186)				
Lattice parameter, Å	a = 5.73982(10) | b = 5.73982(10) |c = 5.61960(6)				
Secondary phase Mo_5N_6 - P63/m (176 sg)	5.49% phase fraction , Lattice parameter : a = 4.916165 | b = 4.916165 | c = 11.1330(9)				
Site | Element	**x**	**y**	**z**	**Occupancy**	**Uiso, 10^2 Å^2**
Site 2(a), 3m | Mo(1)	0	0	0.60946(5)	0.947(15) Mo	0.13(3)
Site 6(c), m | Mo(2)	0.48865(6)	0.51135(6)	0.60942(5)	0.998(7)Mo	0.095(11)
Site 2(b), 3m | N(1)	1/3	2/3	0.88576(5)	1 (fixed) N	0.23(2)
Site 6(c), m | N(2) + O(2) (net occupancy fixed to 1)	0.1672(3)	0.8328(3)	0.3547(5)	0.759(9) N; 0.241(9)O	0.245(11)
Site 6(c), m | H(1)	1/3	1/6	7/8	0.082(8)	1.00(fixed)
Site 6(c), m | H(2)	0	1/2	1/8	0.105(9)	1.00(fixed)
Goodness of Fit	1.87				
Residual wR (%)					
NB	3.89 %				
X-ray	15.43 %				
Combined	8.77 %				

For the best fit co-refinement model (results in Table 4.4-3), weighted residual (wR) of 8.77% was obtained with 3.89% and 15.43% wR for NPD and Xray respectively. Without considering the Mo_5N_6, the fit was bad with increased combined 9.68% wR with higher 17.30% and 4.56% wR values or Xray and NPD respectively. Several of the peaks, marked in yellow * in Figure 4.4-13, could not be visibly addressed with just single 186sg MoOxNyHz phase. It is to be noted that such a secondary phase was not observed in several of the SADP collected under TEM, possibly due to only ~5wt% presence. Since the secondary phase was only about 5%, the CIF file of Mo_5N_6 (PDF# 00-051-1326) was used as is, and the occupancies or thermal displacement parameters (Uiso) were not refined, with lattice parameter and

phase fraction being the only two parameters refined. The co-refinement results using 186 + 176 sg (best fit model) are summarized in Table 4.4-3, and the corresponding ball and stick model of the main 186 sg MoNxOyHz phase is shown in Figure 4.4-14, viewed along c-axis and reciprocal (a*) lattice in Figure 4.4-14a) and Figure 4.4-14b) respectively. Co-refinement shows that for the main 186sg MoNxOyHz phase, while the 2a and 6c sites host the Mo cations, the site occupancies of these two sites differ, such that Molybdenum Mo(1) on site 2a has 7.94% sites vacant, while Molybdenum Mo(2) on site 6c refine to being fully occupied. Mo(1) and Mo(2) atoms are represented by black and dark grey solid balls in Figure 4.4-14. Even bigger distinctions are evident for the 2b and 6c sites, on which the anions reside. While both anion sites are fully occupied (constrained in final refinement, as free refinement consistently resulted in an occupancy factor exceeding 1 for anion sites), 2b site is fully occupied only by Nitrogen N(1), while the 6c site is co-occupied by 24.1% Oxygen O(2), with balance being Nitrogen N(2). Dark Blue solid balls represent N(1) atoms on site 2b, while light blue and dark red balls represent co-occupying N(2) and O(2) atoms on site 6c. Additionally, inverse fourier maps were used to identify 2 possible hydrogen positions in the bulk of the MoNxOyHz sg186 phase, on 6c sites. H(1) at (1/3, 1/6, 7/8) and H(2) at (0, ½, 1/8) with occupancies 8.2% and 10.5% occupancies suggested by the best fit co-refinement model. For clarity purposes H atoms aren't shown on Ball and Stick models. However, detailed NMR studies are being pursued as a continuation of this work in Haile Lab (Courtesy: Hu Group, Florida State University). Some preliminary analysis is discussed in Appendix B.6.

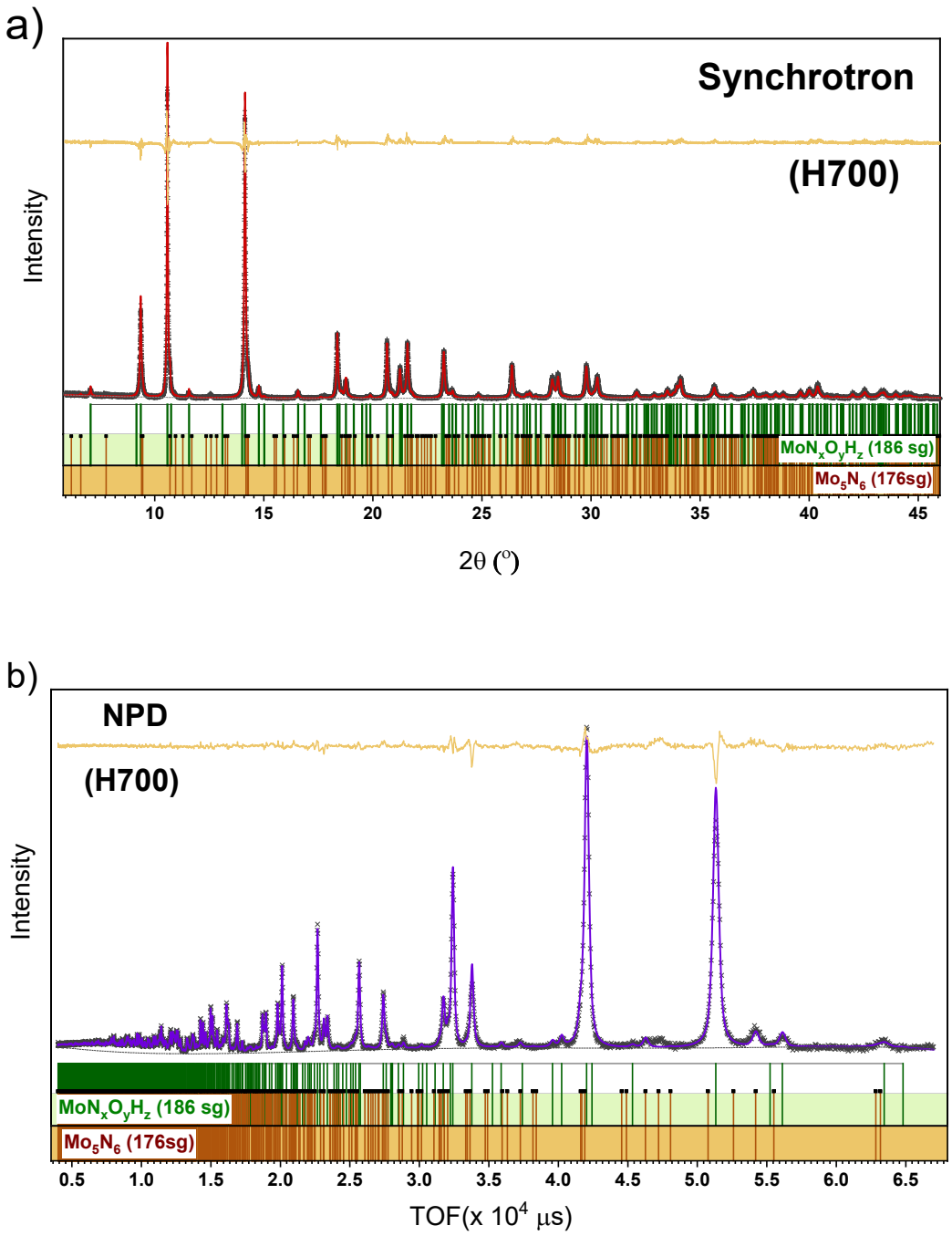

Figure 4.4-12 Measured and calculated diffraction patterns, as well as difference plots (yellow sparklines) for as synthesized delta phase : (a) synchrotron and (b) neutron data. Below each plot, all the reflections positions for both 186 sg and 176 sg are shown.

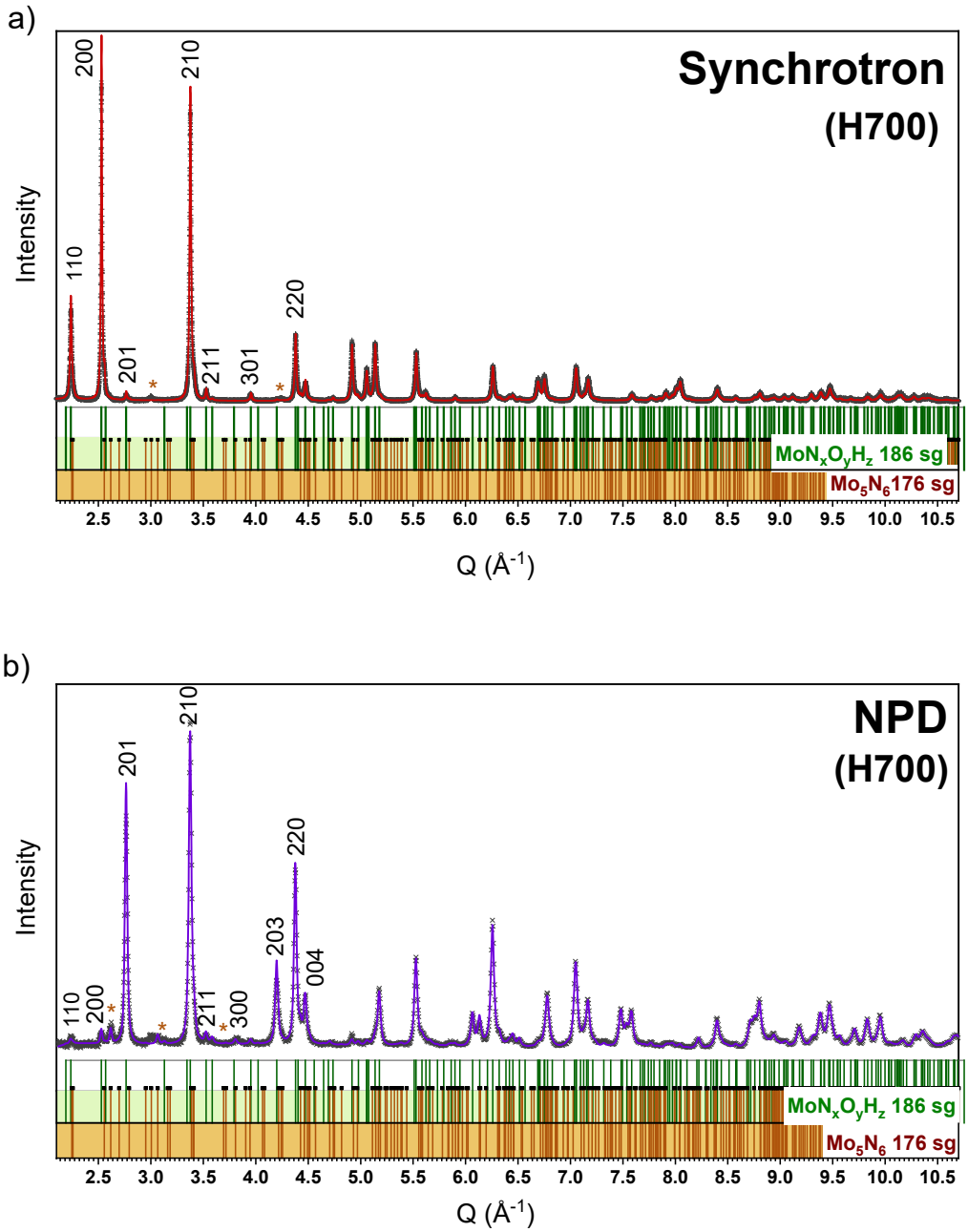

Figure 4.4-13 Measured and calculated powder diffraction patterns, the latter from co-refinement of the as synthesized hexagonal Molybdenum oxynitride hydride using combined (a) synchrotron and (b) Neutron powder diffraction data. For ease of comparison, data are presented as functions of Q ($Å^{-1}$) along the common range of Q scale for both technique, although NPD data was analyzed over much larger Q range. (a) Measured synchrotron data are shown as grey plus (+) and calculations as solid red line. Few prominent 186sg reflections are marked. (b) Measured NPD data are shown as grey cross (x) and calculations as solid purple line. Few prominent 186sg reflections are marked. For both plots. some secondary Mo_5N_6 phase with 176sg peaks are marked with (*). Below each plot, all the reflections positions for both 186 sg (green vertical lines on light green background) and 176 sg (brown vertical lines on yellow background)

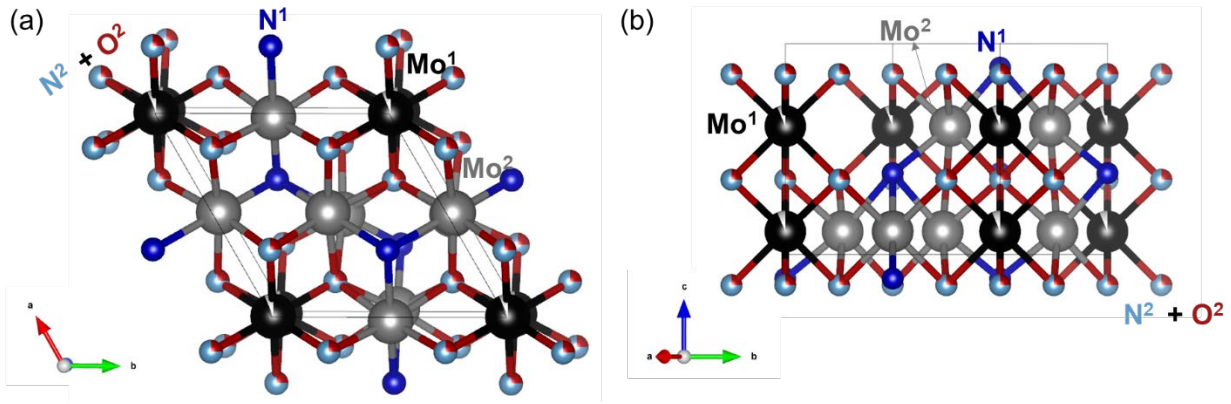

Figure 4.4-14 Structure of the MoNxOyHz Molybdenum Oxynitride hydride phase with space group P63mc (186) identified in this work (a) viewed along the c axis. (b) Viewed along the reciprocal a lattice. Big black and dark grey spheres correspond to the Molybdenum Mo(1) and Mo(2) atoms at 2a and 6c sites respectively. 2a Mo site is slightly vacant. Anion shows with smaller balls fully occupy the anion sites. 2b site fully occupied with only Nitrogen N(1) atoms shown with blue balls. However, quarter of the 6c anion site is co-occupied by Oxygen O(2) atoms shown as red balls, along with Nitrogen N(2) atoms shown as light blue balls. More details available in Table 4.4-3. For clarity purposes, hydrogen atoms are not shown here, but have found to be present in the bulk in possibly at least 2 interstices positions as listed in Table 4.4-3. Note the secondary minor (<6wt%) Mo5N6 phase is not shown here, but can be found for comparison in Figure 4.4-15 below.

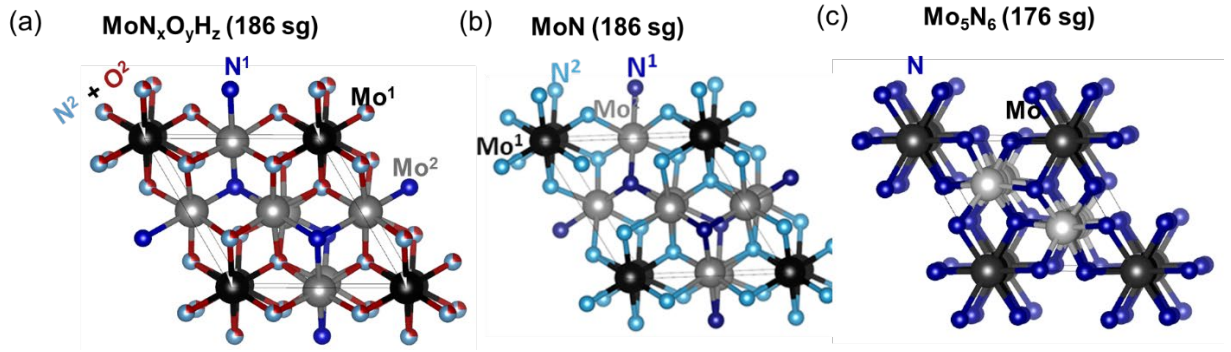

Figure 4.4-15 Ball and Stick models of (a) corefined Molybdenum oxynitride 186sg phase with MoNxOyHz composition. (b) Literature reported stoichiometric 18g sg MoN phase. (c) Mo_5N_6 phase with 176 sg, observed as the secondary phase (<6wt%) in our as synthesized H700 sample.

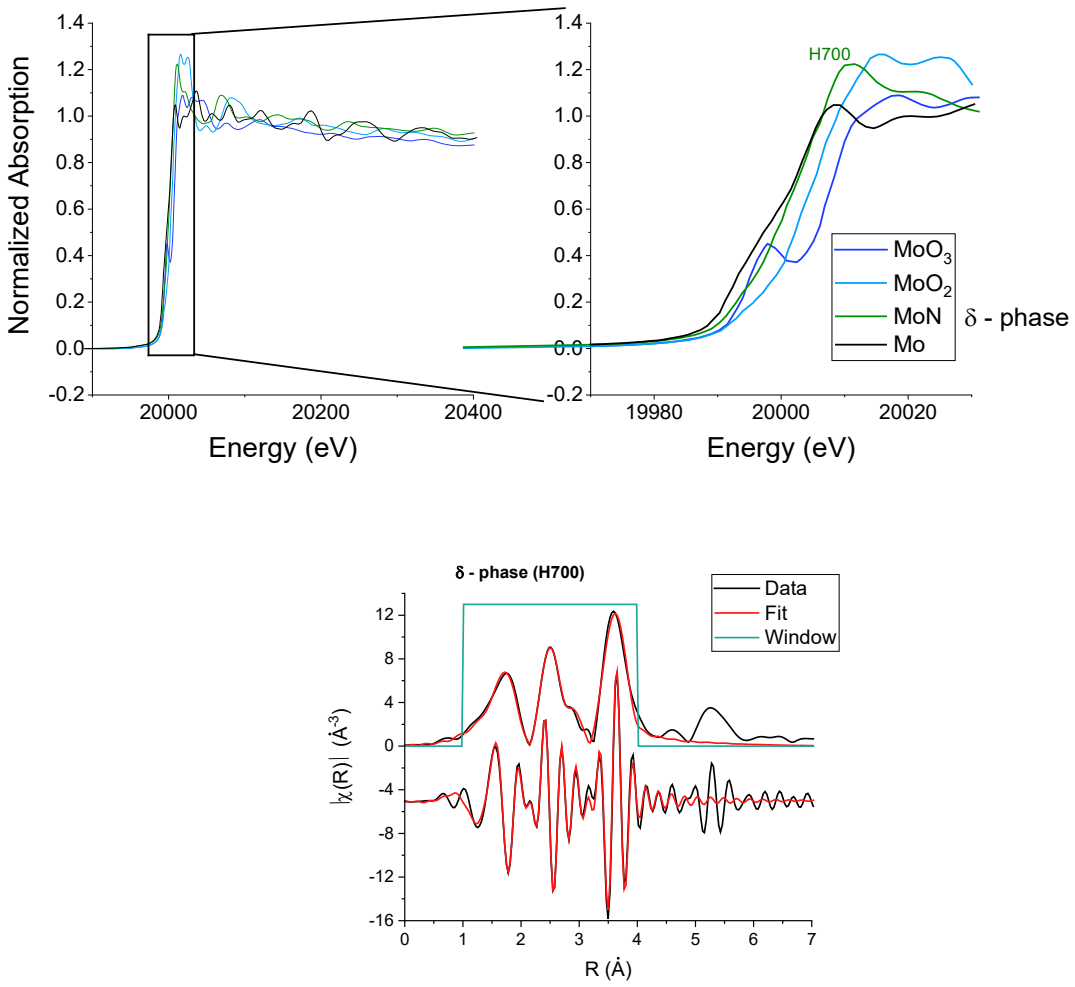

Figure 4.4-16: EXAFS analysis of H700 phase. (Courtesy: EXAFS study by Elise Goldfine, Haile Group, Northwestern University)

The final composition derived for the main $P6_3mc$ (186) space group Molybdenum Oxynitride Hydride phase derived from the co-refinement was $MoN_{0.832(3)}O_{0.183(7)}H_{0.142(11)}$. Combining the fact that 5.46wt% secondary MoN_5N_6 phase with lower symmetry $P6_3/m$ (176) space group, an overall global composition from co-refinement comes out to be $MoN_{0.845(3)}O_{0.177(7)}H_{0.137(12)}$. This global composition from refinement is in general agreement with the chemical analysis suggesting about 86.6wt% as Mo, 10.7wt% as Nitrogen, with remainder anions as Oxygen such that O/(O+N) molar ratio of 0.17 is obtained. Slightly anion rich (anion/cation molar ratio = 1.02) chemistry is suggested, agreeing with chemical analysis.

Slightly higher Mo:N from corefinement compared to PGAA, could be due the adsorbed NH_3 (and some N_2) on the surface, and also due to possible sample to sample variation. Additionally, Figure 4.4-10 compares ball and stick models for the 186 sg MoNxOyHz phase (Figure 4.4-10(a)) found in this work to literature defined 186sg δ-MoN phase (Figure 4.4-10(b)) and the possible secondary phase Mo_5N_6 (Figure 4.4-10(c))with 176 sg. Particularly distinct fact is that unlike suggested for stoichiometric MoN delta phase in literature, for our δ-$MoN_xO_yH_z$ phase, some cation vacancies were observed. This results in slightly lower density from refinement, compared to 9.2g/cm^3 for stoichiometric MoN crystallized in same 186 space group. Additionally, oxygen co-occupies the site 6c, instead of it being fully occupied in stoichiometric MoN. In striking contrast, the space group of secondary Mo_5N_6 phase is much different from our oxynitride main phase, with 5 Mo positions with two of them about half vacant, and 1 nitrogen site, crystalized in $P6_3/m$ (176) space group.

It should be noted that while the positions suggested for H in bulk is only a first approximation guess, and more detailed studies such as 1H-NMR would be required to further probe the hydrogen environment (beyond the scope of this study). However, qualitatively, PGAA, Mo oxidation state from Thermal XPS and comparing it to chemical analysis, and NPD corefinement, all suggest the presence of H in the bulk. While H in bulk has never been discussed for the hexagonal phase, studies on cubic gamma molybdenum nitrides have shown H insertion electrochemically, and analyzing them by X-ray absorption near edge spectroscopy (XANES)[119], as discussed for the C700 and C800 in this chapter. While ammonia used for synthesis is the obvious H source for H found in all of as synthesized phases (H_2O an additional source in case of H700), however it is interesting to recall from Chapter 3, that in-situ Lab XRD experiments showed that MoO_2 ammonolysis to H700 does not proceed through bronze formation, unlike MoO_3 ammonolysis for cubic y-phases (C700 and C800). Bronze, forms upon intercalation of H in orthorhombic MoO_3,[108, 113, 117, 118] and it can be seen as the step where H is introduced (and retained at end of reaction) in the case of C700 and C800 sample. Without the bronze as an intermediate, it is interesting to note that H enters either the oxide itself (which is stable upto 670^{o}C as discussed in Chapter 3), or the nitride after or during its formation, along with nitrogen.

4.5 Summary & Future Outlooks : Cubic & Hexagonal Molybdenum Oxynitrides.

Cubic (C700, C800) and Hexagonal (H700) phases of Molybdenum nitrides synthesized via ammonolysis of molybdenum oxides using optimized recipes described in Chapter 3. Dry ammonolysis of MoO_3 at 700°C and 800°C was used to prepare C700 and C800 cubic samples, whereas wet ammonolysis was realized as a novel method for preparing hexagonal starting with MoO_2 at 700°C . Using advanced characterization protocols, it was established these materials obtained by this process are in fact hydrogen incorporated, molybdenum oxynitrides of general stoichiometry $Mo_{1-x}(N_{1-y}O_y)H_z$. While the presence of oxygen in cubic γ-phase has been speculated in literature, the δ-MoN is never reported as an oxynitride, however it should be noted that mostly δ-MoN synthesis do not use the oxide precursor,[29, 111, 170] which unambiguously is the source of oxygen being retained in the structure at the end. This suggests that wet ammonolysis is a novel method to prepare δ-phase which have the same hexagonal structure as δ-MoN, but is anion rich Molybdenum Oxynitride with considerable fraction of the anions as oxygen, and is slightly anion rich. Infact, cubic samples were also concluded to be anion rich, strikingly different from nominally reported Mo_2N composition.

Ammonolysis results in increase in surface area for all samples, however cubic samples have much higher surface area compered to hexagonal sample. This could be related to the bronze formation in case MoO3 ammonolysis as discussed earlier in Chapter 3. Additionally, all of these micron sized powders for these 3 samples, are single crystals under the TEM, with lots of porosity in the structure, which have much smaller crystallite size compared to starting micron sized precursors. H700 showed alligator type surface morphology under SEM, whereas the Cubic samples were smooth (just like starting oxides), suggesting the possible corrosive action of external H_2O at high temperature being the differentiating factor. Overall sample to sample variability was observed and surface adsorbed species were one of the reasons. About 5-8wt% adsorbed gases (mainly NH_3 and H_2O) was found to be adsorbed

on C700 and C800 samples, however hexagonal sample had much smaller adsorbed species (<2wt%, mainly H_2O and some NH_3), suggesting key difference in surface properties of these samples.

This work also highlights the limitations of using XRD and/or electron diffraction for determining the structures of these complex systems. In particular, these techniques are unable to detect co-occupation of anion sites by O along with N. Here, the true structures and compositions are revealed by Rietveld co-refinement using both powder ND and XRD data, and by quantitative chemical analysis with data from PGAA, combustion analysis, and TGA.

For the Cubic phases, both C700 and C800 crystallize in space group $Pm\bar{3}m$ and do not display the translational symmetry inherent to the $Fm\bar{3}m$ space group of the rock salt prototype structure. The two crystallographically distinct cation sites in the $Pm\bar{3}m$ structure have distinct occupancy factors, with a relatively large difference in the case of the material synthesized at 800°C. Accordingly, superstructure peaks with indices of mixed parity are evident in the XRD and the electron diffraction patterns of this material. Such peaks are absent in the patterns of the C700 material synthesized at 700°C. Differences in the N and O occupancies on the two occupied anion sites are also observed and give rise to the NPD superstructure peaks. The composition deduced for the material synthesized at 700°C is $Mo_{0.775(2)}(N_{0.75},O_{0.25})$, whereas that for the material synthesized at 800°C is $Mo_{0.790(1)}(N_{0.729(5)},O_{0.062(1)})$, in overall agreement with the chemical analysis. About 1/4 of the anion content is due to oxygen under typical preparation conditions, whereas reaction at higher temperature results in a substantially lower oxygen concentration. The high temperature transformation to a stoichiometry richer in cations (upon synthesis at 800°C as compared to synthesis at 700°C) is accompanied by an expansion of the lattice, a preferential shift of the Mo atoms from one cation site to another, loss of specific surface area, and an increase in pycnometry measured density. Furthermore, sites formerly nearly fully occupied by oxygen become nearly fully vacant, while the shift in Mo position results in preferential coordination by the cations of the oxygen-bearing anion sites in both structures. The transformation is also accompanied by a slight decrease in the Mo oxidation state, as detected by both EELS and XANES measurements. The sum of these observations suggest that cation-deficient, rock salt “molybdenum nitride” (A700) is stabilized by

the incorporation of oxygen, whereas the nearly stoichiometric analog (A800) is stabilized by ordered vacancies on the anion sites.

For the hexagonal phase H700 sample, the space group was found to be the same as the δ-MoN (186sg) reported in literature. However, co-refinement to study the anion and hydrogen distribution, including refining for O in bulk, suggested by chemical analysis. H700 sample was found to be an Molybdenum Oxynitride Hydride with $MoN_{0.845(3)}O_{0.177(7)}H_{0.137(12)}$ composition, in good agreement with the chemical analysis. Small (<5wt% secondary Mo5N6 was observed in H700). Particularly distinct fact is that unlike suggested for stoichiometric MoN delta phase in literature, for our δ-MoNxOyHz phase, some cation vacancies were observed, confirming the anion rich chemistry suggested by chemical analysis. This results in slightly lower density from refinement, compared to 9.2g/cm^3 for stoichiometric MoN crystallized in same 186 space group. Additionally, oxygen co-occupies the site 6c, instead of it being fully occupied in stoichiometric MoN.

For the H700 phase the distinguishing synthesis factor is Wet ammonolysis which makes their synthesis from MoO_2 possible, which otherwise would result in significant y-phase as the product under dry ammonia (Chapter 3). Unlike sulphides based δ-MoN synthesis, such a oxide ammonolysis route allows the synthesis of an oxynitride rather than a pure nitride, just like the cubic phases. It would be interesting to synthesize MoN from conventional routes in future and characterize them to confirm this. This would be the first report of a hexagonal Molybdenum oxynitride phase.

These comprehensive studies form a critical first step in establishing the extent of the chemical tunability of these molybdenum oxynitride phase. Chemical tunability may, in turn, enable precise control of the catalytic and electronic properties of these $Mo_{1-x}(N_{1-y}O_y)H_z$.

Chapter 5 Solid Acid Electrolyzer Cells (SAEC) : Proof of Concept using oxynitrides for HER and OER catalysis.

5.1 Electrolysis of Water (Introduction)

As discussed in Chapter 1, hydrogen(H_2) is considered as one of the most sustainable and clean energy vectors for replacing fossil fuel energy.[13] Amongst the various methods to produce hydrogen, electrolysis of water, provides one of the most sustainable solution, especially when coupled with electricity generated from renewable sources for example solar, wind and others. Combine this, with the hydrogen air fuel cells (example SAFC's discussed in Chapter 2), that can be used to convert the chemical energy that is stored in hydrogen back to electricity, completes the sustainable hydrogen economy loop, by providing a carbon neutral cycle.[12, 13, 30, 31]

While water electrolysis has been known for 2 centuries, there has particularly been growing interest in developing water electrolysis technologies (electrolyzers) and designing catalysts for them, in the past couple of decades. Overall water electrolysis technologies or electrolyzers, can be categorized based on their working temperature which is often dictated by the choice of electrolyte. Among the low temperature electrolyzers (~100^{o}C), the main ones are Alkaline water electrolyzers (AWE) and proton exchange membrane electrolyzers (PEM), where the former uses a liquid electrolyte (ex. alkaline KOH, NaOH), and the later uses a solid polymer electrolyte (ex. Nafion). Both of these technologies have been maturing into commercialization.[23, 197] While, the AWE is the oldest and most commercialized,[198] PEM electrolyzers have been researched more recently, given their potential to result in higher efficiencies and current densities compare to AWE.[197, 199] However, both of these operate at lower than 100^{o}C, and unfortunately suffer with the overall sluggish kinetics of both the half cell reactions of water electrolysis : H_2 evolution reaction (HER) and O_2 evolution reaction (OER), with the later process being the most challenging, requiring overall large overpotentials that need to be overcome. Large overpotentials

combined with corrosive conditions, usually requires the use of precious metals (Pt, Pd) as catalysts for these low temperature water electrolysis technologies. Precious catalysts that need to be engineered, along with the manufacturing of complex liquid electrochemistry systems to deal with delivery and removal of reactants and products, overall add to the cost of PEM electrolyzers.

In contrast, high temperature electrolyzers (>500^{o}C, usually >650^{o}C), often use oxide ion conducting electrolytes, called as Solid oxide electrolyzer cells (SOEC).[197, 200] SOEC not only enjoy the thermodynamic advantage of splitting steam rather than liquid water (discussed below), but the high temperature also results in accelerated kinetics (activity scales exponentially with temperature). This makes SOEC very promising for achieving high efficiencies and current densities, with minimum onset potential, requiring non-noble catalysts.[201] However, the heat requirement of these systems are very high, and just like Solid oxide fuel cells, these systems require expensive temperature resistant auxiliary materials, and suffer from poor cycling properties.[37] While there are cases where the waste heat available is enough to make SOEC efficient,[202] recent efforts have been focused on developing solid electrolytes that can decrease the operating temperatures of these SOEC. A lot of high temperature fuel cell research in the last decade has been focused on working with protonic ceramic fuel cells. Sihyuk etal. from our group recently showed peak power densities of 500 mW cm^{-2} at 500 °C in SOFC, using proton conducting solid oxide electrolyte. These advantages of higher conductivity offered by proton conducting electrolytes employed in SOFCs, have recently been translated to SOECs as well. Several SOEC studies using proton conducting $BaZrO_3$ and $BaCeO_3$ perovskites have been conducted, showing current densities upto ~800mA/cm2 at 1.5V. However, both proton and oxide based SOEC suffer from poor ionic conductivity of electrolytes at higher temperatures compared to PEM cells, along with fast electrode and electrolyte degradation.

For these reasons, Solid acid electrolytes which have operating temperatures between 120-300^{o}C, have been actively pursued for various electrocatalytic applications.[16, 22, 26, 43] The advantages offered by using super protonic CDP for applications at intermediate temperatures (250^{o}C) is discussed in Chapter 1. Further, Haile group has been on the frontier of developing Solid Acid Fuel Cells (operating at

250°C) for the past decade using CDP electrolyte.[19, 20, 38, 42, 203] In this chapter we use CDP, to perform preliminary proof of concept study on solid acid electrolyzer cells (SAEC).

5.2 Solid Acid Electrolyzer Cells (SAEC): Mid temperature electrolysis advantages

For understanding the advantages offered by Solid Acid Electrolyzer cells (SAEC), it is important to reflect both on the thermodynamics and kinetics of electrolysis. Thermodynamically, water splitting is an uphill reaction requiring external energy to drive the reaction. When done using electric energy, it is called electrolysis, with the following reaction:

$$H_2O \xrightarrow[electrolysis]{} \frac{1}{2}O_2 + H_2$$

The total energy demand (ΔH, enthalpy of reaction) for the water splitting reaction plotted with temperature is shown in Figure 5.2-1a), green curve. Overall temperature region in Figure 5.2-1 is split upto into 3 regions representing the two conventional electrolysis technologies, PEM (25-100°C) and SOEC (500 – 1000°C). The remaining gap 100-500°C is assigned to proposed SAEC, although it should be noted that most solid acid electrolyte operate between 150-300°C, including our CDP based SAEC operating at 250°.C

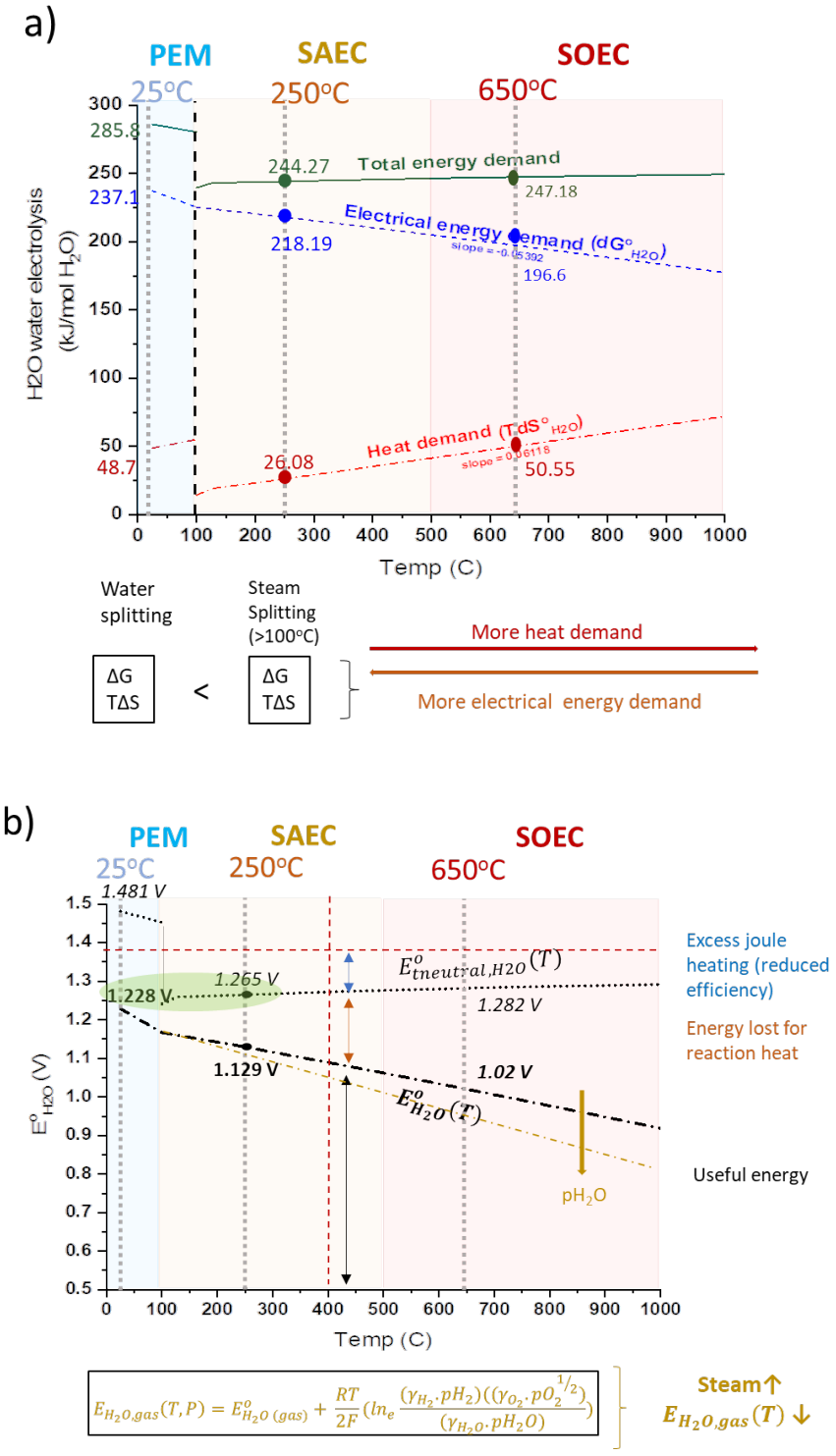

Figure 5.2-1 Thermodynamic of water and steam splitting with temperature, for the three difference electrolysis technologies: PEM (representing room temperature electrolysis), SAEC (this work) and SOEC (high temperature oxide-based electrolysis).

The total energy demand in electrolysis, needs to be met by minimum amount of electrical energy needed (ΔG), and the remaining supplied as maximum heat needed (TΔS). ΔG and TΔS are also plotted in Figure 5.2-1a), as a function of temperature in blue and red curves, based on the reaction: $\Delta H = \Delta G + T\Delta S$. Further reversible voltage $E^{o}_{H_2O}(T)$ and thermoneutral voltage $E^{o}_{tneutral,H_2O}(T)$, can be calculated using $\frac{\Delta G}{nF}$ and $\frac{\Delta H}{nF}$, where n is amount of electrons exchanged in water splitting, and F is faraday constant (96485 C/mol). These two potentials are plotted in Figure 5.2-1b) as a function of temperature. If the heat energy is provided externally, then $E^{o}_{H_2O}(T)$ corresponds to the minimum electric potential required for water electrolysis at that temperature under standard atmospheric pressure. For non-standard conditions, nerst potential can be calculated using the equation shown in yellow box in Figure 5.2-1b). An example effect on electric potential required with increase in pH2O is shown (dotted black curve with more negative slope) due to external humidity.

A sudden drop in total energy demand occurs at 100ºC, after which it rises slightly with temperature. This explains the immediate thermodynamic advantage of SAEC and SOEC over the PEM systems, which split steam instead of liquid water. Beyond 100ºC, the minimum electric voltage required for the electrolysis becomes smaller at higher temperatures. For comparison, at room temperature 1.48V is theoretical electric voltage required to spilt water, however for SAEC at 250ºC, only 1.26V is required. In addition, practical PEM voltages required are often much higher due to sluggish kinetics at low temperatures. In this sense, one can argue that SOEC operating >600ºC should have the most advantage with <1V of electric potential required for steam splitting, and accelerated kinetics with very low relative overpotentials. However, the heat demand (TΔS) at such high temperatures is very high, which makes the overall process challenging, unless external heat is provided which decreases the overall efficiency and sustainable purpose of the reaction. In an ideal hydrogen economy, one would combine electrolyzers with waste heat for thermal energy demand, thereby using the minimum electric energy to drive electrolysis using renewable energy source.

Figure 5.2-2 shows a graph of Global waste heat distributed, as shown by Foreman et.al according to the average temperature (3 categories : <100°C, 100-299 °C and >300°C), for the entire world, and also for the important sector such as transportation, residential, etc.[204] While some successful integrations of waste heat (ex. From marine engines) with SOEC have been demonstrated,[202] it can be seen that only about 21% of the global waste energy has temperatures above 300°C, which is still lower than the lower bound for SOEC technologies developed so far including proton conducting SOEC. This is where our proposed SAEC show clear advantage, where it can be see that ~37% of the world global heat is >100oC which is in the SAEC regime, and infact ~20% of global waste heat (>300°C) can provide the complete heat requirement for our CDP based SAEC.

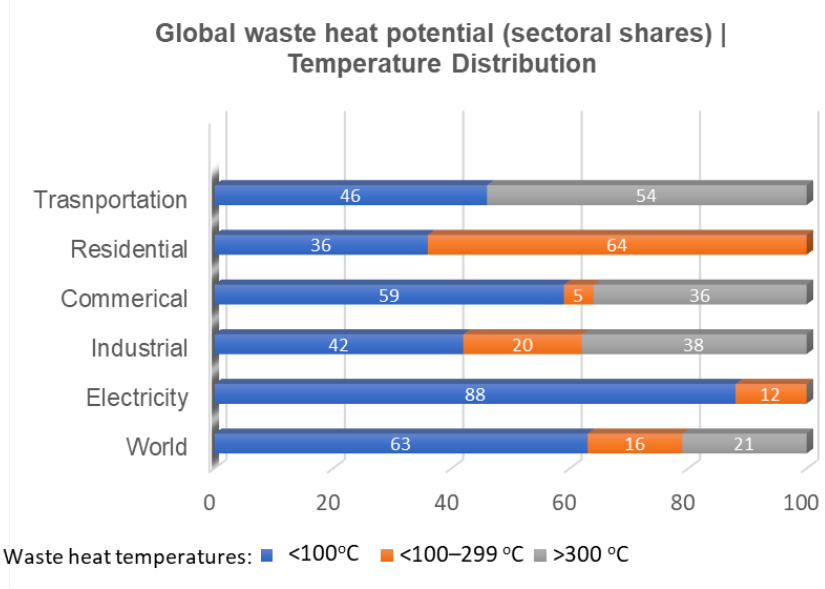

Figure 5.2-2 Global waste heat potential for the world and importance sectors, distributed based on temperature of waste heat. Reproduced using data by global waste study by Forman et.al.[22]

Motivated by above reasons, we demonstrate proof of concept SAEC study here, where in we use oxynitride systems that were identified to be stable with CDP at operating conditions (Mo-O-N and Ta-O-N) are used for the catalysis. Particularly, tantalum oxynitrides were demonstrated as promising OER evolution catalysts, whereas molybdenum oxynitride were studied for HER catalysis.

5.3 Tantalum (Oxy)nitrides for Oxygen Evolution Reaction (OER) in SAEC

5.3.1 Experimental Methods

5.3.1.1 Tantalum oxynitride sample synthesis

Three tantalum oxynitride samples, synthesized in Chapter 3 were tested for OER catalysis in SAEC., including:

- **β-TaON:** Phase pure micron sized β Tantalum oxynitride powder

  Synthesis (from Chapter 3, section 3.7.2) : Wet ammonolysis (1.18% pH_2O) of Ta_2O_5 @850°C for 35 hrs.

- **β + γ – TaON:** ~ equal mixture of micron sized β and γ Tantalum oxynitride phase powder

  Synthesis (from Chapter 3, section 3.7.2): Wet ammonolysis (1.57% pH_2O) of Ta_2O_5 @850°C for 15 hrs | 45% β-TaON + 48% γ-TaON + 7% δ – TaON (via Lab XRD)

- **Nano – TaON:** Nano sized mixture of β and γ Tantalum oxynitride powder

  Synthesis (from Chapter 3, section 3.7.3): Ca-assisted Urea Sol gel rout --- TaCl5 + CaCO3 + Urea with Ca/Ta = 1 and Urea/ Ta ratio = 2 -→ calcined @775C for 2hrs | 65% β-TaON + 35% γ-TaON with ~6nm crystallite sized nanopowder (via Lab XRD)

Additionally, a reference Ta_3N_5 nitride-based cell was also tested. The phase pure Ta_3N_5 was obtained as described in Chapter 3, via dry ammonolysis of Ta_2O_5 @850°C for 24hrs.

5.3.1.2 Electrochemical Cell fabrication and Testing Configuration

Materials

Powders of CsH_2PO_4 (CDP) with specific surface area of 2.4 m^2/g were prepared in-house by aqueous routes using cesium carbonate (Alfa Aesar, 99.9%) and phosphoric acid (Fisher Scientific, 85%) as the electrolyte material[19]. Pt on carbon (20 mass% Pt on carbon black, HiSPEC® 3000), Carbon black (99.9%) naphthalene (99.8%) were procured from Alfa Aesar.

SAEC Button Cells Fabrication based on Tantalum oxynitride for OER

Solid acid electrolyzer cells, 1.9 cm in diameter were fabricated using superprotonic CsH_2PO_4 as the electrolyte and tantalum oxynitride powders as an electrocatalyst for oxygen evolution. Additionally, to provide electronic and protonic conduction pathways in the cathode, carbon black and CsH_2PO_4 were respectively mixed in with the catalyst powder. Figure 5.3-1 shows the schematic of SAEC OER Testing configuration, while also showing the electrode mixtures.

The method for preparing these SAEC cells were motivated from out Lab's experience in making Solid Acid Fuel Cell (SAFC).[42, 45] and also discussed in Chapter 2. Infact, the counter electrode mixture and fabrication technique used here SAEC is the same used for standard Pt on C based Anode for Hydrogen evolution reaction (HOR) in Solid acid fuel cells (SAFC), as Pt/C is the safest bet to minimize overpotentials from the HER on the counter electrode of our SAEC. Following Cell fabrication protocol was used:

Counter Electrode:

- 25 mg of a mixture of CsH_2PO_4 and Pt on carbon (20 mass% Pt on carbon black, HiSPEC® 3000, Alfa Aesar) in a 6:1 mass ratio. – Pt/C Layer
- Above layer is supported on 75 mg of a mixture of CsH_2PO_4, carbon black acetylene (Alfa Aesar, 99.9%) and naphthalene (Alfa Aesar, 99.8%) in a 3:1:2 mass ratio, where the naphthalene serves as a fugitive pore former --- MPL Layer

- These two bilayers are supported on a Gas diffusion layer (GDL), which also acts as a current collector, as shown in Figure 5.3-3). This GDL is same as the one used for SAFC Anodes.

Electrolyte:

- ~50 mg CDP is spread on the anode bilayer supported on GDL, pressed for 1min at 4 ton in uniaxial press, resulting in ~50 mm thick dense electrolyte layer. --- Half Cell

Working Electrode (Anode) - for OER

- ~50mg mixture of CDP, Tantalum oxynitride powder, and C-Black in 3:3:2 ratio, pressed on the half cell electrolyte for 1 second at 1 ton in uniaxial press. --- Working Electrode for OER
- Carbon paper (TGP-H-120 Toray paper) followed by Stainless steel mesh (as diffusion layer), and Teflon tape wrapping on edges was used to complete the SAEC button cell for testing (Figure 5.3-3).

SAEC Electrochemical characterization (OER configuration)

For electrochemical characterization, cells were sealed into an in-house constructed test station, that was used in Chapter 2 for Solif Acid Fuel Cell testing, and has been described elsewhere.[42] SAEC polarization curves were collected at 250 ºC after thermal equilibration. Anode (working electrode) and Cathode (counter electrode) supplied with humidified (pH_2O = 0.38 atm) high purity nitrogen at a flow rate of 40 sccm each side. Data were recorded using a BioLogic SP-300 potentiostat configured with an integrated frequency response analyzer. Polarization curves were obtained every hour over a period of 12 h, by applying a positive voltage bias from 0 to either 1 or 1.5 V (see Table 5.3-1 for cell specific details), at a rate of 10 mV/s.

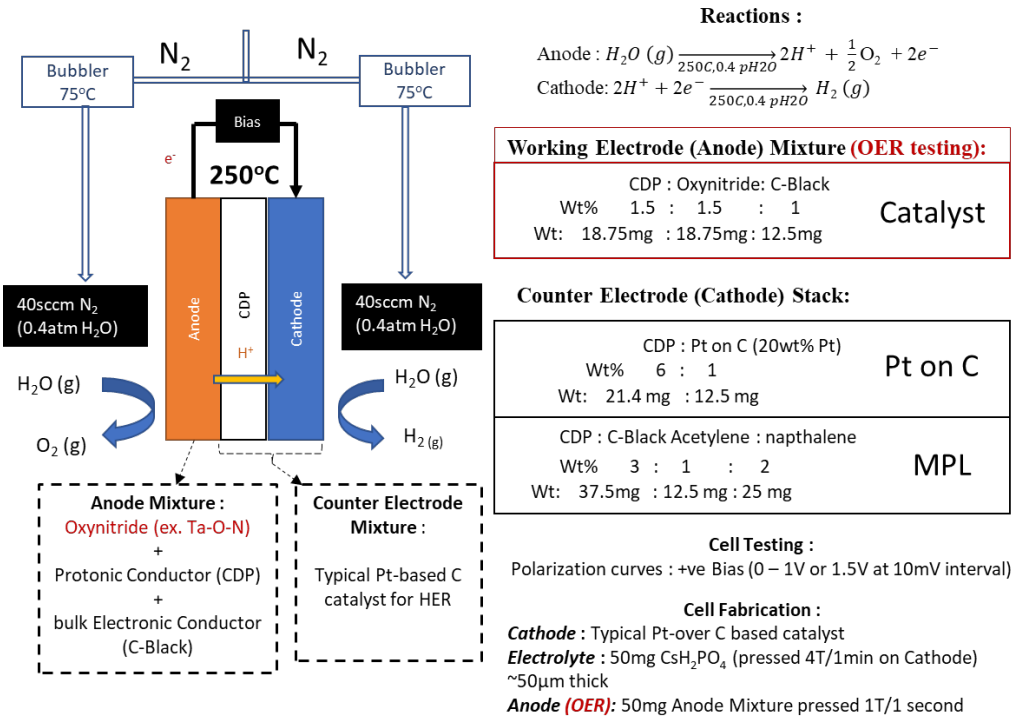

Figure 5.3-1 Schematic of SAEC for Oxygen Evolution Reaction catalysis using Tantalum Oxynitride as the catalyst. Testing configuration, Cell fabrication and Electrode mixtures are shown.

5.3.2 Results and Discussions

Seven SAEC cells with anode based on Tantalum oxynitride powders for OER catalysis were evaluated in this proof-of-concept study for SAEC. Identical fabrication procedures were employed for the cathode and electrolyte components, and the cells differ only in the composition of the oxygen evolution anode, with the details provided in Table 5.3-1

All cells were fabricated using tantalum oxynitride as the catalyst. Cells 1, 2 and 3 are based of phase pure phase pure β-TaON (baddelite type, $P2_1/c$), and are referred to as β-TaON-#1, β-TaON-#2 and β-TaON-#3 respectively. Initial polarization curves for these cells (green curves), when biased from 0-1V, is shown in Figure 5.3-2. At 1V (maximum voltage), the current density ranged from 1.6 to 3.2 mA/cm2 for measurements of three distinct β-TaON based cells. Under the assumption that the entirety of this current

results in water splitting (100% faradaic efficiency) with no parasitic reactions, the computed oxygen evolution rate is 0.06 to 0.12 mmol $O_2/cm^2/h$. It should be noted that the thermodynamic potential required for splitting liquid water at room temperature is 250^{o}C is 1.23V, and often bias voltages over 2V are often applied to overcome additional overpotentials. However, since there is no bubble formation in steam electrolysis in SAEC, positive current densities can be obtained at low voltages, with no apparent take-off voltage, at least for these SAEC OER polarization curves based on active TaON catalyst. However, to push the performance, the bias for the subsequently tested cells was increased to 1.5V, and higher potential stability was studied.

Table 5.3-1 Summary of electrochemical solid acid cells used for the evaluation of oxygen evolution activity of tantalum oxynitride.

Cell	Cell Label	Oxygen evolution catalyst	Electronic Conductor	Polarization Curves (@10mV/s)
1	β - TaON – C-#1	β - TaON	carbon black	0 – 1 V
2	β - TaON – C-#2	β - TaON	carbon black	0 – 1 V
3	β - TaON – C-#3	β - TaON	carbon black	0 – 1 V
4	β+γ – TaON – C-#1	mixed phase TaON*	carbon black	0 – 1.5 V
5	β+γ – TaON – C-#2	mixed phase TaON*	carbon black	0 – 1.5 V
6	β+γ – Nano TaON – C	mixed phase TaON$	carbon black	0 – 1.5 V
7	Ta_3N_5 - C	Ta_3N_5	carbon black	0 – 1 V

*44.8% β-TaON + 48.40% γ-TaON + 6.8% δ – TaON (via Lab XRD)

$65% β-TaON + 35% γ-TaON (via Lab XRD)

It has been shown by Wang Z et.al that Ta-O-N system with metastable γ - TaON polymorph as major phase, has better water splitting catalysis for OER at room temperature, compared to β-TaON dominated mixture.[24] In order to know if having phase – pure β-TaON was beneficial or not, next two cells fabricated using wet ammonolysis Ta-O-N product containing nearly equal wt% of β and γ TaON phases, called as β+ γ-TaON – C - #1 and β+ γ-TaON – C - #2. Both Figure 5.3-2a) and b) have the polarization curves for these two cells which were biased to 1.5V, however in Figure 5.3-2a) the plot of these cells are

just plotted upto 1V to compare them with the β-TaON cells that were only biased to 1V. In comparison to β TaON cells, mixed phase TaON based cells (red curves) tested show similar performance, producing 0.1 mmol $O_2/cm^2/h$ @1V bias (assuming 100% faradic efficiency), highlighting the phase insensitivity of SAEC OER to tantalum oxynitride phases. Interestingly, the spread in performance (compared at 1V) for β TaON cells was larger, however mixed TaON based cells, showed reproducible performance. Exponentially higher current densities (~65 mA/cm^2) was recorded for the mixed-phase cells at 1.5V Figure 5.3-2b), enabling the β + γ – TaON based cells to produce upto 2.5 mmol $O_2/cm^2/h$ (24times compared to that at 1V). In comparison to the characteristic polymer electrolyte membrane electrochemical cells using state of the art Ir-RuO_2 as oxygen evolution catalyst, at least 2 V is required to achieve current densities of approximately 40 mA/cm^2.[199, 205] Here, such current densities are achieved at a voltage of only about 1.4 V, without the use of any noble metal co-catalysts, making these results promising for the proof-of-concept SAEC cells.

Comparing β only and mixed TaON OER cells at 1V, it's clear that the performance does not degrade with γ-phase in the mixture, which means that alternate synthesis routes that result in nanopowders of TaON, even though not phase pure, can be used to further push performance. In Chapter 3, section 3.8.3, we synthesized such TaON nanopowders using Urea based sol-gel route. The technique did not result in any phase pure products, however, it does results in uniform looking nanopowders with an average crystallite size of ~6nm. Given the phase insensitivity realized above, one of these nano TaON products (65% β-TaON + 35% γ-TaON) were tested in this study, and the cell is called β+γ-Nano TaON-C. Polarization curve for this cell is shown in Figure 5.3-2b) comparing with micron-sized mixed TaON cells, and by using nanopowders, current densities exceeding 70mA/cm2 can be obtained, meaning upto 2.75 mmol $O_2/cm^2/h$. Also, the cell performs much better at lower voltages, (0.27 mmol $O_2/cm^2/h$ @1V compared to 0.06-0.10 mmol $O_2/cm^2/h$ for other cells), possibly due to increase active surface area due to nanosized powders. It's noteworthy that the Nano-TaON cell polarization curve for the Nano TaON cell starts to plateau around 1.5V, which could be indicative to mass transport limitation, meaning higher gas flow could help avoid this, and achieve higher results at

1.5V. While promising at first, these Nano-TaON based cells degrade very quickly with time, as discussed later.

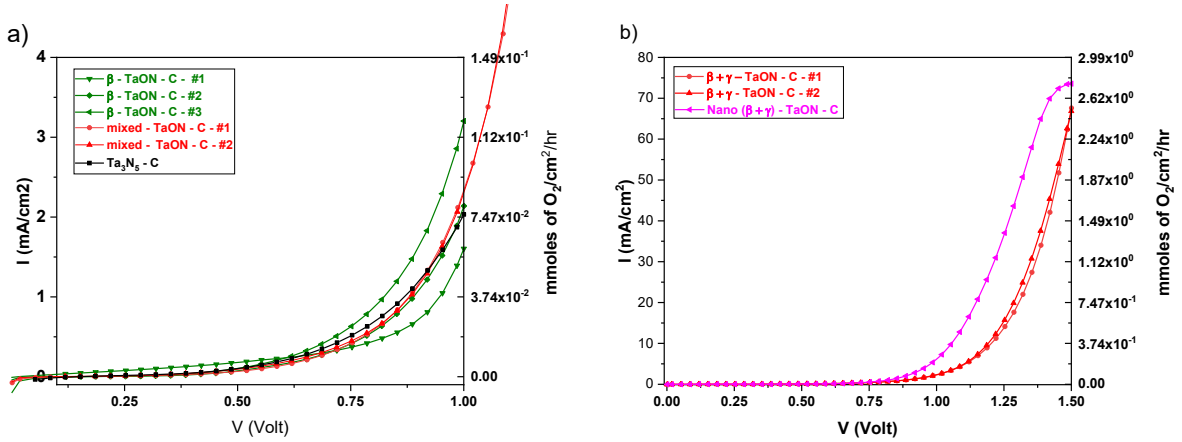

Figure 5.3-2 Intiail polarization Curves (I-V plot) and calculated oxygen evolution rate (mmoles of O_2/cm^2/hr). (a) Performance of phase pure β-TaON based cells (green curves) and mixed TaON based cells (red curves) (b) Exponential performance increase on increasing the bias to 1.5V. Both micron sized mixed TaON cells and Nano-TaON based cell (pink curve) were tested, with nanopowder outperforming the mixed phase micron size TaON powders.

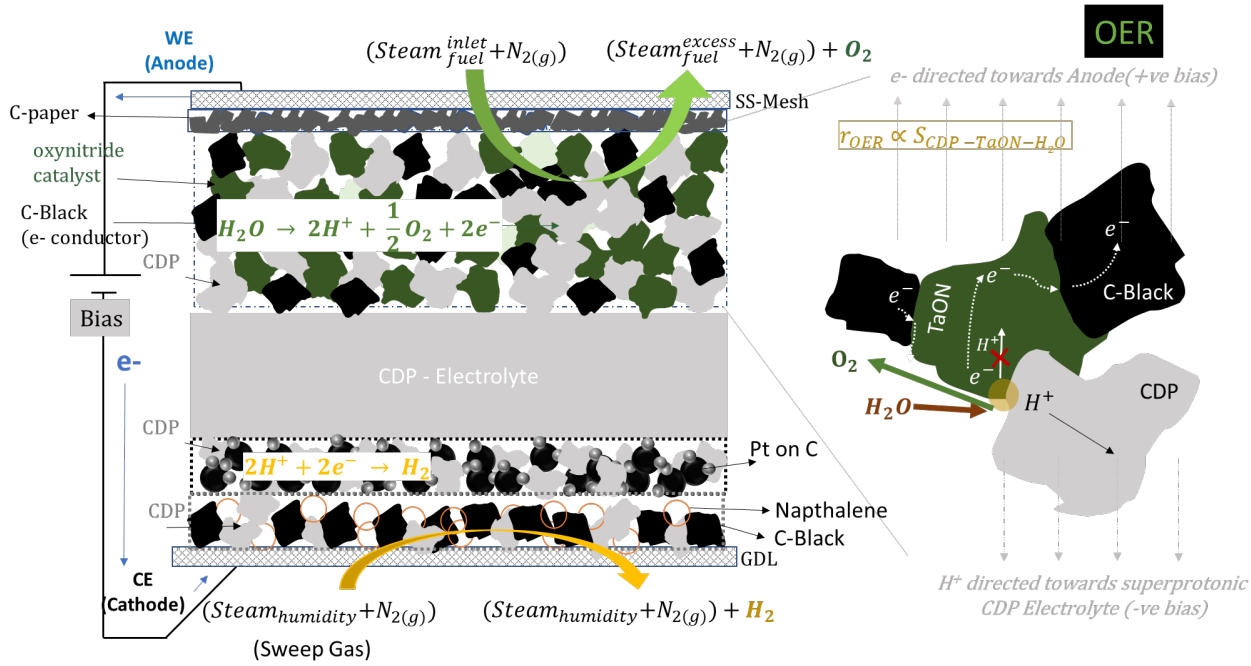

Figure 5.3-3 Schematic of SAEC cell stack showing individual mechanically mixed and pressed layers for OER under humidified N_2 at 250°C. Right: Proposed reaction mechanism for OER in SAEC anode, based on mechanically mixed

(TaON + CDP + C-Black) anode, showing the reaction should be dependent on the triple phase boundaries between electrolyte, catalyst (oxynitride) and steam.

Figure 5.3-3 shows a schematic of the SAEC membrane-electrode assembly of a single button cell, along with the proposed mechanism for the OER reaction in this SAEC anode. The OER reaction involves steam splitting into oxygen along with protons and electrons, where the protons make their way to the cathode through the CDP network (via electrolyte) in the anode, while the electrons reach the current collector. These electrons then pass through the external circuit to combine with protons at the cathode side to complete the water-splitting reaction on the counter electrode via hydrogen evolution. Since the protons are not expected to travel through the bulk of oxynitride, this OER process should be limited by the triple-phase boundaries between CDP – TaON-H_2O as shown in Figure 5.3-3. This assumes that TaON is still conductive (semiconductor) enough to allow e- to reach C-black, which form the main electronic conductivity pathway. Nanopowders of TaON would maximize these triple-phase boundaries explaining the improved initial performance, however, their rapid degradation could be due to rapid agglomeration or possibly their easier oxidation due to nano size.

Performance with time was evaluated by obtaining polarization curves every hour for 12hrs for each of the cells. Figure 5.3-4, shows Current density values at 1V for all TaON based SAEC cells extracted from polarization curves taken each hour for 12hr. Figure 5.3-5a) shows the oxygen evolution rate (mmoles of O_2/hr/cm^2) for each of the cells compared at 1V, initially (solid coloured bar plots) and after 12hrs (patterned same coloured bar plots). It can be seen that at this bias, all cells were relatively stable compared to the Nano-TaON cell, which lost >95% of its performance in 12hrs. All β-TaON based cells, which had oxygen evolution rate between 0.06-0.12 mmoles of O_2/hr/cm^2 @ 1V (solid green bars in Figure 5.3-5a)), perform stably for the whole 12 hrs (green curves in Figure 5.3-4), with only about ~10-15% loss in performance, still resulting upto 0.11 mmoles of O_2/hr/cm^2@1V after 12 hrs of testing (Patterned green bars in Figure 5.3-5a)). In comparison at 1V, both β+γ-TaON based cells show more erratic behavior. Both show an increase in performance for the first couple of hours, with Cell #2 (circle symbol, green curve, Figure 5.3-4) ending back to intial level, whereas Cell#1 (square symbol, green

curve, Figure 5.3-4) ending up with a better performance at the end. However, even at the end of 5hrs, upto 0.15 mmoles of O_2/hr/cm^2 @1V (Patterned red bars in Figure 5.3-5a)) could be achieved, at par with the phase pure β- only cells. However, the current density values at a higher bias (1.5V) for these two mixed-phase cells kept on decreasing with time. Figure 5.3-6 shows complete polarization curves for all cells tested to 1.5V bias, which were all based on mixed-phase TaON. Figure 5.3-6b)) It can be seen that while the current densities of β+γ-TaON #1 (Figure 5.3-6a)) increased with time at 1V, the current densities at 1.5V suffered 36% loss in 12hrs. β+γ-TaON #2 (Figure 5.3-6b)) was even worst at 1.5V and lost 59% performance in the same period. However, it should be noticed that the rate of degradation decreased over time (overlapping I-V curves at the end of 12 hrs), and even at the end of 12 hrs, upto 1.6 mmoles of O_2/hr/cm^2@1.5V.

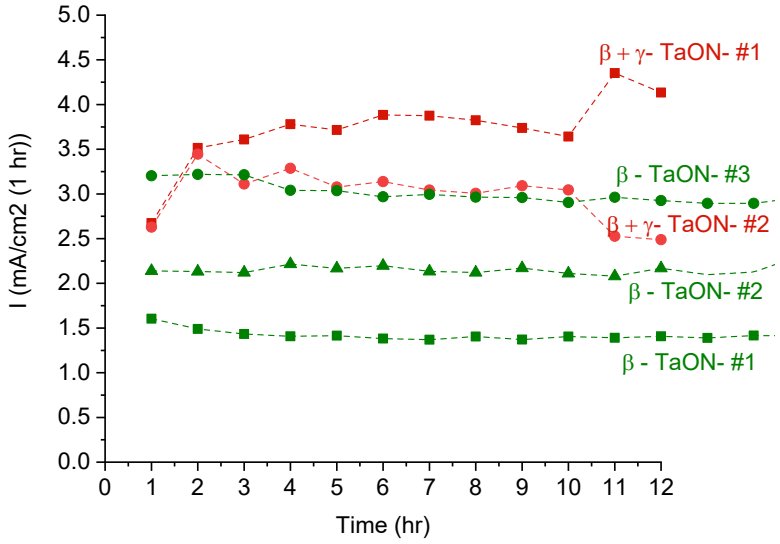

Figure 5.3-4 : Current density values at 1V for all TaON based SAEC cells extracted from polarization curves taken each hour for 12hrs (except Nano-TaON which degraded too quickly and is now shown here).

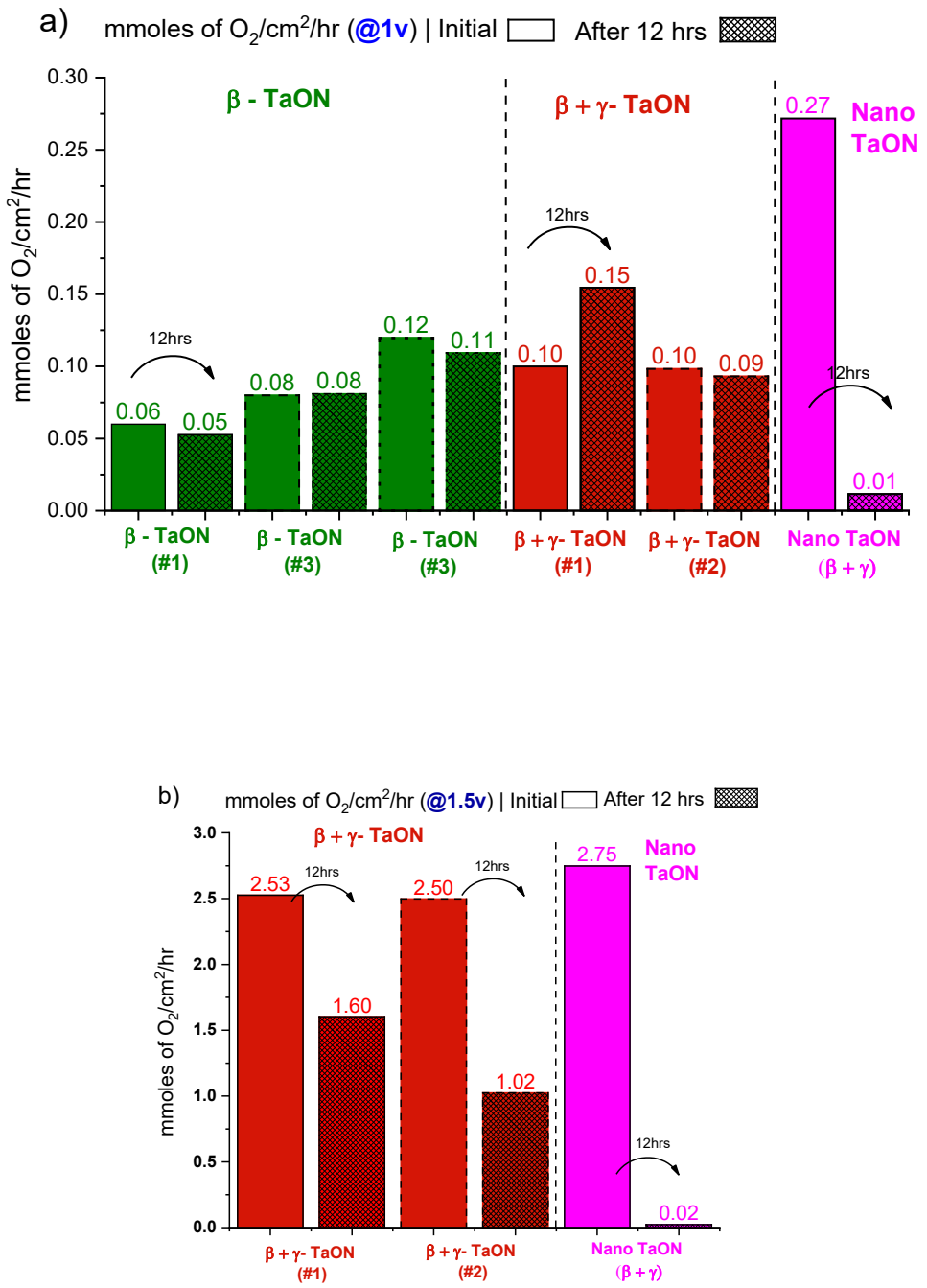

Figure 5.3-5 OER rate (assuming 100% faradaic efficiency) for different Tantalum oxynitride based SAEC cells evaluated in this work. Initial performance is shown in solid color bard, while performance after 12 hrs in patterned bars of same color. β only is green bars, β+γ in red bars and Nano TaON in pink bars. (a) OER of all cells @1V bias (b) OER for mixed phase cells biased to 1.5V.

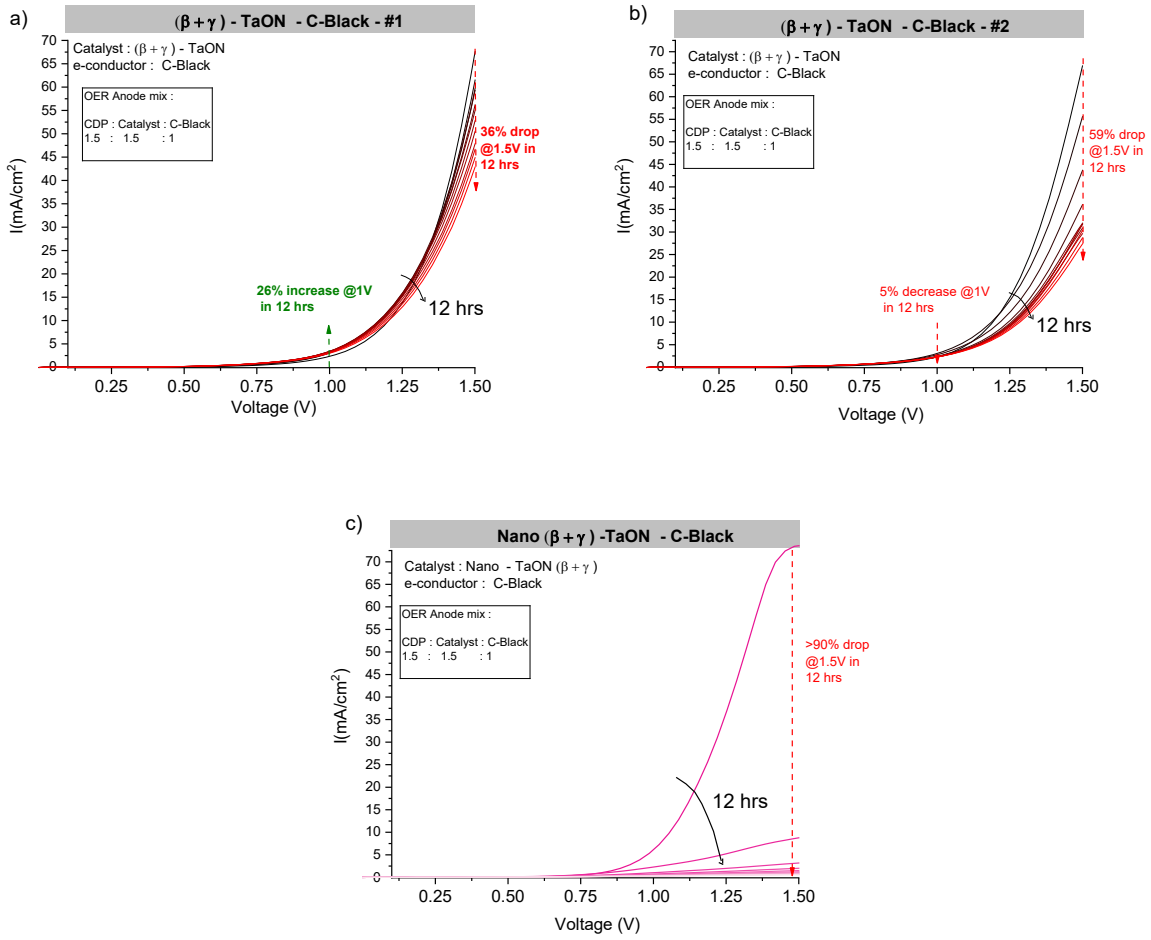

Figure 5.3-6 Polarization curves with time (12 hr period, measured each hour) for mixed phase TaON based SAEC cells. (a) β+γ-TaON-C-#1 cell, (b) β+γ-TaON-C-#1 cell and (c) Nano-TaON-C

5.4 Molybdenum (Oxy)nitrides for Hydrogen Evolution Reaction (HER) in SAEC

5.4.1 Experimental Methods

5.4.1.1 Molybdenum oxynitrides sample synthesis

Three molybdenum oxynitride phases (cubic, hexagonal, and tetragonal), were tested for HER catalysis in SAEC. The cubic and hexagonal phase synthesis were described in Chapter 3, where we also discussed their synthesis pathway using collaborative in-situ XRD studies. These were later characterized to have oxygen and hydrogen in bulk in Chapter 4 using advanced characterization techniques. Tetragonal phase synthesis is described in Appendix C.1, where it's also shown to be an oxynitride hydride. The Lab XRD patterns of these three molybdenum oxynitride hydride samples, with $MoN_xO_yH_z$ type compositions are shown in Figure 5.4-1, with brief recall of synthesis below:

- **Cubic P Molybdenum Oxynitride (γ'-phase) | C800**:

Synthesis (C800 sample from Chapter 3, section 3.6.2) : Dry ammonolysis of MoO3 @800oC for 3 hrs.

Step wise heating profile: Rt – 350oC @3oC/min -> 350-500oC @0.6oC -> 500-700oC @3oC/min

- **Hexagonal Molybdenum Oxynitride (δ -phase) | H700**:

Synthesis (from Chapter 3, section 3.6.3): Wet ammonolysis (2% pH2O) of MoO2 @700oC for 12 hrs

Constant heating profile: Rt – 700oC @3oC/min

- **Tetragonal Molybdenum Oxynitride (β – phase) | T700:**

Synthesis (from Appendix C.1): Nitridation of MoO3 under 3:1 vol/vol H2 + N2 @700oC for 3 hrs

Step wise heating profile: Rt – 350oC @3oC/min -> 350-500oC @0.6oC -> 500-700oC @3oC/min

Note to reader: While variability in composition with different MoO_3 precursor bottles for cubic samples (including the C800 used here) was discussed at length in Chapter 4 and Appendix B.8. However, for this study, only a single bottle of MoO_3 (referred to as Alfa Aeser – 01 ↔ AA-Orig ↔ AA-Original) was used for the cubic phases powders synthesized for this study. Most chemical and structural analyses in Chapter 4 were also performed on samples from this bottle.

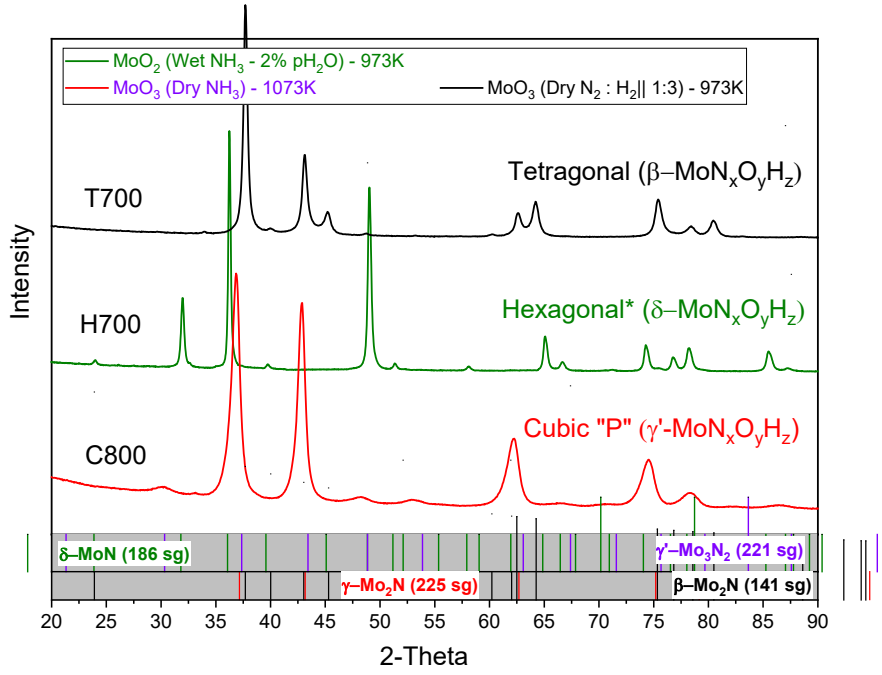

Figure 5.4-1 The Lab XRD pattern of the 3 important Molybdenum oxynitride phases (C800, H700 and T700 samples) used in this work. As discussed in earlier chapters, while these match to Cubic Pm-3m (γ'-Mo_3N_2 PDF# 04-007-1915), Hexagonal (δ-MoN PDF#04-003-5713) and tetragonal β-Mo_2N (PDF#01-075-1150) XRD patterns from literature, all of these actually are Molybdenum oxynitrides with possibility of various amounts of hydrogen in bulk | MoNxOyHz type composition.

5.4.1.2 Electrochemical Cell fabrication and Testing Configuration

Materials

Powders of CsH_2PO_4 (CDP) with specific surface area of 2.4 m^2/g were prepared in-house by aqueous routes using cesium carbonate (Alfa Aesar, 99.9%) and phosphoric acid (Fisher Scientific, 85%) as the electrolyte material.[20] Pt on carbon (20 mass% Pt on carbon black, HiSPEC® 3000), Carbon black (99.9%) naphthalene (99.8%) were procured from Alfa Aesar.

SAEC Button Cells Fabrication based on Molybdenum oxynitrides for HER

The cell fabrication of SAEC for HER, is very similar to the one described above for the case of OER. In this case, the working electrode is the cathode, whereas the Pt/C based standard catalyst was used in the counter electrode. Typically, for HER catalysis, Solid acid electrolyzer cells, 1.9 cm in diameter, were fabricated using superprotonic CsH_2PO_4 as the electrolyte and molybdenum oxynitride bulk powders as an electrocatalyst for hydrogen evolution. Unlike the case of OER, C-Black was not used in working electrode here for HER, as molybdenum oxynitrides are known to have decent electronic conductivity, unlike the case of TaON semiconducting powders. Therefore, only CsH_2PO_4 (for protonic pathway) and conducting catalyst powder were mixed to make the HER working electrode. Figure 5.4-2 shows the schematic of the SAEC HER Testing configuration, along with the details of electrode mixtures.

The method for preparing the SAEC half-cell comprising of the counter electrode and electrolyte layer is exactly the same as putting together SAEC cells for OER using tantalum oxynitrides as described in section 5.3.1.2. Working electrodes were, however, fabricated in the following way :

Working Electrode (Anode) - for OER

- ~50mg mixture of CDP and Molybdenum oxynitride catalyst in 1:3 ratio, pressed on the half-cell electrolyte for 1 second at 2 ton in uniaxial press. --- Working Electrode for OER

- Carbon paper (TGP-H-120 Toray paper) followed by Stainless steel mesh (as diffusion layer), and Teflon tape wrapping on edges was used to complete the SAEC button cell for testing (Figure 5.4-9).

Unlike OER SAEC cell fabrication a higher (2T compared to 1T) uniaxial pressure was used to press the working electrode for HER, as at 1T enough flatness and stability of stack was not observed. This could be because of high hardness of molybdenum nitrides.[205, 206] All three phases (Cubic, Hexagonal and Tetragonal) were tested for HER. Cells fabricated using C800, H700 and T700 for simplicity are called Cubic “P”, Hexagonal and Tetragonal in the plots.

SAEC Electrochemical characterization (HER configuration)

For HER electrochemical characterization, SAEC cells were sealed into an in-house constructed test station, the same one used for OER evolution above, and has been described elsewhere.[42] A series of Impedance spectroscopy, Polarization curve, and Chronoamperometry cycles (current with time under constant voltage) were measured in batch mode for a total run time of ~5hrs, collected at 250^{o}C. Anode (working electrode) and Cathode (counter electrode) were supplied with humidified (pH_2O = 0.38 atm) high purity hydrogen at a flow rate of 40 sccm each side. Data were recorded using a BioLogic SP-300 potentiostat configured with an integrated frequency response analyzer. Impedance spectra were collected over the frequency range 0.1 to 10^6 Hz without bias at open circuit voltage (OCV). Polarization curves were obtained by applying a bias from 0 to either 0.75V, at a rate of 10 mV/s.

After initial thermal equilibrium for about 3 hrs at OCV, first round of impedance spectra followed by polarization curve were collected (called as ‘0hr’ in plots below). Following this, a constant bias of 0.5V was applied and the current was monitored with time for the next 55 minutes. This completes the initial electrochemical characterization. After this, the cell was allowed to equilibrate at OCV, for the next 5mins, following which again the Impedance – Polarization- Chronoamperometry cycle was repeated, followed

by equilibration at OCV again for 5mins. The performance was monitored this way with time, for 5 hrs total.

Slopes from polarization curves (linear region) were used to get the area specific resistance values (R). Note that some non-zero transient current was observed at OCV, and the linear region of I-V curves was obtained beyond 0.25-0.3V, used to calculate R. Ohmic resistance contribution in this (R_{ohmic}) were extracted using the intersection of impedance arcs with the X-axis. Charge transfer resistance (R_{ct}), which is the measure of how good the catalyst in minimizing activation barriers for the steam electrolysis, using $R_{ct} = R - R_{ohmic}$

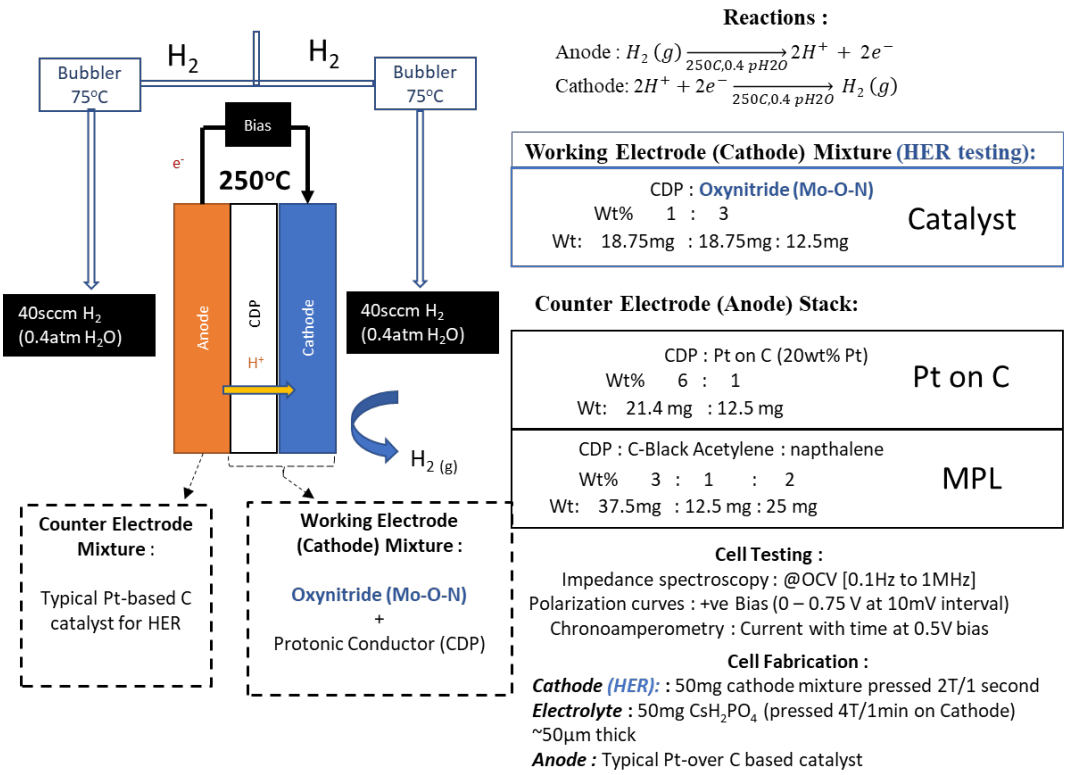

Figure 5.4-2 Schematic of SAEC for Hydrogen Evolution Reaction catalysis using Molybdenum Oxynitride as the catalyst. Testing configuration, Cell fabrication and Electrode mixtures are shown.

Note to reader: Full electrolysis polarization curves were also collected in preliminary experiment at 250°C under humidified N_2 instead of H^2, using C800 (Cubic P sample) as the test sample. Please see Appendix B.9. Polarization curves were collected every hour for 45 hrs biasing from -0.5V to 1.5V. Rapid degradation (see Figure B.9-5, Appendix B.9.5) was observed on the OER side. 85% drop (current densities @1.5V | OER) was observed over 45 hrs, with 60% of the performance drop occurring within first 5 hrs. It is interesting to recall that Mo-O-N was found to be stable with CDP structurally under humidified N_2 (Appendix B.9.3 shows, successful stability test for 60hrs) suggesting that the degradation could be due to oxidative currents on the OER side. More discussion on molybdenum oxynitrides' instability under oxidative conditions is discussed in detail through various applications that were attempted in Appendix B.9. This is the why Molybdenum oxynitrides here were only tested for HER, under reducing humidified H_2 conditions as the sweep gas. Also, since good current densities were observed at <1V, to avoid material breakdown and degradation, the bias was limited to 0.75V.

5.4.2 Results and Discussions

HER Polarization curves and impedance spectra at OCV, collected every hour (from Initial to 5hrs), are shown in Figure 5.4-3 , Figure 5.4-4 and Figure 5.4-4, for the Cubic, Tetragonal and Hexagonal Molybdenum Oxynitride cells below. Blue for Cubic, red for Tetragonal and green for Hexagonal, is used as the color scheme for all the plots in this HER study.

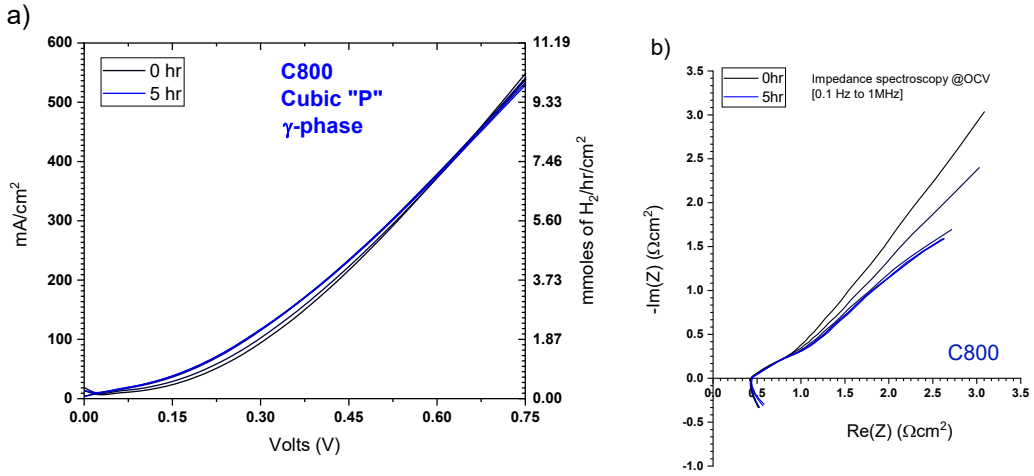

Figure 5.4-3 Polarization curves and impedance spectra (0 – 5hrs, each hour) for HER evolution in SAEC using Cubic Molybdenum oxynitride phase (C800) | γ'-phase.

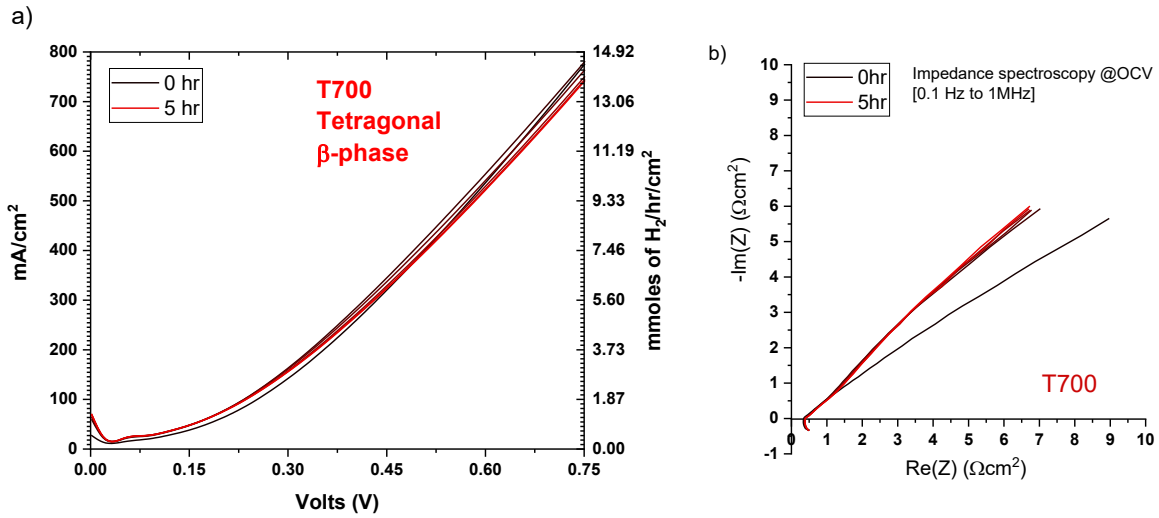

Figure 5.4-4 Polarization curves and impedance spectra (0 – 5hrs, each hour) for HER evolution in SAEC using Tetragonal Molybdenum oxynitride phase (T700) | β -phase.

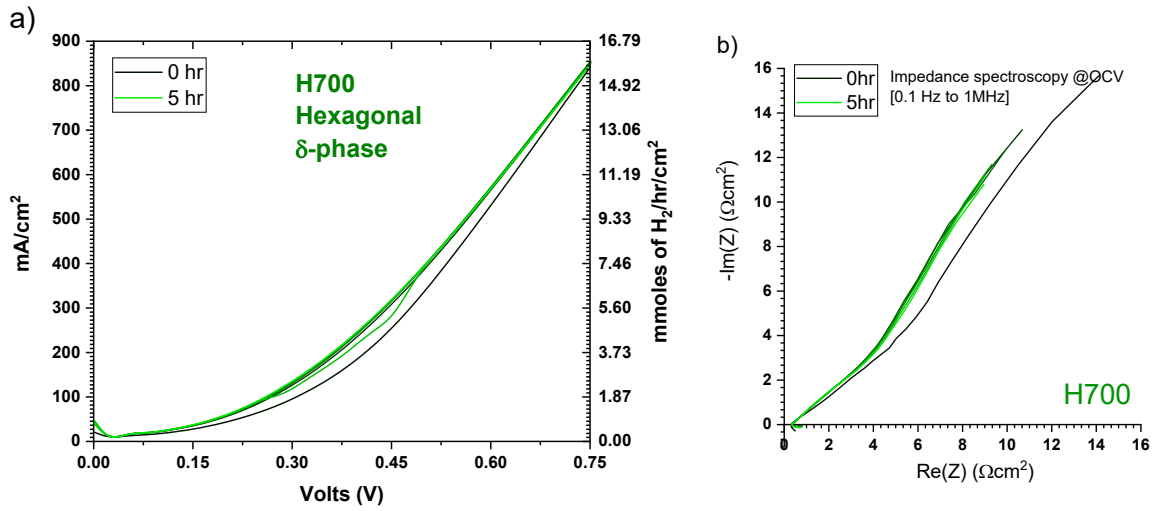

Figure 5.4-5 Polarization curves and impedance spectra (0 – 5hrs, each hour) for HER evolution in SAEC using Hexagonal Molybdenum oxynitride phase (H700) | δ-phase.

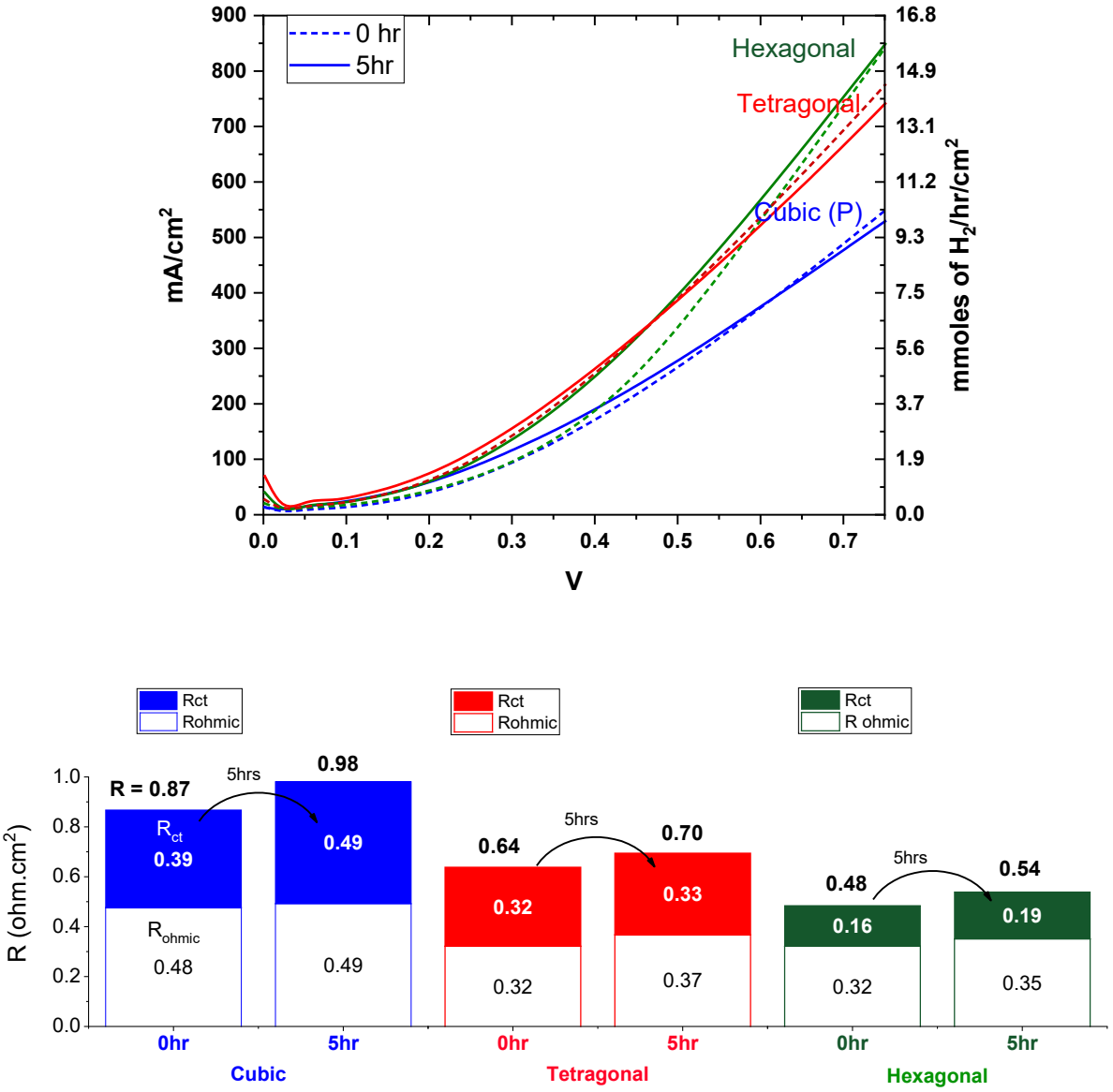

Figure 5.4-6 Top: Polarization curves for HER evolution in SAEC, comparing all 3 Molybdenum oxynitride phases, Cubic (blue curves), Tetragonal (red curves) and Hexagonal (green files). Initial performance in dotted curves and after 5 hrs in solid curves. Bottom: Resistances for HER (R and its breakdown into R_{ohmic} and R_{ct}) for each phase initially and at the end of 5 hrs of testing. Slope of linear regions of I-V curve were used for R calculation. For example, 0.3 -0.75V region was used as the linear region for T700 tetragonal sample.

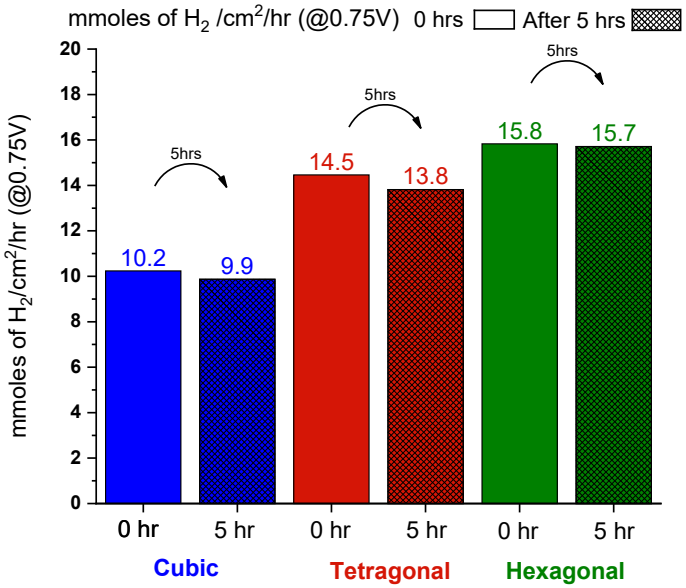

Figure 5.4-7 HER rate for SAEC cells, for all three phases, at 0 (initially) and 5 hrs.

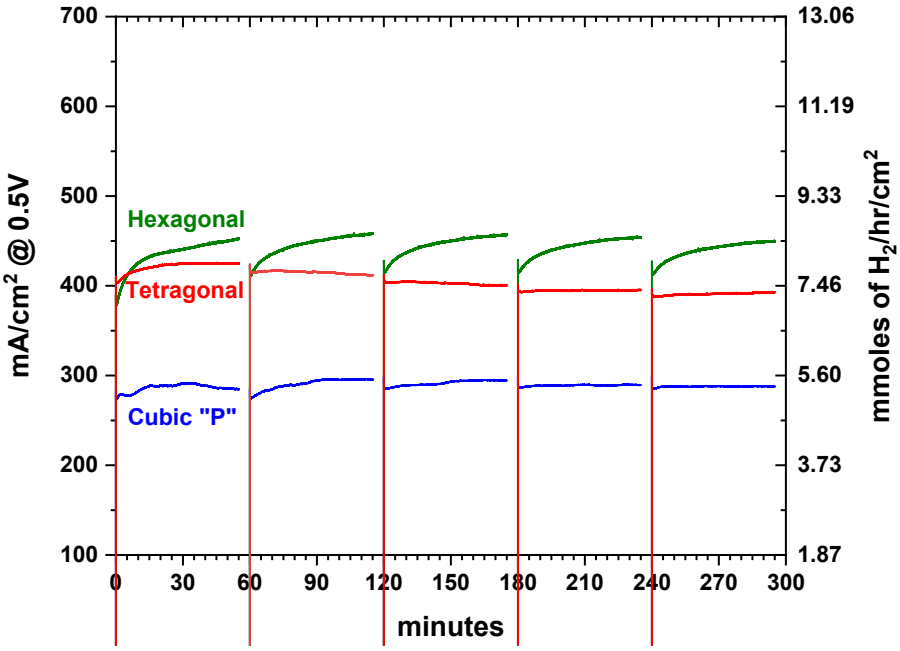

Figure 5.4-8 Chronoamperometry measurements for all 3 SAEC cells, comparing stability of all 3 molybdenum oxynitride phases, cubic (blue), tetragonal (red) and hexagonal (green).

Polarization curves and calculated ohmic and charge transfer resistance (describe in experimental section), for all three molybdenum oxynitride phases for HER is shown in Figure 5.4-6. All three phases (dotted curve, Figure 5.4-6) result in current densities in hundreds of mA/cm^2 (upto 850 mA/cm2 @0.75V for the hexagonal phase). Among the 3 phases Figure 5.4-6 , the following performance order was observed: Hexagonal (~850mA/cm^2@0.75V) > Tetragonal (~775mA/cm^2@0.75V) > Cubic (~550mA/cm^2@0.75V), although tetragonal phase seems to slightly overperform the hexagonal phase for lower bias (<~0.45V).

This is also the overall trend for the net reaction resistance (Ω.cm^2), where the cubic phase (0.48 Ω.cm^2) has 80% more net R than best performing hexagonal phase (0.87 Ω.cm^2), as seen in Figure 5.4-6 bar plots. The bar plots also show the breakdown of net area specific reaction resistance into to ohmic resistance (R_{ohmic}), and remainder to charge transfer (R_{ct}) resistance. Overall ohmic resistance (mostly dependent on electrolyte layer) of cells lied in the range of 0.32-0.48 Ω.cm^2 , where the variation could be due to variability in cell fabrication. In contrast charge transfer (R_{ct}) resistance helps compare catalytic performance of various phases. Overall, cubic cell had both ohmic (0.48 Ω.cm^2) and charge transfer (0.39 Ω.cm^2) resistances higher than the tetragonal and hexagonal cells, where the difference was even larger for the Rct values. Tetragonal and hexagonal cells have almost equal ohmic resistance (~0.32-0.35 Ω.cm^2), therefore the overall higher performance of hexagonal cell is attributed to almost half values of charge transfer resistance (0.16 Ω.cm^2) compared to the tetragonal phase (0.32 Ω.cm^2). Overall, the performance of all the phases is stable over the course of 5 hrs. Even at max 0.75V bias, the loss in current densities for all phases is less than 4%, with only 0.7% of the hexagonal phase, as can be seen by the nearly overlapping dotted (initial, 0hr) and solid curves (after 5 hr), in Figure 5.4-6. Overall resistance R and its constituents ($R_{ohmic,}$ R_{ct}) hold the same trend at 5hr as at 0hr, with only slight increase in values.

Overall, all three cells show hydrogen evolution rate >10 mmoles of H_2/hr/cm^2, with hexagonal phase showing a promising rate of 15.8 mmoles of H_2/hr/cm^2, as seen in Figure 5.4-7. Even after 5hrs of testing (with constant bias of 0.5V being applied between polarization curves), oxygen evolution rates of

10, 13.8, and15.7 mmoles of H_2/hr/cm^2 is observed for the cubic, tetragonal, and hexagonal phases respectively. These values were obtained at 0.75V bias. While very few literatures are available on solid acid based electrolysis, very recently Fujiwara et.al demonstrated HER activity in SAEC operating at 220^{o}C under humidified Argon. In their work, using Pt/C catalyst on both electrodes, and CDP -SiP2O7 composite electrolyte, approximately ~10 mA/cm2 at 1V bias was achieved, where they used mass spec to confirm faradaic efficiency over 75%.[207] While not a direct comparison to this study, as we only evaluate the efficiency of molybdenum oxynitrides for HER reaction catalysis (without overall steam splitting) under humidified H_2, Fujiwara work highlights the advantages of splitting steam at mid temperatures, where upto 100mA/cm^2, at a bias ~5 volts could be achieved. In our preliminary SAEC study, without using any noble metal catalyst, upto 850mA/cm^2 (for hexagonal phase) current density was achieved with just 0.75V bias, demonstrating potential of these molybdenum oxynitrides for HER catalysis in SAEC cells.

Chronoamperometry results, which basically measures the stability of cell under constant load (0.5V in our case), are shown in Figure 5.4-8. All phases, result in reproducible cycles of Chronoamperometry measurements, where at the end of each cycle (~55min), cell is equilibrated for ~5min, following which impedance spectra and polarization curves were drawn, after which the next cycle of Chronoamperometry was repeated. While the hexagonal phase has the highest current densities for HER, it also has the most transient behavior in Figure 5.4-8, that at the start of each chronoamperometry cycle, it takes the most time to reach plateau value, which repeats each cycle. In comparison, tetragonal and cubic phase do show some transient behaviors for the first cycle, however the curves get nominally flat with very less degradation with succeeding cycles.

To hypothesize the possible reasons behind apparent difference in HER activity between the three molybdenum oxynitride phases, it is important to look at the difference in chemical information of these phases, and understand the possible HER mechanism in SAEC. Characterization summary of these 3 phases, discussed at length in other chapters, is summarized in Table 5.4-1. Additionally, Figure 5.4-9 shows the schematic of the full SAEC cell stack based on molybdenum oxynitride cathode for HER

evolution, and the hypothesized reaction mechanism for the same. While the 4e- OER mechanism is more complex and less understood in literature, several studies have explored HER mechanism.[208] The mechanism shown in Figure 5.4-9 is motivated from the learnings from low temperature PEM electrolyzer cells (proton based, acidic media). Overall, in literature, the HER is hypothesized to consist of two main steps, intermediate formation (H*, at an active site, equation 1 below), and its conversion to H_2 molecule, where the later can happen either via reaction between intermediate and another proton and electron (equation 2), or by reacting to itself (equation 3).[208-212] It has been wide considered that the first step is often rate limiting and often the activity is closely related to how the intermediate adsorbs/ interacts with the electrocatalyst, forming the basis of famous volcano plot.[212-214] Very strong or very weak interactions are both not preferred, as the former makes H_2 molecule evolution difficult, while the later inhibits efficient intermediate formation.

$$H^+ + e^- \rightarrow H^* \qquad (1)$$

$$H^* + H^+ + e^- \rightarrow H_2^* \qquad (2)$$

$$H^* + H^* \rightarrow H_2 \qquad (3)$$

HER mechanism in SAEC operating under humidified hydrogen at 250°C, using mechanically mixed molybdenum oxynitride and CDP powder, with Pt/C based counter electrode, and CDP as electrolyte is shown in Figure 5.4-9. Formation of quasi-stable H^* intermediate (neutral H) would be happening at the double phase boundary of CDP and molybdenum oxynitride particles. It is to be noted, that it has been shown in literature,[191] and our characterization studies in our earlier chapters, (Chapter 4, and 1H NMR preliminary studies in Appendix B.6), that molybdenum nitrides synthesized in this study can all incorporate different levels of hydrogen in the bulk. Therefor these intermediates H*, can be hypothesized to combine mostly on the surface, with some formation possible in bulk. However, rapid formation in bulk would have lead to particles cracking, which should have caused transient instabilities in performance which was not observed. However, post performance SEM studies would be needed to confirm this hypothesis. Overall, such a reaction pathway described above would be influenced by different molybdenum oxynitride phases, their crystal structures, anionic and cation distributions in bulk,

along with the surface chemistry of these molybdenum oxynitrides. Additionally, overall SAEC performance would also depend on the e- conductivity of these molybdenum oxynitrides, which would in turn would be influenced bulk nitrogen and oxygen content, with conductivity potentially increasing with decreasing oxygen in bulk.[167] Several of the bulk and surface characterization results (Chapter 4 for C800 and H700, and Appendix C.1 for T700) for the 3 molybdenum oxynitride phase samples used in this work are summarized in Table 5.3-1, and has been used for the discussion below.

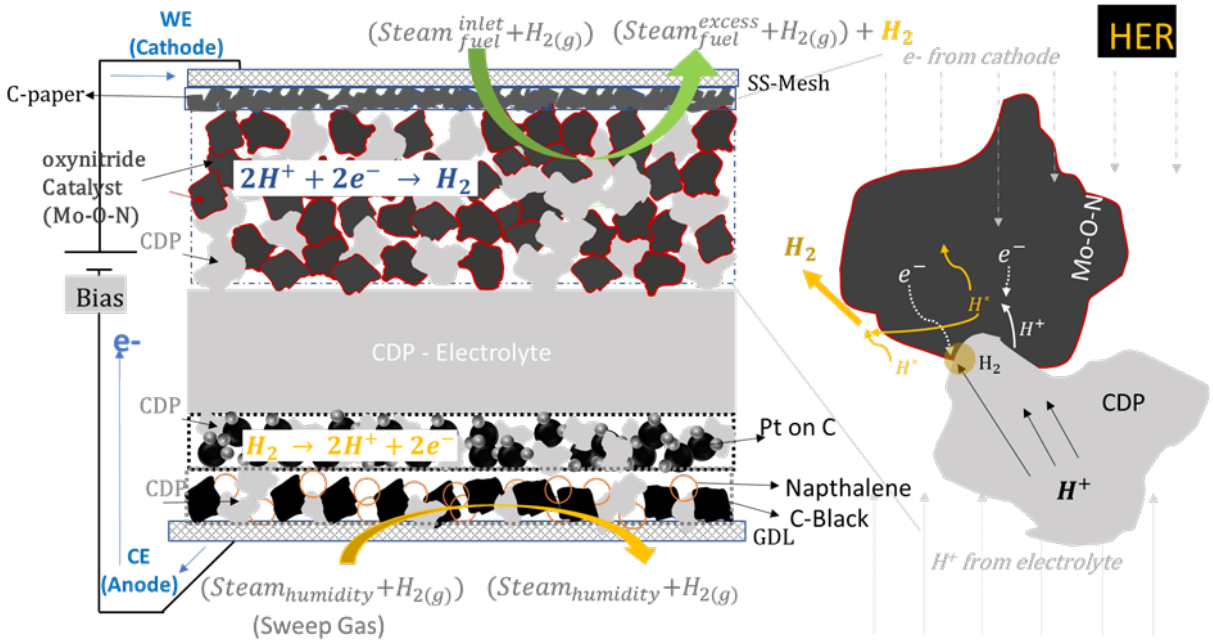

Figure 5.4-9 Schematic of SAEC cell stack showing individual mechanically mixed and pressed layers for HER under humidified H_2 at 250°C. Right: Proposed reaction mechanism for HER in SAEC anode, based on mechanically mixed (Mo-O-N + CDP) anode.

It is interesting to note that the Cubic C800 sample has the highest specific surface area (BET), and higher Nwt% compared to Tetragonal T700 sample, however, it still has the least activity (relatively) out of the 3 phases. One of the possible reasons, could be due to cubic phases' too strong binding affinity towards hydrogen, which is apparent by max retention of adsorbed gases on its surface (mainly composed of NH_3 and H_2O). This combined with its maximum oxide/bulk ratio (a measured of possible oxide layer %, within the depth probed by XPS ~10nm), and most oxygen incorporation in the bulk (potentially low conductivity) could be the main reasons behind relatively lower performance of the cubic

phase for HER. It is expected that the adsorbed gases (on as synthesized) on these molybdenum oxynitrides would evolve at 250ºC (TPR results in Appendix B.5, and discussion in Chapter 4). Although initially ~2-3 hrs is given for cell stabilization before drawing any bias, the apparently visible wavy nature of the chronoamperometry curve (Figure 5.4-8) in the first cycle of cubic cell, could be due to the transient changes happening on surface due to desorption. Given cubic phase has most adsorbed gases compared to other phases, this could explain the initial wavy nature observed in chronoamperometry data for the first couple of cycles for the cubic cell (Figure 5.4-8, blue plots).

Several other correlations can be negated by comparing performance with phase property trends in Table 5.3-1. For example, the performance does not trend with oxidation state of these phases, or with the bulk Nwt%, as both hexagonal and tetragonal phase have similar performance, but very different expected bulk oxidation state and Nwt%. With the surface properties are similar, possible reasons for H700 to outperform T700, could be due to lower oxygen in bulk and its single crystalline like nature, both of which could favor better electron conductivity. Additionally, H700 alligator type surface morphology, provides higher surface area with overall higher active sites, for improved reaction kinetics. More controlled studies would be required to reveal prominent correlations in phase sensitive catalytic performance with bulk and surface properties of these molybdenum oxynitrides for HER catalysis in SAEC.

Table 5.4-1 Chemical characterization summary of the three molybdenum oxynitrides used for HER here. These measurements were described in Chapter 4 (for C800 and H700) and Appendix D.1 (for T700)

Property (Analysis)	Cubic "P" (C800)	Hexagonal (H700)	Tetragonal (T700)
Bulk Properties			
Bulk N wt% (CSHN post desorption)	9.0(3) wt%	11.0(3) wt%	5.8(3) wt%
Bulk Composition (TGA + CHSN (post-desorption)	$MoN_{0.75}O_{0.60}$*	$MoN_{0.88}O_{0.23}$	$MoN_{0.44}O_{0.21}$
Bulk O:N ratio[&]	~0.80	~0.26	~0.47
Bulk Anion/Cation ratio[&]	~1.35	~1.11	~0.65
Mo :N | Mo:H (PGAA)	1.13(3) | 2.53(6)	1.03(2) | 4.05(10)	2.19(5) | 10.1(2)
Crystallinity (TEM SADP)	Single Crystal like	Single Crystal like	Polycrystalline
Surface morphology (SEM)	Smooth micron particles	Smooth micron particles	Alligator skin particles
Surface Properties			
Surface Area (BET)	48-70 m^2/g	30 m^2/g	20 m^2/g
Adsorbed gases (wt%) (TGA – Ar@400C)	6.34(9) wt%	2.18(9) wt%	0.76(9) wt%
Surface Oxide/Bulk ratio[!]	~1.1	~ 0.5	~0.4
Surface Anion/cation ratio[%]	~1.5	~1.3	~2.0
Surface O:N ratio[#]	~0.8	~0.7	~0.8
Esimated bulk Mo oxidation state[@]	~2.6	~2.5	~1.5

*sample to sample variation $MoN_{[0.69-0.71]}O_{[0.13-0.60]}$ | however for this work only Alfa Aaser -01 bottle was used (refer Appendix B.8)

[&] Calculated using bulk composition

% - Thermal XPS: (Area(N1s) +Area(O1s))/Area ($Mo3p_{3/2}^{(\delta+)+(4+)+(6+)}$)

[#] - Thermal XPS: Area(O1s)/ Area(N1s)

[!] - Thermal XPS: Area ($Mo3d_{5/2}^{(4+)+(6+)}$)/Area($Mo3d_{5/2}^{\delta+}$) | assumed all of the 4+ and 6+ is assigned to surface oxide

[@] - based on Thermal XPS Mo^{d+} B.E.

5.5 Summary and Future Outlooks

5.5.1 Summary

Preliminary studies were done as a proof of concept to study SAEC cells based on CDP electrolyte, operating at 250^{o}C. By operating at intermediate temperatures, SAEC enjoy improved kinetics and lower electrical energy requirement for water splitting compared to PEM fuel cell (<100oC operating temperature). At the same time, SAEC are also expected to not suffer from the cycling issues and high-cost requirement for thermal components as in the case of SOEC (>600^{o}C operating temperature). Further, about 1/3rd of the world's waste heat has average temperature above 100^{o}C (> 1/5th above 300^{o}C), which is enough to couple with our proposed SAEC system (operating temperature of 250^{o}C), to completely provide the required heat energy, thereby minimizing the electrical energy required for water splitting. However, SOEC heat requirement is too high compared to SAEC, again highlighting the potential of splitting steam around 250^{o}C.

Solid acid electrolyzer cells, 1.9 cm in diameter were fabricated using superprotonic CsH_2PO_4 as the electrolyte. Oxynitride that were found stable in Chapter 3 with CDP, especially Ta-O-N and Mo-O-N systems were evaluated for OER and HER catalysis in SAEC respectively. Half cells based on Pt/C counter electrode and CDP electrolyte were fabricated in the exact same way for both HER and OER testing.

Tantalum oxynitride powders (in combination with some carbon black and CDP) were tested as effective OER catalysts for OER in SAEC under humidified N_2 at 250^{o}C. Both phase pure β-TaON and phase mixture of β + γ – TaON (in nearly equal ratio), show good performance, with performance not effected by presence of the metastable γ – TaON phase. All β-TaON based cells had oxygen evolution rate between 0.06-0.12 mmoles of O_2/hr/cm^2 @ 1V, with stable performance tested for 12hrs, resulting in upto 0.11 mmoles of O_2/hr/cm^2@1V at the end of testing. Mixed phase cells tested to higher bias (1.5V vs

1.0V for phase pure cells) result in exponentially higher initial OER rate of 2.5 mmol $O_2/cm^2/h$, however higher bias did result in considerable loss in performance over 12 hrs. Interestingly, the current densities at lower bias for the same cells remained equal or even got better. While these are proof of concept SAEC cell, as there is no OER study in literature at the time of writing for OER in SAEC, it should be noted that the OER rates achieved here are promising. In comparison to the characteristic polymer electrolyte membrane electrochemical cells using Ir-RuO_2 which are the state of the art oxygen evolution catalyst, at least 2 V is required to achieve current densities of approximately 40 mA/cm^2.[128, 199] Here, such current densities are achieved at a voltage of only about 1.4 V, most importantly without the use of any noble metal co-catalysts.

SAEC cells with cathodes based on Molybdenum oxynitride powders, were evaluated for HER catalysis in this proof-of-concept study of SAEC operating at 250^oC under humidified hydrogen. All three phases (Cubic, Hexagonal and Tetragonal) were tested for HER. Overall, all three cells show very promising HER catalysis, with hydrogen evolution rate >10 mmoles of $H_2/hr/cm^2$, with hexagonal phase showing a promising rate of 15.8 mmoles of $H_2/hr/cm^2$. Even after 5hrs of testing (with constant bias of 0.5V being applied between polarization curves), oxygen evolution rates of 10, 13.8, and15.7 mmoles of $H_2/hr/cm^2$ is observed for the cubic, tetragonal, and hexagonal phases respectively, with very stable performance. These values were obtained at 0.75V bias. Upto $850mA/cm^2$ (for hexagonal phase) current density at just 0.75V bias, while remaining stable after remaining under constant bias of at least 0.5V for chronoamperometry, with reproducible current densities in each cycle. It's noteworthy that no noble metal or cocatalyst like C-Black was used in this study, demonstrating both the excellent electronic and catalytic potential of molybdenum oxynitrides in SAEC for HER catalysis. Unlike OER, which was phases insensitive to Ta-O-N, the HER showed a clear trend amongst the molybdenum oxynitride phases : hexagonal > tetragonal > cubic. Overall, high oxygen in bulk of cubic phase, combined with high surface oxide layer and surface adsorbed species, is speculated to be the case of its relatively lower performance.

5.5.2 Future Outlook: Thin Films Design for SAEC

This preliminary study uses mechanical mixed electrode for SAEC electrode fabrication. However, in order to pursue this further with strategies to improve performance, stability and decrease catalyst loading, thin film (oxy)nitride based SAEC can be pursued. Figure 5.5-1, compares the OER mechanism in SAEC anodes that are (a) mechanical mixed vs (b) proposed thin films design. One can appreciate that the overall triple phase boundary (TaON-CDP-H_2O) is maximized in case of thin films design. Additionally with thin enough films (processed using ALD), it is possible for proton to conduct through the TaON ALD film, thereby making the reaction possible on entire active area of the TaON-H_2O interface. Jill Wenderrott, from Haile group, has worked recently to establish TaON ALD recipe for its deposition at temperatures suitable for CDP. These can be explored in future. Similar analogy can be made for the HER case using Molybdenum (oxy)nitride based thin films for SAEC cathodes, see Figure 5.5-2. ALD literature on Molybdenum nitride is very limited with most ALD depositions happening >150^oC,[215, 216] therefore as a side project ALD of Molybdenum (oxy)nitride films was studied for potential future application in such SAEC cells. By using exposure mode of ALD at NUFab cleanroom, Northwestern University, recipe to coat MoNx films (x = 0.66, XPS) on Silicon wafer at 150^oC was demonstrated. Please refer Appendix C.6 for details.

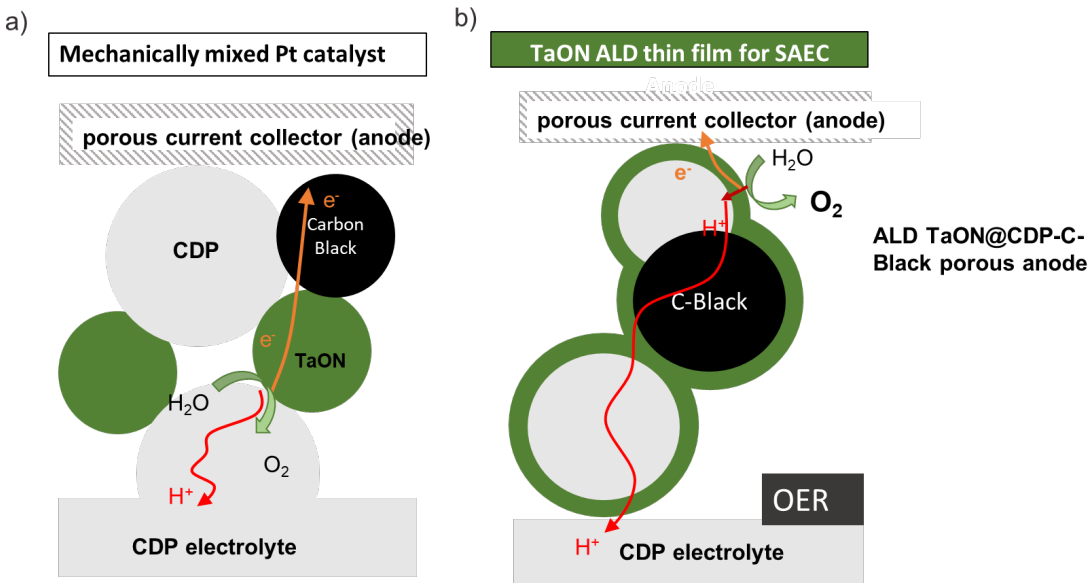

Figure 5.5-1 Future Outlook: Thin films of Tantalum oxynitride for OER catalysis in SAEC anode fabrication

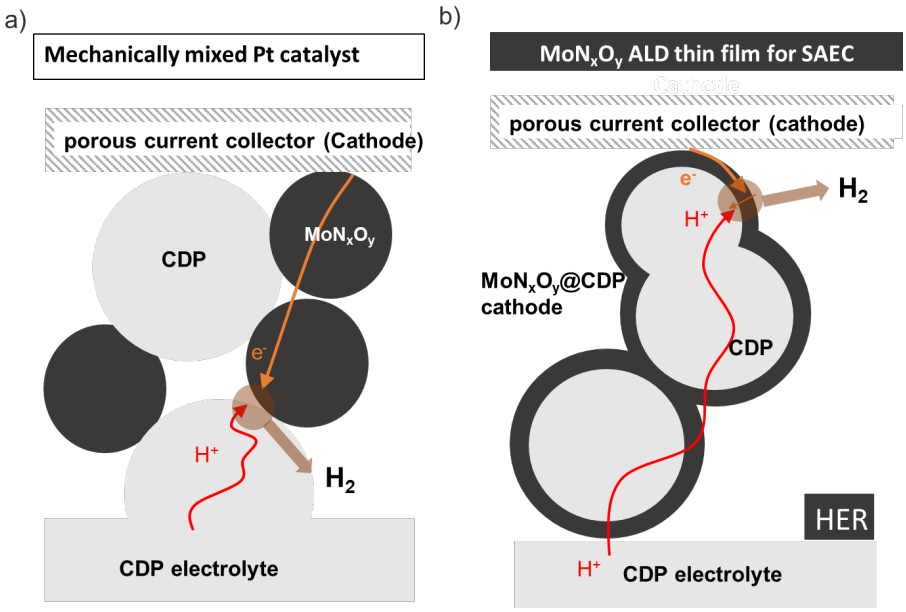

Figure 5.5-2 Future Outlook: Thin films of Molybdenum oxynitride for HER catalysis in SAEC cathode fabrication

5.5.3 Future Outlook: Solid Acid Photo Electrolyzer Cell (SAPEC)

As an extension of SAEC study, proposed Solid Acid Photo electrolyzer cells (SAPEC) can be conceptualized as new device for high temperature solar steam splitting. Such a system would enjoy all the thermodynamic and electrocatalytic advantages of SAEC system, however instead of using electrical energy to drive electrolysis, solar energy will be used. By using a photoactive oxynitride stable with CDP (ex. Ta-O-N) under operating conditions, one can harness the visible light solar energy, to produce a photo-voltage driving force large enough to drive the steam electrolysis at 250°C. Theoretically, for any photo-electrolyzer cells, the reaction can be driven, if the optical band gap of oxynitride used is larger than the minimum steam splitting potential required at 250°C (~1.13V), however, practical band gap requirements are higher due to the penalty of keeping these electron-hole pair separate, and the overpotential involved in water splitting, as shown by the equation below:[217-219]

$$E_g(T) \geq E^o_{H_2O}(T) + \varepsilon_{echem\ overpotential} + \varepsilon_{separation}$$

Given SAPEC would enjoy lower overpotential and $E^o_{H_2O}(T)$ by operating at intermediate temperatures compared to room temperature solar water splitting technologies, lower band gap materials can be used to drive the SAPEC reaction. Using lower band gap materials allows for capturing more of the solar spectrum, thereby promising an increased overall solar to hydrogen efficiency.[220]

Figure 5.5-3 shows the schematic of SAPEC using TaON thin films as photoactive catalyst. Incoming solar energy (photo-anode side), would be aborbed by the photo-active TaON layer, resulting in electron-hole pairs. These holes would then react at the CDP-TaON interface with steam to result in oxygen gas evolution and protons. Simultaneously, the electrons would be collected by the transparent electronic conductor, and would make their way externally to the cathode, where they would react with incoming protons to complete the other counter HER reaction on cathode side.

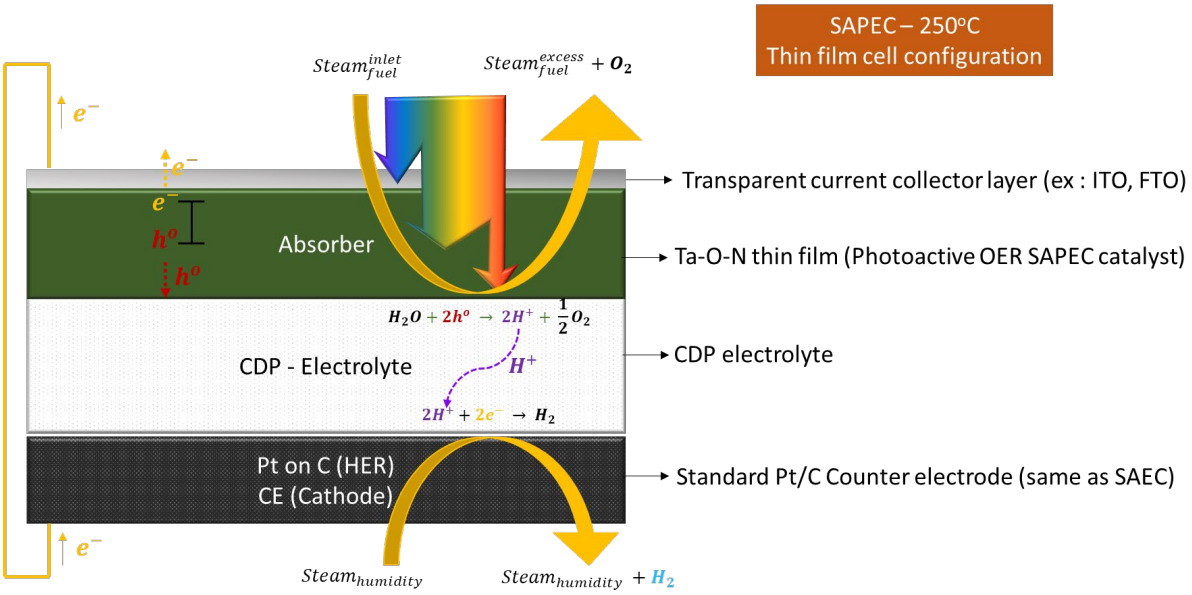

Figure 5.5-3 Propose SAPEC schematic, using TaON thin films as photoactive catalyst.

Appendix A GSAS Simulations for Pm-3m Cubic Molybdenum Oxynitride Structure

A.1 Overview of Simulations

To understand the power of corefinement in distinguishing N and O, and how the occupancies and distribution of cation, anions and hydrogen in interstices effect the substructure and superstructure peaks. All simulations were carried out on Pm-3m space group (221 sg). GSAS was used for simulations.

Reference case (221sg) : fully occupied Mo 1a, 3c and N 1b, 3d sites with Mo_4N_4 composition

Simulation categories :

Category 1 : Different Anion Elements/ Occupancies at 1b and 3d :

Anion vacancy on 1b or 3d (X, N) | Replace N with O on 1b or 3d (N)

Category 2 : Different Cation Occupancies at 1a and 3c :

Mo vacancy on 1a and 3c (X, N)

Category 3 : H in interstices **:**

H around anions 1b (8g, 6f) or 3d [24m, 12h, 6e] (N) | H around cations 1a (8g, 6e) or 3c (24m, 12h, 6f) (N). For simplicity, normalized for H:Mo ratio of ~0.8 which is what was found for the Cubic 700 “Gamma phase” Molybdenum oxynitride samples discussed in Chapter 4.

These simulations point out to the fact that superstructure peaks are visible in following techniques due to following factors (disrupting the translational symmetry between both cation and anion sites if they were fully occupied with only Mo and N):

Xray : Mo vacancy difference

Neutron : Mo vacancy difference | Anion vacancy difference | O replacing N | H present in interstices

Substructure peaks relative intensity vs (111) in Xray varies with :

Mo vacancy : I(200), I(220), I(311) increase vs I(111)

N vacancy : I(200), I(220), I(311) decrease vs I(111) – less evident

A list of all the simulations attempted are summarized in Table A1.1 below (H excluded). When plotting simulated patterns, the highest peak intensities are normalized in all the plots.

Table A.1-1 : Pm-3m synchrotron and NPD simulation models.

Category	Formula	1a (Mo)	1b (N/O)	3c (Mo)	3d (N/O)	Density
All sites Full[#]	Mo_4N_4	1.0	1.0	1.0	1.0	9.724
Vac on Mo site(s)[#]	Mo_7N_8	0.5	1.0	1.0	1.0	8.663
	Mo_5N_8	1.0	1.0	0.5	1.0	6.542
	MoN_2	0.5	1.0	0.5	1.0	5.481
Vac on N site(s)[#]	Mo_8N_7	1.0	0.5	1.0	1.0	9.569
	Mo_8N_5	1.0	1.0	1.0	0.5	9.259
	Mo_2N	1.0	0.5	1.0	0.5	9.104
Vac on both cation and anion[#]	MoN	1.0	1.0	0.5	0.5	6.077
	MoN	0.5	0.5	1.0	1.0	8.508
	Mo_7N_5	0.5	1.0	1.0	0.5	8.199
	Mo_5N_7	1.0	0.5	0.5	1.0	6.387
Replacing N with O	Mo_4O_4	1.0	1.0 O	1.0	1.0 O	9.900
	Mo_4O_3N	1.0	1.0	1.0	1.0 O	9.856
	$Mo_4O_{0.5}N_{3.5}$	1.0	0.5 N + 0.5 O	1.0	1.0	9.746
	$Mo_4O_{1.5}N_{2.5}$	1.0	1.0	1.0	0.5 N + 0.5 O	9.790
	Mo_4ON_3	1.0	1.0 O	1.0	1.0	9.900

A.2 X-Ray : Reference Mo_4N_4, Effect of anion and cation vacancies

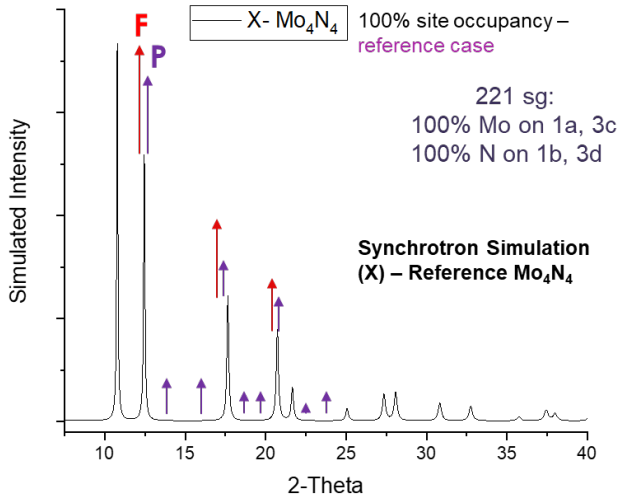

Figure A.2-1 Simulated Synchrotron pattern for Pm-3m Cubic P structure with both pairs of cation and anion sites full – Mo_4N_4. The red and purple arrows suggest the relative direction/ intensity in which the peaks need to increase to make the pattern closer to as collected synchrotron bank for C700 and C800 samples in Chapter 4

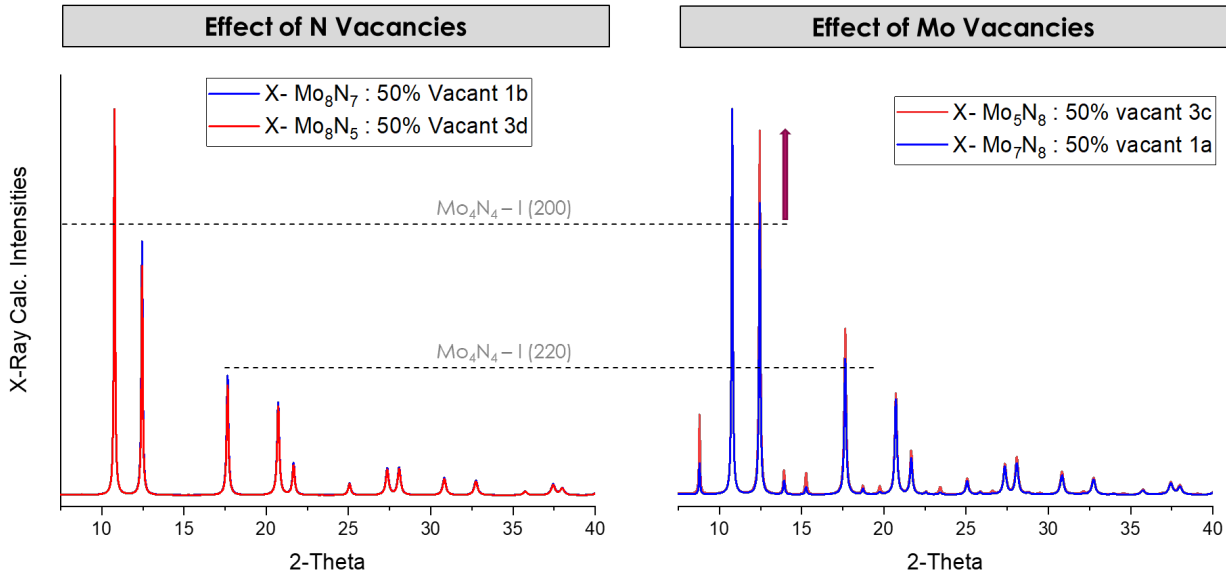

Figure A.2-2 Simulated Synchrotron pattern for Pm-3m Cubic P structure, showing the effect of anion and cation vacancies. Dotted line tracks the intensity of reference Mo_4N_4 (200) and (220) peaks. Difference in vacancy concentration between 1a and 3c site introduces super structure peaks, with same concentration of vacancy on 3c having more effect due to higher multiplicity of site. Anion vacancies don't result in superstructure peaks, and have lower effect on substructure peaks compared to cation vacancies, as Mo is a much stronger scatterer.

A.3 NPD : Reference Mo_4N_4, Effect of Nitrogen and cation vacancies

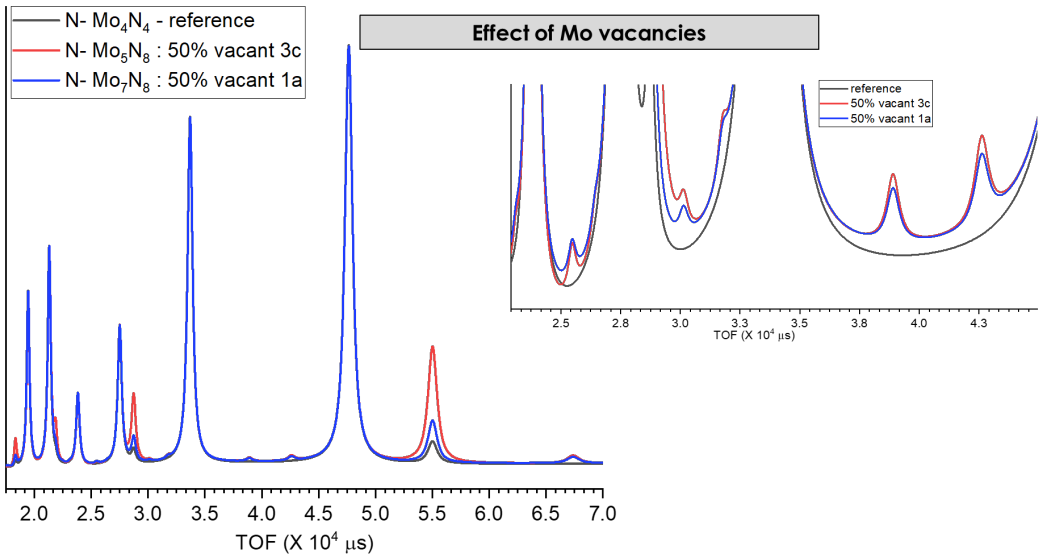

Figure A.3-1 NPD simulation of reference fully occupied Pm-3m Mo_4N_4 structure (black), 50% vacancy on cation site 3c (red) and anion site 1a(blue). Both anion and cation vacancies in case of NPD result in superstructure peaks (unlike XRD).

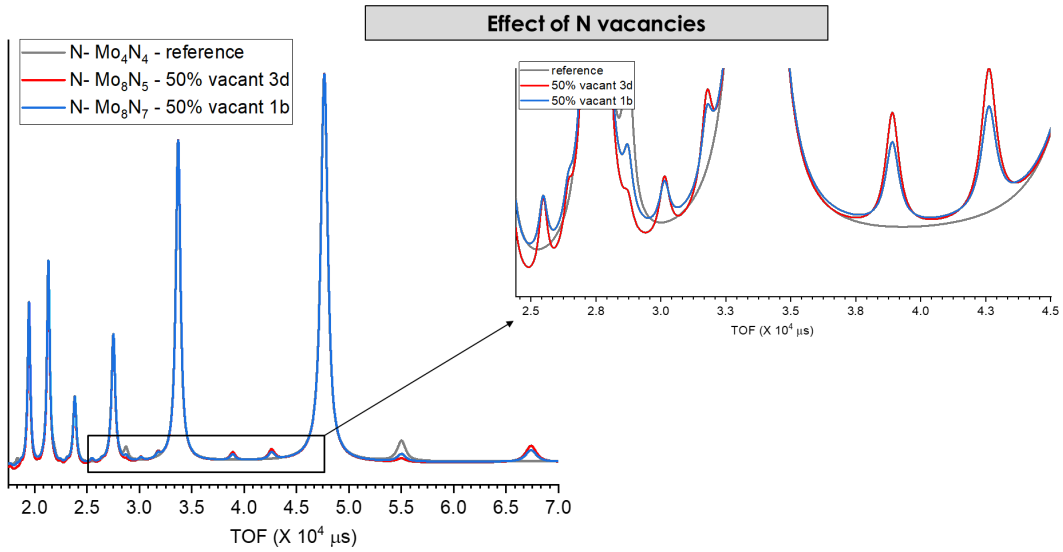

Figure A.3-2 NPD showing sensitivity appearance of superstructure peaks by introducing vacancies on either of the two anion sites. Also evident is the negligible effect of substructure peak intensities which aren't different compared to reference case.

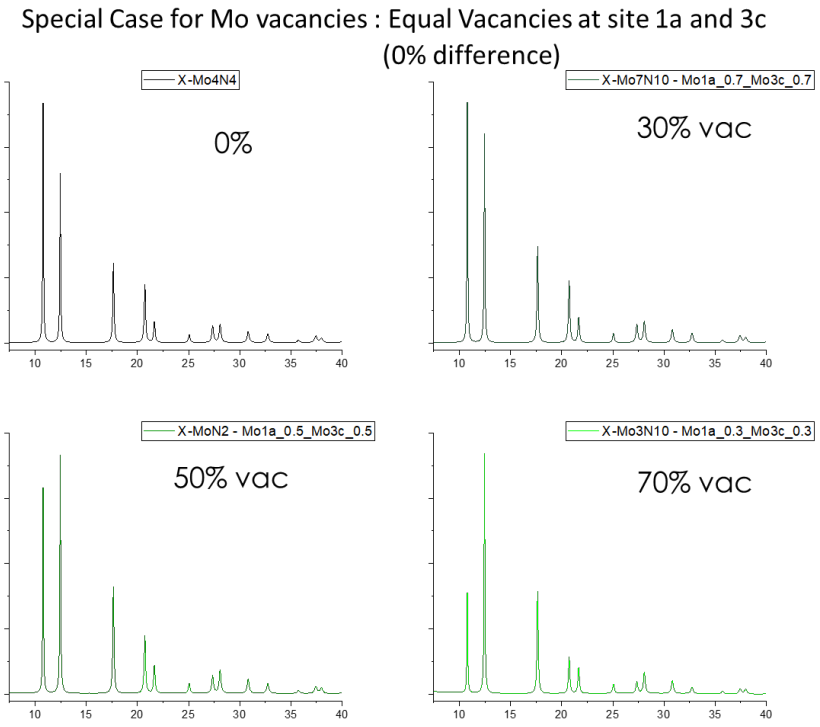

Figure A.3-3 Special case XRD simulation patterns of having equal concentration of vacancies on both sites, wherein the superstructure peaks do not show up as the symmetry is not broken. However with increasing cation vacancy concentration an increase in I(200)/I(111) is observed. Similar case can be made for NPD.

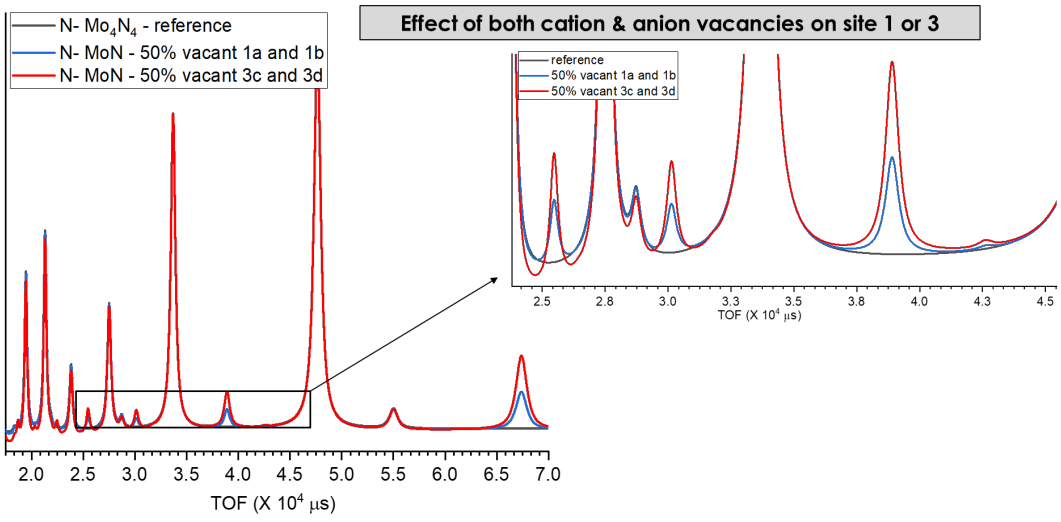

Figure A.3-4 NPD simulation showing the case of having either both 1a and 1b sites 50% vacant, or 3c and 3d sites 50% vacant. The effect of vacating higher multicity sites results in higher superstructure peaks.

A.4 NPD : Effect of Hydrogen in bulk

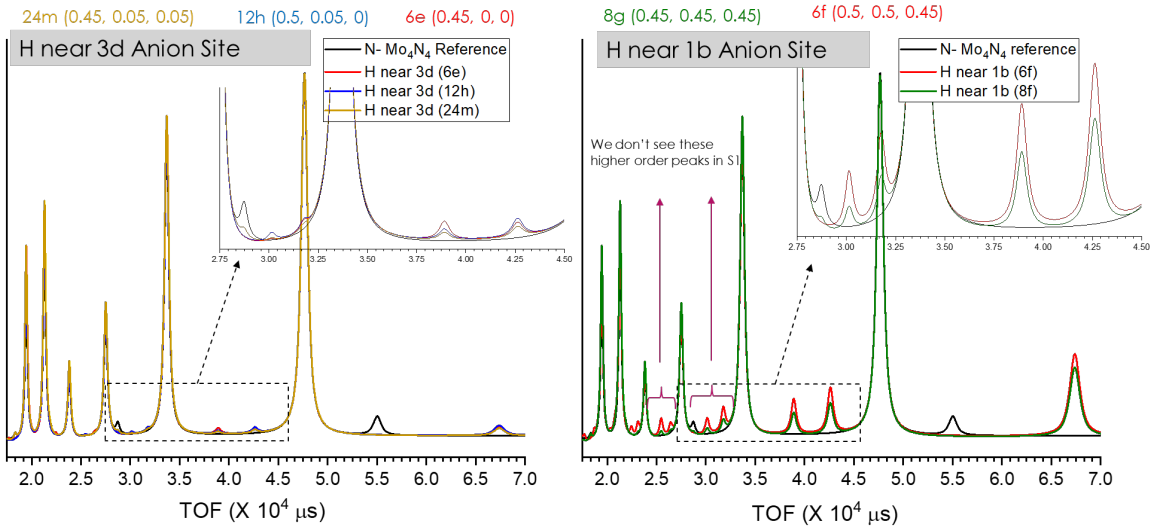

Figure A.4-1 NPD wherein H is inserted in special sites (221 Pm-3m sg) close to, 3d anion site (24m, 12h, and 6e site positions), and 1b anion site (8g and 6f type site positions). Hydrogen unlike XRD, could result in strong superstructure peaks in NPD for the concentration here used in simulation which was equal to what was found for the C700 sample in Chapter 4. Simulation also suggests that the intensity of superstructure peaks (including the higher order peaks) are more visible when hydrogen in same concentration is close to 1b anion site comped to 3d.

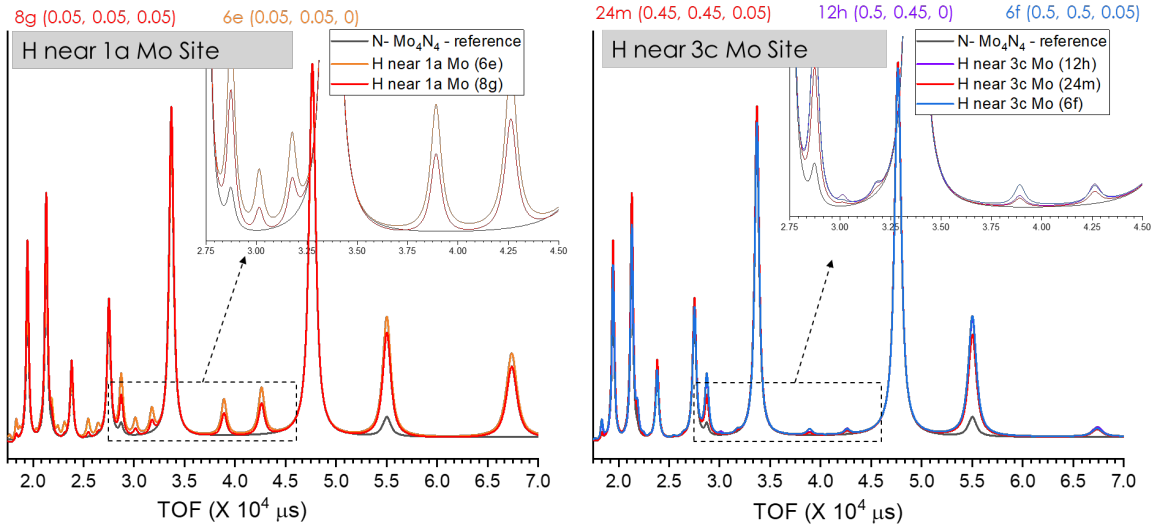

Figure A.4-2 NPD wherein H is inserted in special sites (221 Pm-3m sg) close to 1a anion site (8g and 6e site positions), and 3c anion site (24m, 12h, and 6f site positions).Similar to anions case more prominent superstructure peaks are expected if hydrogen is close to 1a anion site compared to 3c, specially the higher order peaks.

Appendix B Auxiliary Experiments

B.1 : Pt ALD Recipe development (Supplementary information)

The most applied and commercially available Pt ALD precursor, that is (methylcyclopentadienyl) trimethylplatinum ($MeCpPtMe_3$) was used. Conventionally, this precursor has been used extensively in the literature with oxygen as the oxidant, to deposit metallic Pt, following the combustion-like reactions that occur during both ALD half cycles. In brief, O_2 is first dissociatively chemisorbed on the Pt surface, inducing combustion of the remaining ligands of the adsorbed $MeCpPtMe_3$ molecules and the formation of a layer of adsorbed O atoms on the surface; followed by the reaction of these O atoms with some of the precursor ligands during the incoming precursor pulse. When the temperature of this process is maintained from 250 – 300^{o}C (ALD Window of $MeCpPtMe_3$ + Oxygen process), this process repeats per ALD cycle to produce self-limited metallic film growth at maximum rate of 0.45A^{o}/cycle. While following the optimized recipe in literature at 300 ^{o}C would have been straightforward, however, due to the thermally fragile nature of CDP, we were constrained to 150^{0}C as the upper limit for the ALD process. While its clearly that temperatures above 300^{o}C would lead to decomposition of the precursor, however no clear data was present for the ALD deposition at 150^{o}C, except for a warning of lower growth rate than maximum. Thus, our first attempt was to perform the QCM study of Pt ALD of $MeCpPtMe_3$ + Oxygen system at 150^{o}C following the ALD sequence of 1/20/2/20 (all in seconds) respectively for precursor/purge/oxygen/purge. However, it resulted in disappointingly slow Pt growth rate of 0.0014A/cycle (Figure B.1-1), leading us to drop the idea of $MeCpPtMe_3$ plus Oxygen system for Pt ALD for economic considerations.

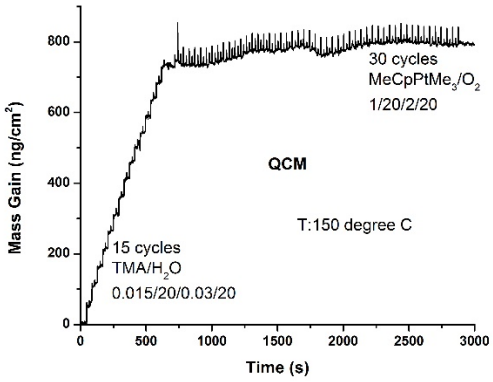

Figure B.1-1 : QCM of MeCpPtMe3 plus Oxygen Pt ALD system at 150C. Extremely low growth rate of 0.0014A/cycle was obtained.

As the next step, we investigated recent Pt ALD systems in the literature which promised the ALD window to include 150°C, using the same precursor. It was realized that using either Plasma enhanced ALD or ozone enabled ALD was required to attain similar high growth rate at 150°C, which one could get from conventional ALD using oxygen at 300°C. Ozone based process was chosen over Plasma process for threefold reason; first due to availability of the system at Northwestern, second considering that Plasma based ALD at 15O°C, resulted in PtOx rather than metallic Pt, which would require further step of hydrogenation before exploiting its catalytic activity, and finally ozone based Pt ALD at 150°C promised crystalline metallic Pt film with strong <111> orientations, with an expected 0.45A/cycle high growth rate, following plausibly the same mechanism as for the $MeCpPtMe_3$ plus oxygen described above; with the difference of nascent oxygen atoms already available in the Ozone this time. Considering, high surface area fine CDP powder were to be coated with ALD, the reported ozone ALD process (for flat Silicon substrate) was modified, to add wait time to allow adequate diffusion/ exposure of both precursor and ozone for high aspect ratio coating. The ALD sequence followed was 1s/60s/60s/30s/30s which correspond to precursor pulse / wait time/ purge time (Nitrogen)/ ozone exposure/ purge time (Nitrogen). To validate the recipe, silicon wafer was also added in the same reactor. 150 such cycles were performed, expecting around 6.75nm of Pt on at least on Silicon wafer, with similar (probably less) Pt film thickness on the CDP powder depending upon relative surface energy, and presence of hydroxyl groups, which play important role in adsorption of precursor, followed by nucleation-controlled growth of Pt films.

The deposition of Platinum was confirmed on both fine CDP (Figure B.1-3) and Silicon Wafer (Figure B.1-2), by the XPS, with the peaks corresponding to Pt (4f7/2 and 4f5/2 peaks) clearly visible. Additionally, to verify that the Pt film adapted the continuous film post the island formation phase, Image mode of XPS was also performed on approx. 6mm2 area, with 30 grid points, using spot size of 500microns. The result (Figure B.1-4 d) suggests the presence of continuous Pt film on mm scale. Thus, depth profile and Image mode analysis together suggest the Pt film is continuous with most area coated with 5-7.5nm Pt, however some preferential spots had more than 7.5nm Pt coating.

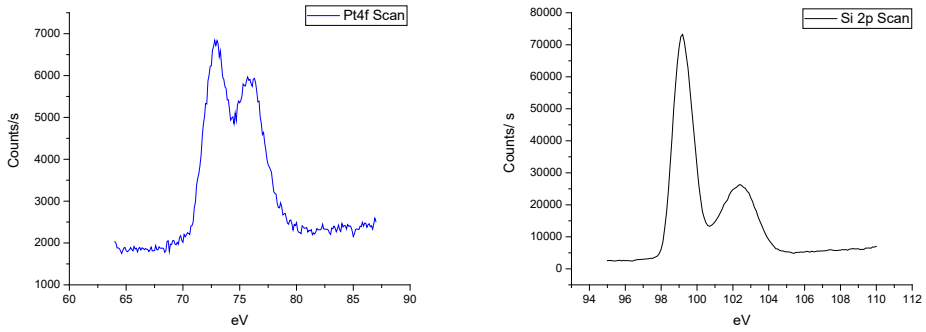

Figure B.1-2: Pt4f Scan on ozone ALD coated Silicon wafer

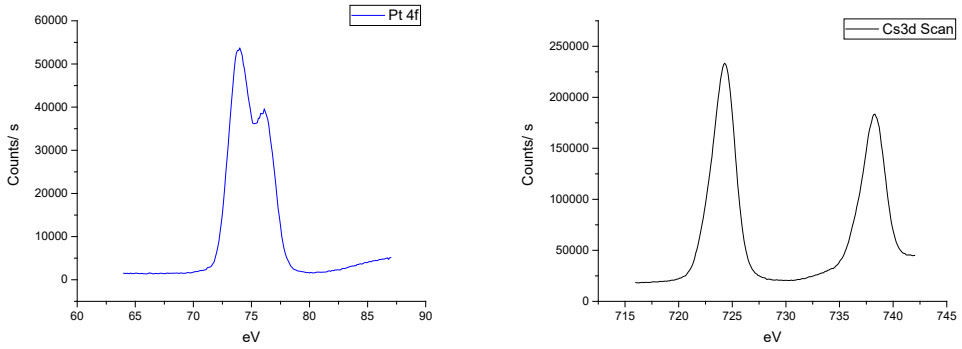

Figure B.1-3 : Pt4f Scan on ozone ALD coated fine CDP powder

The possible morphological and/ or chemical effect of powerfully oxidative ozone exposure on the fine CDP was given a check; as maintaining the CDP phase, and high surface area (without agglomeration) was critical for catalytic performance ahead. SEM images of pristine fine CDP (Figure B.1-5a) and Pt ALD coated fine CDP (Figure B.1-5b) confirms that there was no evident agglomeration effect of ozone, and the overall ALD procedure. Additionally, XRD confirmed no phase change post ALD treatment (not shown), thereby confirming no immediate negative point of adopting ozone based Pt ALD deposition on fine CDP.

For the final Pt ALD runs to coat CDP particles to be used in SAFC cathodes, the wait and purge times were further increased as a precautionary measure to ensure the CDP particles are fully coated with uniform smooth Pt films, as discussed in Chapter 2.

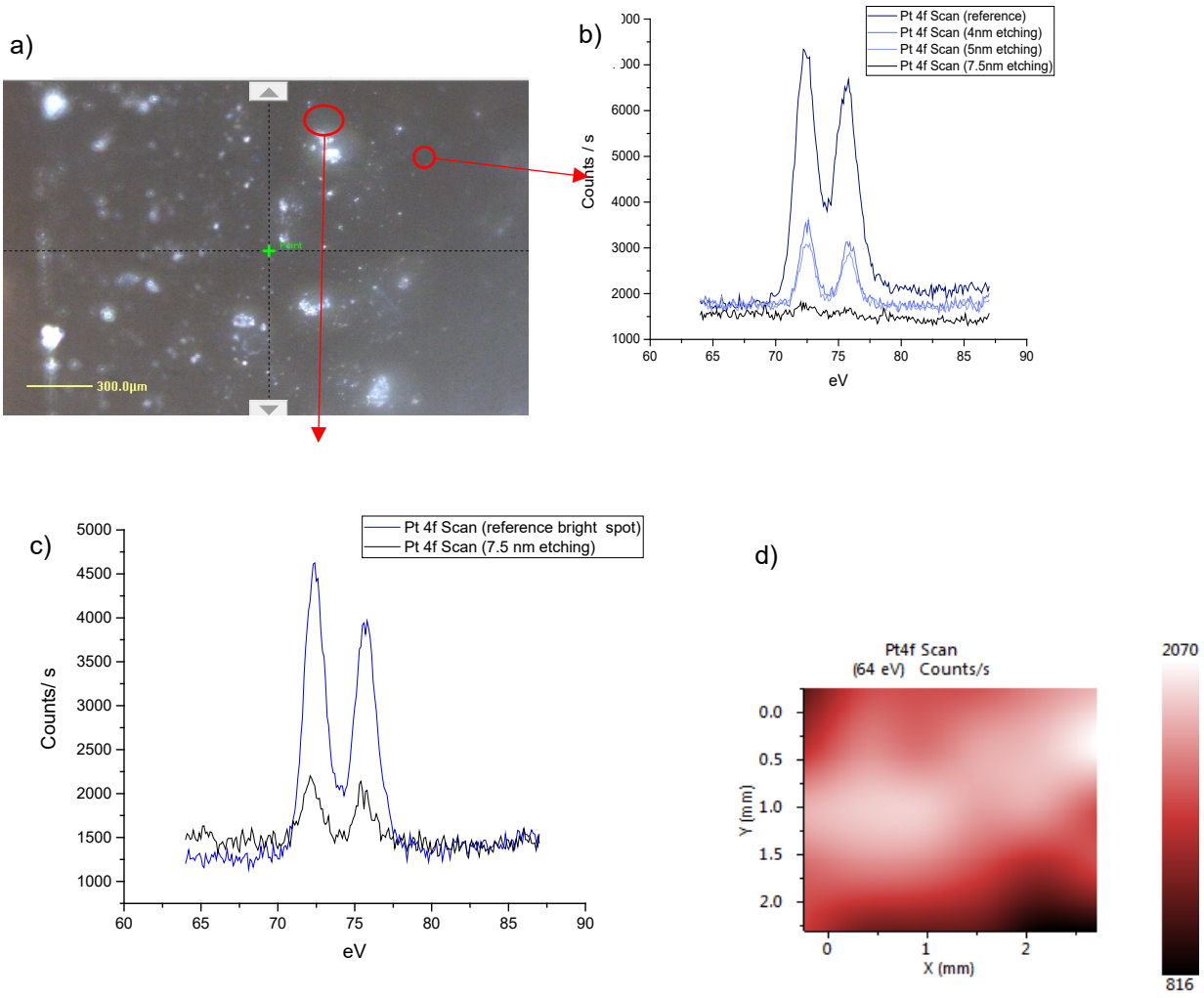

Figure B.1-4 : Depth profiling and Image mode XPS Analysis of Pt ALD coated Silicon Wafer

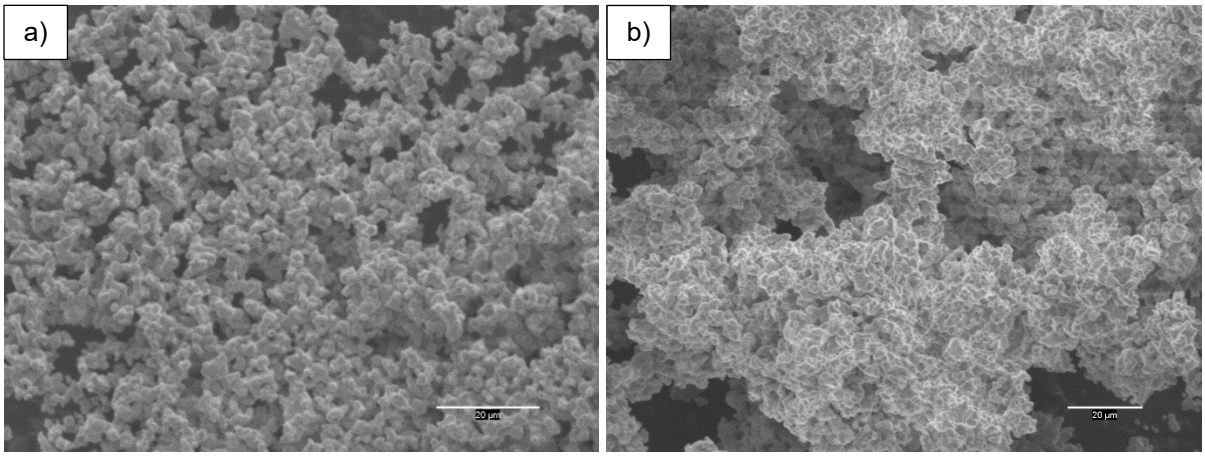

Figure B.1-5 : SEM Micrographs of a) fine CDP and b) Pt ALD coated fine CDP at same magnification; confirming no sign of suspected agglomeration

B.2 Ammonia Decomposition% measurement at 850C (with flow rate)

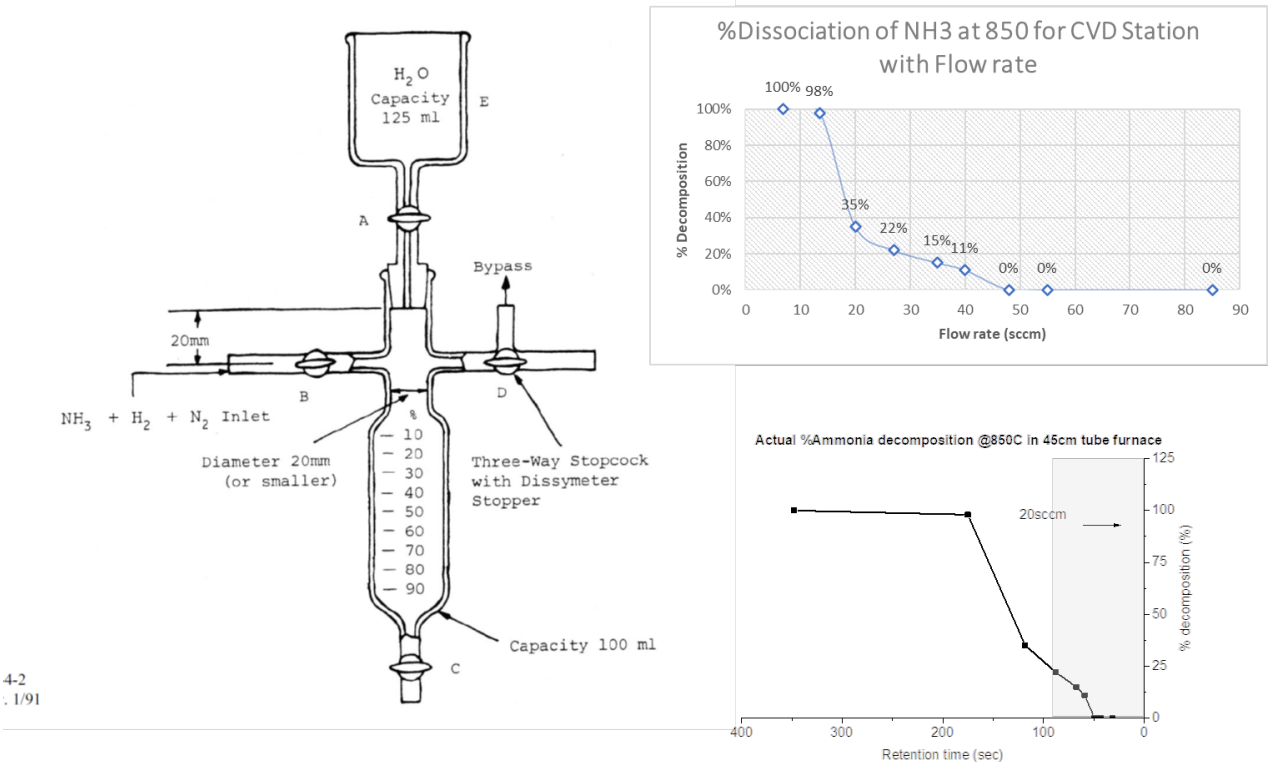

Figure B.2-1 Ammonia decomposition buret (on the left) used to measure the % of decomposed ammonia in the exhaust side of the ammonolysis CVD furnace.[221] Top right graph shows that at 850°C, nearly all the ammonia dissociates for flow rates <20sccm (depends on retention time along with temperature).). However exponential increase in total undissociated ammonia retained in exhaust is observed on increasing flow rates >50sccm. Bottom right plots the same data wherein x-axis is now the retention time (dictated by flow rate and tube dimensions). ~125 sec at 850°C is enough to completely dissociate ammonia as suggested by thermodynamics.

B.3 Synthesis of hydrogen bronzes (H_2MoO5, $H_{1.7}MoO_3$, $H_{0.3}MoO_3$)

The term bronze was originally coined for Na_xWO_3 compounds by Wohler in 1825.[222] Bronzes have general formula of $A_xM_zO_y$, where M is often Ti, V, Mn, Nb, Ta, Mo, W, or Re, and A is H, NH^{4+}, or an alkali, alkaline earth, rare earth. These are often characterized by their intense color, metallic luster, metallic or semiconducting properties, and are resistant to attack by nonoxidizing acids. In the literature various types of bronzes are reported,[223-228] which can generally be categorized into 5 major types:

Type I: Hydrogen Molybdenum Bronze ($HxMoO_3$ continuous over range $0.23 < x < 0.4$)

Blue; Orthorhombic

Type II: Hydrogen Molybdenum Bronze (H_xMoO_3 continuous over range $0.85 < x < 1.04$)

Blue; Monoclinic

Type III: Hydrogen Molybdenum Bronze (H_xMoO_3 continuous over range $1.55 < x < 1.72$)

Red; Monoclinic

Type IV: Hydrogen Molybdenum Bronze (H_2MoO_3)

Green ; Monoclinic

Type V: Hydrogen Molybdenum Bronze (H_2MoO_5)

Yellow ; Monoclinic

Layered structure of MoO_3 acts as a perfect setup to intercalate its layers with hydrogen atoms leading up to the definition of a hydrogen-molybdenum bronze. In earlier chapters, in house synthesized Bronzes (Type III and Type V) were used for the synthesis of high surface area Gamma Mo-O-N phases. Additionally, Type I bronze was also used to understand reaction pathways of MoO_3 ammonolysis which is shown to move via Bronze (Type I Bronze) and MoO_2 intermediates.

B.3.1 Synthesis of Type III (H_xMoO_3 , x = 1.7)

Type II red Monoclinic bronze confirmed in space group C2/m using Lab XRD with composition H1.7MoO3 was prepared by the reduction of MoO_3 with nascent H from reacting Zn metal and HCl originally-described by Glemser et al.[224-226] The optimal Zn:MoO3 ratio of 1:1 for phase pure $H_{1.7}MoO_3$ was determined after trying various ratios, with lower Zn content resulting in mixtures of various reduced bronzes of the H_xMoO_3 family. 2g MoO_3 (Sigma Aldrich, 99.99%) was added to 50 ml DI water and stirred for 10 min with a magnetic stirrer to obtain a uniform suspension. 10 ml of concentrated HCl was added slowly, and the suspension was stirred for 5 min. The suspension was then cooled to 0 °C using a dry ice bath. 2g of Zn granules was divided into ~10 equal batches, each of which was slowly added with intermittent stirring and 5 min wait period between each batch. The obtained bubbling suspension due to release of nascent reducing H, was stirred well for 15 min, where it gradually changed color from blue to red. The suspension was left at room temperature for 24 hrs. The final dark red suspension was filtered and washed with DI water and 1-2M HCl multiple times. Finally, a powder with a deep red metallic luster was vacuum dried and stored in the glove box.

The red characteristic color is seen in Figure B.3-2a), with Lab XRD pattern shown in Figure B.3-2c), red curve.

B.3.2 Synthesis of Type I ($HxMoO_3$, x = 0.3)

Type I blue Orthorhombic bronze confirmed in space group Cmcm using Lab XRD with composition $H_{0.28}MoO_3$ was prepared by the reduction of MoO_3 with nascent H from reacting Zn metal and HCl originally-described by Glemser et al. [224-226] It's similar to above procedure, except the Zn:Mo ratio is 0.15:1, meaning to 2g Zinc granules, only 0.3g of Zinc was added. While, there are a range of x values for Type I, best CIF and further confirmation by lattice constant value in literature with x,[228] confirms $H_{0.28}MoO_3$ which is what was needed for studying the MoO3 ammonolysis pathways via in-situ XRD

(Courtesy : Elise (Bedzyk Group, NU)). The Lab XRD pattern and shiny metallic blue color powder is shown in Figure B.3-1. This is often also written as $H_{0.3}MoO_3$ in this thesis, especially when used in Chapter 3.

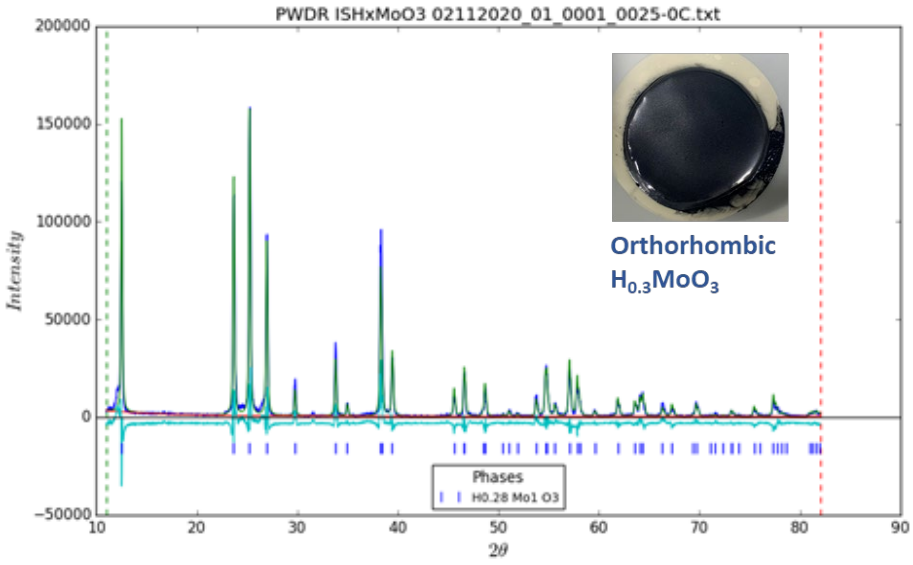

Figure B.3-1 : $H_{0.28}MoO_3$ bronze as synthesized verified by Lab XRD.

B.3.3 Synthesis of Type V (H_2MoO_5) and ex-situ ammonolysis (650 and 700C)

The synthesis of H_2MoO_5 was performed by oxidation of MoO_3 using H_2O_2 solution based on earlier reports.[119, 229] 100 ml of 30% wt H_2O_2 solution was heated to 40°C under constant stirring on a magnetic stirrer. 2g MoO_3 (Sigma Aldrich, 99.99%) was added slowly under constant stirring. The solution was heated and maintained at~55°C under constant stirring overnight until the initial suspension changed color from white to light green to bright yellow solution. The solution was naturally evaporated off by storing it for 48hrs in a fume hood. Finally, the bright yellow powder (H_2MoO_5) was collected and further dried in an oven at 80°C overnight in air. Figure B.3-2d) shows the platelet like long thin particles morphology for as synthesized oxidized bronze.

Ammonolysis was also performed at 650°C and 700°C (0.15g bronze precursor, 3°C/min ramp, hold for 3 hrs, under 100sccm dry NH_3) for this yellow monoclinic oxidized bronze precursor, which converts these into black γ-phase nitride. Lab XRD of precursor (yellow curves), and that of 650°C and 700°C post ammonolysis samples obtained, which corresponding reitvald refinement patterns (red dotted lines) overlayed on top is shown in Figure B.3-3. While both the temperature the patterns match to γ-Mo2N PDF card in Lab XRD, the lattice constant of the higher temperature phase is higher. The lattice constant range is also similar to C700 samples processed in Chapter 4. More discussion on using these bronze to synthesized highest reported surface area γ-Mo2N samples at lowest reported temperature was achieved in a collaborative work within MRSEC IRG 2 effort (*Elise Goldfine's Thesis, Haile group, Northwestern University*).

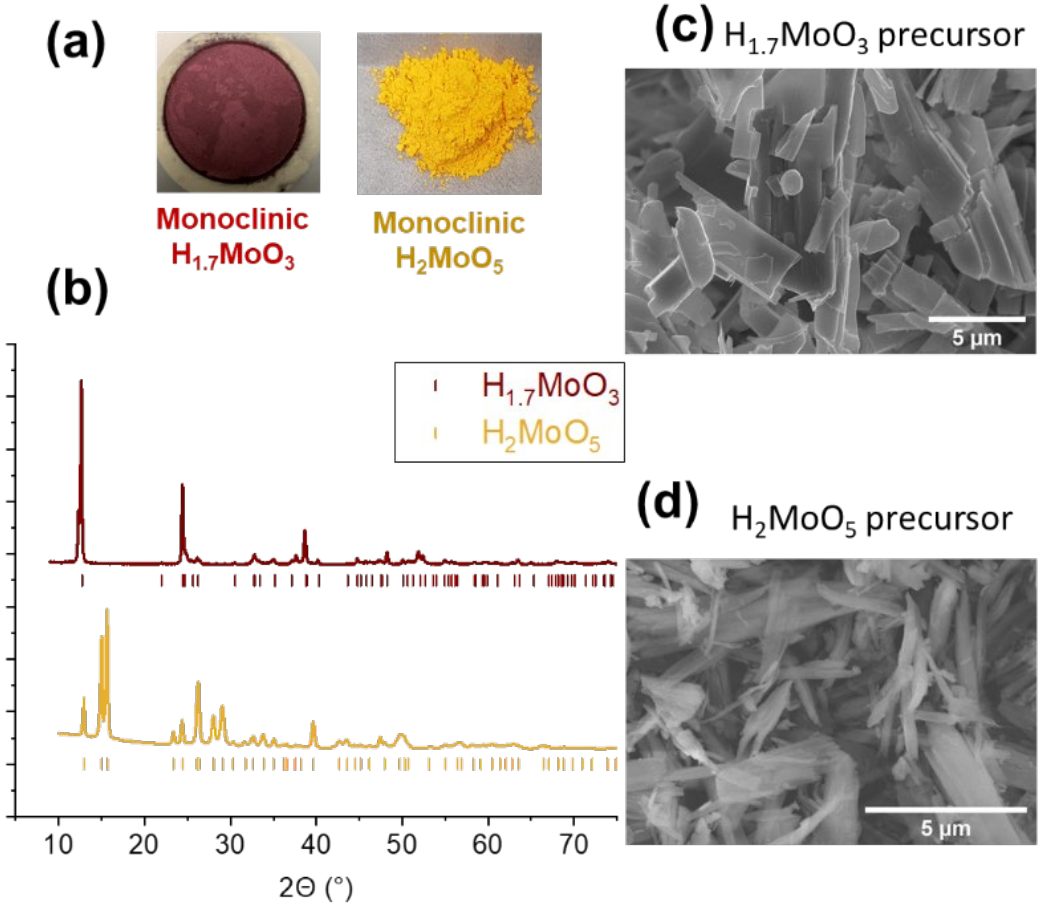

Figure B.3-2 : (a) Optical images of Monoclinic reduced ($H_{0.3}MoO_3$) and oxidized (H_2MoO_5) bronzes

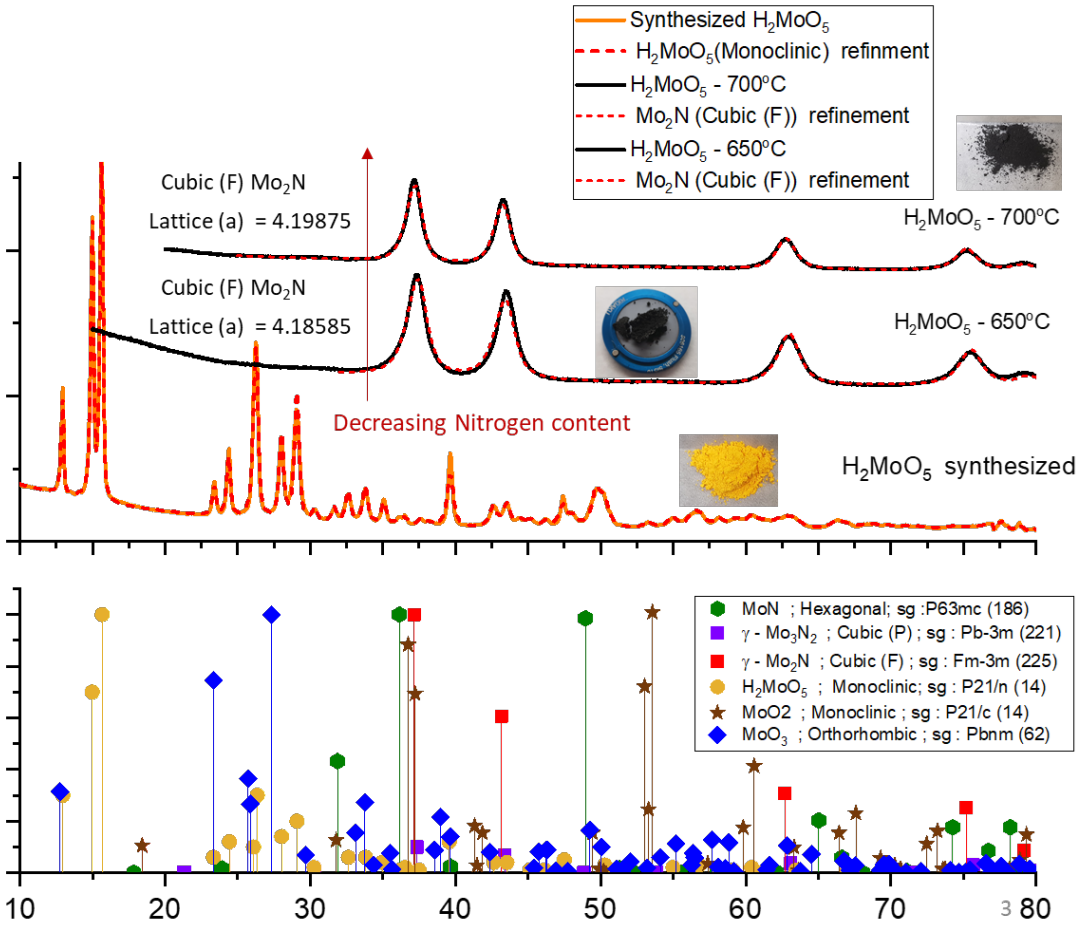

Figure B.3-3 lab XRD of as synthesized H_2MoO_5 precursor and resulting y-Mo_2N nitrides upon dry ammonolysis at 650°C and 700°C for 3hrs.

B.4 High Temperature DFT phase diagram of Mo-O-N system

The DFT calculations were performed by Jiahong Shen (Wolverton Group, Northwestern University), which help collaborate some of the ex-situ and in-situ experiments, that were studied in Chapter 3, as a part of understanding reaction pathway of MoO_3 ammonolysis.

Computational details:

In this work, all density functional theory (DFT)[230, 231] calculations were carried out using the Vienna ab initio simulation package (VASP)[232, 233] with the projector augmented wave (PAW)[234] method, and the Perdew-Burke-Ernzerhof (PBE)[235, 236] generalized gradient approximation (GGA) was used as the exchange-correlation functional. The primitive cells of ordered structures were directly taken from the experiments while the disordered structures (structures with partial site occupancies) were simulated by supercells based on the special quasi-random structure [237] (SQS) method. The mcsqs code implemented in Alloy Theoretic Automatic Toolkit (ATAT)[238] was utilized in generating these supercell structures. The temperature-dependent chemical potential map (stability map, phase diagram) was constructed using the phase_diagram module within the pymatgen package and the temperature effects were included by correcting the chemical potentials of reference gaseous phases (i.e., oxygen and nitrogen) as

$$\mu_O(T, p_{O_2}) = \frac{1}{2}[\mu_{O_2}^{298K} + \Delta H_{O_2}(T) - T\Delta S_{O_2} + RTln(p_{O_2}/p_{O_2}^0)]$$

where $\mu_{O_2}^{298K}$ is the chemical potential of oxygen gas fitted to 298 K experimental condition as implemented in the Open Quantum Materials Database (OQMD)[238-241], $\Delta H_{O_2}(T)$ and ΔS_{O_2} are standard experimental enthalpy and entropy of oxygen gas taken from NIST-JANAF thermochemical tables[242] and the partial pressure of oxygen and nitrogen were chosen as 0.2 and 0.8, respectively.

To calculate the formation energies of the disordered structures, a 32-atom and a 48-atom special quasi-random structures (SQS) are constructed for cubic-F and cubic-P Molybdenum nitrides, respectively. Both SQS are built on the rocksalt structure where the nitrogen and vacancies are mixing at anion sites in

cubic-F structure while vacancies are mixing at both anion and cation sites in a sublattice of cubic-P structure. As shown in Figure B.4-1, the temperature dependent chemical potential maps (i.e., stability map, phase diagram) are then constructed by including all phases in the Mo-O-N phase space. At ground state (i.e., T=0 K), cubic-F (Mo_2N) structure is not stable, and thus disappears on the phase diagram. The stable region (i.e., chemical potential window) of cubic-F structure becomes wider while that of MoN structure becomes narrower as the temperature increases, indicating that cubic-F structure is more likely to be synthesized at higher temperature. MoN structure becomes unstable and cubic-F structure is the only existing Molybdenum nitride when the temperature reaches 1200 K, and they all become unstable when the temperature is over 1500 K. At all temperature ranges, a boundary phase (MoO_2) exists between MoO_3 and the Molybdenum nitrides, which means MoO_3 phase should go through reduced MoO_2 phase first before forming the nitrides. The final compositions are Mo_2N and Mo_3N_2 for cubic-F and cubic-P structures used for the DFT calculations here, respectively, this is different than what we found the Cubic phase Molybdenum oxynitrides via MoO_3 dry ammonolysis. However, it does dictate the importance of competing gamma and delta phase of nitride product, and MoO_2 sharing the boundary with both, even though this boundary shall shift due to these gamma and delta phase being oxynitrides.

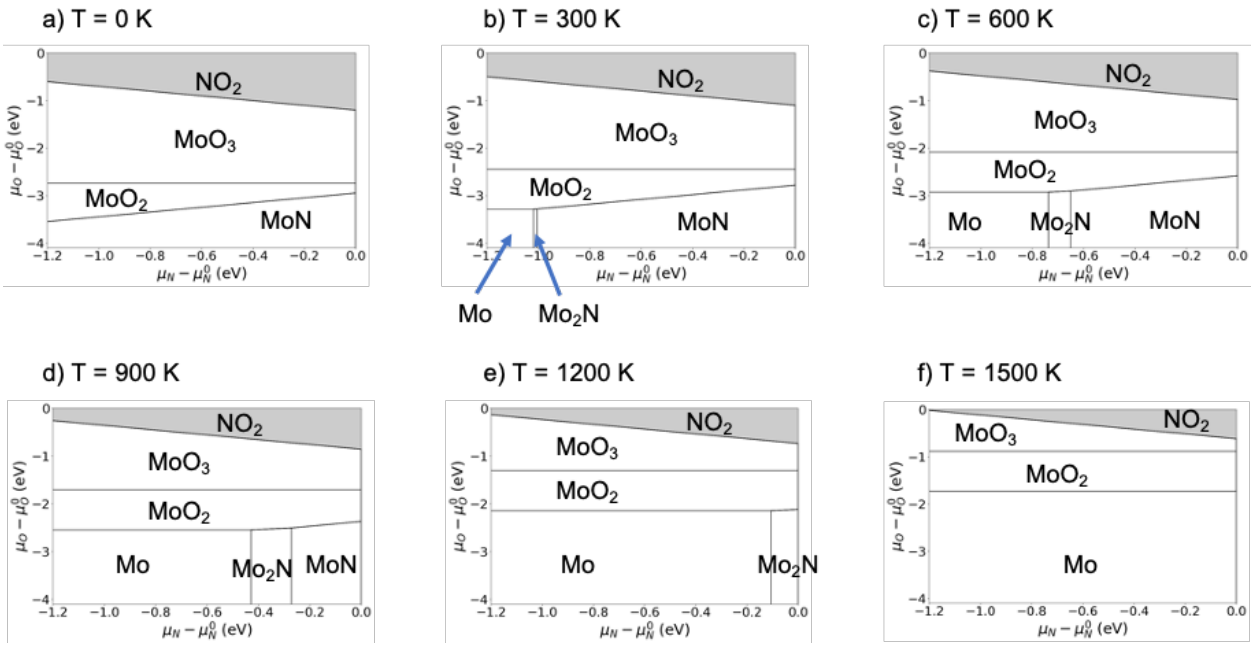

Figure B.4-1: Chemical potential map of Mo-O-N phase space at a) 0 K, b) 300 K, c) 600 K, d) 900 K, e) 1200K and f) 1500 K. Mo_2N is the cubic-F structure.

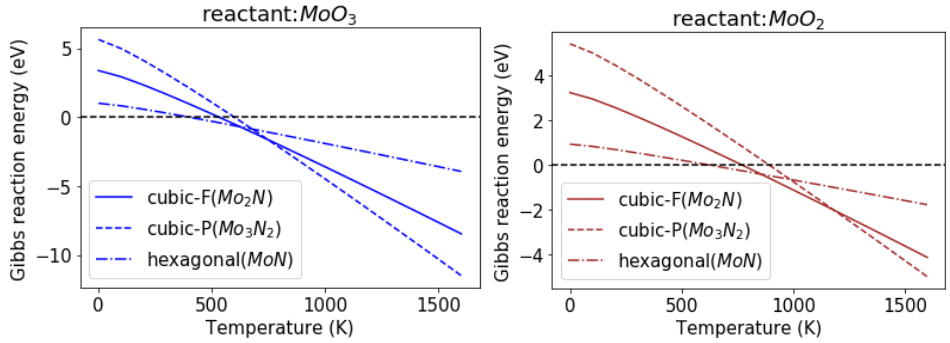

Figure B.4-2 : Gibbs reaction energies (per mole Molybdenum nitride) for a) MoO3 and b) MoO2 as the reactant, and different Molybdenum nitrides as the product

In order to theoretically understand the synthesis pathway, the Gibbs energies are calculated for reactions where MoO_3 or MoO_2 is the reactant and Molybdenum nitride is the product. The reaction equations can be found in the Supplemental Information. Configurational entropy is considered for disordered structures and experimental entropy and enthalpy is used to correct the formation energies for gaseous phases. As shown in Figure B.4-2, formation of MoN becomes favorable (i.e., Gibbs reaction

energy becomes negative) first, followed by cubic-F and then cubic-P in both cases. When the temperature increases, the most favorable products (i.e., the lowest Gibbs reaction energy at a specific temperature) follow the trend that $T_{MoN} < T_{Mo_2N} < T_{Mo_3N_2}$, regardless of the reactant choice. This agrees with the overall behaviour observed while performing in-situ XRD studies on ammonolysis of MoO3 and MoO2. While a small hexagonal phase appears early in reaction, quickly the main phase is gamma Cubic F phase ("Mo2N") at 973K is stable followed by reduced symmetry primitive Cubic P phase being stable at around 1073K (starts forming earlier).

Reaction equations:

$$MoO_3 + 2NH_3 \rightarrow MoN + 3H_2O + \frac{1}{2}N_2$$

$$2MoO_3 + 4NH_3 \rightarrow Mo_2N + 6H_2O + \frac{3}{2}N_2$$

$$3MoO_3 + 6NH_3 \rightarrow Mo_3N_2 + 9H_2O + 2N_2$$

$$MoO_2 + \frac{4}{3}NH_3 \rightarrow MoN + 2H_2O + \frac{1}{6}N_2$$

$$2MoO_3 + \frac{8}{3}NH_3 \rightarrow Mo_2N + 4H_2O + \frac{5}{6}N_2$$

$$3MoO_3 + 4NH_3 \rightarrow Mo_3N_2 + 6H_2O + N_2$$

B.5 TPR of Cubic Molybdenum Oxynitride with Mass Spec to determine surface adsorbed species: NH_3 and H_2O ratio on surface

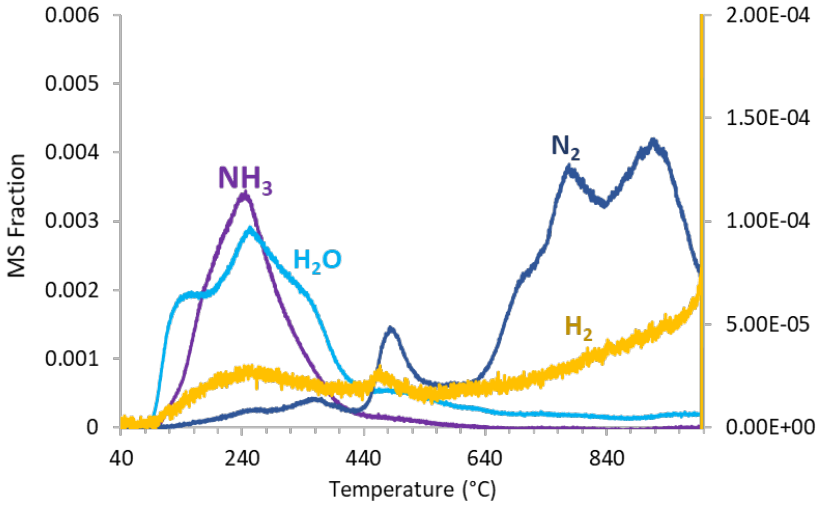

Figure B.5-1 Temperature programmed reduction – Mass spectroscopy (TPR-MS) of Cubic P (C800) sample.

The samples were heated to 1000°C under Helium and the exhaust gases were throughout tracked using a mass spec. While the result is not directly quantifiable to get absolute wt% of adsorbed species, the experiment sheds light on the fact that below 450C when mostly adsorbed species are expected to come off, main signal were from NH_3 and H_2O making them the dominant surface species. Also, commensurate amount of H_2O and NH_3 were observed. Also interesting is the fact that H2 signal (yellow curves, magnified 10x here for visualization) rises even at temperatures >800C highlighting the findings of Chapter 4, that these cubic samples have hydrogen in the bulk.

B.6 Preliminary NMR for Molybdenum Oxynitride phases

Preliminary NMR (performed by *Sawankumar Patel - Florida State University)* for all the four Molybdenum Oxynitride Hydride phases discussed in Chapter 4 and Appendix C.1 (Cubic F, Cubic P, Hexagonal and Tetragonal). Additionally, some NMR theoretical simulations (by *Haoyu Liu - Florida State University)* were performed to understand the peak convolution of N15N NMR for the Cubic phases. Samples were synthesized at Northwestern and shipped to Prof. Hu's group at Florida State University for following NMR measurements.

1H NMR was collected at 500 MHz spectrometer using a 2.5 mm probe at spin rate of 10 kHz as the samples were conductive. In particular, the tetragonal and hexagonal phases. Rotor synchronized spin-echo pulse was used to collect the spectra at π/2 pulse of 1.8 μs and recycle delay of 10 sec. Adamantane was used the calibrate the chemical shift at 1.84 pm.

15N NMR was collected at 830 MHz spectrometer at Larmor frequency of 84.2 MHz with a home built 3.2 mm probe. Static CPMG (Carr-Purcell-Meiboom-Gill) pulse sequence was used with a π/2 pulse of 5 μs and recycle delay of 5 sec. Glycine was used to calibrate the chemical shift at 32.4 ppm.

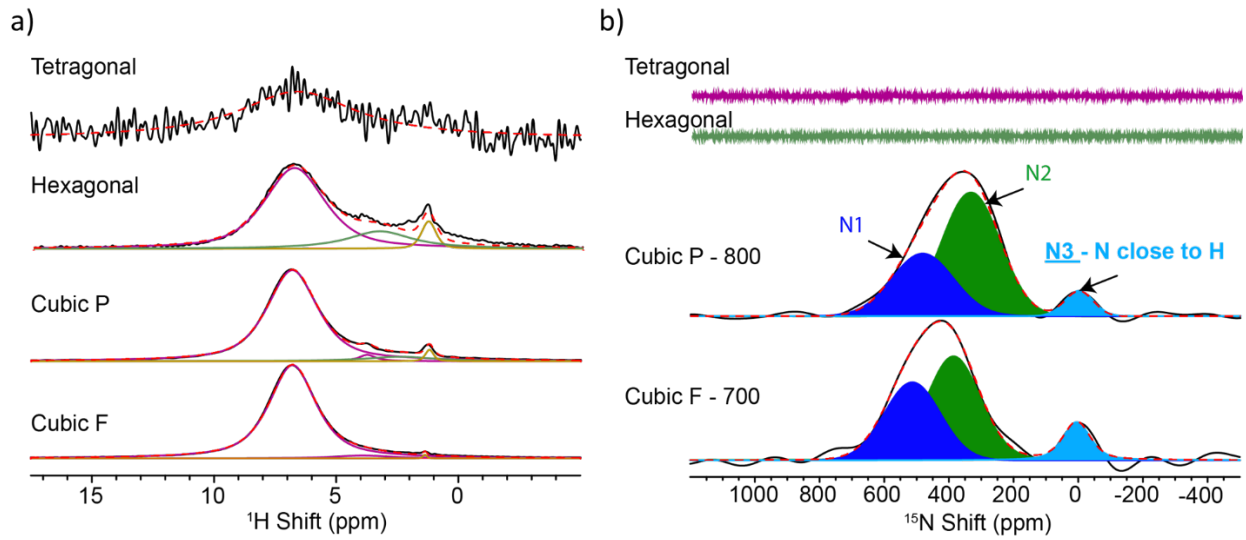

Figure B.6-1 1H and 15N NMR analysis of all four molybdenum nitride phase samples (C700, C800, H700 and T700). The conductive nature makes nitrogen NMR tough, with no signal obtained for the Tetragonal and Hexagonal phase. Interesting all of these show H in the phases, which at first pass cannot be associated to surface adsorbed species (which would have much sharper peaks).

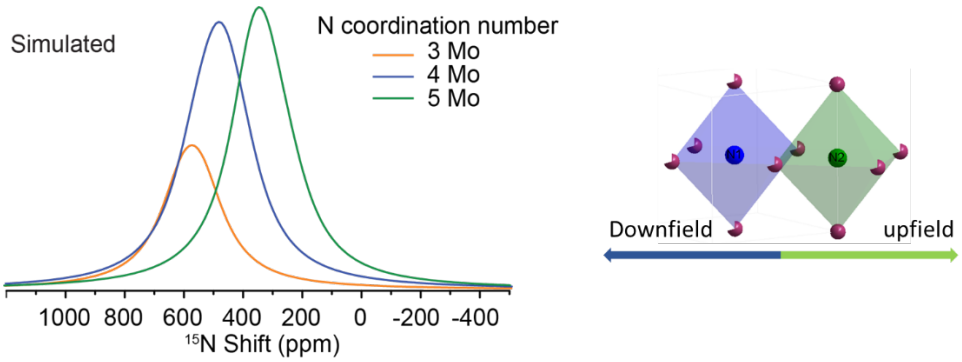

Figure B.6-2 Simulation of 15N NMR for the Pm-3m space group.

^{1}H NMR in Figure B.6-1a) reveals that the H in all phases resonates around 6.8 ppm. Since the chemical shift does not change with the structure, the H may be in a similar chemical environment for all structures. Additional peaks around 2 and 3 ppm are from the rotor and instrument background.

Additionally comparing H in cubic F vs P, we do observe higher amount of H in cubic F. (Ratio of H in cubic F vs P is 2.2:1). Due to Hexagonal and tetragonal samples being conductive, the signal to noise ratio was poor in 1H NMR for any quantitative comparison, however surely H was detected positively in the hexagonal phase, with a broad signal, which is not representative of any adsorbed gas which usually have sharp peak profile. Given the low% adsorbed gas on hexagonal phase in comparison to Cubic phase, and the peak shape, this makes the possibility of hydrogen in the bulk of hexagonal phase real.

^{15}N in Figure B.6-1b) reveal three resonances N_1, N_2 and N_3 for the cubic phases. The N1 and N2 refer to the nitrogen in the structure with different coordination to Molybdenum. NMR DFT calculation reveal that Nitrogen is sensitive to the near neighbors Molybdenum and vacancies in the Mo site will cause a chemical shift to lower ppm values. N_3 is assigned to N-in close proximity to H and was confirmed by DFT calculations as shown in Figure B.6-2.

More detailed NMR studies to distinguish H and N amount and positions in different phases, mainly by focusing by NMR instrument optimization and sample preparation (pre-desorption under Ar at 673K) to get better Signal to Noise ratio with least interference possible from adsorbed gases. Separately, O-

17enriched MoO3 is now being converted into Cubic Molybdenum oxynitrides, with the hope to perform NMR to get information about the Oxygen in these phases and how they different co-occupy with Nitrogen on different sites in different phases.

B.7 Room temperature vs Thermal XPS of Cubic Molybdenum Oxynitrides

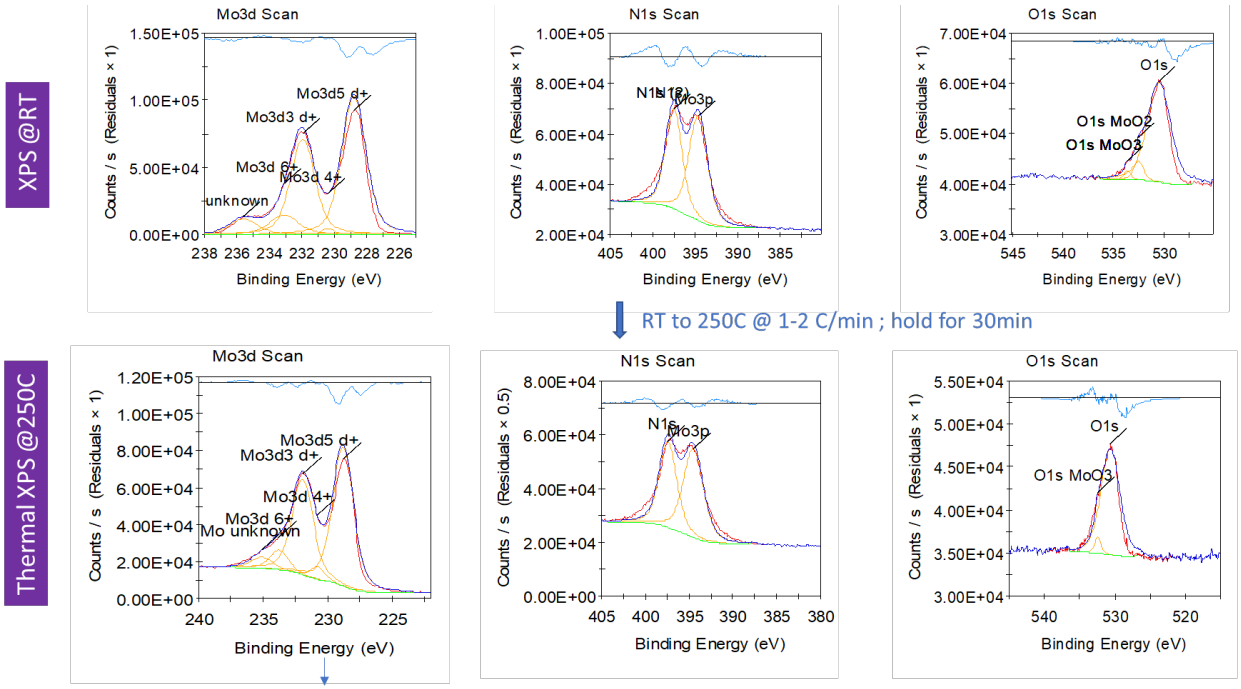

Figure B.7-1 Room temperature vs Thermal XPS (225°C)plots of Cubic P (C800) Molybdenum oxynitride. Thermal XPS was performed to remove surface adsorbed species under high vacuum and temperature in-situ in XPS. By doing so the unknown shoulder peak around 236 eV in Mo3d scan, which could be due to surface bonds of Mo with surface adsorbed species is almost lost. No shift in peak position was observed. Similar observation could be made for all the other 3 phase pure molybdenum nitride samples (C700, H700 and T700 : Cubic F, Hexagonal and Tetragonal).

B.8 Effect of MoO_3 precursor vendor choice (Alfa Aeser vs Sigma results)

For the purpose of this section these names are interchangeably used for the 3 MoO_3 precursor bottles that were used in the various Molybdenum nitride synthesis discussed in Chapter 3 and Chapter 4.

Two bottles from Alfa Aesar :

- Alfa Aesar – 01 ↔ AA – original ↔ AA-01↔Orig-AA
- Alfa Aesar – 02 ↔ AA – New ↔ AA-02↔New-AA

One bottle from Sigma Aldrich :

- Sigma – 01 ↔ Sigma

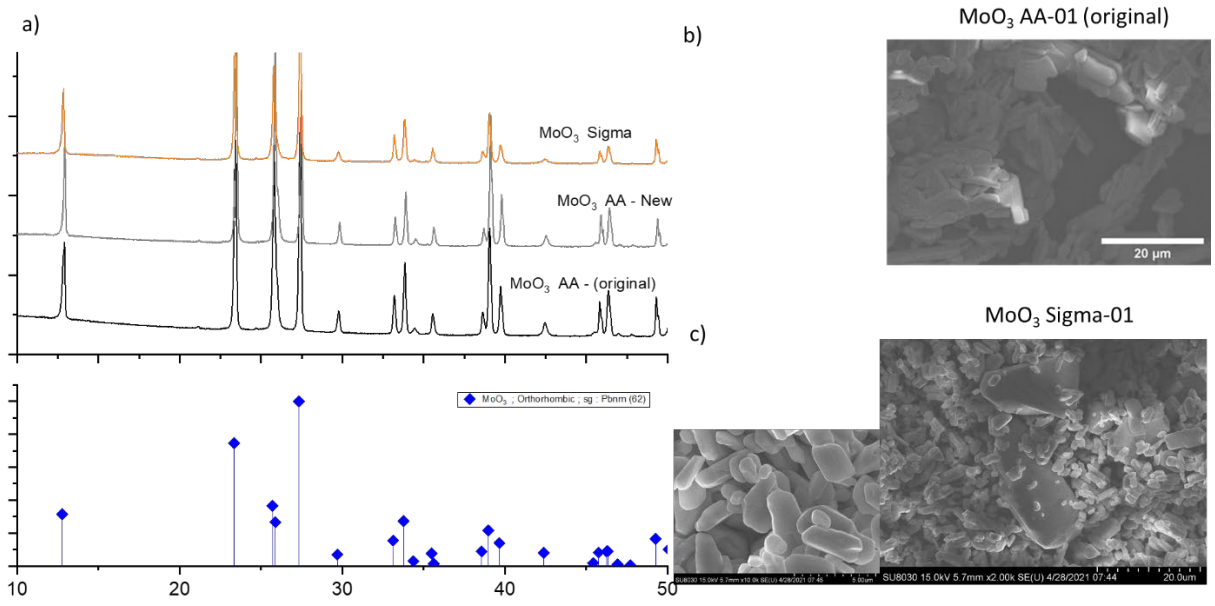

Figure B.8-1: (a) Lab XRD of three different bottles of MoO3 (two from Alfa Aesar : AA-Original (AA-01) and AA-New (AA-02) and one from Sigma Aldrich (Sigma-01)). SEM of (b) AA-01-MoO3 and (c) Sigma-01-MoO3, showing in both case micron sized particle. The size of particles seemed more uniform for the Alfa Aesar bottle. These were used for

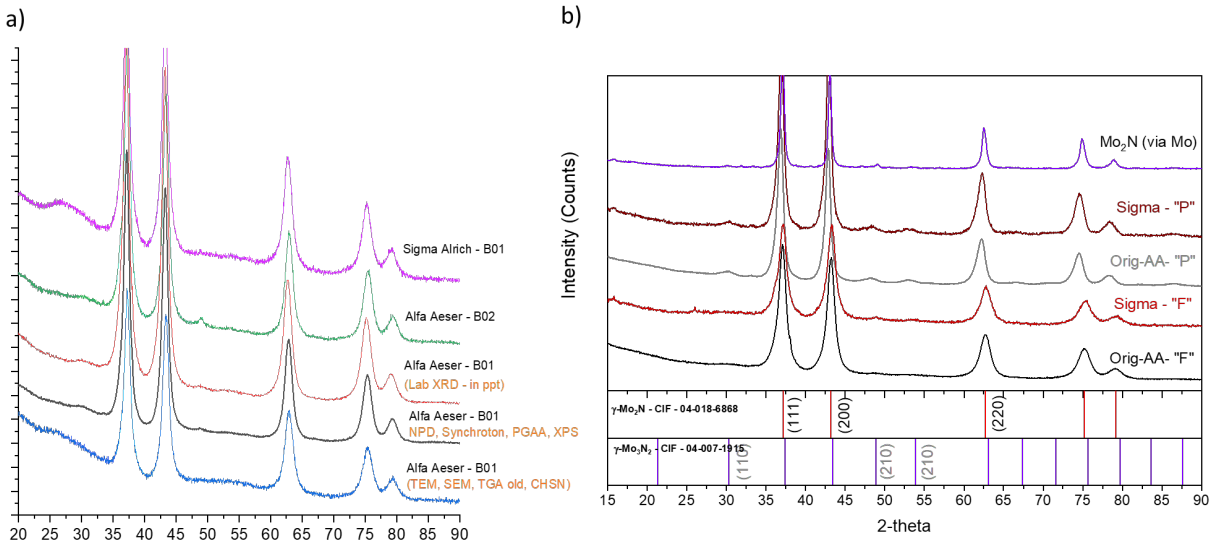

Figure B.8-2 : (a) Lab XRD patterns of C700 (Cubic F) sample batches that were used for several groups of characterizations (written in yellow), synthesized using AA-01 in previous figure (or Alfa Aesar B01 here). Additionally, some Lab XRD patterns from C700 synthesized from other MoO_3 bottles are shown. (b) Representative Lab XRD patterns of Cubic F and Cubic P samples derived from AA-01 and Sigma based precursor bottles.

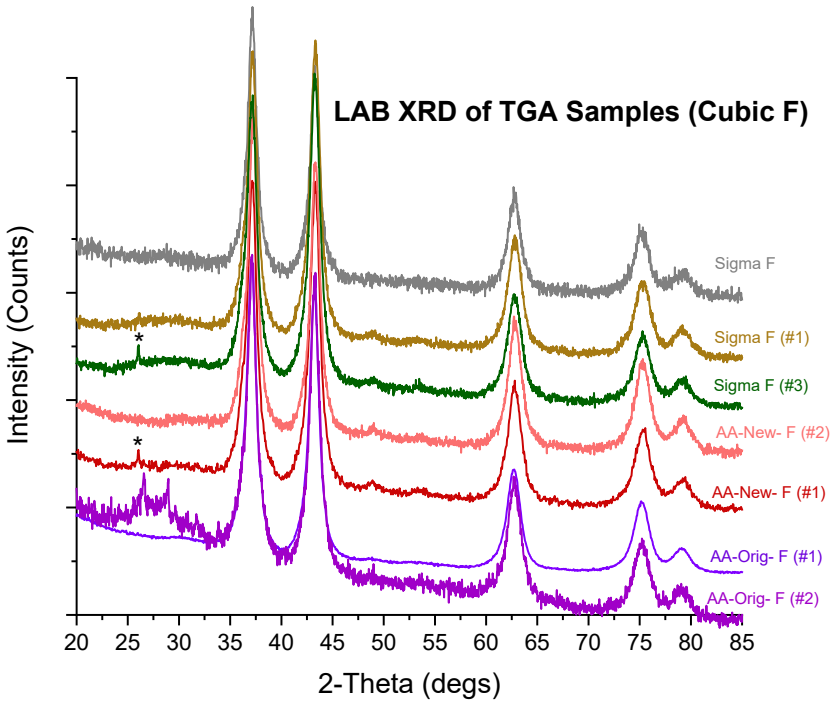

Figure B.8-3 Lab XRD of various Cubic F samples (from vairous MoO_3 bottles) processed for TGA samples.

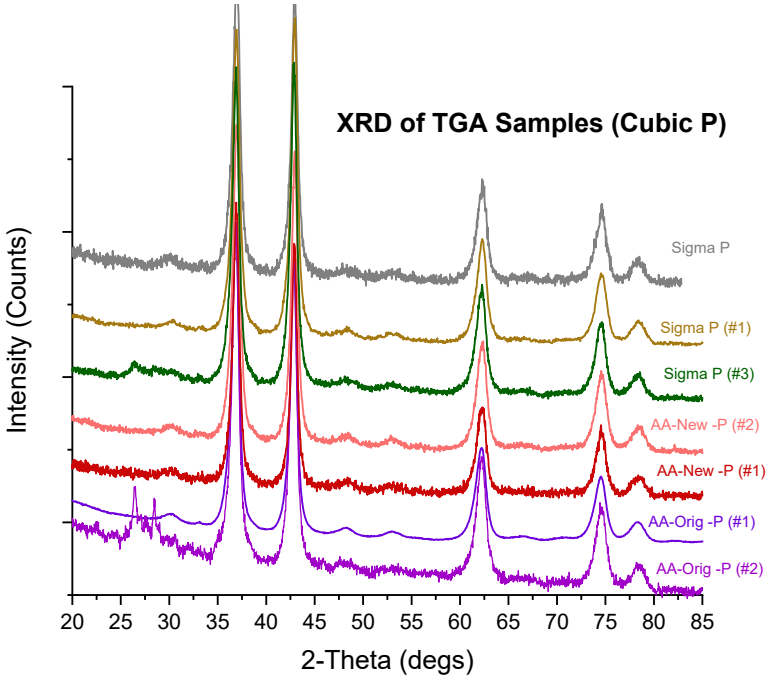

Figure B.8-4 Lab XRD of various Cubic P samples processed for TGA samples as listed in Table B.8-2

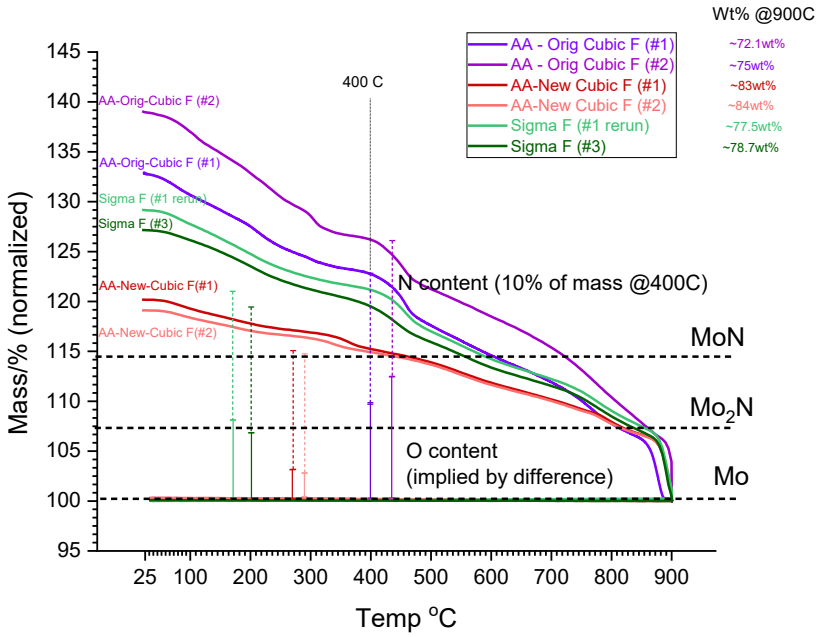

Figure B.8-5 TGA profile of various Cubic F (C700) samples derived from both Alfa Aesar and Sigma Aldirch botthles. Dotte and Solide bars indicate the relative presense of N and O in the bulk of these Cubic F structures. Details of samples and analysis results in Table B.8-1

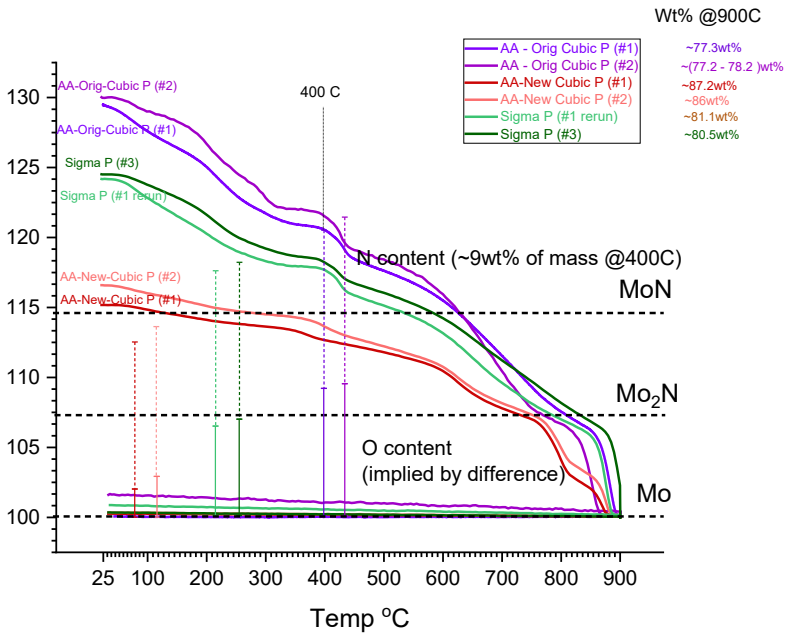

Figure B.8-6 TGA profile of various Cubic P (C800) samples derived from both Alfa Aesar and Sigma Aldirch botthles. Dotte and Solide bars indicate the relative presense of N and O in the bulk of these Cubic F structures. Details of samples and analysis results in Table B.8-2

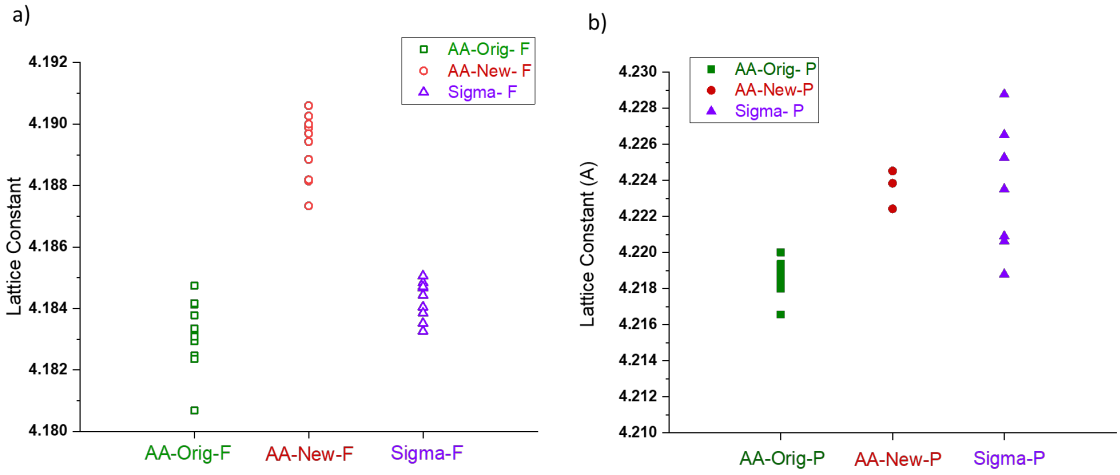

Figure B.8-7 Lattice constant of various (a) Cubic F and (b) Cubic P samples, categorized based on MoO_3 bottle, derived from Lab XRD usinf JADE. Green for AA-Orig, Red for AA-New and Purple for Sigma based data points. . AA-New of both P and F have higher lattice constant compared to AA-Orig, showing variation within the same vendor.

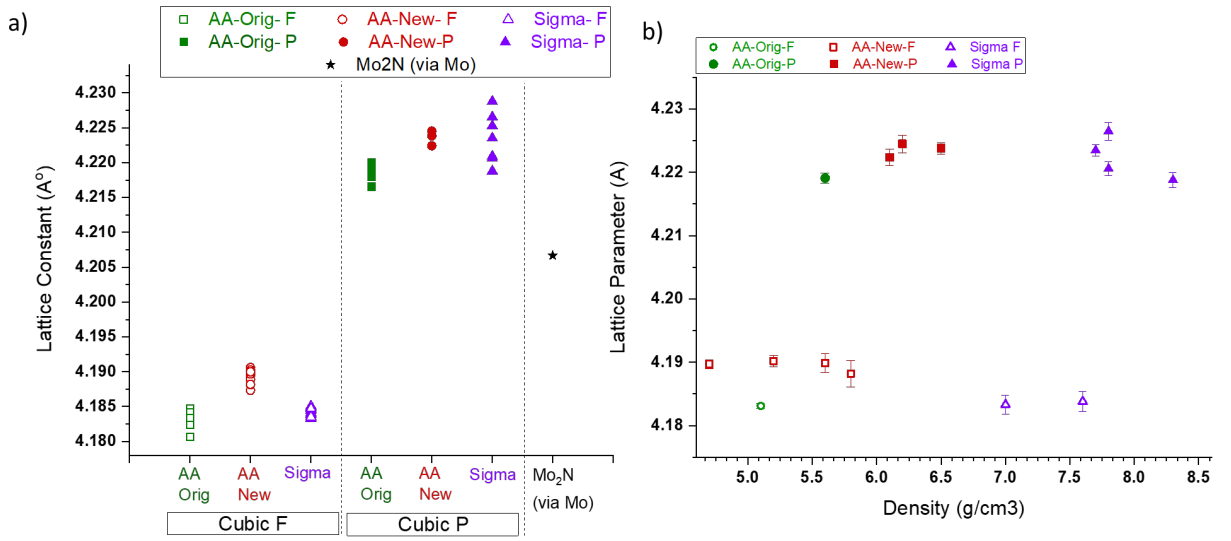

Figure B.8-8 (a) Lattice constant of all Cubic F and Cubic P samples in above figure, plotted on same scale. All Cubic P samples have higher lattice constant compared to Cubic F, with most spread observed in Cubic P samples synthesized from Sigma Aldrich. (b) Density vs Lattice pramter for various Cubic F and Cubic P samples from different vendors. No direct correlation was observed, within datapoints of subgroups. Overall, Cubic P samples are denser than Cubic F samples as discussed in Chapter 4.

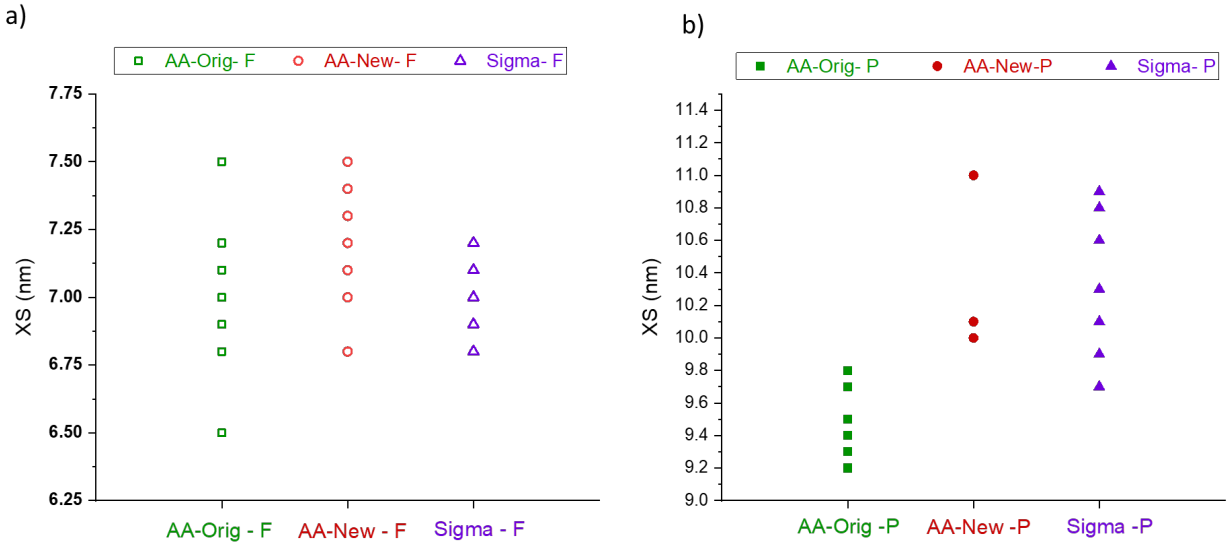

Figure B.8-9 Crystallite Size of various (a) Cubic F and (b) Cubic P sample (JADE analysis of Lab XRD patterns) synthesized from various MoO_3 bottles. No particular trend is observed, and no effect of choice of vendor is visible.

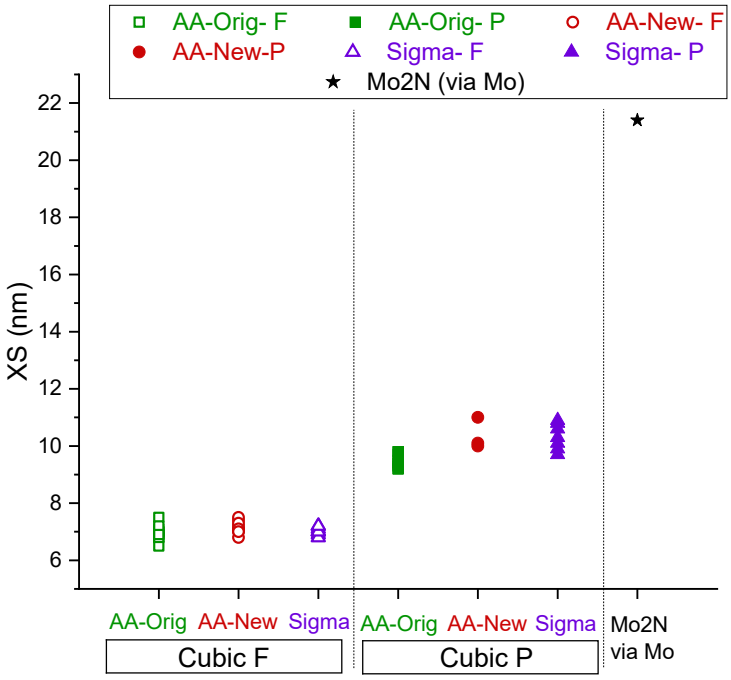

Figure B.8-10 Crystallite size of Cubic F, Cubic P and Mo_2N (via Mo). Mo_2N (via Mo) is sample synthesized via first reduction of MoO_3 to Mo metal and then immediate ammonolysis at 700C without removing the sample from furnace. This possibly oxygen free gamma Mo2N sample, has much high crystalline size (and possibly small surface are), again hightlighting the power of ammonolysis of oxides as a technique to get small crystalline size sample with high surface area.

Table B.8-1 Summary of Cubic F samples for TGA analysis and Density measurement. Sample IDs refer to sample batches that were used for the experiment. Whenever same batch of sample used for TGA was also measured for density, those values are listed as well. For some sample IDs only density measurements were done and not the TGA.

Precursor	TGA Run ID	Sample ID	Bench Time# (Sample synthesis to TGA)	Adsorbed gases (@400C) Wt%	O wt% (in Bulk) Cubic P : ~10wt% N of mass @400C	N/O atomic ratio (Bulk)	Density (g/cm^3) Pycnometry
AA-Orig-F	AA-orig- F (in paper)	*SR005 – B07 – Gamma	~ Avg : 2-3 months	7.6 %	8.6 %	1.3	5.1 (in paper) | 5.1 (repeat)
	AA-Orig-F (#2)	SP082619 – SR005 – Gamma	~ 2.5 years	9.3 %	10.7 %	1.1	
AA-New -F	AA-new- F (#1)	SP05282021	2 days	4.4 %	3.0 %	3.8	5.8
	AA-new-F (#2)	SP06182021	Same day	3.5 %	3.0 %	3.8	5.2
		SP06062020					4.7
Sigma -F	Sigma- F #1	SP06022021	1day	5.0 %	6.0 %	1.9	
	Sigma- F #1-re	SP06022021	~10 days	6.2 %	7.5 %	1.5	
	Sigma-F #3	SP04252021	~50 days	6.0 %	6.3 %	1.8	7.0
	Sigma-F 7%H2	SP05162021	8 days				
		SP06062021					7.6

Table B.8-2 Summary of Cubic P samples for TGA analysis and Density measurement

Precursor	TGA Run ID	Sample ID	Bench Time# (Sample synthesis to TGA)	Adsorbed gases (@400C) Wt%	O wt% (Bulk) Cubic P : ~9wt% N of mass @400C	N/O atomic ratio (in Bulk)	Density (g/cm^3) Pycnometry
AA-Orig - P	AA-orig- P (#1)	*SR012 – B01 – Cubic (P)	~ Avg: 2-3 months	6.5 %	8.4 %	1.2	5.6 (in paper) | 5.5 (repeat)
	AA-orig- P (#2)	S2NDS-PTS22898	~ 1.5 years	7.0 %	8.3 %	1.2	
AA-New -P	AA-new- P (#1)	SP05312021	1 day	2.3 %	2.1 %	4.8	6.1
	AA-new- P (#2)	SP04292021	~ 50 days	2.6 %	2.9 %	3.5	6.5
		SP06052020					6.2
Sigma - P	Sigma- P #1	SP06042021	Same day	2.8 %	4.3 %	2.4	
	Sigma- P #1-re	SP06042021	~12 days	5.2 %	6.1 %	1.7	
	Sigma-P #3	SP05232021	~22 days	5.0 %	6.5 %	1.6	
	Sigma- P 7%H2	SP05152021	8 days				
		SP05242021					7.8
		SP07012021					7.7
		SP05152020					7.8
		SP04102020					8.3

Table B.8-3 : Summary of Cubic F and Cubic P samples categorized based on precursor bottles.

Precursor	F (700C) Or P (800C)	CHSN | Nwt%		Adsorbed[&] gases (@400C) Wt%	O wt% (Bulk)	N/ O atomic ratio (Bulk)	Density g/cm^3	Surface Area (m^2/g)
		As synthesized (Bulk + Surface)	Desorbed @400C (Bulk)					
AA-Orig	Cubic F	11.1 wt%		[7.6-9.3]%	[8.6 - 10.7]%	[1.1 – 1.3]	5.1 g/cm^3	135 m^2/g
	Cubic P	10.0 wt%		[6.5-7.0]%	[8.3 – 8.4]%	1.2	[5.5 - 5.6] g/cm^3	55 m^2/g
AA-New	Cubic F			[3.5-4.4]%	3%	3.8	[4.7 – 5.8] g/cm^3	
	Cubic P			[2.3-2.6]%	[2.1-2.9]%	[2.2 – 2.9]	[6.1 – 6.5] g/cm^3	
Sigma	Cubic F	11.1 wt%	10.1 wt%	[2.3-2.6]%	[6.0 – 7.5]%	[1.5 – 1.9]	[7.0 – 7.6] g/cm^3	111 m^2/g
	Cubic P	10.2 wt%	9.2 wt%	[2.8-5.2]%	[4.3 – 6.5] %	[1.7 – 2.4]	[7.7 – 8.3] g/cm^3	70 m^2/g

[&]Cubic F : ~10wt% N of mass @400C (Bulk) | Cubic P : ~9wt% N of mass @400C (Bulk)

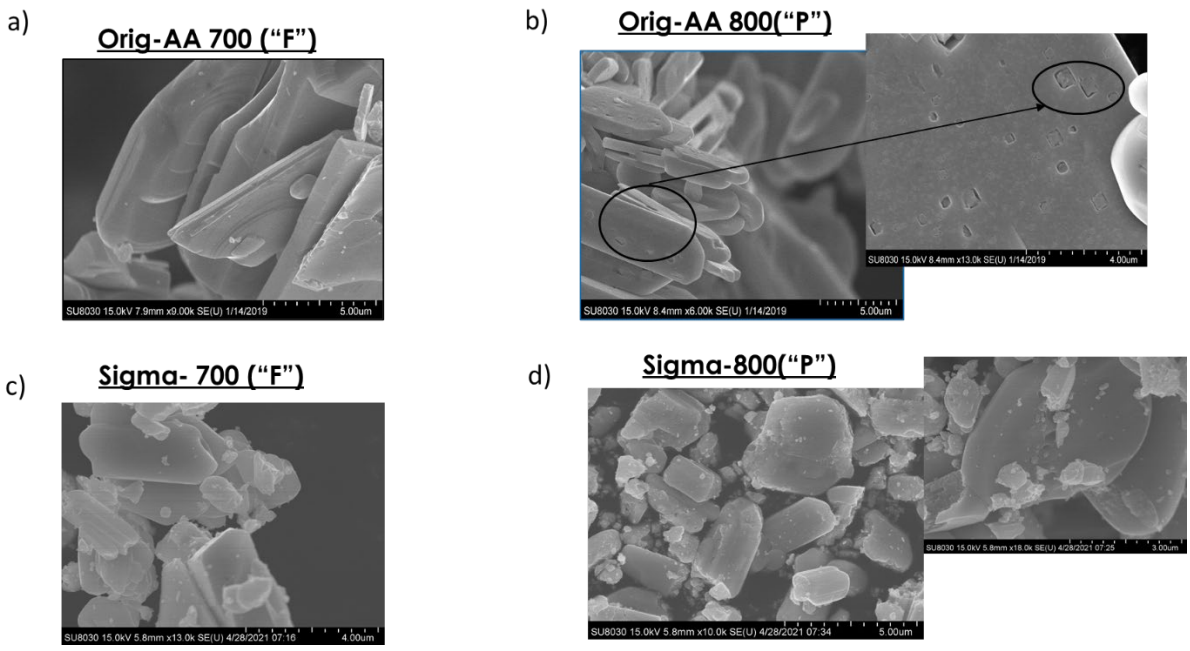

Figure B.8-11 SEM of Cubic F and Cubic P samples derived from Sigma vs AA-Orig precursor bottle.

B.9 Stability issue of Molybdenum Oxynitrides under oxidative environment

Molybdenum oxynitrides in general were found to be unstable under oxidizing environments. Several studies on Molybdenum oxynitrides stability and applications that were pursued beyond the HER application discussed in detail in Chapter 5, are summarized below, highlighting the shortcoming of these oxynitrides for use under oxidizing conditions.

B.9.1 Rapid degradation in SAFC Cathode

Cubic P Molybdenum oxynitride (C800 sample in Chapter 4, section 4.3) was evaluated as oxygen reduction reaction catalyst in Solid Acid Fuel Cell cathodes. SAFC testing was done in Haile Lab at 250ºC, with hydrogen and air respectively on anode and cathode side, as described in Chapter 2, section

2.3.1. For the cell fabrication, half cell based on Pt/C as for counter electrode in SAFC studies in Chapter 2 were fabricated. The cathode was fabricated onto the electrolyte, with CDP and MoON mixed (grinded for 30 min in ethanol) in 1:1 ratio. Polarization curves are shown in Figure B.9-1. While the OCV and current densities are much low compared to Pt based SAFC cells discussed in Chapter 2,[203] the bigger issue was the rapid degradation in performance. This can be attributed to instability of Molybdenum nitrides with CDP at 250C under humidified air discussed in section B.9.3 of this appendix.

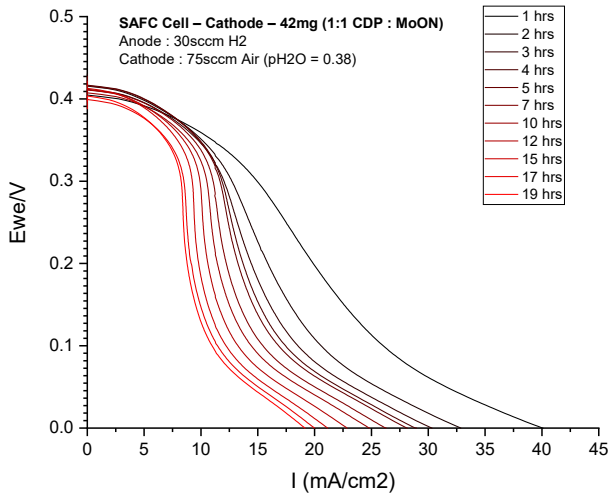

Figure B.9-1 SAFC polarization curves with Cubic P Molybdenum oxynitride based cathode mixture for ORR. Rapid degradation in performance is observed.

B.9.2 Rapid degradation for Room temperature HER (Liquid Electrochemistry)

Both Cubic and hexagonal molybdenum nitrides are reported in literature as potential room temperature liquid oxygen evolution reaction (OER) catalysis.[154, 155] This work was done in collaboration with Linsey Group here at Northwestern University, wherein sample synthesized in work was used for catalysis testing.

Cubic F (C700 sample in Chapter 4, section 4.3) were tested for oxygen evolution reaction (OER) catalysis in room temperature liquid electrochemistry rotating disk electrode setup as described in literature.[154, 155] OER activity was measured using Cyclic Voltammetry curves (CV's),[32, 43] using typical cell fabrication approach using Glassy carbon electrode and spin coating technique, as detailed in Figure B.9-2. The reported voltage on the plot is the potential of the working electrode with respect to the reference. The counter electrode is allowed to float in order to balance current, thus driving OER. CV's were measured started with -0.15 to 0.6V (just below OCV) which was relatively stable and exhibited activity normal for that reported for Mo_2N in literature. On increasing potential, an oxidative current peak formed, after which the activity started to rapidly decline, suggesting the oxidation of the catalysts as the possible reason, again suggesting that against whats reported in literature, molybdenum nitrides are not good catalysts under oxidative conditions.

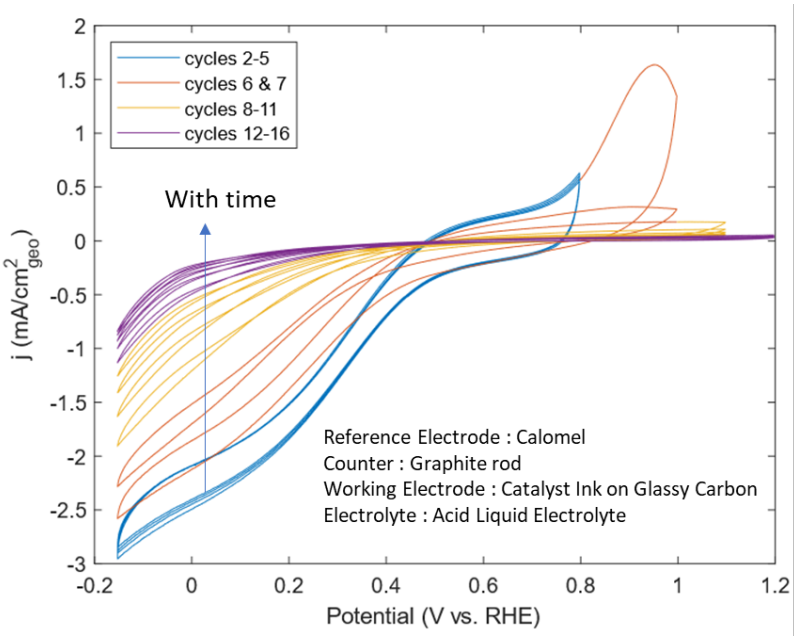

Figure B.9-2 : CV curves for evaluating OER activity of Cubic F Molybdenum oxynitride (C700) at room temperature using liquid electrochemistry glass carbon rotating disk setup. (*Courtesy : Matthew Sweers, Linsey Group, Northwestern University*)

B.9.3 Instability with CDP under humidified air @250C

As synthesized Cubic “F” γ-phase (C700 sample in Chapter 4, section 4.3) which is a reported metallic conductor with good water splitting catalytic activity for both oxygen evolution,[227] and hydrogen evolution[151-154, 243] was studied for long term stability test with CDP (1:1 γ-MO_2N and CDP, pressed together into a dense pellet) under humidified N_2 and air conditions @250C, to understand which half reaction of a CDP based Solid acid electrolyzer cell would these be good catalyst for (OER or HER).

For the case of humidified N_2, no structural change was observed and the post test CDP + Mo_2N Lab XRD pattern (grey curve, Figure B.9-3, with refinement in dotted red) could completely be refined using only CDP and Mo2N phases suggesting negligible reaction at 60hrs. This supports the negligible reaction result at the end of 24hrs in Chapter 3, in preliminary screening of these molybdenum nitrides with CDP (similar humidified N_2 @250C). No further reaction beyond 60hrs was tested under humidified N_2

In strike contrast, Lab XRD pattern of post stability test sample (CDP + Mo2N pellet) under humidified air (black curve, Figure B.9-3) shows the presence of amorphous bump between 25-20 degrees, with the disappearance of several CDP peaks, even at 32hrs. Upon increasing the reaction time to 96hrs, this deleterious effect is exemplified to a much larger extend, with no more CDP peaks visible, with a large amorphous bump (~50% phase fraction) formed in the Lab XRD pattern (blue curve, Figure B.9-3) of post test sample. The pellet after 96 hrs turned more darker after test, as shown in the optical images in inset in Figure B.9-3.

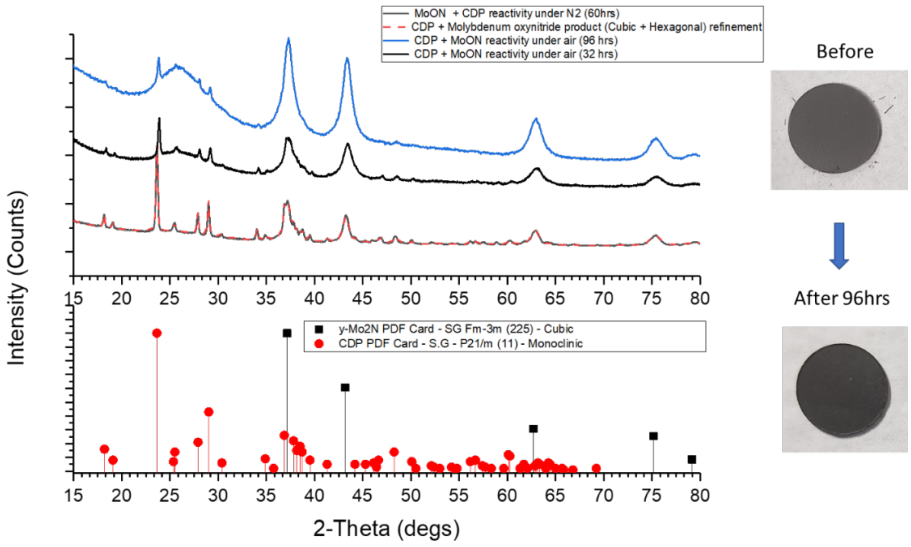

Figure B.9-3 Lab XRD pattern of CDP + Mo2N pellet post stability test under (a) humidified N2 for 60hrs, (b) humidified air for 32 hrs, and (c) 96 hrs.

B.9.4 Resistivity measurement (Cubic P) at 250C under humidified Air and N_2

Same Cubic F (C700) sample tested above for stability with CDP under humidified air and nitrogen, were also tested for bulk conductivity using Impedance Spectroscopy, [20, 244, 245] with the conditions for testing show on the right in inset of Figure B.9-4.

Bulk Mo2N pellet was formed by pressing ¾ inch pellets (~500mg 4T, 5 min), and sandwiched between current collector and gas diffusion (carbon paper and stainless steel mesh) electrodes, and determining the ohmic resistance from the offset in impedance plots under humidified N_2 and air conditions. Offset values on impedance plots (not shown here, recorded at OCV, every 10 min for the first 50min, and then every hour for the next 10 hrs) was used for resistivity calculations. Temporal evolution of electronic resistivity in Figure B.9-4, shows that the γ-phase shows degradation (5 fold increase in resistivity within 10hours) in conductivity with time under humidified air (red curve, Figure B.9-4) @250°C with time, however is relatively much stable under neutral humidified nitrogen conditions (blue curve, Figure B.9-4).

This dictates why rapid degradation in performance was observed in SAFC discussed above in section B.9.1, and for OER evolution side of full polarization curves for SAEC shown in Chapter 5.

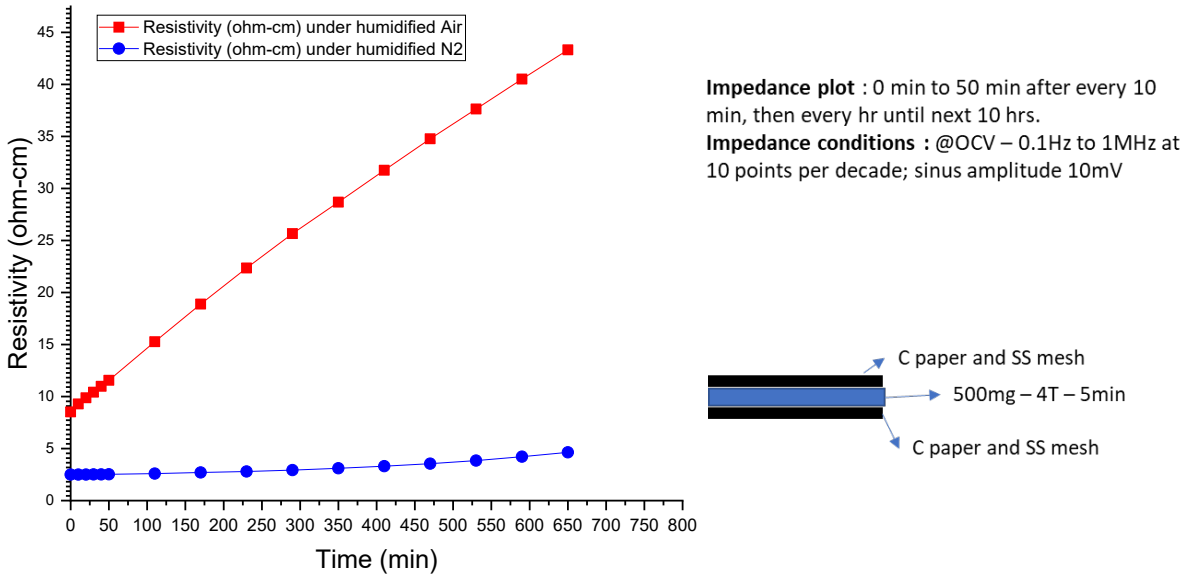

Figure B.9-4 Resistivity plot with time of Cubic F (C700) Molybdenum Oxynitride at 250C measured using Impedance Spectroscopy under humidified N_2 (blue) and Air (red).

B.9.5 SAEC full polarization curve at 250C under humidified N_2 using Cubic P Molybdenum Oxynitride (C800 sample)

Supporting experiment for Chapter 5, section 5.4 on Molybdenum oxynitrides for HER in SAEC.

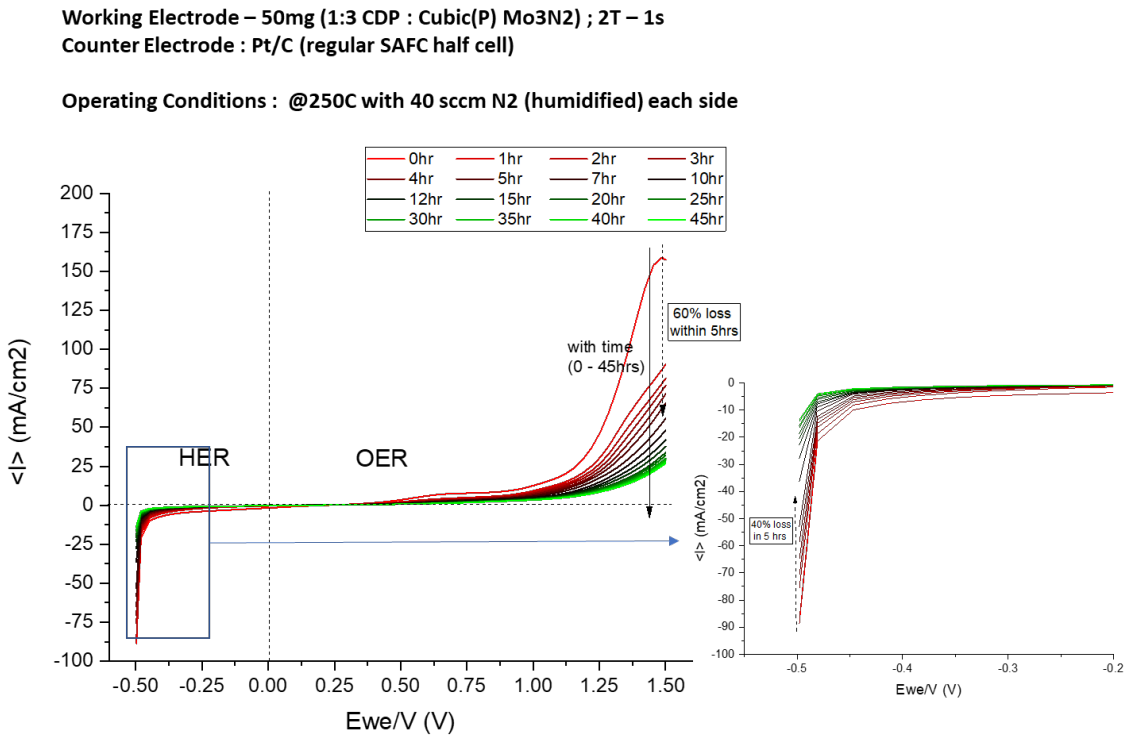

Figure B.9-5 Full SAECelectrolysis polarization curves at 250°C under humidified N_2 instead of hydrogen, using C800 (Cubic P sample) as the test sample. Polarization curves were collected biasing from -0.5V to 1.5V, collected every hour for 45 hrs. Rapid degradation hypothesized by oxidation of the catalyst under oxidizing current occurred on the OER side (also effecting the HER side).

Appendix C Miscellaneous Experimental Projects

C.1 Phase pure synthesis and chemical characterization of Tetragonal "β-Mo2N" phase

Synthesis and Characterization of Phase pure Cubic F, Cubic P and Hexagonal molybdenum nitrides obtained from the ammonolysis of oxides at high temperature is studied in detail in Chapter 3 and 4 respectively. Tetragonal phase was synthesized via high temperature nitridation of MoO_3 (0.25g) at 700°C under 1:3 volume ratio of N2 (33 sccm) and H3 (200sccm) gas mixture following the same heating profile used for C700 and C800 synthesis. This sample is referred to as T700 ↔ β-phase ↔β-Mo_2N, as the Lab XRD can be matched with Tetragonal β-Mo_2N (PDF#01-075-1150) reported in literature.

Similar chemical characterization as discussed for Cubic and Hexagonal phases in Chapter 5, were performed for the Tetragonal sample (T700), however co-refinement studies are still pending.

A summary of all the chemical analysis results in summarized in Table C.1-1. These just like C700, C800 and H700 samples, turn out to be oxynitrides. Overall, the Mo content is much higher compared to Cubic and Hexagonal samples as shown by the TGA plots comparing all four phases in Figure C.1-2. Also, the tetragonal phase has least adsorbed gases on the surface, which is not surprising as NH_3 isnt used for synthesis and it was shown by TPR measurement that NH_3 and H_2O are the dominant surface species at least on the cubic phase. This is also confirmed by combustion Nwt% measurement of as synthesized samples, and that after desorbing samples under Argon at 400C to remove adsorbed gases if any, where only 0.1wt% N content is reduced in desorbed samples compared to 5.9wt% in as synthesized samples (within the CHSN error of 0.3wt%), Table C.1-1. Stoichiometric Mo_2N would mean 6.8wt% N, which suggests the Mo:N is slightly more compared to reported 2:1 in literature for the β-phase. Unlike Cubic phases (C700 and C800) where PGAA suggested much lower Mo:N ratio (close to 1) compared to y-

Mo_2N phase composition, the PGAA of Tetragonal phase Figure C.1-5, suggests Mo:N ratio of 2.19, which supports the slightly lower Nwt% measured from CHSN compared to Mo_2N composition. Unlike Cubic samples, the PGAA determined values are much more reliable as bulk Mo:N value due to negligible adsorbed gases on surface. The Mo:H ratio of 10.1 from PGAA suggests least hydrogen incorporation in bulk (if any) compared to Cubic and Hexagonal phases, however positive hydrogen wt% was detected in combustion analysis of desorbed tetragonal samples, although the value is too small o=to be reliable, needing NMR studies to further probe the possibility of low yet measurable H in bulk of the tetragonal phase.

90.7wt % Mo in bulk of these materials from TGA and 5.8wt% N in bulk from CHSN analysis still leave for considerable wt unaccounted for, which is suspected to be oxygen in the bulk, just like it was found for Cubic and Hexagonal samples. Thermal XPS for T700 is shown in Figure C.1-3, with the Mo3d and Mo3p-N1s peak deconvolution (similar to other phases XPS analysis in Chapter 4). High O signal was detected along with the Mo and N signals. Overall, Mod+ bulk average oxidation binding energy was determined as 228.3eV, lower than all other phases, suggesting least anion to cation ratio amongst all the phases. Other values such as O/N on surface, By combining TGA, PGA and CHSN analysis within5% error the composition of T700 sample is found to be $MoN_{[0.42\text{-}0.47]}O_{[0.18\text{-}0.23]}H_{[0.09\text{-}0.10]}$. Using only TGA and pre and post desorption combustion N wt% values, the true bulk composition of $MoN_{0.44}O_{0.21}$ can be calculated. This suggests a rather high 1:2 atomic ratio of N and O in the bulk making these molybdenum oxynitrides.

Structural characterizations under TEM, Figure C.1-4a), reveal that these samples are dense, with irregular particles, where the SADP patterns, Figure C.1-4b) that can be indexed to Tetragonal I41/amd–(141) space group, same as Lab XRD. Unlike Cubic and Hexagonal phases synthesized via ammonolysis which leads to single crystalline like SADP pattern in TEM, the SADP pattern for tetragonal phase is polycrystalline rings. BET surface area of $12 m^2/g$ was measured which makes it the lowest surface area phase compared to C700, C800 and H700 samples.

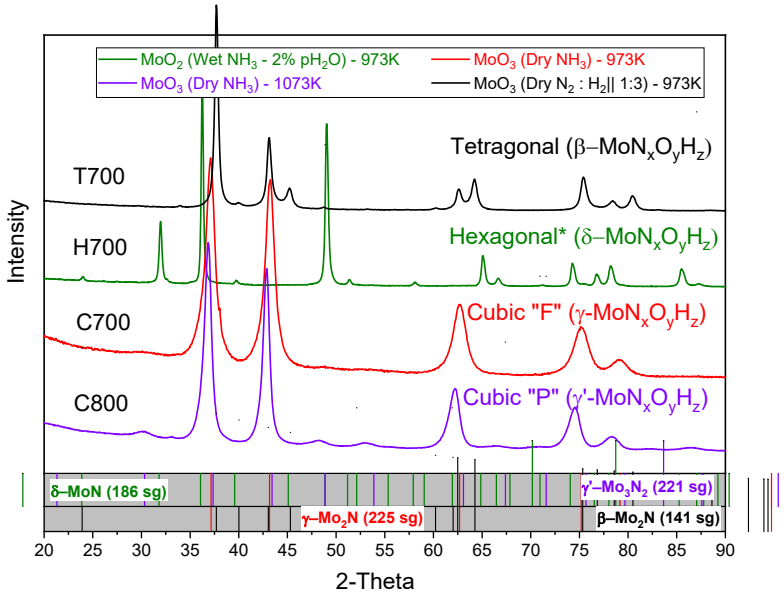

Figure C.1-1 : The Lab XRD pattern of all 4 important Molybdenum oxynitride samples (C700, C800, H700 and T700) synthesized in this work. While these match to tetragonal β-Mo_2N PDF#01-075-1150 |Hexagonal (δ-MoN PDF#04-003-5713 | Cubic “F” (Fm-3m) γ-Mo_2N PDF# 04-018-6868 | Cubic Pm-3m γ’-Mo_3N_2 PDF# 04-007-1915), all of these actually are Molybdenum oxynitrides with different level of oxygen and hydrogen in the bulk | MoNxOyHz type composition.

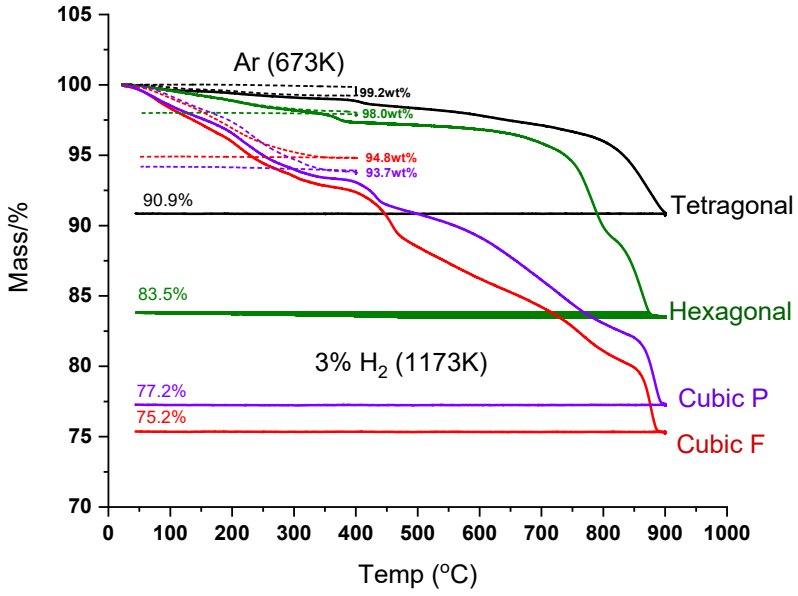

Figure C.1-2 TGA reduction of all four molybdenum oxynitride phases under 3%H_2 at 900°C to Mo.

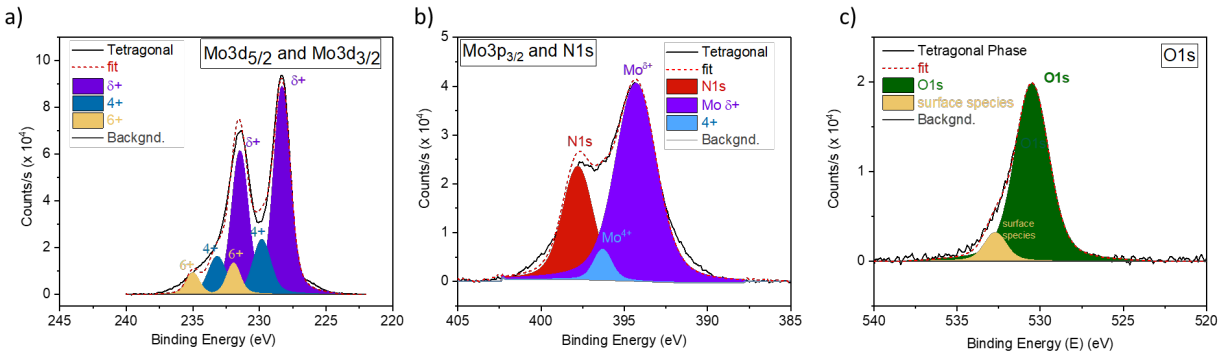

Figure C.1-3 Thermal XPS of Tetragonal molybdenum oxynitride phase (T700)

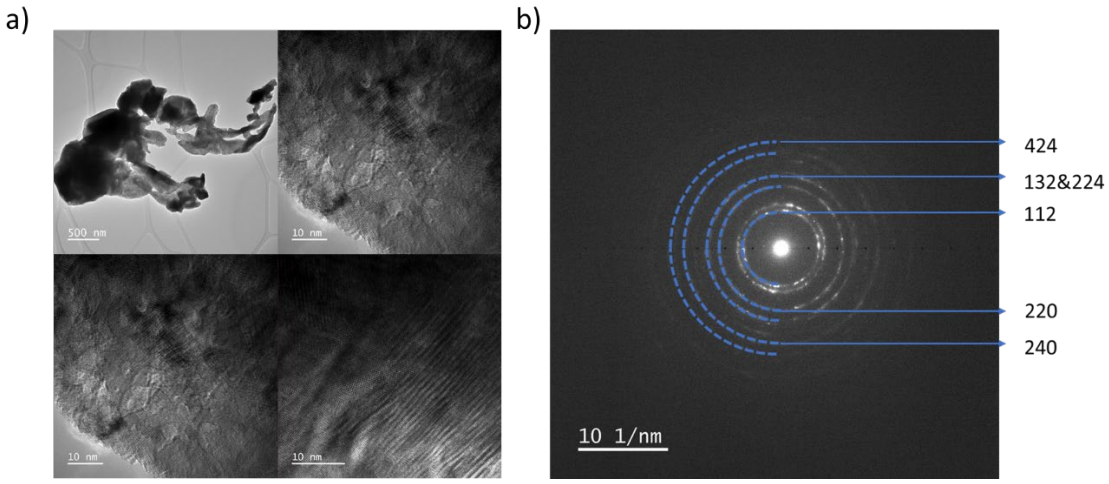

Figure C.1-4 (a) TEM images showing the irregular particles, with not much pores in the structure. (b) SADP reveal the polycrystalline nature of these samples, while confirming the Tetragonal I41/amd–(141) space group.

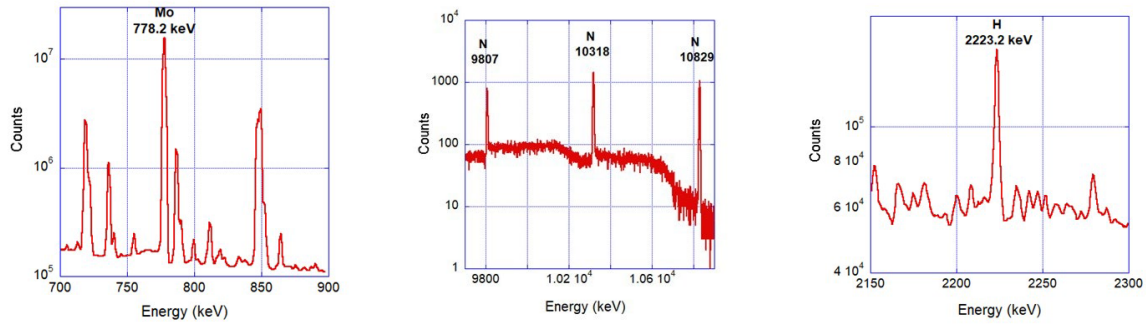

Figure C.1-5 PGAA spectra of Tetragonal Molybdenum oxynitride sample (T700) | β-phase

Table C.1-1 : Summary of chemical and structural characterization of the Tetragonal phase (T700)

Chemical Analysis (Tetragonal Molybdenum Oxynitride)	
Thermal XPS spectra	
Elements detected	Mo, N and O
Binding Energy (BE) for $Mo^{\delta+}$	228.3(1) eV
Combustion Analysis	
Absolute N content, as-synthesized	5.9(3) mass %
Absolute N content, surface-desorbed	5.8(3) mass %
Absolute H content, as-synthesized	0.2(3) mass %
Absolute H content, surface-desorbed	0.1(3) mass %
PGAA Analysis	
Mo: N atomic ratio	2.19(5)
Mo: H atomic ratio	10.1(2)
Chemical Composition	
Pre-desorption :	
Within 5% (TGA + PGAA + CHSN)	$MoN_{[0.42-0.47]}O_{[0.18-0.23]}H_{[0.09-0.10]}$
Post-desorption :	
Deduced from TGA + CHSN	$MoN_{0.44}O_{0.21}$
TGA Results	
Mass loss under Ar TGA @400°C	0.76(9) wt%
Mass loss at 400°C under H_2 TGA (900°C, 3% H_2/Ar)	2.18(1)wt%
Net anion loss H_2 TGA (900°C, 3% H_2/Ar)	9.1(2) wt%
Mo(bulk) using H_2 TGA	90.7(2) %
Structural Characterization (Tetragonal Molybdenum Oxynitride)	
Crystallinity (TEM SADP)	Polycrystalline
BET Measurement	
Surface Area	12.21(8) m^2/g
Pycnometry:	
Measured density	8.72(3) g/cm^3

C.2 Interconversion of Cubic and Hexagonal Molybdenum Oxynitrides

Several ex-situ interconversion experiments were performed to understand if one phase could be readily converted to the other, within the 3 Molybdenum oxynitride phases: γ-phase ("Cubic F"), γ'-phase ("P") and δ-phase. In all these experiments ~0.15g of sample was subjected to Dry or Wet ammonolysis. For dry ammonolysis, 100sccm of NH3 was used, while for wet ammonolysis additional 100sccm humidified Ar is flown (pH_2O = 2%). Following heating profiles acronyms are referred to in the discussion:

HP1 : RT to 700ºC at 3ºC/min; hold for 12 hrs ; cooldown to ambient temperature

HP2 : RT to 350ºC at 5 ºC/min ; 350ºC to 500ºC at 0.6 ºC/min ; 500ºC to 700ºC or 800ºC at 3 ºC/min ; hold 12 hrs ; cooldown to ambient temperature

HP3 : RT to 350ºC at 5 ºC/min ; 350ºC to 500ºC at 0.6 ºC/min ; 500ºC to 700ºC or 800ºC at 3 ºC/min ; hold 3 hrs ; cooldown to ambient temperature

In first set of experiments, Figure C.2-1a), ex-situ synthesized Cubic F γ-phase (C700, Chapter 3 and 4) from MoO_3 via dry ammonolysis at 700ºC (HP3 heating profile) (details in Chapter 3), was converted to Cubic P γ'-phase (C800 type) by increasing ammonolysis temperature to 800ºC (HP2 heating profile). Isothermal hold under dry ammonia at lower 650ºC temperature (for ~50hrs) does not lead to conversion to delta phase as suggested by Gomathi etal,[246] although they used nanoparticles of γ-phase to start with. Subjecting Cubic γ-phase ("F") to wet ammonolysis (2% pH_2O) at 700ºC following HP1 heating profile (details in Chapter 3), does not lead to conversion to δ-phase. The possibility was suggested by the in-situ Lab XRD wet ammonolysis experiments that suggested under adequate pH_2O the initially formed γ-phase converts completely to δ-phase over the time, as discussed in Chapter 3, section 3.6.2. Interestingly (Figure C.2-1b), the conversion to δ-phase was possibly if the starting material has some δ-phase in the mixture (like a seed phase). For this γ+ δ-phase mixture with 25% δ-phase, was synthesized via dry ammonolysis of MoO_2 at 700ºC (HP1 heating profile). The same mixture when heated to 800ºC

(HP3 heating profile) converts the entire phase to nearly phase pure Cubic γ'-phase ("P"), just like phase pure Cubic γ-phase ("F") did.

Alternatively, δ-phase (H700, details in Chapter 3 and Chapter 4) synthesized from MoO_2 wet ammonolysis (2% pH_2O) at 700°C (HP1 heating profile) was also used for such interconversion experiments (Figure C.2-1c). Dry ammonolysis at 700°C does not cause any phase change for the δ-phase. However, when subjected to dry ammonolysis at slightly higher temperature 750°C, leads to 60% of δ-phase converted to Cubic γ-phase ("F"), suggesting high enough temperature under dry ammonolysis can make the interconversion possible.

In general, Figure C.2-2 shows a first pass preliminary interconversion schematic between the 2 Cubic and 1 hexagonal phase. Using higher temperature (1073K) either Cubic γ-phase ("F") or δ-phase can be converted to Cubic γ'-phase ("P") phase under dry ammonolysis. Conversion back from Cubic γ'-phase ("P") to any other phase was not seem possible within these set of experiments. As synthesized Cubic γ-phase ("F") can be converted to δ-phase via wet ammonolysis only if there is enough seed hexagonal phase present (how low still needs to be determined). Finally, δ-phase can be converted first to Cubic γ-phase ("F") and then to Cubic γ'-phase ("P") by simply raising temperature under dry ammonia.

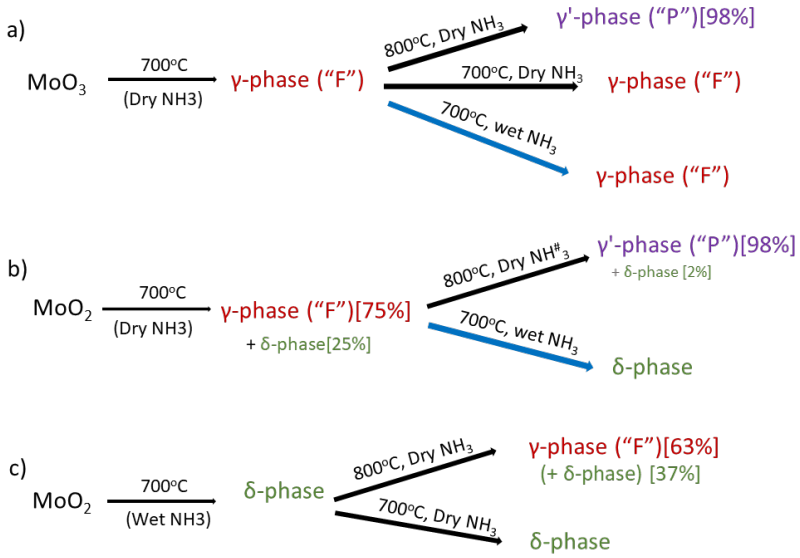

Figure C.2-1 Interconversion experiments between Cubic and Hexagonal Molybdenum nitrides. (a) Cubic F (γ-phase) under dry ammonolysis at 700°C and 800°C, where later results in Cubic P formation. (b) Mixture of mainly Cubic F (γ with 25% δ) sample can be converted to Cubic P by performing ammonolysis at 800°C. In strike contrast, using wet ammonolysis at 700°C, the hexagonal phase can be maximized in final product. (c) Dry ammonolysis of phase pure δ-phase at 700°C and 800°C, where change to Cubic phase was only observed at 800°C.

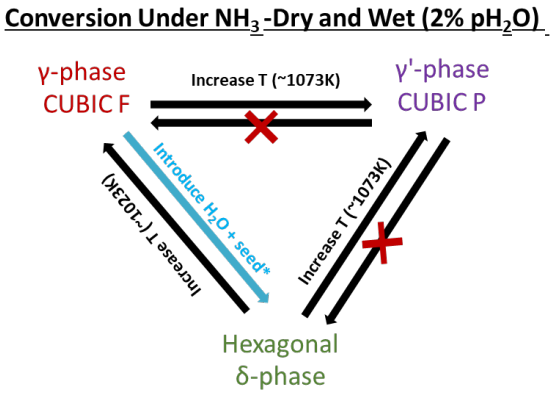

Figure C.2-2 Interconversion diagram between Cubic F, Cubic P and Hexagonal molybdenum nitrides based on various dry and wet ammonolysis interconversion experiments discussed in this section

C.3 Mo_2N – Ru nanoparticles composite synthesis for ammonia decomposition

Molybdenum nitrides are reported as ammonia decomposition catalysts, specially the γ-Mo_2N phase.[105, 114] Simultaneously, Ruthenium is considered as one of the best-in-class catalyst for ammonia decomposition. Austin, from Haile group, has used Ru nanoparticles for application in Solid Acid Hydrogen Pump.[27] Metal nanoparticle – Mo_2N composites were Mo_2N properties as a support layer is exploited have been investigated in literature for various electrocatalytic applications.[157, 247] Motivated by these, an attempt to make Ruthenium nanoparticles – Mo_2N (Ru -Mo_2N) composite was performed. Sodium borohydride chemical solution method was used, aiming for 10% and 30% Ru on Ru-Mo_2N composites, with details below[27] :

10% Ru on Mo_2N : 45mg of y-Mo_2N in 10mL of DI Water under vigorous stirring. Ruthenium Chloride precursor was added (14.35mg $RuCl_3$.xH2O). Ru reduction was induced by the introduction of an ice cold NaBH4 (Sigma Aldrich >98%) solution with 8.8mg in 2.3 mL added dropwise to the main solution. After ruthenium was fully reduced, the particles were separated from the solution by centrifuge and rinsed with deionized water. Ru – Mo2N was dried under Ar @80C in Tube Furnace for 15h.

30% Ru on Mo_2N : 135 mg of y-Mo_2N in 10mL of DI Water under vigorous stirring. Reduction of ruthenium (165 mg $RuCl_3$.xH_2O) was induced by the introduction of an ice cold $NaBH_4$ (Sigma Aldrich >98%) solution with 101 mg in 26.6 mL added dropwise to the main solution. After ruthenium was fully reduced, the particles were separated from the solution by centrifuge and rinsed with deionized water. Ru – Mo2N was dried under Ar @80C in Tube Furnace for 15h.

Lab XRD in Figure C.3-1 shows that no strong Ru peak is separately observed for 10% Ru sample (within the detection limit of XRD) suggesting possible doping of Ru into the bulk of Mo_2N, however metal Ru broad humps (nano crystallite size, at around 58 and 69 degrees) can be seen for the 30% Ru sample. However, XPS analysis in Figure C.3-3 and Figure C.3-4 for 10% and 30% Ru-Mo2N composites show strong Ru and Mo signals with different Ru and Mo environment suggested for both these composites.

Additionally, no leftover chlorine signal was found form synthesis. Lattice constant of Mo_2N phase was refined for the three samples, and plotted in Figure C.3-2. The lattice constant decreases upon composite formation, with 10% having lower lattice constant Ru and Mo have close atomic sizes, however Mo can take a range of oxidation states, unlike Ru. It was shown in Chapter 4 that these Cubic F synthesized from MoO_3 ammonolysis possess Mo vacancies, and it can be hypothesized, that Ru incorporates into the y-phase bulk at 10%, resulting in a structure with lower lattice constant compared to bulk Mo_2N, which increase at 30wt% Ru at which point metal peaks can be detected in XRD.

Preliminary SAHP ammonia decomposition tests at 250°C using CDP as electrolyte were tested using these samples. For this 1:1 CDP:composite mixture was used for the working electrode. For reference, only Mo_2N was also tested. Details of cell processing and testing for SAHP can be found in Ausin's thesis, from Haile Group. Mo_2N by itself was found to be a positive SAHP catalyst, however the OCV (a measure of how good the SAHP catalyst is, which lower values means better catalysis) varied a lot with time. In contrast, 30wt% Ru-Mo_2N composite shows much more improved OCV, which was also stable OCV with time. However, the current densities were 6 times lower than state of the art Ru-CNT based ammonia decomposition values demonstrated for SAHPs.[27] Possibly adding some co-catalyst carbon based electronic support in the electrode mix can help with this. Also, pretreating composite under hydrogen to reduce any oxides on surface of composite can also help further. While preliminary, this study shows the potential of using Mo_2N in combination with Ru for SAHP application.

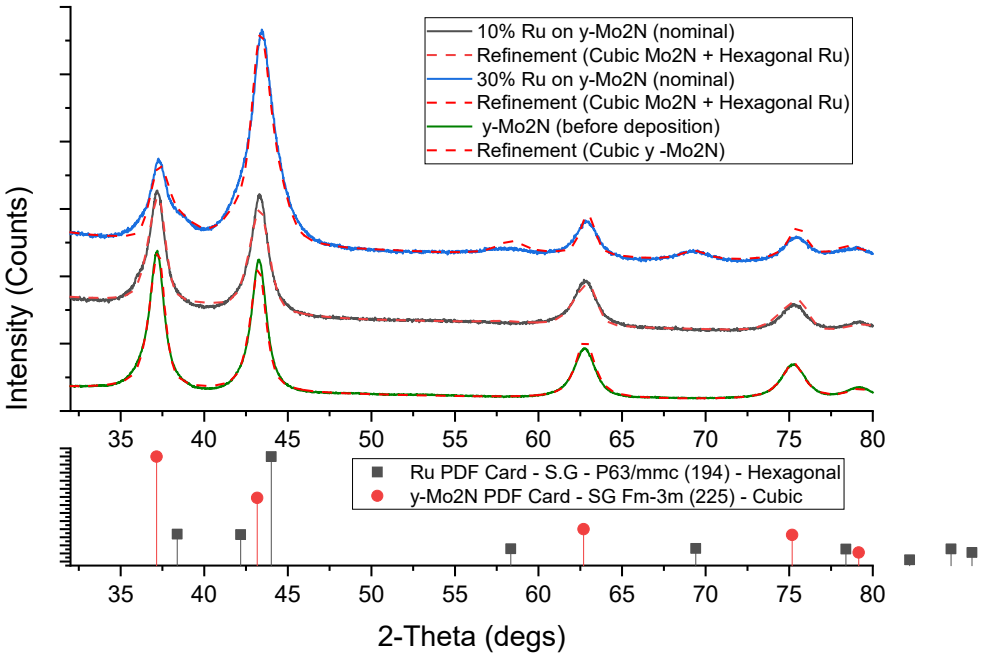

Figure C.3-1 Lab XRD of Mo_2N (Cubic F or C700 sample), 10% Ru-Mo_2N and 30% Ru-Mo_2N composited

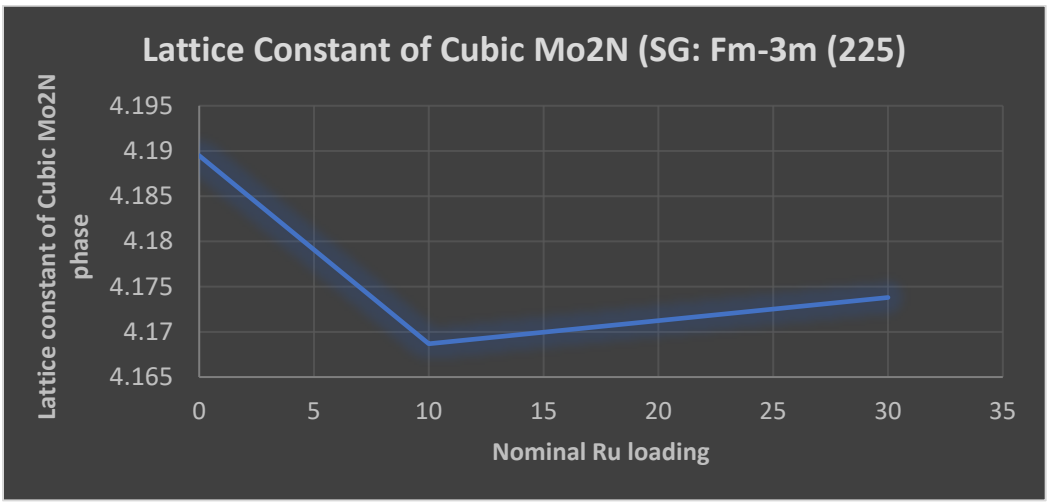

Figure C.3-2 : Lattice constant of Mo_2N with varying Ru loading in Ru-Mo_2N composites.

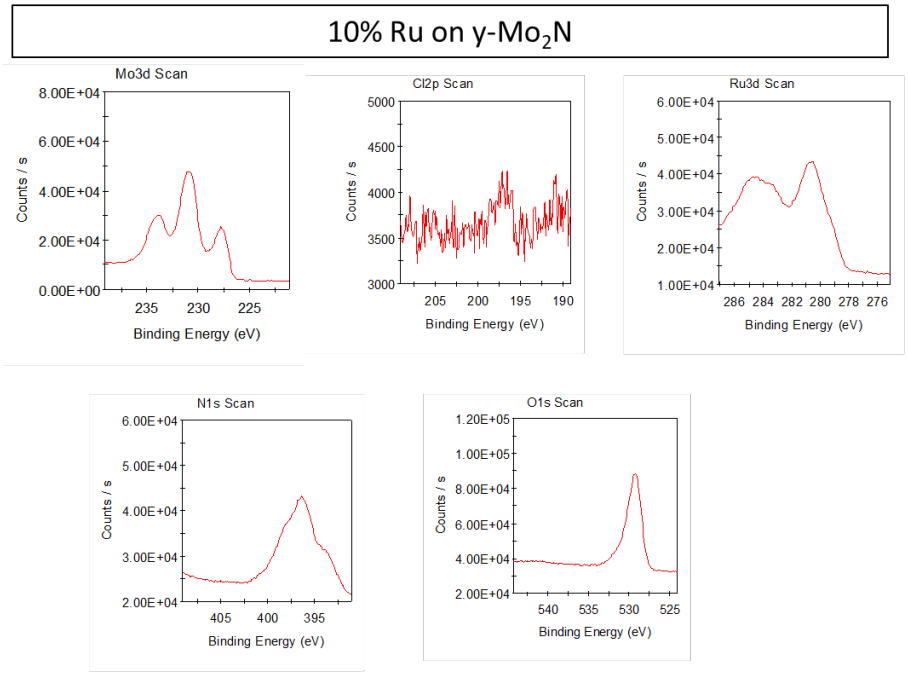

Figure C.3-3 XPS of 10% Ru-Mo_2N composite

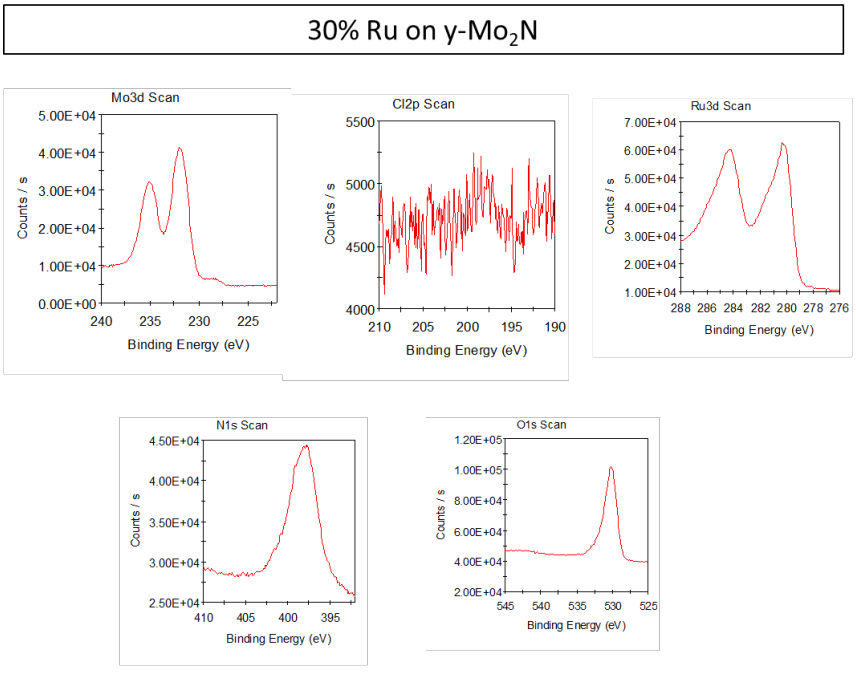

Figure C.3-4 XPS of 30% Ru-Mo_2N composite

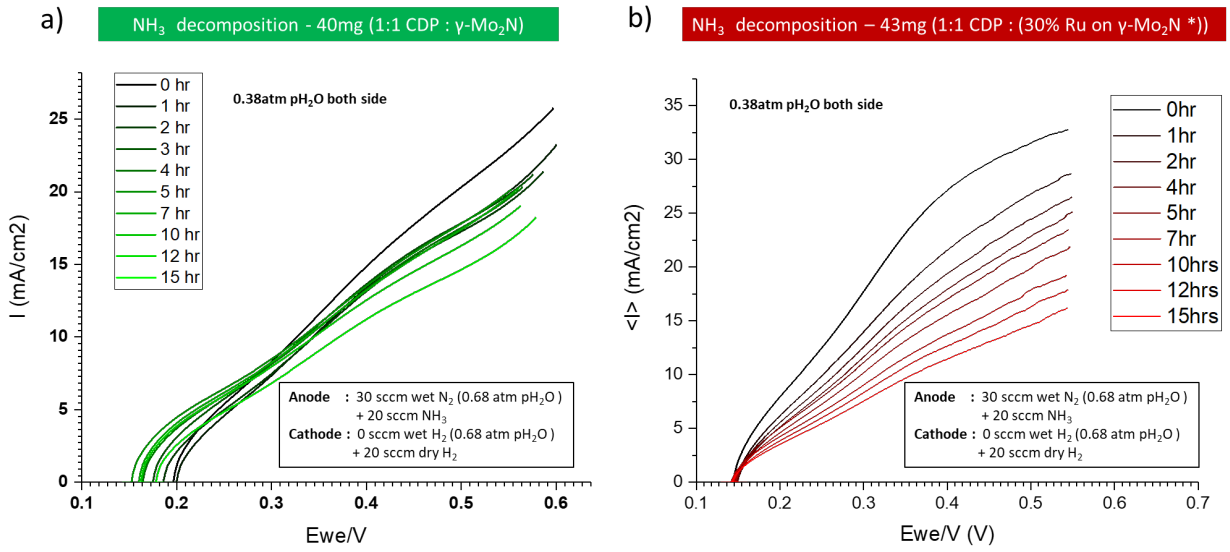

Figure C.3-5 SAHP polarization curves using (a) Mo_2N (b) 30% Ru-Mo_2N.

C.4 Synthesis of $SrTaO_2N$: Ruddlesden-Popper compound

Layered perovskites have shown to improve the photocatalytic water-splitting activity compared to chemically similar non-layered perovskites, and more importantly the oxynitride perovskite further provides the band edge in the visible range for increased solar spectrum utilizaztion at practical conditions.[248] Sr_2TaON_3 ($SrO{\cdot}SrTaO_2N$) is one such example, having only tantalum and an alkaline-earth metal shows K_2NiF_4-type structure; Ruddlesden–Popper (RP) structure. Following work by Sarda et.al,[249] synthesis was carried out by typically mixing strontium carbonate ($SrCO_3$, Alfa Aeser 99.99%) and tantalum oxide (Ta_2O_5, Acros organics, 99.99%) powders in three Sr/Ta ratio ranging from Sr/Ta = 2, 2.5 and 3, using a mortal pestel for 30-40 minutes and then annealing the mixture in a box furnace at 1300°C in air for 5h. Annealing was repeated (max three times) after intermediate grinding until required single phase oxide precursor was obtained. Figure C.4-1 shows the diffraction pattern of the final oxide products. XRD patterns of the oxide precursors fired at 1300°C in air. XRD confirms monophasic, cubic

$Sr_6Ta_2O_{10.188}$ oxide were obtained for Sr/Ta = 2 ([a =8.26746]) and 2.5 ([a =8.30649]), while excess Strontium (Sr/Ta = 3) resulted in formation of the orthorhombic $Sr_6Ta_2O_{10.04}(H_2O)_{0.6}$ oxide phase [a =8.27788, b = 8.34424, c = 8.3328]. The corresponding peak position of PDF patterns of interests are shown below. As reported by Sarda et.al a linear increase in lattice parameter of the oxide phase was observed upon increasing Sr content as seen in Figure C.4-2. Geometric mean of lattice parameters was plotted for the hypothetical lattice constant for the orthorhombic oxide $Sr_6Ta_2O_{10.04}(H_2O)_{0.6}$ at Sr/Ta=3.

It was reported that upon ammonolysis, increasing content of SrO/ $Sr(OH)_2$ by-products was obtained along with Sr_2TaO_3N as the major product for Sr/Ta >=2.0. Thus, ammonlysis of Sr/Ta = 2 based cubic oxide precursor was carried out @1000C under 100sccm (VF = 356cm^3/min) ammonia for 24hrs. Slow ammonlysis kinetics requiring multiple ammonolysis step for the desired Ruddlesden–Popper oxynitride phase have been reported until major phase Sr_2TaO_3N is obtained upon no change by further ammonolysis. Figure C.4-3, shows the ammonolysis product XRD after 24hrs, 48hrs and 96hrs, with intermittent grinding for 30-40 min in ethanol after each 24hrs nitridation step. Unlike reported by Sarda et,al where complete ammonolysis was detected after two ammonolysis steps (total 48hrs), in present work, ammonolysis seems to be incomplete (even after four ammonolysis steps (total 96hrs), probably due to difference in ammonia flow rate, and sample size. Authors had reported the formation of $Sr(OH)_2$, SrO, SrO_2 and $SrTaO_2N$ as the secondary phases, however only $Sr(OH)_2$ and $SrTaO_2N$ were detected in our experiments. The distribution of product phases is shown in Table C.4-1. Finally, to achieve phase pure Sr_2TaO_3N, the 96hrs product from above was subjected to additional 24hrs of nitridation under higher flow rate of ammonia 750sccm, with the Lab XRD shown in Figure C.4-4. The % retained oxide(s) as secondary products with cumulative ammonolysis time is shown in Figure C.4-5.

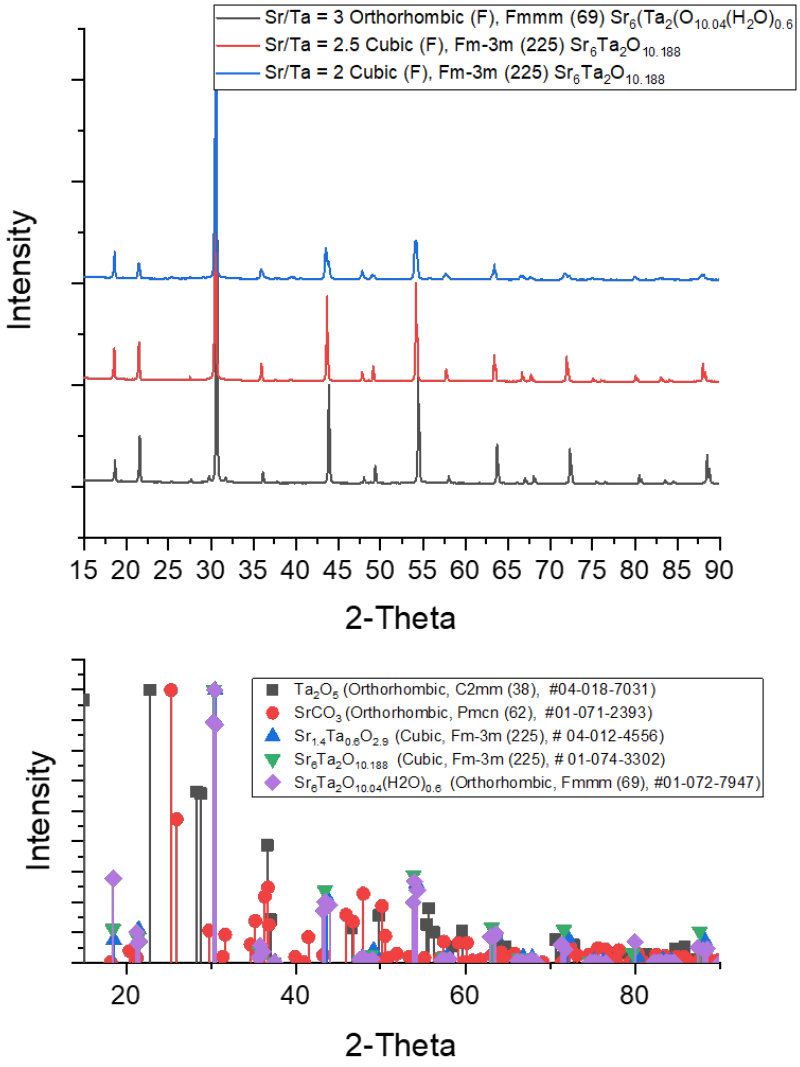

Figure C.4-1 Lab XRD patterns of various oxides mix synthesized starting with different ratio of Sr/Ta in reacting powders of the Solid-State synthesis reaction discussed above.

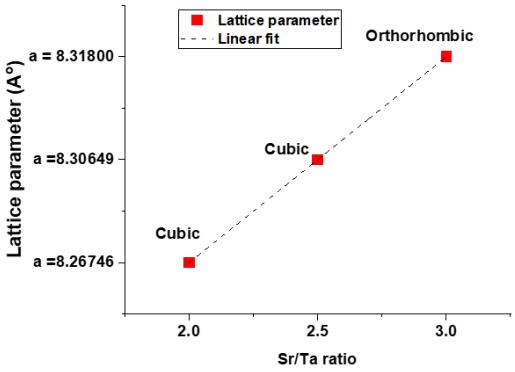

Figure C.4-2 : Linear increase in lattice parameter of the Strontium Tantalum oxide phase was observed upon increasing Sr content.

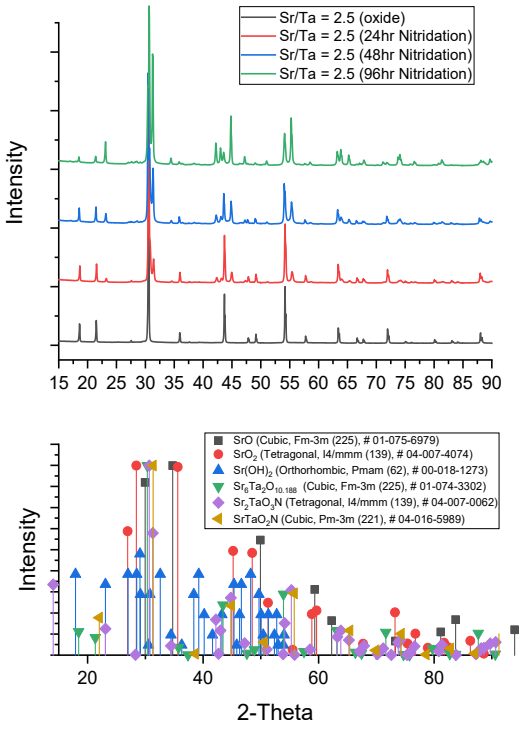

Figure C.4-3 : Lax XRD of ammonolysis products of Sr/Ta = 2.5 oxide precursor at 1273K, for 24hrs, 48hrs and 96hrs.

Table C.4-1 Phase fraction summary of resulting oxynitride mix (with secondary phases) post sequential ammonolysis of oxide precursor (Sr/Ta = 2.5 ratio)

Ammonolysis time @1000C	Cubic Oxide precursor	Phase Fraction post ammonolysis (Lab XRD)		
		Required Phase	Expected Secondary Phase	
		Sr_2TaO_3N	$SrTaO_2N$	Sr(OH)2
24 hr	69.9%	25.5 %	4.5 %	-
48 hr	39.1 %	40 %	6.9 %	13.8 %
96 hr	26.8 %	60.3 %	5.0 %	7.90 %

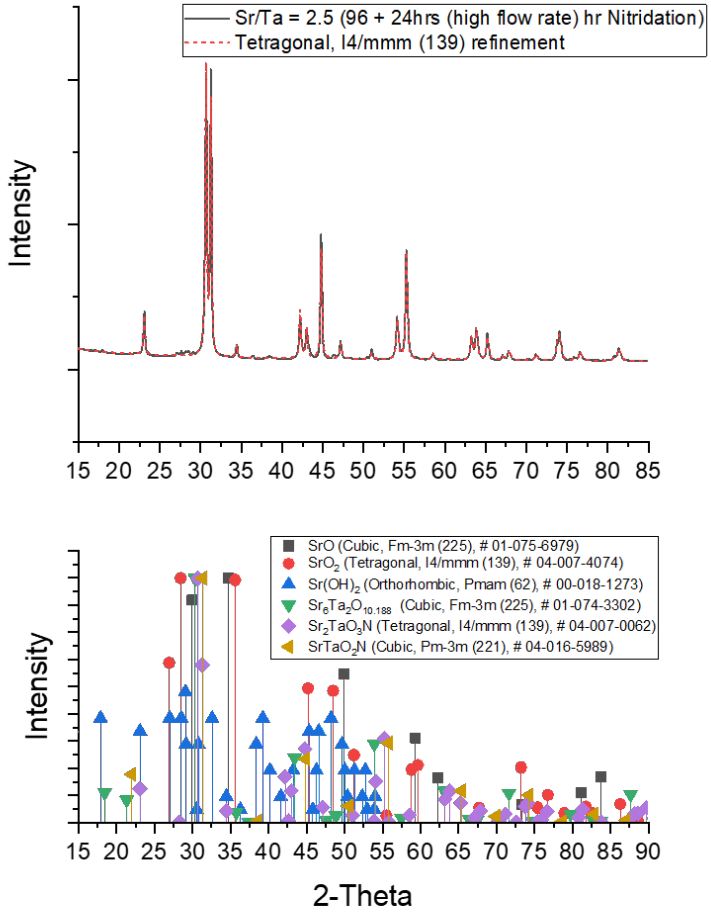

Figure C.4-4 : Lab XRD of targetted Tetragonal Sr_2TaO_3N phase, synthesized via multistep ammonolysis of Cubic Strontium Tantalum Oxide. Refined paramters using JADE; Crystallite size : 472 A |Tetragonal (A): a = 4.04498 ; b = 4.04498 ; c = 12.6103

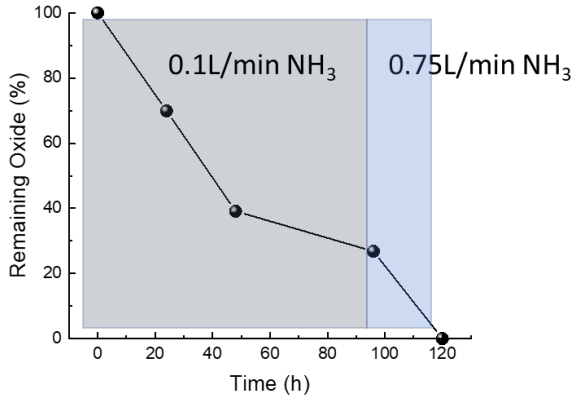

Figure C.4-5 Sequential progress of ammonolysis with decreasing retained oxide in final ammonolysis mixture after each run. However, phase pure oxynitride was only possible, after increasing the flow rate of ammonia by 7.5 times.

C.5 Ellipsometry studies of sputtered ITO thin films on quartz

A side project to sputter ITO films was pursued, wherein using sputtering, various thickness ITO films were coated, and measured to absorption, smoothness and thickness using Ellipsometry. All the films show >75% transmission within solar spectrum wavelengths, wherein 16nm ITO film on glass substrate was measured to be 90% transparent to visible light radiation.

Details of Sputtering parameters (Sputter AJA Orion, NUFAb clean room, Northwestern University) used for depositing these ITO films, including the attempts that failed are summarized with comments in Table C.5-1. Sputtering parameters needed to be optimized, to results in stable plasma for deposition. For each deposition attempt, both Si wafer and Glass slide was used. Films on Si wafer were used for Ellipsometry and those on Glass were analyzed with also with Ellipsometry but in transmission mode that allows from obtaining absorption coefficient with wavelength.

Ellipsometry (J.A. Woollam M2000U, NUANCE, Northwestern University) was performed and models were fit using a 3 layer model. To determine the model for this, ellipsometry of bare Si wafer was performed and fitted with 2 layer model from standard analysis recipe from Woollam, showing the

presence of ~0.7nm SiO2 layer, as shown in Figure C.5-2). For the ITO coated samples data analysis a custom 3 layer model was used to fitting. Layer 1 and Layer 2 combined represent the interface and native SiO2 oxide on Si wafer respectively, similar to reference model above of bare substrate. Additionally, Layer 3 fitted using a General Oscillator model was the actual deposited ITO film. Roughness was also introduced and refined for in the model. The proposed models produced fits with MSE values <10 which are considered good for transparent ellipsometry models, with thickness uncertainties ~0.1nm as shown in Figure C.5-5. Thickness and roughness were extracted from the analysis.

Thickness of ITO films (on Silicon wafer measured via Ellipsometry), with increasing sputtering time is shown along with roughness of films in Figure C.5-3. A sputtering rate of 8nm/min can be extracted from the slope of the linear plot between sputtering time and thickness of ITO films deposited. XPS was conducted on film obtained from 2min deposition (~40nmm thick), wherein all the three expected elements were detected, with quantification suggesting 10wt% Sn, 16wt%% oxygen and remainder Indium, as shown in Figure C.5-1.

Since a wide range of wavelength is used by the Ellipsometer (covering entirety of Solar spectrum wavelength), absorption as a function of wavelength can be obtained by running the Ellipsometer in transmission mode. This lets fit complex refractive index, which can then be used to obtain n and k curves variation with wavelength for different ITO thickness, which can then be used to make absorption plots. Absorption plots result from this study using ITO films coated on Glass substrate, shown in Figure C.5-4. At 16nm, the film is 90% transparent, which drops to 75% for thicker films. Although no linear relation was observed, possibly effected by bad quality of certain films, as some films were much rougher than the others. In future efforts can be taken to produce much smoother films, for which slight addition of O_2 with Ar during sputtering have been shown to help both smoothness and conductivity of films.[250-253]

Table C.5-1 Sputtering parameters for various coating attempts of ITO films.

Attempts	Deposition Pressure	Power Source	Gas	Substrate Temp	Deposition Time	Comment
1	3 mTorr	DC 120	Ar (20sccm)	RT	20 min	No Plasma detected.
2	3 mTorr	DC 140W	Ar (20sccm)	RT	20 min	Unstable Plasma arcing
3	4 mTorr	DC 140W	Ar (20sccm)	RT	20 min	Plasma stable for 1 min approx., then unstable.
4	5 mTorr	DC 140W	Ar (20sccm)	RT	20 min	Stable Plasma
4	5 mTorr	DC 140W	Ar (20sccm)	RT	15 min	Stable Plasma
5	5 mTorr	DC 140W	Ar (20sccm)	RT	10 min	Stable Plasma
6	5 mTorr	DC 140W	Ar (20sccm)	RT	5 min	Stable Plasma
7	5 mTorr	DC 140W	Ar (20sccm)	RT	2 min	Stable Plasma

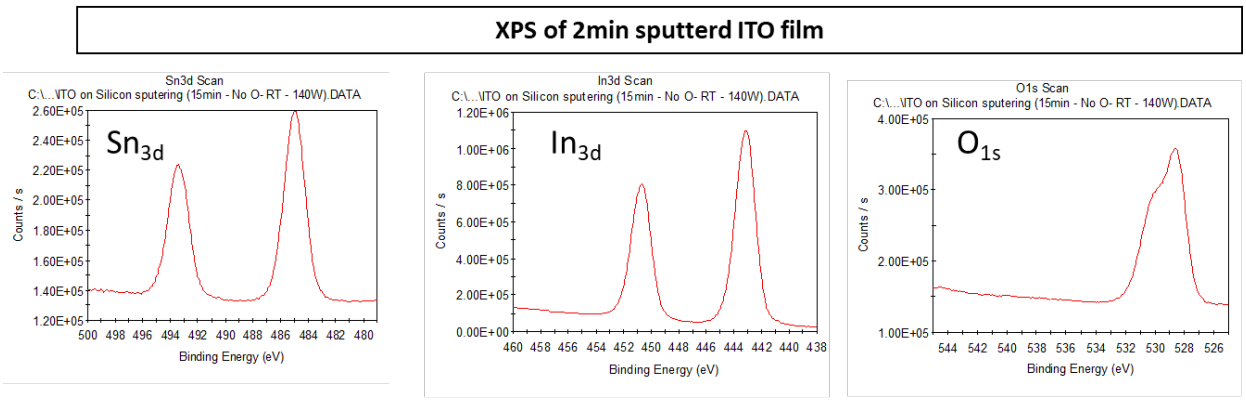

Figure C.5-1 XPS of ~40nm thick ITO film, showing the presence of expected elements.

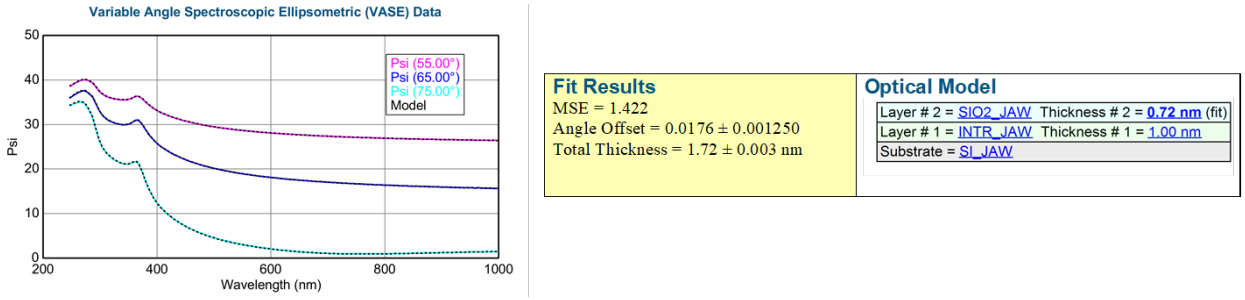

Figure C.5-2 Reference Ellipsometry model of Silicon wafer with native oxide on it.

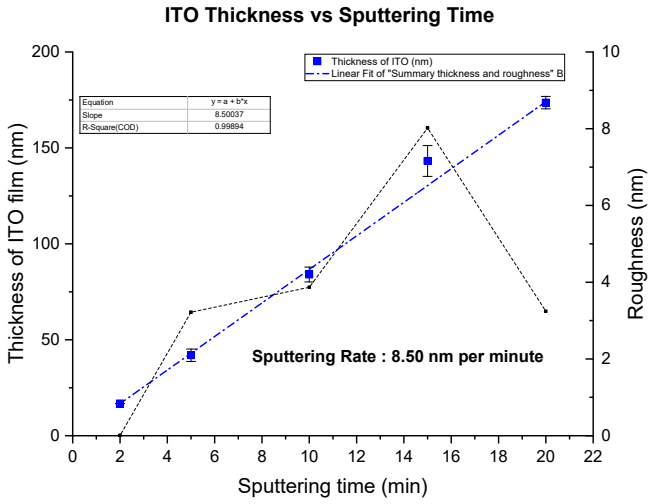

Figure C.5-3 Thickness of ITO films with sputtering time along with their respective roughness as determined from Ellipsometry.

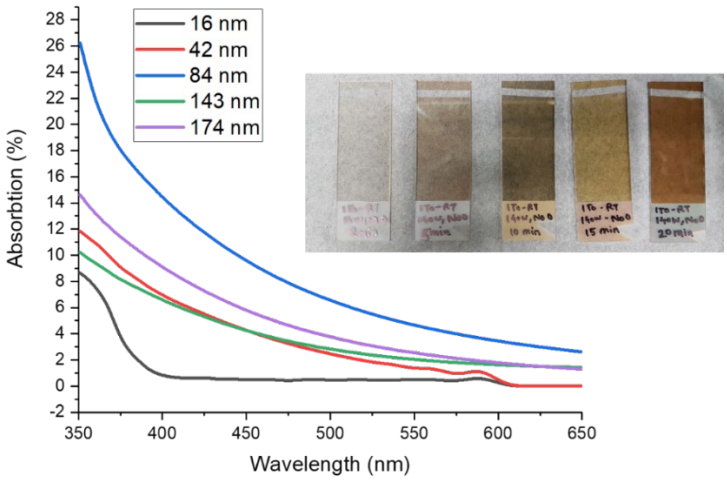

Figure C.5-4 Absorption plots of different thickness of ITO films on Glass substrate.

2 min sputtering

Fit Results
MSE = 3.220
Roughness = 2.62 ± 0.171 nm
E Inf = 1.237 ± 0.0224
IR Amp = 0.00 ± 0.0592
Angle Offset = 0.112 ± 0.0128
Total Thickness = 41.95 ± -0.100 nm

Optical Model
Roughness = **2.62 nm** (fit)
Layer # 3 = B-Spline Thickness # 3 = 40.23 nm
Layer # 2 = SIO2_JAW Thickness # 2 = 0.72 nm
Layer # 1 = INTR_JAW Thickness # 1 = 1.00 nm
Substrate = SI_JAW

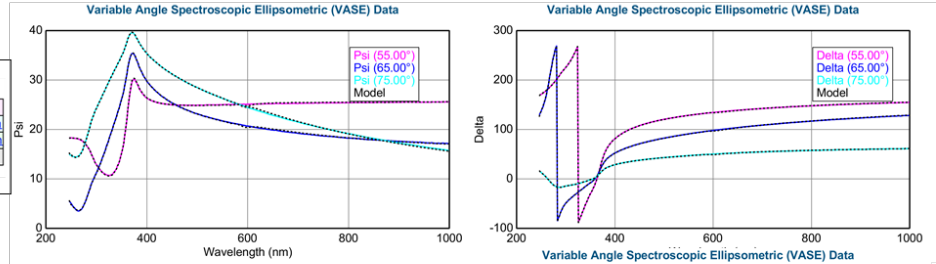

10 min sputtering

Fit Results
MSE = 3.868
Roughness = 0.20 ± 0.195 nm
E Inf = 0.775 ± 0.0390
IR Amp = 0.188 ± 0.0438
Angle Offset = 0.0282 ± 0.0210
Total Thickness = 84.04 ± -0.100 nm

Optical Model
Roughness = **0.20 nm** (fit)
Layer # 3 = B-Spline Thickness # 3 = 82.32 nm
Layer # 2 = SIO2_JAW Thickness # 2 = 0.72 nm
Layer # 1 = INTR_JAW Thickness # 1 = 1.00 nm
Substrate = SI_JAW

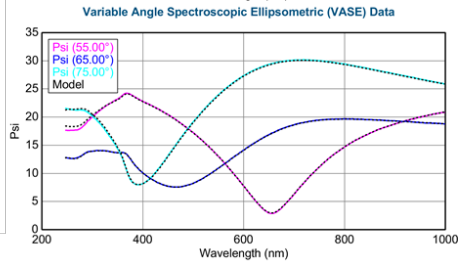

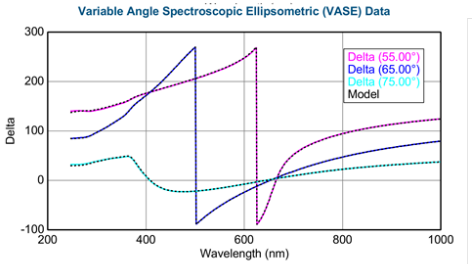

15 min sputtering

Fit Results
MSE = 8.019
Roughness = 2.77 ± 0.093 nm
E Inf = 2.930 ± 0.0799
IR Amp = 0.983 ± 0.0471
Angle Offset = -1.082 ± 0.0131
Total Thickness = 143.18 ± -0.100 nm

Optical Model
Roughness = **2.77 nm** (fit)
Layer # 3 = B-Spline Thickness # 3 = 141.46 nm
Layer # 2 = SIO2_JAW Thickness # 2 = 0.72 nm
Layer # 1 = INTR_JAW Thickness # 1 = 1.00 nm
Substrate = SI_JAW

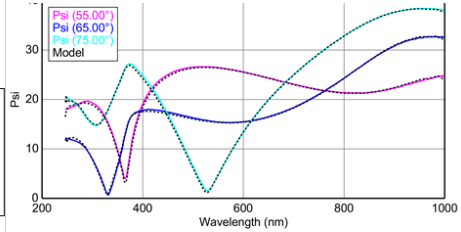

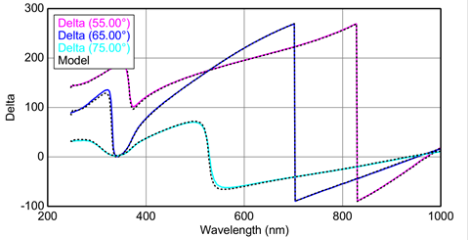

20 min sputtering

Fit Results
MSE = 3.242
Roughness = 6.07 ± 0.028 nm
Thickness # 3 = 171.87 ± 0.194 nm
E Inf = 1.800 ± 0.0648
IR Amp = 0.00 ± 0.0442
Angle Offset = -0.127 ± 0.0161
Total Thickness = 173.59 ± 0.194 nm

Optical Model
Roughness = **6.07 nm** (fit)
Layer # 3 = B-Spline Thickness # 3 = **171.87 nm** (fit)
Layer # 2 = SIO2_JAW Thickness # 2 = 0.72 nm
Layer # 1 = INTR_JAW Thickness # 1 = 1.00 nm
Substrate = SI_JAW

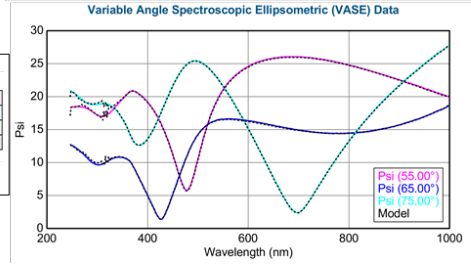

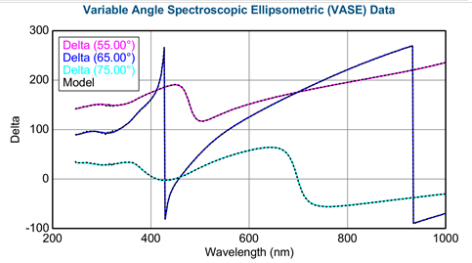

Figure C.5-5 Ellipsometry models of different thickness of ITO coated on Silicon wafer.

C.6 Low temperature ALD recipe development of Molybdenum Nitride Films

Molybdenum oxynitrides (C800, H700 and T700 samples) were shown as effective catalysts for HER in proof of concept SAEC studies in Chapter 5. These are also shown as effective ammonia decomposition catalyst, which can be improved by making a composite with Ru nanoparticles as discussed in Appendix C.3 Other collaborative applications including HER catalysis at room temperature liquid electrochemical application, isomerization and hydrogenation reaction of alkenes, are being pusued, which are proving the potential of this oxynitride system.

Since thin film approach offers various advantages compared to bulk powders. For future, Molybdenum nitride films can be employed to applications where these oxynitrides have shown potential so far. For example, using ALD coated MoN films on CDP particles, the overall active area where HER can occur in SAEC electrodes (discussed in Chapter 5) can be maximized with overall catalyst utilization improved (provided conditions are reducing enough for nm size films). ALD was proven to be an effective technique to deposit Pt catalyst on CDP electrolyte powders which were used for fabricate efficient SAFC cathodes in Chapter 2. Recently Ramesh, etal showed effectiveness of using ALD deposited MoN films on porous carbon substrates for HER at room temperature.[254]

Attempts to develop an ALD recipe for Molybdenum nitride thin films was performed. ALD literature on MoN films is sparse, with only one recipe that uses $Mo(CO)_6$ and NH_3 as the precursors, originally published by Nandi et.al for depositing amorphous MoN thin flims that were crystalized to δ-MoN phase upon high temperature ammonolysis (400^{o}C), and subsequently applied for energy storage in Li-Ion batteries.[216] Recently, same combination of precursors were used to coat thin MoN films for Diffusion barrier,[255] and the HER study by Ramesh et.al. [254]

However, for all these studies ALD deposition temperature of >150^{o}C was used, as 155 – 200^{o}C (slightly higher than the max 150^{0}C CDP stability temperature) was originally shown as the ALD window (with

~0.75nm/cycle growth rate) by Nandi et.al. Most films used for application were processed at temperature closer to 200°C. Therefore recipe optimization was needed.

ALD was performed on the Arradiance GEMStar XT-P reactor (NUFAb Clean room, Northwestern University) equipped with NH_3 gas as one of the reactive gases line, and $Mo(CO)_6$ in one of the precursor bottles. Si wafers were used as substrates, and the deposition temperature was fixed to maximum 150°C. Summary of all ALD parameters, including the 4 failed attempts leading to the successful Trial 5 is presented in Table C.6-1. Trial 1 was based on parameters discussed in literature, where in Flow Type ALD was performed with typical ALD cycle below, with precursor bottle at room temperature :

Mo precursor pulse → Purge → NH3 pulse → Purge.

100 cycles (aiming for ~5nm nominally thick films) did not result in any Mo XPS signal as seen in Figure C.6-1. Increasing the cycles to 200nm (trial 2) did not help. Low pressure of Mo precursor pulse, or inadequate diffusion time, leading to inadequate precursor adsorption on substrate (detected in pressure log and QCM plots of ALD runs, not shown here) was recognized as the reason for no deposition. Subsequently, the method of ALD was changed from “Flow Type” to “Exposure Type”. In this mode the presursors are pulsed and then the actuators are closed and the reactor is allowed to soak with the precursor before being purged. Additionally, this sub cycle is repeated multiple times before introducing the actual purge step. A complete ALD cycle looks like :

(Mo precursor pulse -> Soak Time -> Mini Purge) repeated x times → Purge → (NH_3 purge -> Mini purge) repeated y times → Purge

No soak time was used for NH3 pulse as it is supplied in gaseous form with high diffusion within chamber. This exposure mode was used for Trial 3, 4 and 5. With Trial 3 being unsuccessful, increasing precursor bottle temperature was realized important to increase Mo precursor vapor pressure. However, Mo(CO)6 volatility increases rapidly with temperature, and raising precursor bottle temperature to 85C lead to over pressurizing the ALD chamber in exposure mode in Trial 4. Finally, successful ALD was achieved by reducing the precursor bottle temperature to 40°C in Trial 5.

XPS scan of Mo-N thin film (nominally ~5nm thickness) is shown in Figure C.6-2. Elemental analysis shows $MoN_{0.66}$ composition, determined from scans taken after etching off surface impurities for 10 sec. Etching helps get rid of humps in both N and C scans, possibly due to excess leftover precursor, or adsorbed NH_3 on surface. After etching no oxygen or carbon signal was detected, suggesting the bulk of these films could be oxygen and carbon free. Bulk molybdenum nitrides synthesized in this work all contain oxygen in bulk, and it is interesting to realize that ALD provides a way to make oxygen free amorphous molybdenum nitride films.

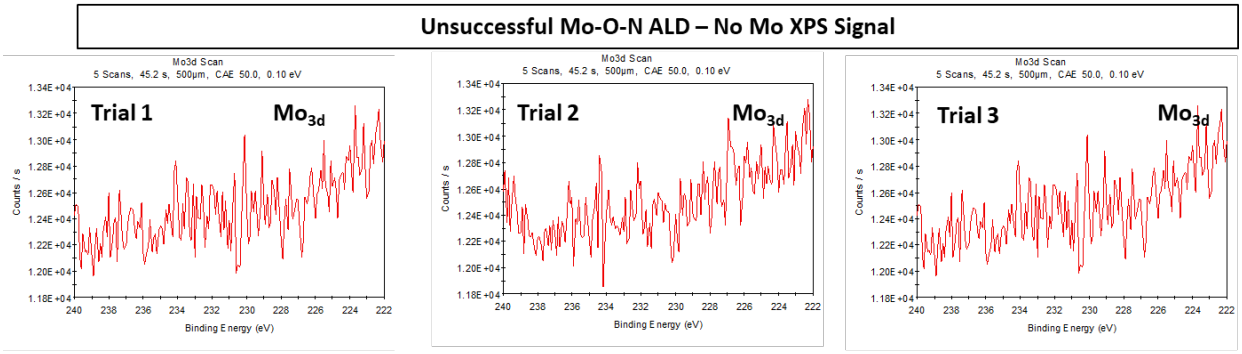

Figure C.6-1 XPS scan of failed ALD attempts to deposit Mo-N films.

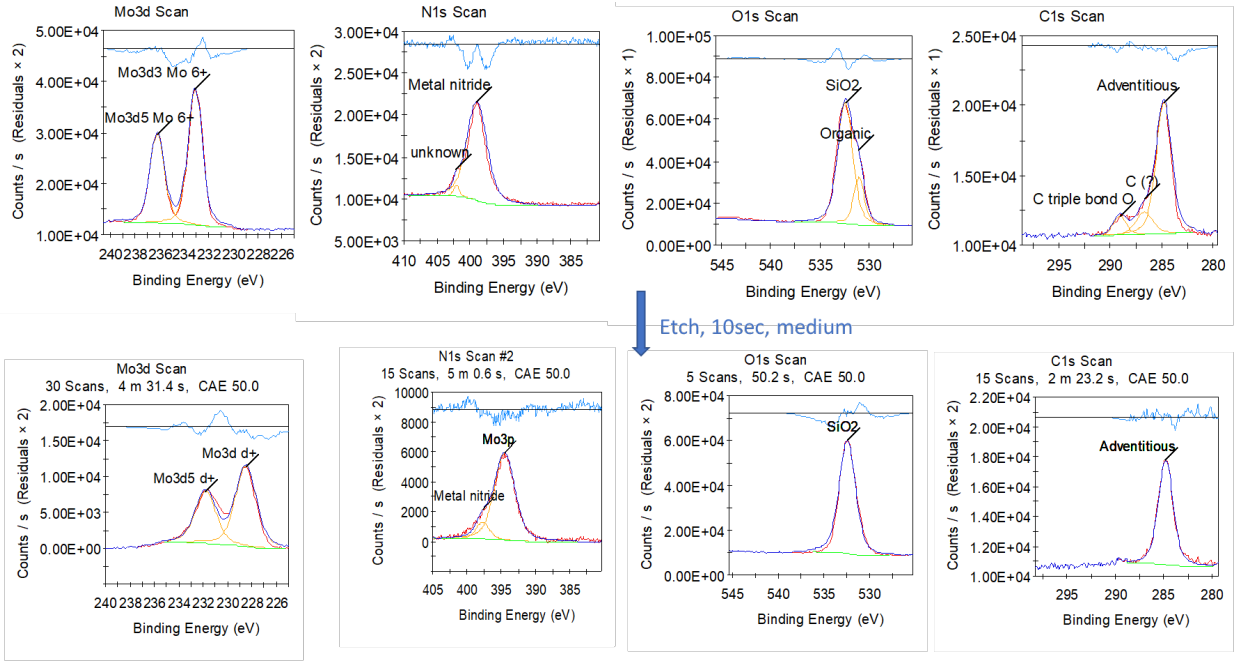

Figure C.6-2 XPS scan of Trial 5 successful MoNx ALD deposition.

Table C.6-1 : Summary of ALD attempts for successful ALD recipe development for MoNx films.

No	ALD Mode	Substrate	Chamber Temp (°C)	Platen Temp (°C)	Prec. Temp	ALD cycle (A/purge/B/purge)	Purge Flow (sccm)	Plasma Head protective gas	No of cycles	Thickness (nom.)[%]
Trial 1	Flow	Si wafer	150°C	150°C	RT	4s/15s/1.5s (40sccm)/15s	10 sccm (throughout)	75 sccm (throughout)	100	5 nm
Trial 2	Flow	Si wafer	160°C	160°C	RT	4s/15s/1.5s (40sccm)/15s	10 sccm (throughout)	75 sccm (throughout)	200	10 nm
Trial 3	Exposure	Si wafer	170°C	160°C	RT	Mo cycles (1s pulse, 2s wait, mini purge 1s) – 6 times Purge (20s) NH3 cycle(40sccm, 1.5s, no wait) – 1 times Purge (20s)	20 sccm (throughout)	75 sccm (throughout)	100	5 nm
Trial 4 (Overpressure)	Exposure	Si wafer	170°C	160°C	85°C	Mo cycles (1s pulse, 2s wait, mini purge 1s) – 4 times Purge (20s) NH3 cycle(40sccm, 1.5s, no wait) – 1 times Purge (20s)	0 sccm exposure 90 sccm (purge)	75 sccm (throughout)	100	5 nm
Trial 5	Exposure	Si wafer	170°C	160°C	40°C	Mo cycles (0.5s pulse, 2s wait, mini purge 1s) – 8 times Purge (20s) NH3 cycle(40sccm, 1.5s, no wait) – 1 times Purge (20s)	0 sccm exposure 20 sccm (Mo cycles purge) 90 sccm (purge)	45sccm (Mo exposure) 10 sccm (throughout)	100	5nm

REFERENCES

1. Pudukudy, M.; Yaakob, Z.; Mohammad, M.; Narayanan, B.; Sopian, K., Renewable hydrogen economy in Asia – Opportunities and challenges: An overview. *Renewable & sustainable energy reviews* **2014,** *30*, 743-757.
2. Lewis, N. S.; Nocera, D. G., Powering the Planet: Chemical Challenges in Solar Energy Utilization. *Proc. Natl. Acad. Sci. U. S. A.* **2006,** *103*, 15729.
3. Hunter, B. M.; Gray, H. B.; Müller, A. M., Earth-Abundant Heterogeneous Water Oxidation Catalysts. *Chem. Rev.* **2016,** *116*, 14120.
4. Bell, T.; Torrente-Murciano, L., H$_2$ Production via Ammonia Decomposition Using Non-Noble Metal Catalysts: A Review. **2016**.
5. Li, W.; Liu, J.; Zhao, D., Mesoporous Materials for Energy Conversion and Storage Devices. *Nat. Rev. Mater.* **2016,** *1*, 16023.
6. Blanco, H.; Faaij, A., A review at the role of storage in energy systems with a focus on Power to Gas and long-term storage. *Renewable & sustainable energy reviews* **2018,** *81* (P1), 1049-1086.
7. Stevenson, R., GETTING TO NEUTRAL: OPTIONS FOR NEGATIVE CARBON EMISSIONS IN CALIFORNIA. WILEY: HOBOKEN, 2020; Vol. 16, pp 1024-1025.
8. Jiang, D.-e.; Mahurin, S.; Dai, S., *Materials for carbon capture*. John Wiley and Sons: Hoboken, NJ, 2020.
9. Wilcox, J., *Carbon Capture*. 1st ed. 2012. ed.; Springer New York: New York, NY, 2012.
10. Ballerat-Busserolles, K.; Wu, Y.; Carroll, J. J., *Cutting-edge technology for carbon capture, utilization, and storage*. John Wiley and Sons: Hoboken, NJ, 2018.
11. Carbon-neutral fuels and energy carriers. Ringgold, Inc: Portland, 2011; Vol. 26.
12. Crabtree, G. W.; Dresselhaus, M. S.; Buchanan, M. V., The hydrogen economy. *Physics today* **2004,** *57* (12), 39-44.
13. Scipioni, A.; Manzardo, A.; Ren, J., *Hydrogen Economy*. 1st edition ed.; Academic Press: 2017.
14. Staffell, I.; Scamman, D.; Velazquez Abad, A.; Balcombe, P.; Dodds, P. E.; Ekins, P.; Shah, N.; Ward, K. R., The role of hydrogen and fuel cells in the global energy system. *Energy & Environmental Science* **2019,** *12* (2), 463-491.
15. Bezinge, A.; Yvon, K.; Muller, J.; Lengaeur, W.; Ettmayer, P., High-pressure high-temperature experiments on δ-MoN. *Solid state communications* **1987,** *63* (2), 141-145.
16. Evoen, V. Electrocatalysis in Solid Acid Fuel Cells. California Institute of Technology, California, United States (2016), 2016.
17. West, A. R., *Solid state chemistry and its applications*. Wiley: Chichester [West Sussex] ;, 1984.
18. Boysen, D. A.; Uda, T.; Chisholm, C. R. I.; Haile, S. M., High-Performance Solid Acid Fuel Cells Through Humidity Stabilization. *Science* **2004,** *303* (5654), 68-70.
19. Chisholm, C. R. I.; Boysen, D. A.; Papandrew, A. B.; Zecevic, S.; Cha, S.; Sasaki, K. A.; Varga, A.; Giapis, K. P.; Haile, S. M., From laboratory breakthrough to technological realization: The development path for solid acid fuel cells. *Electrochemical Society Interface* **2009,** *18* (3), 53-59.
20. Haile, S. M.; Chisholm, C. R. I.; Sasaki, K.; Boysen, D. A.; Uda, T., Solid acid proton conductors: from laboratory curiosities to fuel cell electrolytes. *Faraday Discuss.* **2007,** *134*, 17-39.
21. Navarrete, L.; Andrio, A.; Escolástico, S.; Moya, S.; Compañ, V.; Serra, J. M., Protonic Conduction of Partially-Substituted CsH_2PO_4 and the Applicability in Electrochemical Devices. *Membranes (Basel)* **2019,** *9* (4), 49.
22. Paik, H. DEVELOPMENT OF ELECTROCATALYSTS IN SOLID ACID FUEL CELLS. 2019.
23. Yan, Z.; Hitt, J. L.; Turner, J. A.; Mallouk, T. E., Renewable electricity storage using electrolysis. *Proceedings of the National Academy of Sciences - PNAS* **2020,** *117* (23), 12558-12563.
24. Fan, Z.; Chao, C.-C.; Hossein-Babaei, F.; Prinz, F. B., Improving solid oxide fuel cells with yttria-doped ceria interlayers by atomic layer deposition. *Journal of Materials Chemistry* **2011,** *21* (29).
25. Milewski, J.; Świrski, K.; Santarelli, M.; Leone, P., *Advanced Methods of Solid Oxide Fuel Cell Modeling*. 1st ed. 2011. ed.; Springer London: London, 2011.

26. Goñi-Urtiaga, A.; Presvytes, D.; Scott, K., Solid acids as electrolyte materials for proton exchange membrane (PEM) electrolysis: Review. *International journal of hydrogen energy* **2012,** *37* (4), 3358-3372.
27. Plymill, A., Application of Cesium Dihydrogen Phosphate in Intermediate Temperature Electrochemical Devices. ProQuest Dissertations Publishing: 2021.
28. Sanghvi, S., Superprotonic Solid Acids: Structure and Discovery. ProQuest Dissertations Publishing: 2019.
29. Bull, C. L.; McMillan, P. F.; Soignard, E.; Leinenweber, K., Determination of the crystal structure of δ-MoN by neutron diffraction. *Journal of Solid State Chemistry* **2004,** *177* (4-5), 1488-1492.
30. Gao, F., Fuel cell technology for automotive applications. Fuel cell vehicle applications and introduction to hydrogen economy. IEEE: United States, 2015.
31. Hultman, M.; Nordlund, C., Energizing technology: expectations of fuel cells and the hydrogen economy, 1990-2005. *History and technology* **2013,** *29* (1), 33-53.
32. O'Hayre, R. P., *Fuel cell fundamentals*. 2nd ed. ed.; John Wiley & Sons: Hoboken, N.J, 2009.
33. Srinivasan, S., *Fuel Cells : From Fundamentals to Applications*. 1st ed. 2006. ed.; Springer US: New York, NY, 2006.
34. Vielstich, W.; Lamm, A.; Gasteiger, H. A., *Handbook of fuel cells : fundamentals, technology, and applications*. Wiley: Chichester, England ;, 2003.
35. Stimming, U.; Jones, D.; Bele, P., Fuel Cells - from Fundamentals to Systems - Past, Present and Future. *Fuel cells (Weinheim an der Bergstrasse, Germany)* **2013,** *13* (1), 3-3.
36. Sammes, N.; Bove, R.; Stahl, K., Phosphoric acid fuel cells: Fundamentals and applications. *Current opinion in solid state & materials science* **2004,** *8* (5), 372-378.
37. Singhal, S. C.; Kendall, K., *High-temperature solid oxide fuel cells : fundamentals, design, and applicatons*. Elsevier Advanced Technology: New York, 2003.
38. Chisholm, C. R. I. Superprotonic phase transitions in solid acids: Parameters affecting the presence and stability of superprotonic transitions in the MH(n)XO(4) family of compounds (X = sulfur, selenium, phosphorus, arsenic; M = lithium, sodium, potassium,ammonium, rubidium, cesium). Ph.D., California Institute of Technology, Ann Arbor, 2003.
39. Ikeda, A.; Haile, S. M., The thermodynamics and kinetics of the dehydration of CsH 2PO 4 studied in the presence of SiO 2. *Solid State Ionics* **2012,** *213*, 63-71.
40. Louie, M. W.; Haile, S. M., Platinum thin film anodes for solid acid fuel cells. *Energy & environmental science* **2011,** *4* (10), 4230.
41. Louie, M. W.; Kislitsyn, M.; Bhattacharya, K.; Haile, S. M., Phase transformation and hysteresis behavior in Cs1−xRbxH2PO4. *Solid State Ionics* **2010,** *181* (3), 173-179.
42. Uda, T.; Haile, S. M., Thin-membrane solid-acid fuel cell. *Electrochemical and Solid-State Letters* **2005,** *8* (5), A245-A246.
43. Louie, M. W. C. Electrocatalysis in Solid Acid Fuel Cells. California Institute of Technology, 2011.
44. Sasaki, K. Electrochemical Characterization of Solid Acid Fuel Cell Electrodes. California Institute of Technology, Pasadena, 2010.
45. Papandrew, A. B.; Chisholm, C. R. I.; Elgammal, R. A.; Özer, M. M.; Zecevic, S. K., Advanced electrodes for solid acid fuel cells by platinum deposition on CsH2PO4. *Chemistry of Materials* **2011,** *23* (7), 1659-1667.
46. Lu, J.; Elam, J. W.; Stair, P. C., Atomic layer deposition—Sequential self-limiting surface reactions for advanced catalyst “bottom-up” synthesis. *Surface science reports* **2016,** *71* (2), 410-472.
47. George, S. M., Atomic layer deposition: An overview. *Chemical Reviews* **2010,** *110* (1), 111-131.
48. Choy, K. L., Chemical vapour deposition of coatings. *Progress in Materials Science* **2003,** *48* (2), 57-170.
49. Puurunen, R. L., Surface chemistry of atomic layer deposition: A case study for the trimethylaluminum/water process. *Journal of applied physics* **2005,** *97* (12), 121301.
50. Suntola, T.; Hyvarinen, J., Atomic Layer Epitaxy. *Annual Review of Materials Science* **1985,** *15* (1), 177-195.
51. Lu, J.; Elam, J. W.; Stair, P. C., Synthesis and Stabilization of Supported Metal Catalysts by Atomic Layer Deposition. *Accounts of Chemical Research* **2013,** *46* (8), 1806-1815.

52. Alén, P.; Ritala, M.; Arstila, K.; Keinonen, J.; Leskelä, M., Atomic Layer Deposition of Molybdenum Nitride Thin Films for Cu Metallizations. *Journal of The Electrochemical Society* **2005,** *152* (5).
53. Dasgupta, N. P.; Lee, H.-B.-R.; Bent, S. F.; Weiss, P. S., Recent Advances in Atomic Layer Deposition. *Chemistry of Materials* **2016,** *28* (7), 1943-1947.
54. Gordon, R. G.; Rahtu, A.; Lim, B. S., Atomic layer deposition of transition metals. *Nature materials* **2003,** *2* (11), 749-754.
55. Hämäläinen, J.; Ritala, M.; Leskelä, M., Atomic layer deposition of noble metals and their oxides. *Chemistry of Materials* **2014,** *26* (1), 786-801.
56. Chen, Y. W.; Prange, J. D.; Dühnen, S.; Park, Y.; Gunji, M.; Chidsey, C. E. D.; McIntyre, P. C., Atomic layer-deposited tunnel oxide stabilizes silicon photoanodes for water oxidation. *Nature Materials* **2011,** *10* (7), 539-544.
57. O'Neill, B. J.; Jackson, D. H. K.; Lee, J.; Canlas, C.; Stair, P. C.; Marshall, C. L.; Elam, J. W.; Kuech, T. F.; Dumesic, J. A.; Huber, G. W., Catalyst Design with Atomic Layer Deposition. *ACS catalysis* **2015,** *5* (3), 1804-1825.
58. Cullity, B. D., *Elements of x-ray diffraction*. 2d ed. ed.; Addison-Wesley Pub. Co.: Reading, Mass, 1978.
59. Dendooven, J.; Ramachandran, R. K.; Devloo-Casier, K.; Rampelberg, G.; Filez, M.; Poelman, H.; Marin, G. B.; Fonda, E.; Detavernier, C., Low-temperature atomic layer deposition of platinum using (methylcyclopentadienyl)trimethylplatinum and ozone. *Journal of Physical Chemistry C* **2013,** *117* (40), 20557-20561.
60. Ahmed, M.; Xinxin, G., A review of metal oxynitrides for photocatalysis. *Inorganic chemistry frontiers* **2016,** *3* (5), 578-59.
61. Fuertes, A., Metal oxynitrides as emerging materials with photocatalytic and electronic properties. *Materials Horizons* **2015,** *2* (5), 453-461.
62. Ghosh, S.; Jeong, S. M.; Polaki, S. R., A review on metal nitrides/oxynitrides as an emerging supercapacitor electrode beyond oxide. *Korean Journal of Chemical Engineering* **2018,** *35* (7), 1389-1408.
63. Maeda, K., (Oxy)nitrides with d0-electronic configuration as photocatalysts and photoanodes that operate under a wide range of visible light for overall water splitting. *Phys Chem Chem Phys* **2013,** *15* (26), 10537-48.
64. Maeda, K.; Domen, K., Oxynitride materials for solar water splitting. *MRS Bulletin* **2011,** *36* (1), 25-31.
65. Pozo-Gonzalo, C.; Kartachova, O.; Torriero, A. A. J.; Howlett, P. C.; Glushenkov, A. M.; Fabijanic, D. M.; Chen, Y.; Poissonnet, S.; Forsyth, M., Nanoporous transition metal oxynitrides as catalysts for the oxygen reduction reaction. *Electrochimica Acta* **2013,** *103*, 151-160.
66. Marchand, R.; Laurent, Y.; Guyader, J.; L'Haridon, P.; Verdier, P., Nitrides and oxynitrides: Preparation, crystal chemistry and properties. *Journal of the European Ceramic Society* **1991,** *8* (4), 197-213.
67. Chun, W.-J.; Ishikawa, A.; Fujisawa, H.; Takata, T.; Kondo, J. N.; Hara, M.; Kawai, M.; Matsumoto, Y.; Domen, K., Conduction and Valence Band Positions of Ta2O5, TaON, and Ta3N5 by UPS and Electrochemical Methods. *The journal of physical chemistry. B* **2003,** *107* (8), 1798-1803.
68. https://personal.icv.csic.es/fmunoz/oxynitride_electrolytes.html.
69. Böttger, P. H. M.; Lewin, E.; Patscheider, J.; Shklover, V.; Cahill, D. G.; Ghisleni, R.; Sobiech, M., Thermal conductivity of hard oxynitride coatings. *Thin Solid Films* **2013,** *549*, 232-238.
70. Kartachova, O.; Glushenkov, A. M.; Chen, Y.; Zhang, H.; Dai, X. J.; Chen, Y., Electrochemical capacitance of mesoporous tungsten oxynitride in aqueous electrolytes. *Journal of Power Sources* **2012,** *220*, 298-305.
71. Wu, H.; Lian, K., The Development of Pseudocapacitive Molybdenum Oxynitride Electrodes for Supercapacitors. *ECS Transactions* **2014,** *58* (25), 67-75.
72. Zhou, D.; Wu, H.; Wei, Z.; Han, B. H., Graphene-molybdenum oxynitride porous material with improved cyclic stability and rate capability for rechargeable lithium ion batteries. *Phys Chem Chem Phys* **2013,** *15* (39), 16898-906.

73. Abe, R.; Higashi, M.; Domen, K., Facile Fabrication of an Efficient Oxynitride TaON Photoanode for Overall Water Splitting into H2 and O2 under Visible Light Irradiation. *Journal of the American Chemical Society* **2010,** *132* (34), 11828-11829.
74. Abe, R.; Takata, T.; Sugihara, H.; Domen, K., Photocatalytic overall water splitting under visible light by TaON and WO3 with an IO3-/I- shuttle redox mediator. *Chem Commun (Camb)* **2005,** (30), 3829-31.
75. de Respinis, M.; Fravventura, M.; Abdi, F. F.; Schreuders, H.; Savenije, T. J.; Smith, W. A.; Dam, B.; van de Krol, R., Oxynitrogenography: Controlled Synthesis of Single-Phase Tantalum Oxynitride Photoabsorbers. *Chemistry of Materials* **2015,** *27* (20), 7091-7099.
76. Ahmad, H.; Kamarudin, S. K.; Minggu, L. J.; Kassim, M., Hydrogen from photo-catalytic water splitting process: A review. *Renewable and Sustainable Energy Reviews* **2015,** *43*, 599-610.
77. Fu, J., Advancing Synthetic Strategies to Materials for Solar-to-Fuel Conversion. ProQuest Dissertations Publishing: 2017.
78. Ebbinghaus, S. G.; Abicht, H.-P.; Dronskowski, R.; Müller, T.; Reller, A.; Weidenkaff, A., Perovskite-related oxynitrides – Recent developments in synthesis, characterisation and investigations of physical properties. *Progress in Solid State Chemistry* **2009,** *37* (2-3), 173-205.
79. Kanhere, P.; Chen, Z., A review on visible light active perovskite-based photocatalysts. *Molecules* **2014,** *19* (12), 19995-20022.
80. Rao, B. G.; Mukherjee, D.; Reddy, B. M., Chapter 1 - Novel approaches for preparation of nanoparticles. In *Nanostructures for Novel Therapy*, Ficai, D.; Grumezescu, A. M., Eds. Elsevier: 2017; pp 1-36.
81. Fuertes, A., Synthetic approaches in oxynitride chemistry. *Progress in Solid State Chemistry* **2018,** *51*, 63-70.
82. Gupta, S.; Tripathi, M., A review on the synthesis of TiO2 nanoparticles by solution route. *Open Chemistry* **2012,** *10* (2), 279-294.
83. Ikeda, S.; Hara, M.; Kondo, J. N.; Domen, K.; Takahashi, H.; Okubo, T.; Kakihana, M., Preparation of K2La2Ti3O10 by Polymerized Complex Method and Photocatalytic Decomposition of Water. *Chemistry of Materials* **1998,** *10* (1), 72-77.
84. Parashar, M.; Shukla, V. K.; Singh, R., Metal oxides nanoparticles via sol–gel method: a review on synthesis, characterization and applications. *Journal of Materials Science: Materials in Electronics* **2020,** *31* (5), 3729-3749.
85. Danks, A. E.; Hall, S. R.; Schnepp, Z., The evolution of 'sol–gel' chemistry as a technique for materials synthesis. *Materials Horizons* **2016,** *3* (2), 91-112.
86. Kakihana, M., Invited review "sol-gel" preparation of high temperature superconducting oxides. *Journal of Sol-Gel Science and Technology* **1996,** *6* (1), 7-55.
87. de Coelho Escobar, C.; dos Santos, J. H. Z., Effect of the sol–gel route on the textural characteristics of silica imprinted with Rhodamine B. *Journal of Separation Science* **2014,** *37* (7), 868-875.
88. Kajihara, K., Recent advances in sol–gel synthesis of monolithic silica and silica-based glasses. *Journal of Asian Ceramic Societies* **2013,** *1* (2), 121-133.
89. Isley, S. L.; Penn, R. L., Titanium Dioxide Nanoparticles: Effect of Sol−Gel pH on Phase Composition, Particle Size, and Particle Growth Mechanism. *The Journal of Physical Chemistry C* **2008,** *112* (12), 4469-4474.
90. Yoldas, B. E., Monolithic glass formation by chemical polymerization. *Journal of materials science* **1979,** *14* (8), 1843-1849.
91. Scherer, G. W., Aging and drying of gels. *Journal of Non-Crystalline Solids* **1988,** *100* (1), 77-92.
92. Pechini, M. P. U.S. Patent No. 3,330,697 1967.
93. Petrykin, V.; Kakihana, M., Chemistry and Applications of Polymeric Gel Precursors. In *Handbook of Sol-Gel Science and Technology: Processing, Characterization and Applications*, Klein, L.; Aparicio, M.; Jitianu, A., Eds. Springer International Publishing: Cham, 2018; pp 81-112.
94. Anderson, H. U.; Pennell, M. J.; Guha, J. P., *Polymeric synthesis of lead magnesium niobate powders*. American Ceramic Society Inc: United States, 1987.

95. Kakihana, M.; Arima, M.; Sato, T.; Yoshida, K.; Yamashita, Y.; Yashima, M.; Yoshimura, M., Highly active BaTi4O9/RuO2 photocatalyst by polymerized complex method. *Applied physics letters* **1996,** *69* (14), 2053-2055.
96. Huang, G.; Lu, C.-H.; Yang, H.-H., Chapter 3 - Magnetic Nanomaterials for Magnetic Bioanalysis. In *Novel Nanomaterials for Biomedical, Environmental and Energy Applications*, Wang, X.; Chen, X., Eds. Elsevier: 2019; pp 89-109.
97. Chirayil, T.; Zavalij, P. Y.; Whittingham, M. S., Hydrothermal Synthesis of Vanadium Oxides. *Chemistry of Materials* **1998,** *10* (10), 2629-2640.
98. Feng, S.; Xu, R., New Materials in Hydrothermal Synthesis. *Accounts of Chemical Research* **2001,** *34* (3), 239-247.
99. Mu, J.; Wang, J.; Hao, J.; Cao, P.; Zhao, S.; Zeng, W.; Miao, B.; Xu, S., Hydrothermal synthesis and electrochemical properties of V2O5 nanomaterials with different dimensions. *Ceramics International* **2015,** *41* (10, Part A), 12626-12632.
100. Sōmiya, S.; Roy, R., Hydrothermal synthesis of fine oxide powders. *Bulletin of Materials Science* **2000,** *23* (6), 453-460.
101. Chithambararaj, A.; Bose, A. C., Hydrothermal synthesis of molybdenum oxide microbelts. *AIP Conference Proceedings* **2012,** *1447* (1), 311-312.
102. Giardi, R.; Porro, S.; Topuria, T.; Thompson, L.; Pirri, C. F.; Kim, H.-C., One-pot synthesis of graphene-molybdenum oxide hybrids and their application to supercapacitor electrodes. *Applied Materials Today* **2015,** *1* (1), 27-32.
103. Michailovski, A.; Patzke, G. R., Hydrothermal Synthesis of Molybdenum Oxide Based Materials: Strategy and Structural Chemistry. *Chemistry – A European Journal* **2006,** *12* (36), 9122-9134.
104. Brophy, M. R.; Pilgrim, S. M.; Schulze, W. A., Synthesis of BaTaO2N Powders Utilizing NH3 Decomposition. *Journal of the American Ceramic Society* **2011,** *94* (12), 4263-4268.
105. Zaman, S. F.; Jolaoso, L. A.; Podila, S.; Al-Zahrani, A. A.; Alhamed, Y. A.; Driss, H.; Daous, M. M.; Petrov, L., Ammonia decomposition over citric acid chelated γ-Mo2N and Ni2Mo3N catalysts. *International Journal of Hydrogen Energy* **2018,** *43* (36), 17252-17258.
106. Tauc, J.; Grigorovici, R.; Vancu, A., Optical Properties and Electronic Structure of Amorphous Germanium. *physica status solidi (b)* **1966,** *15* (2), 627-637.
107. Jehn, H.; Ettmayer, P., The molybdenum-nitrogen phase diagram. *Journal of the Less Common Metals* **1978,** *58* (1), 85-98.
108. Dewangan, K.; Patil, S. S.; Joag, D. S.; More, M. A.; Gajbhiye, N. S., Topotactical Nitridation of α-MoO3 Fibers to γ-Mo2N Fibers and Its Field Emission Properties. *The Journal of Physical Chemistry C* **2010,** *114* (35), 14710-14715.
109. Gajbhiye, N. S.; Ningthoujam, R. S., Structural, electrical and magnetic studies of nanocrystalline δ-MoN and γ-Mo2N. *physica status solidi (c)* **2004,** *1* (12), 3449-3454.
110. Troitskaya, N. V.; Pinsker, Z. G., On the cubic nitride of molybdenum. *Soviet Phyics Crystallography* **1959,** *4*, 33-36.
111. Ganin, A. Y.; Kienle, L.; Vajenine, G. V., Synthesis and characterisation of hexagonal molybdenum nitrides. *Journal of Solid State Chemistry* **2006,** *179* (8), 2339-2348.
112. Sayag, C.; Bugli, G.; Havil, P.; Djéga-Mariadassou, G., Surface Studies of Passivated Molybdenum Oxynitride. *Journal of Catalysis* **1997,** *167* (2), 372-378.
113. Choi, J.-G.; Curl, R. L.; Thompson, L. T., Molybdenum nitride catalysts: I. Influence of the synthesis factors on structural properties. *Journal of Catalysis* **1994,** *146* (1), 218-227.
114. Tagliazucca, V.; Schlichte, K.; Schüth, F.; Weidenthaler, C., Molybdenum-based catalysts for the decomposition of ammonia: In situ X-ray diffraction studies, microstructure, and catalytic properties. *Journal of catalysis* **2013,** *305*, 277-289.
115. Tagliazucca, V.; Leoni, M.; Weidenthaler, C., Crystal structure and microstructural changes of molybdenum nitrides traced during catalytic reaction by in situ X-ray diffraction studies. *Phys Chem Chem Phys* **2014,** *16* (13), 6182-8.
116. Volpe, L.; Boudart, M., Compounds of Molybdenum and Tungsten with High Specific Surface Area. *J. Solid State Chem.* **1985,** *59*, 332.
117. Zhang, Y.; Xin, Q.; Rodriguez-Ramos, I.; Guerrero-Ruiz, A., Temperature dependence of the pseudomorphic transformation of MoO3 TO γ-Mo2N. *Materials Research Bulletin* **1999,** *34* (1), 145-156.

118. Volpe, L.; Boudart, M., Compounds of molybdenum and tungsten with high specific surface area: I. Nitrides. *Journal of solid state chemistry* **1985,** *59* (3), 332-347.
119. Panda, R. N.; Kaskel, S., Synthesis and characterization of high surface area molybdenum nitride. *Journal of materials science* **2006,** *41* (8), 2465-2470.
120. Marchand, R.; Gouin, X.; Tessier, F.; Laurent, Y., New routes to molybdenum nitrides and oxynitrides: preparation and characterization of new phases. In *The Chemistry of Transition Metal Carbides and Nitrides*, Oyama, S. T., Ed. Springer: 1996.
121. Jaggers, C. H.; Michaels, J. N.; Stacy, A. M., Preparation of High-Surface-Area Transition-Metal Nitrides: Mo2N and MoN. *Chem. Mater.* **1990,** *2*, 150.
122. Ludtke, T.; Schmidt, A.; Gobel, C.; Fischer, A.; Becker, N.; Reimann, C.; Bredow, T.; Dronskowski, R.; Lerch, M., Synthesis and crystal structure of delta-TaON, a metastable polymorph of tantalum oxide nitride. *Inorg Chem* **2014,** *53* (21), 11691-8.
123. Hitoki, G.; Takata, T.; Kondo, J. N.; Hara, M.; Kobayashi, H.; Domen, K., An oxynitride, TaON, as an efficient water oxidation photocatalyst under visible light irradiation (lambda < or = 500 nm). *Chem Commun (Camb)* **2002,** (16), 1698-9.
124. Swisher, J. H.; Read, M. H., Thermodynamic properties and electrical conductivity of Ta3N5 and TaON. *Metallurgical Transactions* **1972,** *3* (2), 493-498.
125. Yoon, S.; Maegli, A. E.; Matam, S. K.; Trottmann, M.; Hisatomi, T.; Leroy, C. M.; Grätzel, M.; Pokrant, S.; Weidenkaff, A., The Influence of the Ammonolysis Temperature on the Photocatalytic Activity of β-TaON. *International journal of photoenergy* **2013,** *2013*, 1-8.
126. Schilling, H.; Stork, A.; Irran, E.; Wolff, H.; Bredow, T.; Dronskowski, R.; Lerch, M., Gamma-TaON: a metastable polymorph of tantalum oxynitride. *Angew Chem Int Ed Engl* **2007,** *46* (16), 2931-4.
127. Orhan, E.; Tessier, F.; Marchand, R., Synthesis and energetics of yellow TaON. *Solid state sciences* **2002,** *4* (8), 1071-1076.
128. Wang, Z.; Hou, J.; Yang, C.; Jiao, S.; Huang, K.; Zhu, H., Hierarchical metastable γ-TaON hollow structures for efficient visible-light water splitting. *Energy & Environmental Science* **2013,** *6* (7).
129. Gao, Q.; Wang, S.; Ma, Y.; Tang, Y.; Giordano, C.; Antonietti, M., SiO(2)-surface-assisted controllable synthesis of TaON and Ta3N5 nanoparticles for alkene epoxidation. *Angew Chem Int Ed Engl* **2012,** *51* (4), 961-5.
130. Higashi, M.; Domen, K.; Abe, R., Fabrication of efficient TaON and Ta3N5 photoanodes for water splitting under visible light irradiation. *Energy & Environmental Science* **2011,** *4* (10).
131. Lu, D.; Hitoki, G.; Katou, E.; Kondo, J. N.; Hara, M.; Domen, K., Porous Single-Crystalline TaON and Ta3N5 Particles. *Chemistry of Materials* **2004,** *16* (9), 1603-1605.
132. Zhang, P.; Zhang, J.; Gong, J., Tantalum-based semiconductors for solar water splitting. *Chem Soc Rev* **2014,** *43* (13), 4395-422.
133. Zhou, Y.; Jin, P.; Chen, S.; Zhu, Y., Tantalum nitride nanowires: Synthesis and characterization. *Materials Letters* **2014,** *136*, 168-170.
134. George, P. P.; Gedanken, A.; Makhlouf, S. B.-D.; Genish, I.; Marciano, A.; Abu-Mukh, R., Synthesis and characterization of titanium nitride, niobium nitride, and tantalum nitride nanocrystals via the RAPET (reaction under autogenic pressure at elevated temperature) technique. *Journal of Nanoparticle Research* **2009,** *11* (4), 995-1003.
135. Lee, Y.-J.; Kim, D.-Y.; Nersisyan, H. H.; Lee, K.-H.; Han, M.-H.; Kang, K.-S.; Bae, K.-K.; Lee, J.-H., Rapid solid-phase synthesis for tantalum nitride nanoparticles and coatings. *International Journal of Refractory Metals and Hard Materials* **2013,** *41*, 162-168.
136. Terao, N., Structure of Tantalum Nitrides. *Japanese Journal of Applied Physics* **1971,** *10* (2), 248-259.
137. Stamnfl, C.; Freeman, A. J., Stable and metastable structures of the multiphase tantalum nitride system. *Physical review. B, Condensed matter and materials physics* **2005,** *71* (2), 024111.1-024111.5.
138. Gao, Q.; Giordano, C.; Antonietti, M., Controlled Synthesis of Tantalum Oxynitride and Nitride Nanoparticles. *Small (Weinheim an der Bergstrasse, Germany)* **2011,** *7* (23), 3334-3340.
139. Oró-Solé, J.; Clark, L.; Kumar, N.; Bonin, W.; Sundaresan, A.; Attfield, J. P.; Rao, C. N. R.; Fuertes, A., Synthesis, anion order and magnetic properties of RVO3−xNx perovskites (R = La, Pr, Nd; 0 ≤ x ≤ 1). *Journal of Materials Chemistry C* **2014,** *2* (12), 2212-2220.

140. Zhang, L.; Song, Y.; Feng, J.; Fang, T.; Zhong, Y.; Li, Z.; Zou, Z., Photoelectrochemical water oxidation of LaTaON2 under visible-light irradiation. *International Journal of Hydrogen Energy* **2014,** *39* (15), 7697-7704.
141. Park, N.-Y.; Kim, Y.-I., Morphology and band gap variations of oxynitride LaTaON2 depending on the ammonolysis temperature and precursor. *Journal of Materials Science* **2012,** *47* (13), 5333-5340.
142. Si, W.; Pergolesi, D.; Haydous, F.; Fluri, A.; Wokaun, A.; Lippert, T., Investigating the behavior of various cocatalysts on LaTaON2 photoanode for visible light water splitting. *Phys Chem Chem Phys* **2016,** *19* (1), 656-662.
143. Higashi, M.; Abe, R.; Takata, T.; Domen, K., Photocatalytic Overall Water Splitting under Visible Light Using ATaO2N (A = Ca, Sr, Ba) and WO3 in a IO3−/I− Shuttle Redox Mediated System. *Chemistry of Materials* **2009,** *21* (8), 1543-1549.
144. Rasaki, S. A.; Zhang, B.; Anbalgam, K.; Thomas, T.; Yang, M., Synthesis and application of nano-structured metal nitrides and carbides: A review. *Progress in Solid State Chemistry* **2018,** *50*, 1-15.
145. Afify, H. H.; Hassan, S. A.; Abouelsayed, A.; Demian, S. E.; Zayed, H. A., Synthesis, characterization and structural control of nano crystalline molybdenum oxide MoO3 single phase by low cost technique. *Materials Chemistry and Physics* **2016,** *176*, 87-95.
146. Aika, K.-i.; Ozaki, A., Mechanism and isotope effect in ammonia synthesis over molybdenum nitride. *Journal of Catalysis* **1969,** *14* (4), 311-321.
147. Hargreaves, J. S. J., Nitrides as ammonia synthesis catalysts and as potential nitrogen transfer reagents. *Applied Petrochemical Research* **2014,** *4* (1), 3-10.
148. McKay, D.; Hargreaves, J. S. J.; Rico, J. L.; Rivera, J. L.; Sun, X. L., The influence of phase and morphology of molybdenum nitrides on ammonia synthesis activity and reduction characteristics. *Journal of Solid State Chemistry* **2008,** *181* (2), 325-333.
149. Volpe, L.; Boudart, M., Ammonia Synthesis on Molybdenum Nitride. *J. Phys. Chem.* **1986,** *90*, 4874.
150. Wyvratt, B. M.; Gaudet, J. R.; Pardue, D. B.; Marton, A.; Rudić, S.; Mader, E. A.; Cundari, T. R.; Mayer, J. M.; Thompson, L. T., Reactivity of Hydrogen on and in Nanostructured Molybdenum Nitride: Crotonaldehyde Hydrogenation. *ACS Catalysis* **2016,** *6* (9), 5797-5806.
151. Cao, B.; Veith, G. M.; Neuefeind, J. C.; Adzic, R. R.; Khalifah, P. G., Mixed close-packed cobalt molybdenum nitrides as non-noble metal electrocatalysts for the hydrogen evolution reaction. *J Am Chem Soc* **2013,** *135* (51), 19186-92.
152. Chen, W. F.; Sasaki, K.; Ma, C.; Frenkel, A. I.; Marinkovic, N.; Muckerman, J. T.; Zhu, Y.; Adzic, R. R., Hydrogen-evolution catalysts based on non-noble metal nickel-molybdenum nitride nanosheets. *Angew Chem Int Ed Engl* **2012,** *51* (25), 6131-5.
153. Morozan, A.; Goellner, V.; Zitolo, A.; Fonda, E.; Donnadieu, B.; Jones, D.; Jaouen, F., Synergy between molybdenum nitride and gold leading to platinum-like activity for hydrogen evolution. *Phys Chem Chem Phys* **2015,** *17* (6), 4047-53.
154. Ma, L.; Ting, L. R. L.; Molinari, V.; Giordano, C.; Yeo, B. S., Efficient hydrogen evolution reaction catalyzed by molybdenum carbide and molybdenum nitride nanocatalysts synthesized via the urea glass route. *Journal of Materials Chemistry A* **2015,** *3* (16), 8361-8368.
155. Cao, B.; Neuefeind, J. C.; Adzic, R. R.; Khalifah, P. G., Molybdenum Nitrides as Oxygen Reduction Reaction Catalysts: Structural and Electrochemical Studies. *Inorganic chemistry* **2015,** *54* (5), 2128-2136.
156. Lee, K.-H.; Lee, Y.-W.; Kwak, D.-H.; Moon, J.-S.; Park, A.-R.; Hwang, E.-T.; Park, K.-W., Single-crystalline mesoporous Mo2N nanobelts with an enhanced electrocatalytic activity for oxygen reduction reaction. *Materials Letters* **2014,** *124*, 231-234.
157. Pan, X.; Song, X.; Lin, S.; Bi, K.; Hao, Y.; Du, Y.; Liu, J.; Fan, D.; Wang, Y.; Lei, M., A facile route to graphite-tungsten nitride and graphite-molybdenum nitride nanocomposites and their ORR performances. *Ceramics International* **2016,** *42* (14), 16017-16022.
158. Sun, T.; Wu, Q.; Che, R.; Bu, Y.; Jiang, Y.; Li, Y.; Yang, L.; Wang, X.; Hu, Z., Alloyed Co–Mo Nitride as High-Performance Electrocatalyst for Oxygen Reduction in Acidic Medium. *ACS Catalysis* **2015,** *5* (3), 1857-1862.

159. Li, X.-l.; Xing, Y.; Wang, H.; Wang, H.-l.; Wang, W.-d.; Chen, X.-y., Synthesis and characterization of uniform nanoparticles of γ-Mo2N for supercapacitors. *Transactions of Nonferrous Metals Society of China* **2009,** *19* (3), 620-625.
160. Ruan, D.; Lin, R.; Jiang, K.; Yu, X.; Zhu, Y.; Fu, Y.; Wang, Z.; Yan, H.; Mai, W., High-Performance Porous Molybdenum Oxynitride Based Fiber Supercapacitors. *ACS Appl Mater Interfaces* **2017,** *9* (35), 29699-29706.
161. Gates-Rector, S.; Blanton, T., The Powder Diffraction File: a quality materials characterization database. *Powder Diffraction* **2019,** *34* (4), 352-360.
162. Gouin, X.; Marchand, R.; L'Haridon, P.; Laurent, Y., Action de l'ammoniac sur l'oxyde de molybdene MoO3. Caractérisation physico-chimique de la phase oxynitrure de type Mo2N γ. *Journal of Solid State Chemistry* **1994,** *109* (1), 175-180.
163. Miga, K.; Stanczyk, K.; Sayag, C.; Brodzki, D.; Djéga-Mariadassou, G., Bifunctional Behavior of Bulk MoOxNyand Nitrided Supported NiMo Catalyst in Hydrodenitrogenation of Indole. *Journal of Catalysis* **1999,** *183* (1), 63-68.
164. Lyutaya, M. D., Formation of nitrides of group 6 transition metals of the Periodic system. *Poroshkovaya Metallurgiya (Kiev)* **1979,** (3), 60-66.
165. Bull, C. L.; Kawashima, T.; McMillan, P. F.; Machon, D.; Shebanova, O.; Daisenberger, D.; Soignard, E.; Takayama-Muromachi, E.; Chapon, L. C., Crystal structure and high-pressure properties of γ-Mo2N determined by neutron powder diffraction and X-ray diffraction. *Journal of Solid State Chemistry* **2006,** *179* (6), 1762-1767.
166. Balasubramanian, K.; Huang, L.; Gall, D., Phase stability and mechanical properties of Mo1-xNx with 0 ≤ x ≤ 1. *Journal of Applied Physics* **2017,** *122* (19).
167. Kreider, M. E.; Stevens, M. B.; Liu, Y.; Patel, A. M.; Statt, M. J.; Gibbons, B. M.; Gallo, A.; Ben-Naim, M.; Mehta, A.; Davis, R. C.; Ievlev, A. V.; Nørskov, J. K.; Sinclair, R.; King, L. A.; Jaramillo, T. F., Nitride or Oxynitride? Elucidating the Composition–Activity Relationships in Molybdenum Nitride Electrocatalysts for the Oxygen Reduction Reaction. *Chemistry of Materials* **2020,** *32* (7), 2946-2960.
168. Chen, W.-F.; Muckerman, J. T.; Fujita, E., Recent developments in transition metal carbides and nitrides as hydrogen evolution electrocatalysts. *Chemical communications (Cambridge, England)* **2013,** *49* (79), 8896-899.
169. Chen, G.; Song, X.; Wang, S.; Chen, X.; Wang, H., Two-dimensional molybdenum nitride nanosheets modified Celgard separator with multifunction for Li S batteries. *Journal of power sources* **2018,** *408*, 58-64.
170. Du, R.; Yi, W.; Li, W.; Yang, H.; Bai, H.; Li, J.; Xi, G., Quasi-metal Microwave Route to MoN and Mo2C Ultrafine Nanocrystalline Hollow Spheres as Surface-Enhanced Raman Scattering Substrates. *ACS nano* **2020,** *14* (10), 13718-13726.
171. Guan, H.; Yi, W.; Li, T.; Li, Y.; Li, J.; Bai, H.; Xi, G., Low temperature synthesis of plasmonic molybdenum nitride nanosheets for surface enhanced Raman scattering. *Nature communications* **2020,** *11* (1), 3889-3889.
172. Wang, S.; Ge, H.; Han, W.; Li, Y.; Zhang, J.; Yu, X.; Qin, J.; Quan, Z.; Wen, X.; Li, X.; Wang, L.; Daemen, L. L.; He, D.; Zhao, Y., Synthesis of Onion-Like δ-MoN Catalyst for Selective Hydrogenation. *Journal of physical chemistry. C* **2017,** *121* (35), 19451-19460.
173. Lengauer, W., Formation of molybdenum nitrides by ammonia nitridation of MoCl5. *Journal of crystal growth* **1988,** *87* (2-3), 295-298.
174. Schönberg, N., *Acta Chem. Scand.* **1954,** (8), 204-207.
175. G. Ha¨gg, Z., *Phys. Chem. B* **1930,** *7*, 339.
176. N.V. Troitskaya, Z. G. P., *Kristallografiya* **1963,** *8*, 548–555.
177. Wang, S.; Antonio, D.; Yu, X.; Zhang, J.; Cornelius, A. L.; He, D.; Zhao, Y., The Hardest Superconducting Metal Nitride. *Scientific reports* **2015,** *5* (1), 13733-13733.
178. Song, X.; Yi, W.; Li, J.; Kong, Q.; Bai, H.; Xi, G., Selective Preparation of Mo2N and MoN with High Surface Area for Flexible SERS Sensing. *Nano letters* **2021,** *21* (10), 4410-4414.
179. Wang, L.; Zhang, K.; Pan, H.; Wang, L.; Wang, D.; Dai, W.; Qin, H.; Li, G.; Zhang, J., 2D molybdenum nitride nanosheets as anode materials for improved lithium storage. *Nanoscale* **2018,** *1* (4), 18936-18941.
180. Sears, V. F., Neutron scattering lengths and cross sections. *Neutron News* **1992,** *3* (3), 26-37.

181. Scott, J.; Thomas, P. J.; MacKenzie, M.; McFadzean, S.; Wilbrink, J.; Craven, A. J.; Nicholson, W. A. P., Near-simultaneous dual energy range EELS spectrum imaging. *Ultramicroscopy* **2008,** *108* (12), 1586-1594.
182. Egerton, R. F., *Electron Energy-Loss Spectroscopy in the Electron Microscope*. 3rd ed. 2011. ed.; Springer US: New York, NY, 2011.
183. Paul, R. L.; Şahin, D.; Cook, J. C.; Brocker, C.; Lindstrom, R. M.; O'Kelly, D. J., NGD cold-neutron prompt gamma-ray activation analysis spectrometer at NIST. *J. Radioanal. Nucl. Chem.* **2014,** *304*, 189.
184. Turkoglu, D.; Chen-Mayer, H.; Paul, R.; Zeisler, R., Assessment of PGAA capability for low-level measurements of H in Ti alloys. *Analyst (London)* **2017,** *142* (2), 3822-3829.
185. Popescu, G.; Herman, S.; Glover, S.; Spitz, H., Compton background suppression with a multi-element scintillation detector using high speed data acquisition and digital signal processing. *J. Radioanal. Nucl. Chem.* **2016,** *307*, 1949.
186. Toby, B. H.; Von Dreele, R. B., GSAS-II: the genesis of a modern open-source all purpose crystallography software package. *Journal of Applied Crystallography* **2013,** *46* (2), 544-549.
187. Ravel, B.; Newville, M., ATHENA, ARTEMIS, HEPHAESTUS: data analysis for X-ray absorption spectroscopy using IFEFFIT. *Journal of Synchrotron Radiation* **2005,** *12* (4), 537-541.
188. Lajaunie, L.; Boucher, F.; Dessapt, R.; Moreau, P., Quantitative use of electron energy-loss spectroscopy Mo-M2,3 edges for the study of molybdenum oxides. *Ultramicroscopy* **2015,** *149*, 1-8.
189. Cowley, J. M.; Spence, J. C. H.; Smirnov, V. V., The enhancement of electron microscope resolution by use of atomic focusers. *Ultramicroscopy* **1997,** *68* (2), 135-148.
190. Choi, J. G.; Thompson, L. T., XPS study of as-prepared and reduced molybdenum oxides. *Applied Surface Science* **1996,** *93* (2), 143-149.
191. Pande, P.; Deb, A.; Sleightholme, A. E. S.; Djire, A.; Rasmussen, P. G.; Penner-Hahn, J.; Thompson, L. T., Pseudocapacitive charge storage via hydrogen insertion for molybdenum nitrides. *Journal of Power Sources* **2015,** *289*, 154-159.
192. Statistical Descriptors of Crystallography. http://ww1.iucr.org/iucr-top/comm/cnom/statdes/recomm.html (accessed 31 July 2021).
193. Balasubramanian, K.; Khare, S. V.; Gall, D., Energetics of point defects in rocksalt structure transition metal nitrides: Thermodynamic reasons for deviations from stoichiometry. *Acta Materialia* **2018,** *159*, 77-88.
194. Ozsdolay, B. D.; Balasubramanian, K.; Gall, D., Cation and anion vacancies in cubic molybdenum nitride. *Journal of Alloys and Compounds* **2017,** *705*, 631-637.
195. Sing, M.; Neudert, R.; von Lips, H.; Golden, M. S.; Knupfer, M.; Fink, J.; Claessen, R.; Mücke, J.; Schmitt, H., The electronic structure of metallic K0.3MoO3 and insulating MoO3 from high-energy spectroscopy. *Physical review. B, Condensed matter and materials physics* **1999,** *60*, 8559-8568.
196. Chen, J.; Wei, Q., Phase transformation of molybdenum trioxide to molybdenum dioxide: An in-situ transmission electron microscopy investigation. *International journal of applied ceramic technology* **2017,** *14* (5), 1020-1025.
197. Buttler, A.; Spliethoff, H., Current status of water electrolysis for energy storage, grid balancing and sector coupling via power-to-gas and power-to-liquids: A review. *Renewable & sustainable energy reviews* **2018,** *82*, 2440-2454.
198. David, M.; Ocampo-Martínez, C.; Sánchez-Peña, R., Advances in alkaline water electrolyzers: A review. *Journal of energy storage* **2019,** *23*, 392-403.
199. Carmo, M.; Fritz, D. L.; Mergel, J.; Stolten, D., A comprehensive review on PEM water electrolysis. *International journal of hydrogen energy* **2013,** *38* (12), 4901-4934.
200. Ebbesen, S. D.; Jensen, S. H.; Hauch, A.; Mogensen, M. B., High Temperature Electrolysis in Alkaline Cells, Solid Proton Conducting Cells, and Solid Oxide Cells. *Chemical reviews* **2014,** *114* (21), 10697-10734.
201. Yamate, S.; Oishi, J.; Kayamori, T.; Otomo, J., Comprehensive Evaluation of Manufacturing Costs and Environmental Impacts for Solid Oxide Electrolyzer Cell Systems. *ECS Meeting Abstracts* **2020,** *MA2020-02* (40), 2626-2626.

202. Wang, F.; Wang, L.; Zhang, H.; Xia, L.; Miao, H.; Yuan, J., Design and optimization of hydrogen production by solid oxide electrolyzer with marine engine waste heat recovery and ORC cycle. *Energy Conversion and Management* **2021,** *229*, 113775.
203. Lim, D.-K.; Liu, J.; Pandey, S. A.; Paik, H.; Chisholm, C. R. I.; Hupp, J. T.; Haile, S. M., Atomic layer deposition of Pt@CsH2PO4 for the cathodes of solid acid fuel cells. *Electrochimica acta* **2018,** *288* (C), 12-19.
204. Forman, C.; Muritala, I. K.; Pardemann, R.; Meyer, B., Estimating the global waste heat potential. *Renewable & sustainable energy reviews* **2016,** *57*, 1568-1579.
205. Wang, C.; Lan, F.; He, Z.; Xie, X.; Zhao, Y.; Hou, H.; Guo, L.; Murugadoss, V.; Liu, H.; Shao, Q.; Gao, Q.; Ding, T.; Wei, R.; Guo, Z., Iridium-Based Catalysts for Solid Polymer Electrolyte Electrocatalytic Water Splitting. *ChemSusChem* **2019,** *12* (8), 1576-1590.
206. Anitha, V. P.; Vitta, S.; Major, S., Structure and properties of reactivity sputtered γ-Mo2N hard coatings. *Thin solid films* **1994,** *245* (1-2), 1-3.
207. Fujiwara, N.; Nagase, H.; Tada, S.; Kikuchi, R., Hydrogen Production by Steam Electrolysis in Solid Acid Electrolysis Cells. *ChemSusChem* **2021,** *14* (1), 417-427.
208. Chen, M.; Smart, T. J.; Wang, S.; Kou, T.; Lin, D.; Ping, Y.; Li, Y., The coupling of experiments with density functional theory in the studies of the electrochemical hydrogen evolution reaction. *Journal of Materials Chemistry A* **2020,** *8* (18), 8783-8812.
209. de Chialvo, M. R. G.; Chialvo, A. C., Hydrogen evolution reaction: Analysis of the Volmer-Heyrovsky-Tafel mechanism with a generalized adsorption model. *Journal of Electroanalytical Chemistry* **1994,** *372* (1), 209-223.
210. Gennero de Chialvo, M. R.; Chialvo, A. C., Kinetics of hydrogen evolution reaction with Frumkin adsorption: re-examination of the Volmer–Heyrovsky and Volmer–Tafel routes. *Electrochimica Acta* **1998,** *44* (5), 841-851.
211. Skúlason, E.; Tripkovic, V.; Björketun, M. E.; Gudmundsdóttir, S. d.; Karlberg, G.; Rossmeisl, J.; Bligaard, T.; Jónsson, H.; Nørskov, J. K., Modeling the Electrochemical Hydrogen Oxidation and Evolution Reactions on the Basis of Density Functional Theory Calculations. *Journal of physical chemistry. C* **2010,** *114* (42), 18182-18197.
212. Sheng, W.; Myint, M.; Chen, J. G.; Yan, Y., Correlating the hydrogen evolution reaction activity in alkaline electrolytes with the hydrogen binding energy on monometallic surfaces. *Energy & Environmental Science* **2013,** *6* (5), 1509-1512.
213. Ping, Y.; Nielsen, R. J.; Goddard, W. A., The Reaction Mechanism with Free Energy Barriers at Constant Potentials for the Oxygen Evolution Reaction at the IrO2 (110) Surface. *Journal of the American Chemical Society* **2017,** *139* (1), 149-155.
214. Hinnemann, B.; Moses, P. G.; Bonde, J.; Jørgensen, K. P.; Nielsen, J. H.; Horch, S.; Chorkendorff, I.; Nørskov, J. K., Biomimetic Hydrogen Evolution: MoS2 Nanoparticles as Catalyst for Hydrogen Evolution. *Journal of the American Chemical Society* **2005,** *127* (15), 5308-5309.
215. Miikkulainen, V.; Suvanto, M.; Pakkanen, T. A., Bis(tert-butylimido)-bis(dialkylamido) Complexes of Molybdenum as Atomic Layer Deposition (ALD) Precursors for Molybdenum Nitride: the Effect of the Alkyl Group. *Chemical Vapor Deposition* **2008,** *14* (3-4), 71-77.
216. Nandi, D. K.; Sen, U. K.; Choudhury, D.; Mitra, S.; Sarkar, S. K., Atomic layer deposited molybdenum nitride thin film: a promising anode material for Li ion batteries. *ACS Appl Mater Interfaces* **2014,** *6* (9), 6606-15.
217. Murphy, A. B.; Barnes, P. R. F.; Randeniya, L. K.; Plumb, I. C.; Grey, I. E.; Horne, M. D.; Glasscock, J. A., Efficiency of solar water splitting using semiconductor electrodes. *International Journal of Hydrogen Energy* **2006,** *31* (14), 1999-2017.
218. Hisatomi, T.; Kubota, J.; Domen, K., Recent advances in semiconductors for photocatalytic and photoelectrochemical water splitting. *Chem Soc Rev* **2014,** *43* (22), 7520-35.
219. Zhang, J.; Wang, X., Solar Water Splitting at lambda=600 nm: A Step Closer to Sustainable Hydrogen Production. *Angew Chem Int Ed Engl* **2015,** *54* (25), 7230-2.
220. Navarro Yerga, R. M.; Álvarez Galván, M. C.; del Valle, F.; Villoria de la Mano, J. A.; Fierro, J. L. G., Water Splitting on Semiconductor Catalysts under Visible-Light Irradiation. *ChemSusChem* **2009,** *2* (6), 471-485.

221. Scientific, T. S. W.-L. A. D. B. https://www.thomassci.com/Laboratory-Supplies/Manual-Burets/_/Ammonia-Dissociation-Buret.
222. Wohler, F., *Ann. Chim. Phys* **1825**, 29.
223. Bussan, D. D., Applications of molybdenum utilized in sensing devices. ProQuest Dissertations Publishing: 2011.
224. Glemser, O., Hauschild, U. & Lutz, G., Darstellung von Hydroxyden durch Anlagerung von atomarem Wasserstoff an Oxyde. . *Z. Für Anorg. Allg. Chem.* **1952,** *269*.
225. Glemser, O., Lutz, G. & Meyer, G., Über niedere Molybdänhydroxyde. *Z. Für Anorg. Allg. Chem.* **1956,** *285*, 173–180.
226. Glemser, O. L., G. Über Molybdänblau., *Z. Für Anorg. Allg. Chem.* **1951,** *264*, 17-33.
227. Birtill, J. J.; Dickens, P. G., Phase relationships in the system H xMoO 3 (0<x⩽2.0). *Materials research bulletin* **1978,** *13* (4), 311-316.
228. Dickens, P. G.; Birtill, J. J., Hydrogen molybdenum bronzes. *Journal of Electronic Materials* **1978,** *7* (5), 679-686.
229. Kurusu, Y., Thermal Behavior of a New Type Molybdenum Oxide Obtained by Oxidation of Molybdenum Powder or Molydenum Trioxide with Hydrogen Peroxide. *Bulletin of the Chemical Society of Japan* **1981,** *54* (1), 293-294.
230. Hohenberg, P.; Kohn, W., Inhomogeneous Electron Gas. *Physical review* **1964,** *136* (3B), B864-B871.
231. Baerends, E. J., Perspective on “Self-consistent equations including exchange and correlation effects”: Kohn W, Sham LJ (1965) Phys Rev A 140:133–1138. *Theoretical chemistry accounts* **2000,** *103* (3), 265-269.
232. Kresse, G.; Furthmüller, J., Efficiency of ab-initio total energy calculations for metals and semiconductors using a plane-wave basis set. *Computational Materials Science* **1996,** *6* (1), 15-50.
233. Kresse, G.; Furthmüller, J., Efficient iterative schemes for ab initio total-energy calculations using a plane-wave basis set. *Physical Review B* **1996,** *54* (16), 11169-11186.
234. Blöchl, P. E., Projector augmented-wave method. *Physical Review B* **1994,** *50* (24), 17953-17979.
235. Kresse, G.; Joubert, D., From ultrasoft pseudopotentials to the projector augmented-wave method. *Physical Review B* **1999,** *59* (3), 1758-1775.
236. Perdew, J. P.; Burke, K.; Ernzerhof, M., Generalized Gradient Approximation Made Simple. *Physical Review Letters* **1996,** *77* (18), 3865-3868.
237. Zunger, A.; Wei, S. H.; Ferreira, L. G.; Bernard, J. E., Special quasirandom structures. *Physical Review Letters* **1990,** *65* (3), 353-356.
238. van de Walle, A.; Asta, M.; Ceder, G., The alloy theoretic automated toolkit: A user guide. *Calphad* **2002,** *26* (4), 539-553.
239. Ong, S. P.; Richards, W. D.; Jain, A.; Hautier, G.; Kocher, M.; Cholia, S.; Gunter, D.; Chevrier, V. L.; Persson, K. A.; Ceder, G., Python Materials Genomics (pymatgen): A robust, open-source python library for materials analysis. *Computational Materials Science* **2013,** *68*, 314-319.
240. Kirklin, S.; Saal, J. E.; Meredig, B.; Thompson, A.; Doak, J. W.; Aykol, M.; Rühl, S.; Wolverton, C., The Open Quantum Materials Database (OQMD): assessing the accuracy of DFT formation energies. *npj Computational Materials* **2015,** *1* (1), 15010.
241. Saal, J. E.; Kirklin, S.; Aykol, M.; Meredig, B.; Wolverton, C., Materials Design and Discovery with High-Throughput Density Functional Theory: The Open Quantum Materials Database (OQMD). *JOM* **2013,** *65* (11), 1501-1509.
242. M. W. Chase, J., C. A. Davies, J. R. Downey, Jr., D. J. Frurip, R. A. McDonald, and A. N. S., JANAF Thermochemical Tables. *J. Phys. Chem.* **1985,** *Third Edition.*, Data 14.
243. Tang, C.; Hu, Q.; Li, F.; He, C.; Chai, X.; Zhu, C.; Liu, J.; Zhang, Q.; Zhu, B.; Fan, L., Coupled molybdenum carbide and nitride on carbon nanosheets: An efficient and durable hydrogen evolution electrocatalyst in both acid and alkaline media. *Electrochimica Acta* **2018,** *280*, 323-331.
244. Wagner, M.; Dreßler, C.; Lohmann-Richters, F. P.; Hanus, K.; Sebastiani, D.; Varga, A.; Abel, B., Mechanism of ion conductivity through polymer-stabilized CsH2PO4 nanoparticular layers from experiment and theory. *Journal of materials chemistry. A, Materials for energy and sustainability* **2019,** *7* (48), 27367-27376.

245. Yuan, X.-Z.; Song, C.; Wang, H.; Zhang, J., *Electrochemical Impedance Spectroscopy in PEM Fuel Cells : Fundamentals and Applications*. 1st ed. 2010. ed.; Springer London: London, 2010.
246. Gomathi, A.; Sundaresan, A.; Rao, C. N. R., Nanoparticles of superconducting γ-Mo2N and δ-MoN. *Journal of solid state chemistry* **2007,** *180* (1), 291-295.
247. Nandi, D. K.; Sahoo, S.; Kim, T. H.; Cheon, T.; Sinha, S.; Rahul, R.; Jang, Y.; Bae, J.-S.; Heo, J.; Shim, J.-J.; Kim, S.-H., Low temperature atomic layer deposited molybdenum nitride-Ni-foam composite: An electrode for efficient charge storage. *Electrochemistry Communications* **2018,** *93*, 114-118.
248. Kudo, A.; Miseki, Y., Heterogeneous photocatalyst materials for water splitting. *Chemical Society reviews* **2009,** *38* (1), 253-278.
249. Sarda, N. G.; Hayashi, T.; Takeuchi, Y.; Harada, K.; Murai, K.-I.; Moriga, T., A new synthesis route of perovskite-related Sr2TaO3N oxynitride via Sr2Ta6O10.188. 2016; Vol. 1790.
250. Amalathas, A. P.; Alkaisi, M. M., Effects of film thickness and sputtering power on properties of ITO thin films deposited by RF magnetron sputtering without oxygen. *Journal of materials science. Materials in electronics* **2016,** *27* (10), 11064-11071.
251. Chen, A.; Zhu, K.; Zhong, H.; Shao, Q.; Ge, G., A new investigation of oxygen flow influence on ITO thin films by magnetron sputtering. *Solar energy materials and solar cells* **2014,** *120*, 157-162.
252. Kosarian, A.; Shakiba, M.; Farshidi, E., Role of sputtering power on the microstructural and electro-optical properties of ITO thin films deposited using DC sputtering technique. *IEEJ transactions on electrical and electronic engineering* **2018,** *13* (1), 27-31.
253. Yang, S.; Sun, B.; Liu, Y.; Zhu, J.; Song, J.; Hao, Z.; Zeng, X.; Zhao, X.; Shu, Y.; Chen, J.; Yi, J.; He, J., Effect of ITO target crystallinity on the properties of sputtering deposited ITO films. *Ceramics international* **2020,** *46* (5), 6342-6350.
254. Ramesh, R.; Sawant, S. Y.; Nandi, D. K.; Kim, T. H.; Kim, D. H.; Han, S. M.; Jang, Y.; Ha, M. G.; Cho, M. H.; Yoon, T.; Kim, S. H., Hydrogen Evolution Reaction by Atomic Layer-Deposited MoNx on Porous Carbon Substrates: The Effects of Porosity and Annealing on Catalyst Activity and Stability. *ChemSusChem* **2020,** *13* (16), 4159-4168.
255. Kim, T. H.; Nandi, D. K.; Ramesh, R.; Han, S.-M.; Shong, B.; Kim, S.-H., Some Insights into Atomic Layer Deposition of MoN x Using Mo(CO)6 and NH3 and Its Diffusion Barrier Application. *Chemistry of materials* **2019,** *31* (20), 8338-8350.